Imperial College London
Department of Physics

Polymer/Fullerene Solution Processing: Impact on thin film morphology

Rajeev Dattani

30 September 2014

Submitted in part fulfilment of the requirements for the degree of
Doctor of Philosophy in Physics of Imperial College London
and the Diploma of Imperial College London

Declaration of Originality

The contents of this thesis is my own work. Any work carried out alongside collaborators is identified. Figures which have been reproduced or adapted from other sources are also identified and referenced.

Rajeev Dattani

The copyright of this thesis rests with the author and is made available under a Creative Commons Attribution Non-Commercial No Derivatives licence. Researchers are free to copy, distribute or transmit the thesis on the condition that they attribute it, that they do not use it for commercial purposes and that they do not alter, transform or build upon it. For any reuse or redistribution, researchers must make clear to others the licence terms of this work.

Abstract

Polymer:fullerene blends are commonly used in organic solar cells (OSCs) and solution based processing is currently the most widely used fabrication method (Vandewal et al., *Macromolecules*, **2013**, Thompson et al. *Angewandte Chemie*, **2008**) [1, 2]. However, the solution behaviour, polymer chain conformation and thermodynamic interactions within these systems, which critically impact thin film morphology, is not well understood.

In this work, a model ternary system is systematically investigated polystyrene (PS), C_{60} and toluene. PS was chosen as it is a flexible polymer and has been extensively studied in solution, thin films and melt, and C_{60} is an exceptionally well defined molecule. A range of PS molecular weights is investigated, from 18 to 1000 kg/mol, dilute to semidilute polymer solution regimes and the fullerene solutions (below and above its miscibility limit in toluene). No change in the polymer chain dimensions (R_g, R_h or ξ) is found. C_{60} is shown to aggregate in solution below the miscibility limit in toluene and is shown to be dependent on PS M_w, PS concentration and time. The results are consistent with polymer/colloid theory in the protein-limit. (Dattani et al. *Macromolecules*, **2014**) [3] Thin films with thicknesses ranging from 60 to 130 nm are fabricated from solutions in a homogenous and precipitated regime and the consequences for film formation and morphology under thermal annealing is investigated and quantified.

C_{60} clusters are grown in solution via light exposure and are the result of light-induced oxidation. C_{60} epoxides are present in the solution and an aggregation mechanism is proposed. C_{60} epoxidation and aggregation is found to be dependent on C_{60} concentration, laser power, solvent, temperature and time.

The knowledge gained from the model PS/C_{60}/toluene system is applied to systems containing the much-studied poly-3-hexylthiophene (P3HT)/phenyl-C61-butyric acid methyl ester (PCBM) pair, with qualitatively similar results observed. The change in film morphology, accessible by a simple change in processing conditions, offers a unique method for tuning device efficiencies with respect to the size of the fullerene domains.

Acknowledgements

I would like to thank my supervisor, Dr. João Cabral for his advice and guidance on the research presented in this thesis. I am indebted to Prof. Klaus Huber (Universität Paderborn, Germany) for his fantastic insights and suggestions which have helped shape the work in Chapters 4 and 5 and for the use of the ALV-CGS3 Static and Dynamic Light Scattering system. I also thank Prof. Jenny Nelson for useful discussions contributing to Chapter 6 and Prof. Natalie Stingelin for discussions at the early stages of this project. Funding is acknowledged from the Plastic Electronics DTC and EPSRC grant no. EP/G037515/1.

Small angle neutron time from Institut Laue-Langevin, Grenoble, France and ISIS, Didcot, UK is gratefully appreciated, without which the experiments presented in Chapter 4 would not have been possible. Assistance from Dr. Ralf Schweins (ILL) and Dr. Ann Terry (ISIS) during the experiments is also appreciated.

A number of colleagues have assisted with the results presented throughout this thesis who I would like to thank: Dr. Rolf Michels (Universität Paderborn, Germany) with light scattering experiments using the ALV-CGS3, Sheridan Few for quantum chemical calculations, James Bannock for synthesis and supply of P3HT and finally, Peter Haycock, Dr. Kirsty F. Gibson and Aaron J. Borg for NMR, FTIR and mass spectroscopies on C_{60} and $C_{60}O_x$ respectively.

I would like to thank my friends from Polymers and Microfluidics group and others from the Plastic Electronics DTC and Chemical Engineering department who are too numerous to list and were always good source of distractions and entertainment. In particular I acknowledge: Matthew Allinson, for his good humour, Carlos Gonzalez Lopez, always giving an alternate viewpoint and something else to consider, Dr. Him Cheng Wong for suggestions and conducting much of the background work on thin polymer/fullerene films and of course Dr. Alisyn Nedoma for a regular dose of encouragement and being instrumental in the development of all respects of my education.

Finally, I am grateful to my parents and sister for their patience and support throughout my several years of studying.

હું આ મહાનિબંધ નાની, બા અને દાદાને અર્પણ કરું છું.

I dedicate this thesis to Nani, Ba and Dada.

Contents

Abstract i

Acknowledgements ii

Introduction vii

1 Polymers and Colloids in Solution 1

1.1 Polymer Chains . . . 1
1.2 Polymer Dimensions . . . 2
1.3 Polymer Solutions . . . 3
1.4 Flory-Huggins Theory . . . 4
1.5 Hansen Solubility Parameters . . . 6
1.6 Polymer/Colloid Solution Theory . . . 7
1.7 Mechanisms of Colloid Aggregation . . . 8
1.7.1 Reaction-limited . . . 9
1.7.2 Ballistic . . . 10
1.7.3 Diffusion-limited . . . 10

2 Literature Review 11

2.1 Solutions of Polymers and Colloids . . . 11
2.1.1 Polymers . . . 11
2.1.2 Fullerene Aggregation . . . 13
2.1.3 Polymer Composite Solutions . . . 15
2.1.4 Summary . . . 17
2.2 Bulk Polymers and Composites . . . 17
2.2.1 Polymer/Polymer Blends . . . 17
2.2.2 Fullerenes . . . 18
2.2.3 Polymer Nanocomposite Melts . . . 19
2.2.4 Summary . . . 23
2.3 Thin Polymer Nanocomposite Films . . . 24
2.3.1 Pattern formation: dewetting and phase separation . . . 24
2.3.2 Polystyrene/C_{60} Thin Films . . . 25
2.3.3 Surface segregation . . . 27

2.3.4 Summary . . . 28
2.4 Applications of polymer nanocomposites . . . 28
2.4.1 Mechanical Reinforcement . . . 28
2.4.2 Active and Self Healing Materials . . . 29
2.4.3 Organic Solar Cells . . . 29
2.4.4 Summary . . . 30
2.5 Processing Methods . . . 30
2.5.1 Nucleating Agents . . . 30
2.5.2 Solvent Mixtures and Additives . . . 31
2.6 Overview and Problem Statement . . . 31

3 Experimental Techniques 33
3.1 Scattering Techniques . . . 33
3.1.1 Light Scattering . . . 33
3.1.2 Small Angle Neutron Scattering . . . 37
3.2 Thin Films . . . 42
3.2.1 Thin film preparation . . . 42
3.2.2 Optical Microscopy and Image Analysis . . . 42
3.2.3 Atomic Force Microscopy . . . 43
3.3 Rheology and Spectroscopy . . . 44
3.3.1 Rheology . . . 44
3.3.2 UV-Visible Spectroscopy . . . 44
3.3.3 Nuclear Magnetic Resonance . . . 45
3.3.4 Mass Spectroscopy . . . 45
3.3.5 Fourier Transform Infrared Spectroscopy . . . 45

4 Conformation and interaction of polystyrene in dilute to semidilute polymer/fullerene solutions 46
4.1 Introduction . . . 46
4.2 Experimental . . . 48
4.2.1 Materials . . . 48
4.2.2 Sample Preparation . . . 48
4.2.3 Data Analysis . . . 51
4.3 Preliminary Control Experiments . . . 52
4.3.1 UV-Visible Spectroscopy . . . 52
4.3.2 Static Light Scattering . . . 53
4.3.3 Rheology . . . 54
4.3.4 Dynamic Light Scattering . . . 55
4.3.5 Small Angle Neutron Scattering . . . 56
4.4 Results and Discussion . . . 59

4.5 Conclusions . . . 71

5 Polymer induced Fullerene Clustering: Impact on thin films 73
5.1 Fullerene clusters in solution . . . 73
5.1.1 Experimental . . . 73
5.1.2 C_{60} miscibility in toluene . . . 76
5.1.3 Results and Discussion . . . 77
5.2 Fullerene clusters in thin films . . . 89
5.2.1 Preliminary Experiments . . . 89
5.2.2 Results and Discussion . . . 91
5.2.3 Mechanism . . . 107
5.3 Bulk Samples . . . 112
5.4 Other systems studied . . . 115
5.5 Conclusions . . . 121

6 Pre-processed fullerene solutions impact on polymer composite thin films 124
6.1 Fullerene oxidation and clustering in solution . . . 126
6.1.1 Experimental . . . 126
6.1.2 Fitting DLS Correlation Functions . . . 127
6.1.3 Results and discussion . . . 128
6.1.4 Cluster Formation . . . 136
6.2 Oxidised C_{60} Clusters in Thin Films . . . 141
6.2.1 Experimental . . . 141
6.2.2 Results and Discussion . . . 141
6.3 Other systems studied . . . 149
6.4 Conclusions . . . 152

7 Summary and Outlook 154
7.1 Summary . . . 154
7.2 Outlook . . . 155

Appendices 157

Introduction

This thesis will focus on the configuration and streamlined fabrication of a model polymer/fullerene system towards the processing of an organic solar cell (OSC). These devices commonly consist of a polymer acceptor with a fullerene derivative such as phenyl-C61-butyric acid methyl ester (PCBM). Initially, a model system comprising of C_{60}, the simplest of the fullerene family, and polystyrene (PS) is studied. Polystyrene was selected because it codissolves with C_{60} in toluene, as well as the wide availability of its monodisperse and deuterated forms. In addition, PS is a widely studied polymer both in solution [4, 5], melt [6, 7] and thin films [8–10]. Also, recent work on OSC's has focussed on amorphous polymer/fullerene solar cells [11–13], the efficiencies of which are reported to be more consistent compared to semi-crystalline polymer/fullerene blends. Once the behaviour of the model system is understood, the concepts and ideas are transferred to PCBM and poly-3-hexylthiophene (P3HT).

OSCs have the potential to be processed via a range of techniques, from spin coating to ink jet printing, with the majority of techniques requiring a solution stage prior to thin film formation. Therefore, it is important that the solution properties of these three-component blends are well understood in order to successfully control thin film morphology and thus device performance.

An introduction to the theoretical aspects of polymers and polymer/colloid/solvent and colloid/solvent mixtures is given, followed by a detailed literature review covering the fundamental work on model polymer/colloid systems in solution, bulk and thin films as well as a number of applications for polymer nanocomposites with desired morphological qualities. The first results chapter examines the effect of fullerene addition to a polymer solution, then fullerene cluster formation due to polymer addition is reported and its effect on as cast and annealed thin film morphology and finally, the role of light processing is quantified in regards to fullerene clustering in solution, and the ramifications for thin film morphology are discussed.

1 Polymers and Colloids in Solution

This chapter will give an introduction to the theory of polymer physics and the techniques used. Initially the focus will be on properties of polymers in solution, characterised by the radius of gyration (R_g) and hydrodynamic radius (R_h), solvent quality, Flory-Huggins, polymer/colloid/solvent theories and colloid aggregation mechanisms.

1.1 Polymer Chains

A polymer consists of a series of monomers linked to form a long chain. Polymers are typically characterised by: the number of repeat units (monomers), N, which relates to their molecular weight, M_w, polydispersity (PDI) and of course the chemical structure of the repeat unit.

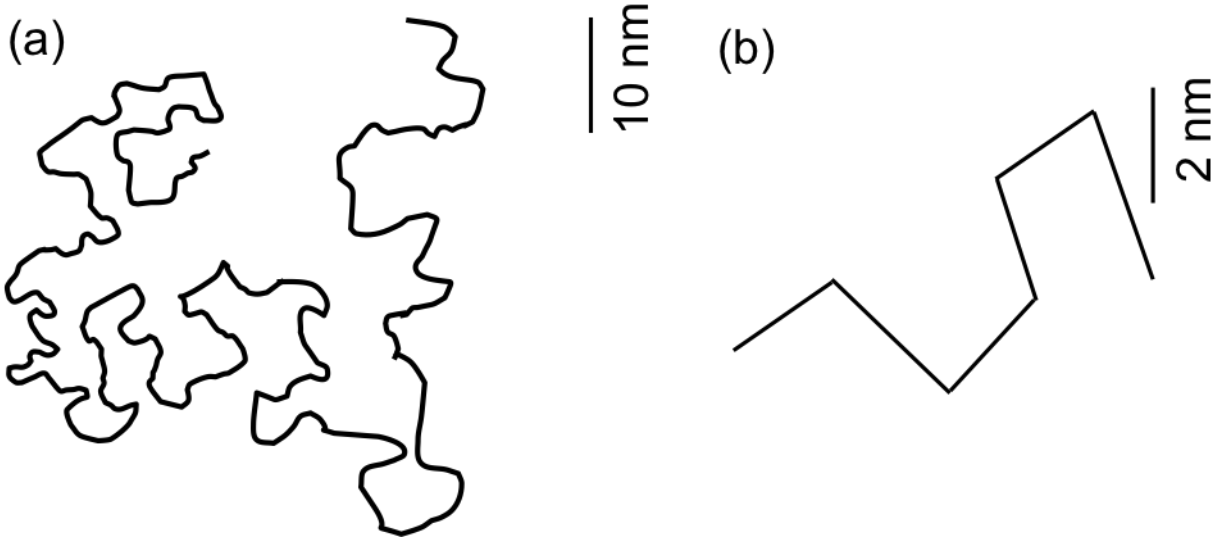


Figure 1.1: Schematic of a polymer chain under (a) low and (b) high magnification, illustrating a random walk compromising short rigid segments.

Polymer chains can be viewed in terms of a low magnification, depicted in Figure 1.1a, which illustrates their global properties. Zooming into a part of the polymer yields the high magnification shown in Figure 1.1b, i.e. the local properties such as the segment conformation and motion of monomers. Physical properties depend globally on the concentration of polymer in a solvent, and locally on the number density of volumetric units occupied by monomers as opposed

to solvent [14]

The concept of local and global properties are necessary to gain an understanding of a particular polymer for a given application, or conversely, finding a suitable polymer for a given application. Polymer chains are commonly idealised as a self avoiding random walk on a periodic lattice. In a polymer/solvent system the lattice sites are occupied by either the polymer or solvent molecules. This walk has a number of steps with the length of one step being the segment length, a. A polymer under theta conditions (theta conditions and solvent quality will be discussed in Section 1.3) is a self avoiding random walk, known as a Gaussian coil.

1.2 Polymer Dimensions

There are two characteristic radii used to quantify the 'size' of a polymer chain. The radius of gyration, R_g, and hydrodynamic radius, R_h. R_g can be described as the average distance between the segment length and the center of mass of the polymer [15]. Mathematically this is defined as:

$$R_g^2 = \frac{1}{N}\sum_{i=1}^{N} < r_i^2 > \tag{1.1}$$

where $r_i = |\mathbf{r}_i - \mathbf{r}_{cm}|$ is the distance of point i to the centre of mass and is a spatial average taken over all chains in the sample. Empirical scaling laws also exist for common flexible polymers which follow the form of $R_g \propto M_w^{\alpha}$, α is equal to 0.5 for Gaussian chains. This has been characterised for various polymers and for polystyrene $R_g = 0.27 \times M_w^{0.5}$ in the melt or θ conditions [16].

R_h is defined as the radius of a spherical particle which has the same frictional coefficient (ζ) as a colloid of the same radius [15]. To calculate this for a spherical colloid, the Navier-Stokes equation has to be solved assuming a no slip boundary condition, resulting in $\zeta = 6\pi R\eta$. When considering a system which is not a solid sphere such as a neutral polymer in solution, R is replaced with R_h.

Polymers in a good solvent are assumed to behave as hard spheres and so R_g and R_h are related by $R_h \cong \frac{2}{3}R_g$, using this alongside the Einstein relation ($D = \mu k_B T$) [14] yields Equation 1.2, where D, k_B, T and η are diffusion coefficient [m^2s^{-1}] (although commonly reported in cm^2s^{-1}), Boltzmann's constant [$1.38{\times}10^{-23}$ $m^2kgs^{-2}K^{-1}$], temperature [K] and the viscosity of the solvent [Pa.s] respectively [17].

$$R_h = \frac{k_B T}{6\pi\eta D} \tag{1.2}$$

1.3 Polymer Solutions

There are three types of solvents which are commonly used in literature: theta, good and bad solvents. Theta conditions occur when the interactions between monomers and monomer solvent interactions are identical, the repulsive excluded volume (v_e) effect balances with the attractive forces between the segments. For a good solvent v_e increases as the interactions between polymer segments and solvent molecules are thermodynamically favourable and the coil expands. In a bad solvent polymer coils will contract as these interactions are now unfavourable

In the dilute limit (Figure 1.2a), polymer chains are well separated, with $R_g \simeq N^v$, where N and v are the number of monomers per chain and characteristic exponent, respectively. For a polymer in a good solvent (e.g. PS in toluene) v = 0.588 [14]. Dilute polymer solutions are defined as being below the M_w-dependent overlap concentration (c^*) (Figure 1.2b), at this concentration individual polymer chains will begin to interpenetrate and entangle with one another. Above c^* the solution is said to be the semidilute regime (Figure 1.2c). There are a variety of definitions for c^*: $3M_w/4\pi N_A R_g^3$, $M_w/N_A R_g^3$, $C/A_2 M_w$ and $[\eta]^{-1}$. Where M_w is the molecular weight, N_A is Avogadro's constant, R_g is the radius of gyration of a single polymer chain in the dilute limit, C is a system dependent constant, A_2 is the second virial coefficient and η is the intrinsic viscosity. In the dilute limit the coils are assumed to behave as hard spheres due to the entropic penalty of the chains interpenetrating. For all calculations of c^* used here the first definition of c^* along with a value of R_g of polystyrene (PS) in toluene as defined by Huber et al. [4] (R_g [nm]=$0.0125 M_w^{0.595}$) is used. The approximation for c^* arises from the hard sphere approximation where the volume of a polymer sphere is $4\pi R_g^3/3$, the mass of a polymer is given by M_w/N_A, leading to the concentration at which the spheres will come into contact, $3M_w/4\pi N_A R_g^3$. At c^* there is the most efficient unit cell packing structure with 74% of space occupied by the polymer chains. In good solvents, polymers have an excluded volume. This is a repulsion of chain segments from other segments leading to an increase in R_g when compared to the theta conditions, e.g. in the melt.

Theoretically, above c^* solutions enter the semidilute regime and at which the coils begin to become packed, however it is important to note that there is no 'overlap point'. It is well known that the crossover from the dilute to the semidilute regime does not occur at the predicted value of c^*. Instead there is a wide concentration regime and a gradual shift in which solutions display semidilute properties, even if they are below c^* [18, 19]. Semidilute solutions are characterised by the correlation length, ξ, this is the length within which chains are screened from other chains. Scaling theory predicts that ξ depends on concentration as, $\xi \propto c^{-v/(3v-1)}$ [14], so that $\xi \propto c^{-0.77}$ for PS (using v = 0.588). Semidilute polymer solutions in good solvents, such as toluene, have been studied extensively by numerous groups [19–21] and the scaling law was found to be accurate by Hamada et al. [21] who found a scaling law of -0.77 for PS/toluene solutions above c^*, Brown and Nicolai [19] collated data from a range of sources for PS in several good solvents to find an expression relating ξ and c to be ξ[nm]=$0.27 \pm 0.1 \times c$[g/ml]$^{-0.72\pm0.01}$, and thus

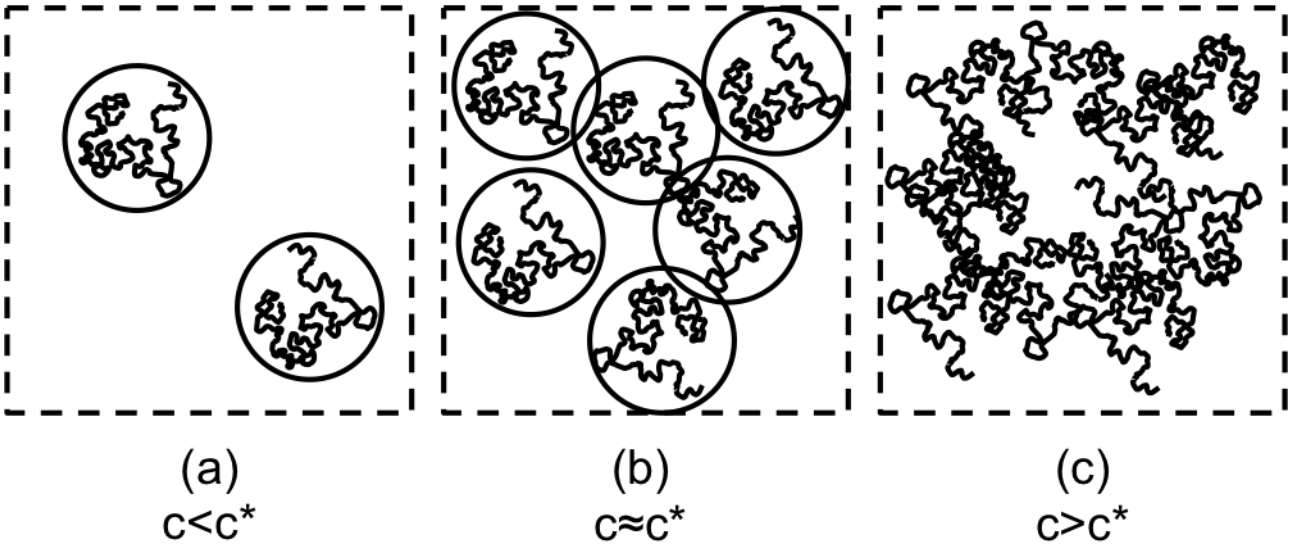


Figure 1.2: Polymer in solution from (a) dilute through to (b) overlap and (c) semidilute.

an exponent close to the predicted value of -0.77.

The Gibbs' free energy of a polymer/solvent system, as described by Flory [22], has the two usual terms - entropy and enthalpy. The entropy, S, describes how many arrangements of a chain can exist on the lattice for a given ϕ (where ϕ is the fraction of sites occupied by the monomer units). The energy term on the other hand describes the interaction between adjacent molecules, namely monomer-monomer, monomer-solvent and solvent-solvent interactions. These interactions are combined in the excess energy captured by the Flory interaction parameter, χ (discussed in more detail in Section 1.4). This is a dimensionless parameter which is dependent on the environmental conditions. For good solvents $\chi < 0.5$, bad solvents $\chi > 0.5$ and for theta conditions $\chi = 0.5$.

1.4 Flory-Huggins Theory

The field of polymer blends and the related thermodynamics of phase separation has been studied since the 1940s with publications by Flory [22] and Huggins [23]. Huggins first published on the thermodynamics of long chain polymers in solutions, which was followed by Flory on 'high polymer solutions' [22]. This gave rise to the Flory-Huggins treatment [17] which describes the main aspects of mixing in polymer-polymer binary mixtures. Extensions of the Flory-Huggins theory applicable to nanoparticles have also been proposed [24]. The Gibbs free energy of mixing, ΔG_m, can be used to find out whether mixing is thermodynamically favoured between two polymers, A and B.

$$\Delta G_m = G_{AB} - (G_A + G_B) \tag{1.3}$$

The Flory-Huggins treatment splits ΔG_m into two components: one describing the combinatorial entropy, ΔS_m, and the other given as an enthalpic term, ΔH_m.

$$\Delta G_m = \Delta H_m - (T\Delta S_m) \tag{1.4}$$

Flory-Huggins theory predicts whether two polymers will be miscible based on the entropy and enthalpy of mixing. Mixing will lead to an increase in disorder, hence an increase in ΔS_m, and a decrease in ΔG_m, which favours miscibility. However, ΔH_m is dependent on the type of molecular interaction taking place, such as hydrogen bonding and van der Waals forces. As $T\Delta S_m$ is always positive but small, ΔG_m is mainly dependent on ΔH_m. Endothermic mixing will have a positive ΔH_m and exothermic mixing, as is often the case for miscible polymer blends, will have negative ΔH_m. Another factor to consider is polymer M_w; for long chains (high M_w), mixing is determined by the change in enthalpy as the entropy term becomes insignificant. If polymers have $\Delta H_m < 0$ or $\chi < 0$ they will be miscible, otherwise high M_w polymers are generally immiscible. However, for short chains and oligomers (low M_w) mixing is entropically driven. On the whole for polymers, if $\chi < 0$ then blends are miscible, however if $\chi > 0$ then mixing is temperature dependent. The entropic term in Equation 1.4 is also reliant on temperature and as temperature increases, $-T\Delta S_m$ will become large and so ΔG_m will decrease, promoting mixing. A miscible system will have $\Delta G_m < 0$ and immiscible systems $\Delta G_m > 0$. The miscibility of a system is also dependent on the composition of polymers A and B, ϕ_A and ϕ_B where ϕ is the volume fraction and $\phi_B = (1 - \phi_A)$.

The Flory-Huggins treatment uses Equation 1.4 and breaks down the components ΔH_m and $T\Delta S_m$ to give the Flory-Huggins Equation (Equation 1.5). Here, v_A and v_B are the volumes of monomer A and B respectively, v is an arbitrarily chosen reference volume and is chosen with respect to v_A and v_B so that, $v_A \approx v_B \approx v$. There are a number of different definitions of v used in the literature and there does not appear to be a universal choice. For example: $\sqrt{v_a v_b}$ or it is set to be 100 Å^3. χ is the Flory-Huggins interaction parameter and is a dimensionless number that empirically determines the change in local free energy per reference unit.

$$\frac{\Delta G_m}{k_B T} = \frac{\phi_A}{v_A N_A} \ln \phi_A + \frac{1 - \phi_A}{v_B N_B} \ln(1 - \phi_A) + \frac{\phi_A (1 - \phi_A)}{v} \chi \tag{1.5}$$

As N_A and N_B become large, the terms: $\frac{\phi_A}{v_A N_A} \ln \phi_A$ and $\frac{1-\phi_A}{v_B N_B} \ln(1 - \phi_A)$, that represent the combinatorial entropy, ΔS_m, will be small and close to zero. Thus ΔG_m is dominated by the enthalpic term, and manifested by the Flory-Huggins parameter χ. If a model system is plotted using typical values for v_A, v_B, v, N_A and N_B with a constant temperature the resulting graph would show the compositions at where the phase boundary exists and where polymers A and B are miscible.

It is possible to calculate a value for χ using the equation below, where V_m is the molar volume of the polymer reference segment, δ_A and δ_B are the Hildebrand solubility parameters for polymers A and B. R and T are the universal gas constant and absolute temperature respectively.

It should be noted from Equation 1.6 that χ is independent of concentration and is inversely proportional to temperature, $\chi \propto \frac{1}{T}$, therefore to model the interaction parameter, a form of $\chi = A + \frac{B}{T}$ is used.

$$\chi = \frac{V_m}{RT}(\delta_A - \delta_B)^2 \tag{1.6}$$

Further information regarding Flory-Huggins theory, the resulting phase diagrams, nucleation and growth and spinodal decomposition can be found in a number of sources such as those by Strobl [17] and Doi and Edwards [25].

1.5 Hansen Solubility Parameters

Hansen solubility parameters (HSPs) were developed to predict whether a solute would dissolve in a solvent to form a solution [26]. Put simply, materials with similar HSPs will have a high affinity for each other. The basis of HSPs arises from the concept that the total energy of vaporisation comes from several different contributions. These are dispersion, permanent dipole-permanent dipole and hydrogen bonding forces. Thus it follows that total energy of vaporisation (also the total cohesion energy) is the sum of these different parts:

$$E = E_D + E_P + E_H \tag{1.7}$$

where E_D, E_P and E_H dispersion energy, polar cohesion energy and the electron exchange parameter (from Hydrogen bonding) respectively. Dividing Equation 1.7 by the molar volumes gives the solubility parameters (δ) for each contribution:

$$\delta = \delta_D + \delta_P + \delta_H \tag{1.8}$$

Note that δ is the Hildebrand solubility parameter used in Equation 1.6. Following from this, the 'distance' in parameter space (Ra) between components A and B (Equation 1.9) can be calculated. The constant '4' has been determined theoretically and experimentally and represents the data as a sphere which contains all good solvents.

$$Ra^2 = 4(\delta_{D,A} - \delta_{D,B})^2 + (\delta_{P,A} - \delta_{P,2})^2 + (\delta_{H,A} - \delta_{H,B})^2 \tag{1.9}$$

A convenient measure between a solute and solvent is the relative energy difference (RED) which uses the interaction radius of the solute (Ro). The interaction radius is the sphere within which all good solvents are incorporated and all bad solvents excluded.

$$RED = \frac{Ra}{Ro} \tag{1.10}$$

If RED<1 then the solute will dissolve, if RED>1 then interactions are unfavourable and there will be no dissolution. For RED=1 there is partial dissolution.

1.6 Polymer/Colloid Solution Theory

The theoretical aspect of polymer colloid solvent mixtures have been split into two limits, the colloid limit (CL) (Figure 1.3a) and the protein limit (PL) (Figure 1.3b). These two limits are usually defined by R_g and the radius of the colloid, R_C. In the CL, $R_g \ll R_C$, conversely in the PL $R_g \gg R_C$ [27].

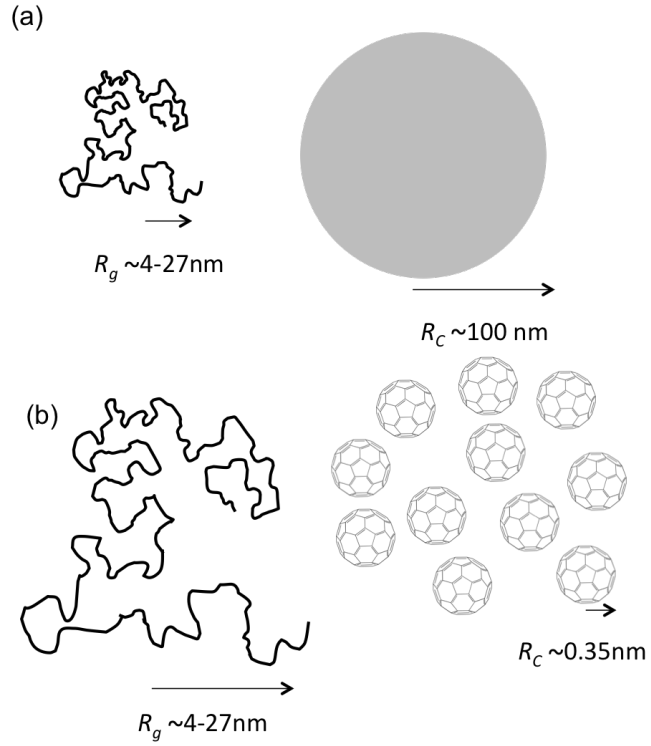


Figure 1.3: Schematics of a polymer/colloid system within the (a) colloid limit (CL) and (b) protein limit (PL). PS/C_{60} is clearly a system within the PL as $R_C \ll R_g^{poly}$.

The Asakura-Oosawa (AO) model provides a framework for understanding polymer/colloid/solvent systems in the CL [28, 29]. They considered a system of two parallel plates in a dilute, monodisperse solution (non-interacting, interpenetrating spheres). If the distance between the plates (d_p) is $< 2R_g$ then the polymer chains cannot enter between the plates. Thus an osmotic pressure acts inwards on each plate, given by $P = kTN\frac{\partial \ln Q}{\partial d_p}$ [i]. If $d_p \ll 2R_g$ then P is negative and there is an attractive force causing the entropy of the polymer to increase. This concept was applied to the case of two spherical colloids, with diameter D_C in a dilute polymer solution. The force is still attractive and is proportional to the osmotic pressure, $P_O = k_BTN/V$. As with the parallel plates, if the distance between the colloids is $< 2R_g$ then the polymer chains are excluded from the solvent between the colloidal particles and the probability of a polymer chain

[i] Q is the partition function of the canonical ensemble and contains information about the volume and number of spheres.

entering the depletion layer is zero. Thus there is a reduction in entropy causing an anisotropic osmotic pressure gradient pushing the colloidal particles together. Others have also shown that at distances ≤100 nm there are also attractive dispersion forces present [30].

In the treatment of the CL, the colloid-colloid interaction is taken as pairwise additive, however this is not possible in the PL as there are now multiple interactions between a polymer coil and the colloids. To address this problem, a polymer chain can be treated as a number of connected spheres with the same length scales as the colloidal particle. The results in the PL from theoretical calculations propose either, homogenous solutions [31, 32] or phase separation [33–35]. Experimentally, phase separation is commonly observed [3, 36–39] and was first observed within protein/polymer solutions by Polson et al. [40], hence the term protein limit.

Phase separation predicted by Sear [34] came from extending the AO model to include interactions between the colloid and polymer in the PL, which predicted a polymer-rich/colloid-poor phase with a polymer-poor/colloid-rich phase. Also modelled was a molecular weight effect, where the critical point of the transition occurs at lower colloid concentrations as R_g^{poly} increases. In other theoretical contributions [33, 35] it has been predicted that polymer coils in solution start to collapse upon addition of spherical particles where $R_C < 0.1R_g$. A coil-globule transition is observed when small colloids are added to a polymer in a good solvent, similar to that experienced polymer chains by a decreasing temperature in θ conditions. As the polymer and colloids demix, colloidal particles are expelled, leading to a decrease in entropy and the formation of a two phase system.

1.7 Mechanisms of Colloid Aggregation

Colloidal aggregation is broken into two broad types: cluster-cluster aggregation and monomer-cluster aggregation. In the first case the two clusters must come together and begin to form aggregates, whereas with the second type, the individual monomers or primary particles (i.e. the individual particles which are aggregating) join onto the clusters. These are somewhat similar to step-growth and chain-growth polymerisation respectively. There are three aggregation regimes within which the two cases can exist: reaction-limited, ballistic and diffusion-limited. The expected 3D fractal dimensions and resulting structures are shown in Figure 1.4. Reaction-limited aggregation requires a 'sticking probability' or some energy barrier to be overcome for aggregation to occur, on the other hand, diffusion-limited aggregation is essentially a barrier-less process. A key difference between ballistic compared to reaction- or diffusion-limited is the trajectory of the primary particles is assumed to be linear (ballistic) compared to the Brownian motion of reaction- and diffusion-limited growth. The six different growth mechanisms are summarised in Figure 1.4 [41]. The characteristic traits for each mechanism can be probed with dynamic light scattering for aggregation rates or static light, small angle neutron or X-ray scattering for fractal power laws.

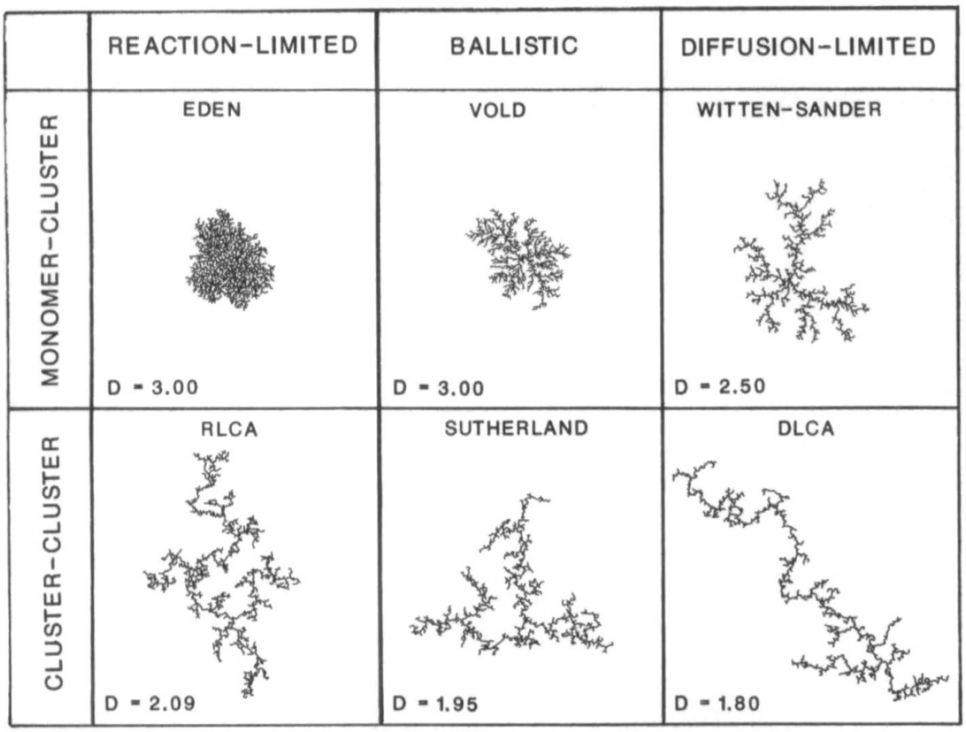


Figure 1.4: Simulated structures from the various kinetic growth models. Fractal dimensions (D) listed are for 3D objects and 2D objects are shown. Simulations were carried out by Meakin [42] and contain 1000 primary particles. Reproduced with permission from Ref. 41. Copyright Cambridge University Press.

1.7.1 Reaction-limited

Reaction-limited aggregation, sometimes termed slow aggregation or chemically limited aggregation [43], has an energy barrier ($\approx 10 k_B T$) [44] for aggregation to take place. The model for reaction-limited monomer-cluster aggregation was first developed by Eden [45] for cell colony growth. The model states that unoccupied perimeter sites are selected randomly and occupied with equal probability. This results in the formation of smooth compact clusters. An alternate of the Eden model, the 'poisoned' Eden model [43, 46], was proposed for primary particles whose aggregation was not only limited by the necessity for a reaction to take place, but also by a limited number of sites where aggregation could take place.

Compared to the Eden model, reaction-limited cluster aggregation (RLCA) is a relatively well understood process [47] and can be controlled for number of different colloidal particles [48]. RLCA is characterised by exponential kinetics and $d_f \simeq 2.1$ [49].

1.7.2 Ballistic

Ballistic aggregation differs from reaction- or diffusion-limited as a ballistic or linear trajectory is assumed for the aggregating species. The mechanism was suggested by Vold in a series of publications [50–53]. The growth process in ballistic aggregation begins with a single stationary particle with other particles travelling in random, linear trajectories. When a moving particle impinges the stationary particle it will stick at the point of contact. Additional particles are added by the same process. This work was criticised by Sutherland [54] with a number of issues raised, one of which was that the model assumed single primary particle addition to the aggregate structure with a handful of aggregates present. Using the work of Vold as a starting point, Sutherland developed a model in which cluster-cluster aggregation was considered as, in the authors opinion, it was more physically relevant [55]. The model begins with primary particle aggregation, until a certain number of primary particles and formed an aggregate. The growth sequence of cluster-cluster aggregation assumed the aggregates were consumed in the order in which the grew. The physical aggregation process assumed, as with Vold's model, that as two clusters touched, they would stick at the first point of contact.

1.7.3 Diffusion-limited

Diffusion-limited aggregation is a barrier-less process and has faster kinetics compared to reaction-limited aggregation. Witten and Sander [56] proposed a diffusion-limited monomer-cluster aggregation model. This model begins with a stationary, seed particle with a second particle some distance away. The second particle follows a random walk until it is adjacent to the seed, at this point the cluster grows. Another particle is then introduced and again follows a random walk until it becomes part of the cluster. There is no barrier to the aggregation process once the primary particle is next to the cluster. Diffusion-limited cluster-cluster aggregation (DLCA) was developed from the Witten-Sander model [57] where aggregation occurred in s similar manner, with the aggregates also allowed to diffuse around the lattice. DLCA follows linear growth kinetics with respect to mass and has $d_f \simeq 1.8$.

Reversible cluster aggregation, is also conceivable. Kolb et al. [58] used a DLCA mechanism with an additional term to take fragmentation into account. Clusters grow until the rates of aggregation and fragmentation are equal. No change in the d_f and a wider size distribution were reported

2 Literature Review

This chapter will provide a review of the literature on polymers, colloids and polymer/colloid blends within solutions, bulk and thin films. Applications, desired properties and processing techniques for polymer nanocomposites are also reviewed. As is commonly done when processing polymer/fullerene/solvent mixtures, the review will begin in the solution state of the individual components after which the solid state is discussed. Current and potential applications for fullerene-based nanocomposites are discussed alongside processing routes to control their structures.

2.1 Solutions of Polymers and Colloids

2.1.1 Polymers

Measurements of neutral polymers in solution can be conducted by easily accessible techniques such as dynamic and static light scattering [4, 5] and also at large-scale facilities using small angle scattering [20, 21]. Scaling laws for well-studied polymers in solution such as polystyrene at a range of M_w in cyclohexane, toluene and other good solvents are easily reproducible and established in the dilute and semidilute regimes [4, 5, 19–21].

With the advent of photoactive polymers [59] measurements of polymer solutions using traditional light based techniques are more complex as the band gap of these materials is commensurate with the wavelengths of the lasers used. For example, a HeNe laser has a wavelength of 633 nm (1.96 eV) which is comparable to the band gap of poly(3-hexylthiophene) (P3HT) at 2.0 eV.

Sehgal and Seery [60] examined polyaniline (PANI), a light conducting polymer and found an unexpected trend with laser power (with $\lambda = 514.5$ nm). As laser power was decreased, the apparent diffusion coefficient (D_{app}) decreased, implying an increase in R_h, and at high laser power D_{app} became constant as seen in Figure 2.1. This apparent change in R_h was thought to be due to local heating and convection that can be caused by light absorption. This heating can change the density, refractive index, and viscosity of the solution. The D_{app} could be extrapolated to 0 W laser power and therefore R_h without the effect of the laser and the thermal energy on the polymer. Recent work by Dadmun [61] has demonstrated the light absorption causing an increase in R_g, measured by SANS, due to polaron formation. This is when light is absorbed by the polymer (in their case P3HT), an electron is excited and this creates an electron-hole pair. This is accompanied by a change in polymer chain conformation as the

monomer changes from an aromatic to quinone structure and thus a stiffening of the polymer chain. These results appear to be conflicting, with Ref. 60 reporting a decrease in R_h and Ref. 61 reporting an increase in R_g with light exposure, highlighting the complexity of using light scattering for light absorbing polymers.

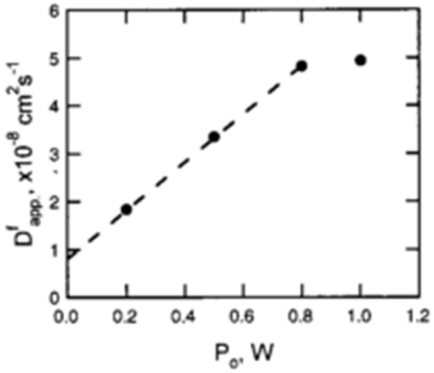


Figure 2.1: Trend of increasing apparent diffusion coefficient as laser power increases, levelling off at high power. Adapted with permission from Ref. 60. Copyright 1999 American Chemical Society.

An early study on P3HT R_h was conducted by Heffner and Pearson [62] in THF and chloroform. A persistence length of 2.4±0.3 nm was found which is equivalent to six P3HT repeat units. However, the route by which the P3HT was synthesised [63] is known to give low regioregularity polymers (≈50%) [64, 65]. As a comparison, polystyrene has a persistence length of 0.67 nm [16]. Commonly in the preparation of P3HT-based OSCs, regioregular P3HT is used [1, 2] giving the report in Ref. 62 limited use. Huang et al. [66] examined the structural evolution of regioregular P3HT in tetrahydrofuran in the dilute regime with DLS, where they found two modes of relaxation in P3HT: a fast mode corresponding to polymer R_h and a slow mode corresponding to aggregates. A thermal study indicated that as temperature increases the percentage of polymer coils decreases and aggregates increases. Given the effects of light absorption [61] and the difficulties in conducting accurate measurements with traditional light scattering techniques [60], small angle neutron scattering (SANS) has been used to characterise a wide range of poly(3-alkylthiophenes) (P3ATs) [67]. It was found that there was a significant effect of the P3AT synthesis (and therefore regioregularity and polydispersity) on the persistence length. For the regioregular, monodisperse, P3ATs the persistence length was between 2.9 and 3.3 nm. This is lower than the conjugation length as measured by UV-Vis spectroscopy. P3HT was found to have a power law of $q^{-1.97}$ in dichlorobenzene (DCB), indicating a close-to Gaussian coil conformation and near theta conditions. A temperature study on P3HT in DCB indicated that increasing temperature decreased the persistence length, atactic polystyrene in the melt shows no dependence on temperature with persistence length [68]. It was not given in the experimental conditions whether the temperature study was conducted under an inert

atmosphere, P3HT is readily oxidised at high temperatures and will change the chemical species of the polymer, which could then change the persistence length. P3HT aggregates have been observed in solution by cryo-tranmission electron microscopy (cryo-TEM) [69], which can provide a number of benefits due to the direct visualisation of aggregate structure as opposed to scattering techniques.

The aggregation of conjugated polymers also causes some difficultly when studying single chain properties and so others have employed fluorescence correlation spectroscopy (FCS) [70] to study extremely dilute solutions. FCS, is somewhat similar to DLS, with a key difference being that the fluctuations detected are from the fluorescing species travelling through an observation window. Wang et al. used MEH-PPV [i] in a number of solvents which were commonly thought to be good solvents for MEH-PPV, however their experiments demonstrate a scaling between R_h and M_w below 0.5, typical of poor solvent behaviour.

Although some polymers, such as polystyrene, are well-understood in solution [4, 5, 19–21] the solution behaviour of relatively novel polymers is less well-understood. The use of alternate techniques to the traditionally used light scattering and small angle scattering, such as FCS, is allowing the measurement of single photoactive polymer chains with lab-based, commercially available techniques [70].

2.1.2 Fullerene Aggregation

Given the IUPAC definition of colloids: "The term refers to a state of subdivision, implying that the molecules or polymolecular particles dispersed in a medium have at least in one direction a dimension roughly between 1 nm and 1 μm, or that in a system discontinuities are found at distances of that order." [71] It is suitable to class fullerenes (≈1 nm) and nanoparticles (NPs) (1~100 nm) as colloids.

The stability of colloidal solutions are of great interest from physics to biology. One of the earliest known aggregating colloids were red blood cells which, given their disc shape, aggregate with the flat sides facing one another similar to a roll of coins [27]. A number of different aggregation mechanisms have been proposed and were summarised in Section 1.7 [41]. Improved chemical synthesis has resulted in suitably stabilised NPs where aggregation is prevented. NPs are thought to synthesise via an initial, fast nucleation step followed by Ostwald ripening over longer times. This is the stage where a low polydispersity is achieved [72]. However, there remain situations where the dissociation of the surface stabilising groups can leave particles with an electrostatic charge. This will have an influential role in colloidal aggregation [73].

The aggregation of colloids via RLCA and DLCA can be easily controlled, via salt concentration in solution, and has been demonstrated for a number of inorganic and organic NPs such as gold (7.5 nm), silica (3.5 nm) and polystyrene (19 nm) colloid/solvent systems [48]. It should be noted that the d_f found by computer simulations such as those by Meakin [42] can

[i] poly(2-methoxy-5-(2'-ethylhexyloxy)-1,4-phenylenevinylene)

experimentally give unexpected results. Discrepancies between predicted fractal dimensions and those obtained experimentally have been attributed to long-range electrostatic interactions, and hydrodynamic interactions [41]. The behaviour of C_{60} and other fullerenes in solution is however less studied and has not yet been fully understood. C_{60} has been shown to exist as molecules dispersed in carbon disulphide, an R_g in the region of 3.76 nm via a Guinier plot was obtained. Additional work via DLS in toluene, chloroform and carbon tetrachloride gave R_h of 0.53 nm [74, 75]. The experiment described in Ref. 74 was also attempted by Tropin et al. [76] who were unable to obtain the same results from C_{60}/carbon disulphide.

There have been a number of outcomes reported for C_{60} solution behaviour: (i) degradation of the fullerene cage, (ii) photo-polymerisation, (iii) photo-oxidation and (iv) aggregation. Each of these outcomes will be discussed in detail below.

The degradation of the C_{60} cage (photolysis) can be induced by UV radiation (with a medium-pressure silica-jacketed Hanovia insertion UV lamp [ii]) in hexane [77]. This was confirmed by mass, UV, NMR and IR spectroscopies. Taylor et al. [77] reported the formation of a brown deposit which could not be re-dissolved, however no experimental data is shown and attempts to reproduce results gave inconsistent results [78]. Juha et al. [78] achieved reproducible results with a XeCl-excimer laser (λ=308 nm, power density of 25 MWcm^{-2}) and a 10:1 mixture of C_{60} and C_{70} in hexane. The decomposition process was characterised by a decrease in the UV absorption signals of the two fullerene species and was found to occur in as received and attempted oxygen-free solvent conditions.

C_{60} photo-polymerisation upon exposure to UV radiation has been investigated by Cataldo [79] using a variety of cholorinated solvents under inert atmosphere with a 125 W high pressure Hg lamp with main emission lines between 280 and 380 nm. The formation of brown deposit was also observed (as with Ref. 77), but rationalised as fullerene 'polymer'. The creation of fullerene polymer was characterised by a change in UV absorption of C_{60}. The trends reported by Juha et al. indicated a decreasing absorbance at 330 nm and an increase at 400 nm with exposure time. This is identical to the results shown by Cataldo. Discriminating between polymerisation and decomposition appears difficult as no raw data is presented in Ref. 77 and only spectroscopic results are reported in Refs. 78 and 79.

Photo-oxidation of C_{60} in solution to form epoxides is a useful synthetic tool [80] This was exploited by Wood et al. [81] and Creegan et al. [82]. Wood et al. [81] formed oxidised C_{60} and C_{70} molecules in hexane or benzene with a 150 W Hg arc lamp. However, further experiments showed there were impurities within their graphite prepared fullerenes which also allowed the formation of other C_{60} adducts such as ethers. Creegan et al. reported the first synthesis and characterisation of C_{60} epoxide via C_{60} photo-oxidation in benzene using a Hanovia lamp in a quartz immersion well (which may be the same as that used by Taylor et al. [77] however insufficient details are given). Cataldo also reported C_{60} photo-oxidation under ambient conditions

[ii] This is likely to be a UV-A source but there is no further information on the light source provided within Ref. 77.

with saturated hydrocarbon solvents such as cyclohexane [79].

Aggregation of fullerenes has been reported in aromatic solvents [83–85], mixed solvents [86, 87] and water electrolyte solutions [88]. Ying et al. [83, 84] reported the aggregation of C_{60} in benzene over a 40-90 day period using static and dynamic light scattering. An increase in scattering intensity (I_0) over time was found, which reversed upon shaking the solution by hand. Solution storage between measurements was not discussed. The aggregates were thought to occur via RLCA and a d_f of 2.1 was reported. The laser wavelength (790 nm) was expected to be sufficiently away from the UV region in which degradation or polymerisation occur. However an insoluble brown residue was reported, which was previously attributed to degradation [77] or photo-polymerisation [79]. Török et al. [85] carried out a SANS study of C_{60} in toluene taking initial measurements, storing the solution for one year and retaking the measurement. Their initial measurement indicated the presence of clusters with R_C of 2.5-3 nm which after a year increased to 100 nm. As with Ying et al., solution storage conditions between measurements were not discussed. Sun and Bunker [86] used C_{70} in a solvent mixture of toluene and acetonitrile to promote aggregation. When the acetonitrile volume fraction was above 60%, the C_{70} peak at 380 nm disappeared and there was stronger absorption above 450 nm. This was also shown to be a reversible process. Building on this work Nath et al. [87] studied the effect of solvent polarity on C_{60} aggregation with UV spectroscopy and DLS in a range of solvents. C_{60} was found to aggregate, via UV spectroscopy, at solvent mixtures with $\epsilon \approx 12.5$ (ϵ is the dielectric constant). Although DLS was used as a characterisation technique of the typical cluster dimensions, values from 250 to 400 nm were given, whether this is a radius or diameter is not given. A common method to control colloidal aggregation is via salt concentration in solution [48]. This was attempted by Meng et al. [88] via simultaneous multiangle SLS/DLS in water electrolyte solutions. This allowed simultaneous measurement of R_h and d_f. R_g was not given, however could have been accessed via Guinier's approximation [89] or Teixeira's fractal model [90]. Broadly, Meng et al. observed an increasing R_h and either a stable, or decreasing d_f over 10 hours.

Although the principles governing nanoparticle and colloidal aggregation have been previously studied and rather well understood, this work was motivated by the need to establish a definitive cause and mechanism for the observed aggregation of fullerenes in solution.

2.1.3 Polymer Composite Solutions

In this section, polymer/colloid solutions will be covered from the colloid-limit (CL) to the protein-limit (PL) (as defined in Section 1.6). As a reminder, in the CL, $R_g \ll R_C$, conversely in the PL $R_g \gg R_C$ [27]. Also, techniques to deconvolute scattering data from multicomponent solutions will be discussed.

Experimentally, it was well known that phase separation occurred in red blood cells (6-8 μm) when proteins were introduced. The link between the theoretical predictions of Asakura and Oosawa [91] and these experimental results was made by De Hek and Vrij [92–94] who

demonstrated the phase separation of polymer/colloid/solvent mixtures using polystyrene (PS) and silica in cyclohexane at 34 °C in the CL, close to the θ temperature (34.5 °C). This system phase separated and silica particles experienced an effective attraction by increasing: PS M_w (and therefore R_g), colloid R_C, and concentration of silica. This agrees with the theoretical predictions described previously. A great deal of work has since been conducted [95]. In the system used in this thesis (PS/fullerene/solvent) the literature within the protein-limit is of interest.

The protein-limit is defined by a ratio of the polymer size to the colloid size, which is significantly larger than one. The theoretical predictions within this limit are less well-defined than for the CL, with both homogenous solutions [31, 32] and phase separation [33–35] predicted. Experimentally it was known for some time that the addition of polymers to proteins causes phase separation, [40] although challenges remained to individually characterise the polymer and colloid.

Kramer et al. [36–39] carried out a series of experiments using isorefractive colloids on three suitable polymer/colloid/solvent systems. In all cases, the polymer was a standard polystyrene chain and the small colloid was SILS [iii] ($R_C = 0.7$ nm), crosslinked poly (ethyl methacrylate) (R_C = 8-42 nm), or hydroxyl functionalized silica nanoparticles (R_C = 11 nm). Significant (≈50%) coil contraction was found in the presence of high enough (≳8 wt%) colloid concentration by means of viscosimetry, light scattering and small angle neutron scattering [36]. The authors could also demonstrate that an increasing polymer content decreases the solubility of SILS. The increased tendency of SILS crystallisation was attributed to an expulsion of SILS from polymer coil domains. This effect has also been observed in microemulsions [96], lipid vesicles [97] and inorganic nanoparticles [98, 99].

The work in Refs. 36–39 are conducted on model systems with flexible polymers and colloid R_C's ranging from 0.7 to 42 nm. Using these concepts on functional systems, such as P3HT and PCBM, the system should be in the PL. However, there are a number of other factors which prevent the predictions of the PL to be observed experimentally, such as the crystallisation of P3HT in solution [100] which would, of course, not occur in flexible, atactic polystyrene which is commonly used for studies in the PL. Sobkowicz et al. [100] used SANS to study the effect of PCBM (a functionalised fullerene) on the crystallisation of P3HT. Using the contrast matching between deuterated dichlorobenzene (DCB) and PCBM, the form factor for P3HT was obtained. A Gaussian coil conformation of P3HT coils was assumed in a PCBM/DCB background. Given the previous work for P3HT in DCB having a Gaussian conformation, [67] which in itself is unlikely, it could be expected that the addition of PCBM would alter solvent quality and so is highly unlikely to be a Gaussian coil. Disregarding the questionable fitting procedure, the trend in the scattering and rheology data demonstrates that the addition of PCBM slows the aggregation of P3HT in solution.

[iii] octa-n-propylsilsesquioxane

2.1.4 Summary

The study of polymer solutions is a mature field with reproducible results and known scaling laws for traditional polymers [4, 5, 14, 19–21]. The study of polymer/colloid/solvent systems also has established models in the CL [91] and results have been determined experimentally [92–94]. Although theory for the PL is still not entirely agreed upon [31–35] the experimental results have been conclusive [36–40].

Given the interest in semicrystalline, conjugated polymers which aggregate in solution these models are not wholly applicable, there are increasing complexities with light absorption, aggregation and crystallisation. Progress has been made in understanding the behaviour of these systems [100]. The range of synthetic methods used [64], giving different physical properties [67], highlights the potential within this field to understand polymer/fullerene systems and to transfer that understanding to a consolidated polymer/colloid/solvent theory.

C_{60} and other fullerenes have been studied with three results commonly reported for light exposure in solution (i) degradation [77, 78], (ii) polymerisation [79] and (iii) oxidation [79, 80, 82] whilst others have reported aggregation with no reports on the storage or measurement environment [83–88]. There are unresolved issues such as the same experimental evidence giving rise to different conclusions [78, 79].

2.2 Bulk Polymers and Composites

Early work on polymer/polymer blends studied the miscibility, with more recent work [101] focussed on polymer/nanoparticle blends. The literature on polymer/polymer blends is briefly discussed followed by a more detailed review on polymer/colloid melts.

2.2.1 Polymer/Polymer Blends

A variety of techniques can be used to quantify the phase behaviour and miscibility of polymer/polymer blends: T_g measurements, using differential scanning calorimetry (DSC), NMR, cloud point, optical microscopy and small angle neutron scattering (SANS) [102–104]. To quantify the miscibility of one component in the other one could observe optical clarity or test mechanical properties. However, samples may appear clear if they are too thin or if the two materials have identical refractive indices. T_g measurements appear to be a more unambiguous property by which to confirm miscibility. For example, the T_g of a homogenous blend will be located between that of the two individual components and it has been shown that a random co-polymer had the same T_g as that of the equivalent blend [105] confirming that the measured T_g was due to the molecular environment being identical. Of course the T_g's of the individual components must be far from one another which limits the systems this method can be used for.

SANS is an extremely useful tool to study polymer/polymer blends, given the ability to provide information from the monomer scale to blend correlation lengths due to the wide q-range

available. With more complex systems under investigation, such as polymer nanocomposites, the contrast matching capabilities of SANS are extremely useful and have been applied to range of systems [6, 7, 101, 106–111].

2.2.2 Fullerenes

The majority of C_{60} studies have been conducted using sublimation of C_{60} powder onto the desired substrate. Solid C_{60} photo-polymerisation can occur upon exposure to a 300 W Hg arc lamp or an Ar-ion laser in an inert atmosphere [112]. The mechanism was determined to be a Diels Alder 2+2 cylcoaddition where the neighbouring fullerenes had to be <0.42 nm apart [113]. A number of C_{60} polymer structures were demonstrated [114], kinetics and thermal decomposition have also been presented [115, 116]. The nanoscale morphology of C_{60} films is also modified with light exposure either simultaneously with deposition [117] or post-deposition [118]. Simultaneous C_{60} monolayer growth and light exposure gave more control of C_{60} nanostructure by modification of the nucleation density with laser power [117]. Oxygen doping of C_{60} films was demonstrated by Rao et al. [119] with light exposure to a 75 W Xe lamp or Ar-ion laser under an O_2 atmosphere at 1 atm. Although the product was not fully identified it was thought to be $C_{60}O_x$. The methods used to identify C_{60} photo-polymerisation and -oxidation were FTIR, Raman and mass spectroscopies. C_{60} polymer showed a decrease in the peak Raman shift intensity and the appearance of a number of peaks in the FTIR spectra between 484 and 800 cm^{-1}. The clearest indication came from mass spectroscopy with individual peaks resolved every 720 g/mol. The indications of photo-oxidation were the appearance of broad absorption regions in FTIR spectra corresponding to regions where C-O stretch modes are expected. The changes in Raman spectra were less clear, and mass spectroscopy results were not presented. C_{60} photo-polymerisation and -oxidation in the solid state are well understood processes [112–114, 119] of which the resulting nanostructures can be controlled [117, 118].

Given the importance of fullerene-based nanocomposites fabricated from solution, there is surprisingly little work to understand the effects of solvents on properties, such as crystal structure, of the final bulk material. There are a variety of techniques which have been used to control the crystallisation of C_{60} and PCBM: liquid-liquid interface precipitation [120–122], evaporation [121], reprecipitation [123], drowning-out crystallisation [124] and dip coating [125]. Most of the techniques have one aspect in common which is the addition of a non-solvent, such as an alcohol, to a fullerene/solvent mixture. There are a range of possible C_{60} nanoparticles which can be made, such as rods [120, 123, 124], hexagons [122–125], spheres/balls [123], stars [123, 124] and bipyraminds [123, 124].

Using C_{60} photo-polymeristion with an irradiation wavelength between 400-500 nm C_{60} crystals were polymerised [121] to form insoluble C_{60} crystals. There is potential for these C_{60} crystals to be used in polymer nanocomposite and so the properties of C_{60} crystals could be tuned for an individual application.

2.2.3 Polymer Nanocomposite Melts

Research on polymer nanocomposites usually falls into two categories, there are fundamental studies using C_{60}, silica NPs, polystyrene (PS) and PDMS [iv] focusing on polymer chain dimensions and NP miscibility and those on functional systems using P3HT and PCBM.

There have been a number of studies on the addition of NPs to polymer matrices which have reported conflicting results on polymer chain dimensions. At least in part, these are due to variability in nanoparticle dispersion which is not always reported. Initial work by Nakatani et al. [101] using 2 nm polysilicate fillers in isotopic mixtures of PDMS, indicates that not only does the filler concentration affect the polymer chain, but so does the size of the filler in comparison to the polymer radius. For systems where polymer R_g is similar to the radius of the nanoparticle R_C, a decrease in chain dimensions was observed and if R_C was larger, there was a decrease in R_g. Tuteja et al. [106] studied the addition of PS NPs (>10 vol%) to a mixture of hydrogenous and deuterated PS, an increase of (up to) 20% in PS R_g was observed when R_C was below polymer R_g. Conversely, Sen et al. [107] and Jouault et al. [126] added 12-14 nm silica NPs (> 30 vol%) to PS. They found the polymer chain dimensions were unperturbed by the addition of silica NPs. Nusser et al. [108] demonstrated a decrease in R_g for 50 kg/mol PEP [v] upon addition of 18 vol% 8.5 nm silica NPs but no change for 3 kg/mol PEP up to 50 vol% NPs. Genix et al. [109] observed no change in R_g for methyl methacrylate and butyl acrylate latex spheres when mixed with up to 20 vol% silica NPs. Recently, Crawford and co-workers [110] used surface functionalised 13 nm silica NPs with PS and again showed no change in PS R_g. The surface functionalisation improved dispersion of silica NPs in the matrix compared to that of Refs. 107 and 126 but did not affect the outcome of the results, i.e. the PS chain dimensions remained unperturbed. Thus, Crawford et al. concluded that the relative ratio of R_g to R_C was not the relevant parameter to consider, as others previously considered this to be an important factor [7]. This is, of course, expected as there would be effects from dispersion, sample preparation method and the interaction between the polymer and NP in the matrix. In a recent review, Kumar et al. [127] developed a composite morphology diagram for polymer grafted nanoparticles in a polymeric matrix where the morphology of a range of nanocomposites were shown to be dependent on the ratio of the grafted polymer M_w and matrix M_w as well as the grafting density. Additionally a number of issues still to be solved were highlighted, one of which was whether the nanocomposites studied within the literature were at equilibrium or if they were kinetically trapped structures.

Although these studies have been carried out in the melt, the processing of these blends often requires the use of a solution step. All the work, bar that on PDMS, presented above involved a solution processing step where the polymer and NP were dissolved in a common solvent. Ref. 106 used rapid precipitation to form their solid composites. This involves adding the polymer composite solution into a non-solvent, such as methanol for PS. This will trap the polymer and

[iv] poly(dimethyl siloxane)
[v] poly(ethylene-propylene)

NPs into a dispersed state. Refs. 107–110 and 126 used a solvent drying method to prepare their samples, which others have claimed can lead to an inadvertently kinetically trapped state [7]. A solvent study using 14.7 to 940 kg/mol poly(2-vinylpyridine)/50 nm silica composites with either methyl ethyl ketone (MEK) (theta solvent) or pyridine (good solvent) was conducted by Jouault et al. [128]. The solid sample preparation method was via solvent drying. Significantly different as cast morphologies were observed depending on the solvent used, MEK gave a well dispersed nanocomposite, whereas there was silica agglomeration from samples made using pyridine. The effect of the solvent on the final dispersion state was though to arise form a number of factors: short range van der Waals attraction, long range electrostatic repulsion, steric repulsion and polymer-induced depletion attraction. The authors suggest the nature of the polymer/solvent interaction will affect the forces listed and thus dispersion. Additionally, there is evidence that even after a long annealing step (150 °C for 10 days), there is a residual effect on dispersion from the initial state.

There are only a handful of studies on C_{60} based composites [6, 7, 129, 130]. C_{60} miscibility limits of 1 [6] and 3 wt% [7] in PS have been proposed, however these are usually M_w dependent (Ref. 6 used a 270 kg/mol PS with PDI of 2.3 and Ref. 7 does not give the M_w used directly although it is likely they used 63 and 393 kg/mol PS) and thus maybe be incomparable, due to polydispersity issues. Additionally, it would be expected that miscibility would be M_w dependent, which is not found in Ref. 7. An interesting experiment by Weng et al. [130] compared two PS/C_{60} fabrication methods, one was via solvent evaporation as is commonly done, and the second via a purely solid route where the components were ground in a mortar, which given the previously mentioned work in Ref. 128 should produce markedly different results. Somewhat surprisingly, two very different PS M_w were used for these experiments, which otherwise would have been extremely useful as guide to the difference between polymer nanocomposites made with a solvent step and those made directly from the solid components. The solvent evaporation route used a higher M_n of 950000 g/mol and the direct mixing used 2727 g/mol. DSC showed an increase in PS T_g for both samples, with a higher T_g seen for the solvent cast samples. Unfortunately the experiments were also carried out with much higher C_{60} loadings (up to 40 wt%) than the proposed miscibility limits.

Mackay et al. [7] gave a general rule for NP miscibility in nanocomposites which was only dependent on the respective radii of the polymer and NP. Given their results, it would appear as though C_{60} is always miscible in a polymer matrix which is of course not a realistic situation as there are a number of other factors which must be considered such as the NP miscibility, polymer/NP interaction and NP/NP interaction [110].

Studies on functional systems in the bulk, such as the ubiquitous OSC pair P3HT/PCBM have tended to focus on the thermal transitions and crystallisation behaviour of the polymer and fullerene as tuning these parameters are necessary for improving performance. Miscibility studies have shown that ~20 vol% PCBM is miscible in 65 kg/mol P3HT [111]. The phase diagram of P3HT/PCBM has been studied in detail by different groups, three of which, Müller et al. [131],

Zhao et al. [132] and Hopkinson et al. [133], are shown in Figure 2.2a-c and combined in Figure 2.2d for comparison. Refs. 131 and 132 used DSC to obtain their scans, from which melting point and crystallisation temperatures were found, whereas Ref. 133 used dynamic mechanical thermal analysis (DMTA). DMTA is seen to be an improvement to DSC as the sample does not to be heated before analysis is carried out. Therefore, there is no thermal history, and is closer to the processing conditions used in OSC device fabrication.

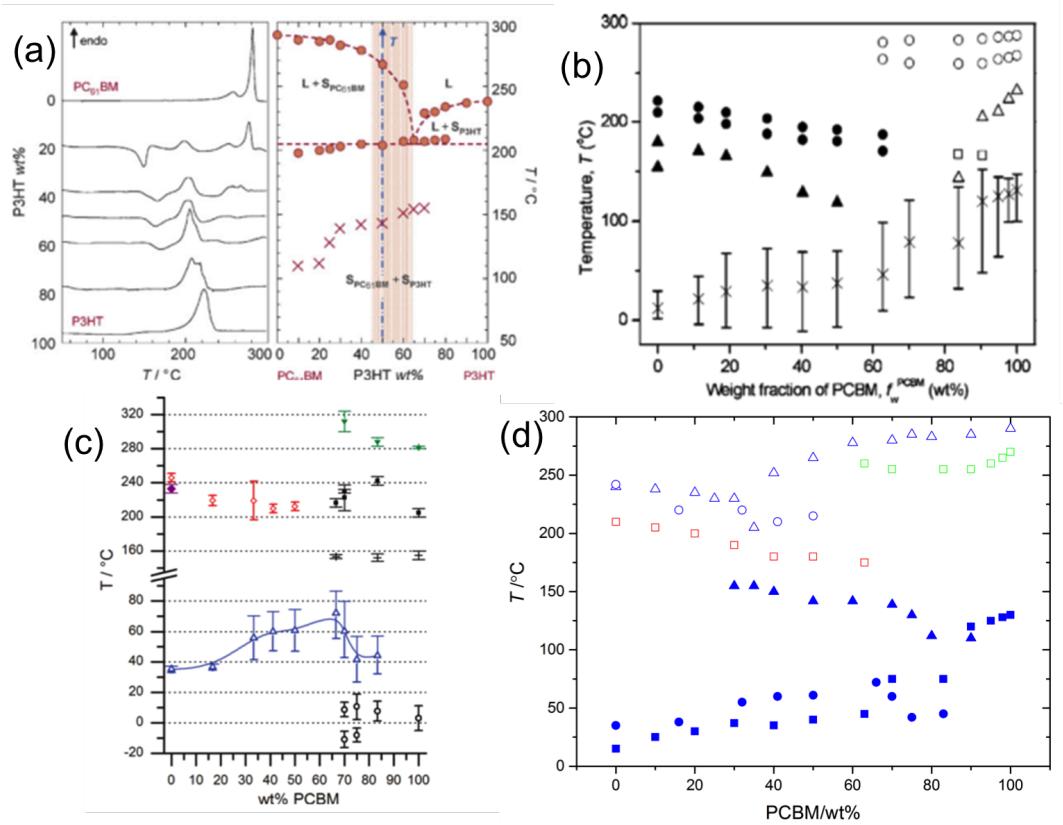


Figure 2.2: Phase diagrams for P3HT/PCBM (a) (Reproduced from Ref. 131) Onset of crystallisation (×) and (•) represent the liquidus lines. (b) (Reproduced from Ref. 132) melt crystallisation temperature of P3HT (▲), T_m of P3HT (●); melt crystallisation temperature (△), cold crystallisation temperature (□), T_m of PCBM (○); blend T_g (×). (c) (Reproduced from Ref. 133) blend T_g (△), blend T_m (◇), transition A (○), transition B (+), transition C (■), transition D (▼), P3HT liquid crystal transition (◆). (d) Combined phase diagrams from (a-c). From Ref. 131 : Blend T_m (△), Onset of recrystallisation (▲); Ref. 132: P3HT T_m (□), PCBM T_m (□) and Blend T_g (■); and Ref. 133: Blend T_g (●) and Blend T_m (○). (a) Adapted with permission from Ref. 131. Copyright 2008 John Wiley and Sons (b) Reprinted with permission from Ref. 132. Copyright 2009 American Chemical Society. (c) Reprinted with permission from Ref. 133. Copyright 2011 American Chemical Society.

Müller et al. [131] proposed a eutectic behaviour (Figure 2.2a • and d △), i.e. a composition (c_e) and temperature (T_e) at which the liquid phase can be quenched directly to a phase separated

solid state. This was not seen in the phase diagrams presented in Refs. 132 and 133, Figs 2.2b and c respectively Nicolet et al. [134] also observe eutectic behaviour for a range of P3HT M_w from 9.6 to 60 kg/mol. There are similarities between the data collected, with some trends occurring at the same compositions, these are seen most clearly in Figure 2.2d. At PCBM loadings greater than 60-75 wt%, Ref. 133 observe a decrease in blend T_g (•) and Ref. 131 observe a decrease in temperature at which crystallisation begins (▲) by 30-40 °C. These changes could be associated with a change from a single phase to a phase separated state. Conversely, the blend T_g observed in Ref. 132 (■) increases steadily and the jumps between 83 wt% and 90 wt% by 25-30 °C. The values and trend for blend T_g between Refs. 132 (■) and 133 (•) are very similar from 0 to 75 wt% PCBM. These differences are rationalised in Ref. 133 as being caused by the different preparation techniques required by DSC. However the trend for the onset of crystallisation from Müller et al. [131] is also from DSC and agrees with the results of Hopkinson et al. [133], therefore it may not be caused by the difference in preparation technique for DSC and DMTA. The T_m is similar for the results shown by all three experiments, depicted by P3HT T_m (△, Ref. 131) and blend T_m (□, Ref. 132 and ○, Ref. 133). Unfortunately Hopkinson et al. [133] do not show any T_m data above 50 wt% PCBM with which to compare T_m at higher PCBM loadings.

The difficulty in mapping an accurate phase diagram for the P3HT/PCBM blend arises from various factors, two of which are the crystallinity observed in P3HT and the possible crystallinity of PCBM [132, 133]. Zhao et al. [132] also noted that this dual crystallisation behaviour results in the crystallisation of one phase hindering that of the second phase. An additional factor which is inherent to the problems associated with DSC and DMTA experiments is the time taken for heating the sample as the components in the blend will start to move as soon as the system is over T_g. Crystallisation, phase separation and wetting are strongly time dependent. Therefore, thermal history, processing history and measurement time should be incorporated into the data shown.

A comparison of the experimental methods of Müller et al. [131], Zhao et al. [132] and Nicolet et al. [134] reveals that all three used regioregular P3HT; Ref. 131 used a low (22 kg/mol) M_w and Ref. 132 used a slightly higher (35 kg/mol) M_w. Ref. 134 used a range of M_w from 9.6 to 60 kg/mol. For completion Ref. 133 used 8 kg/mol P3HT. Refs. 131 and 132 prepared solutions from 1 wt% chlorobenzene solutions. Zhao et al. [132] provide some additional detail as their solutions were stirred overnight at 50 °C. Müller et al. [131] dried their films in ambient conditions whereas Zhao et al. [132] dried under nitrogen. Ref. 134 used dichlorobenzene as their solvent, the solution was drop cast onto a PEDOT:PSS coated substrate, the drop cast film floated off, dried and analysed via DSC. The rate of heating for both experiments also varied, Zhao et al. [132] heated at 2.5 °Cmin^{-1} and both Müller et al. [131] and Nicolet et al. [134] at 10 °Cmin^{-1}, corresponding to a factor of four between the two rates. It could be the difference in heating rates which give the discrepancies in the DSC data. However this does not account for the eutectic behaviour observed in Refs. 131 and 134 and not in Refs. 132 and 133. DMTA requires the drop cast sample to be stored in a stainless steel 'material pocket'. Further reading

into the technique shows that it is possible for the temperatures at which transitions occur to be dependent on the frequency which is used [135].

It should be noted that some data was omitted in Figure 2.2d for clarity, such as the cold crystallisation and melt crystallisation temperatures. Nevertheless, DSC can provide a wealth of information as many different sample characteristic temperatures can be extracted. The results from the two DSC experiments, and DMTA are a useful guide for temperatures to anneal at for improved OSC device performance. The difference in the values in the data between techniques and experiments means that a definite value for the melting, crystallisation and glass transition temperatures is not yet present. If these are known there could be a wider impact on the processing conditions for OSCs. However, there would still be a problem in that the phase diagrams are specific to one polymer/fullerene system at a specific polymer M_w, and although the ideas can be applied, each composition will have its own characteristic transition temperatures.

The importance of having an accurate phase diagram for P3HT/PCBM blends, or indeed any other OSC blend, is that the information will assist in morphology control when used alongside thermodynamic phase separation and crystallisation theories. A criticism of all three phase diagrams described above are that they only consider a two phase system, a pure PCBM phase and a pure P3HT phase. It has been noted by various authors [111, 136, 137] that P3HT and PCBM are indeed readily miscible. Thus the resulting structure of a P3HT/PCBM mixture will consist of a PCBM-rich phase, P3HT-phase and a phase consisting of miscible P3HT and PCBM [111]. Initially Yin and Dadmun [111] showed a 15-20 vol% dispersion of PCBM in P3HT and at higher loadings the PCBM phase separates into larger domains.

Additional work by Jamieson et al. [138] described the resulting morphology of a PBTTT [vi]/PCBM thin film in terms of a "solid solution" or "co-crystal" of PBTTT and PCBM along with domains of crystalline PCBM. DSC data on PBTTT/PCBM binary blends showed a two eutectic phase diagram at 10 wt% PCBM and 43 wt% PCBM. However this interesting observation is not discussed further by the authors.

2.2.4 Summary

Light exposure of C_{60} in the solid state has been shown to produce C_{60} polymers [112–114] and oxides [119]. The crystallisation of fullerenes can also be controlled with a range of crystal structures reported [120, 122–125].

A number of factors must be considered to produce well-dispersed polymer/NP composites. (i) Whether a solvent step should be used, and if so which solvent [128] or whether solid state processing is adequate [101]. (ii) If a solvent step is used would it be rapid precipitation [106] or a solvent drying method [107–109, 126]. (iii) Whether the samples are at thermodynamic equilibrium or a kinetically trapped state [7, 128]. A remaining question in the literature is the effect

[vi] poly(2,5-bis(3-tetradecyllthiophen-2-yl)thieno[3,2,-*b*]thiophene)

of NP addition on polymer chain dimensions. This is well-known for polymer/colloid/solvent systems theoretically and experimentally [27, 36, 91, 128] and has yet to be fully resolved for a range of polymer nanocomposites [110]. The miscibility of NPs in a polymer matrix is another topic where although some attempts have been made to apply a general rule [7] these are not very accurate.

The phase behaviour for P3HT/PCBM has been studied by a number of groups with some showing eutectic behaviour [131, 134] which is not seen by others [132, 133]. Of course given the previous discussion on solvent(s) used and sample processing, the disagreement is not surprising. However the trends observed are similar for the different studies and this gives credit to the results.

2.3 Thin Polymer Nanocomposite Films

Thin polymer nanocomposite films have a wide range of uses: OSCs [2], paints [139], membranes [140], self healing networks [141] and mechanical reinforcement [142]. The desired properties for some of these will be reviewed in Section 2.4. The stability of thin films for these applications is of utmost importance and thus so is the understanding of dewetting and pattern formation [143].

2.3.1 Pattern formation: dewetting and phase separation

The dewetting of <100 nm PS films heated above T_g on silicon substrate with different surface energies (contact angles (θ_C) were 22° and 42°) has been known for some time [143]. Three stages to the dewetting process were identified: (i) films break up with the properties of the holes dependent on the substrate, (ii) the holes grow larger due to surface tension (and is dependent on θ_C^3) and merge to form polygon patterns (iii) polymer droplet formation into Voronoi patterns [8, 144–146]. A number of different timescales have been attributed to the dewetting process [145] which is highly thickness dependent [146]. Both interfaces polymer/substrate and polymer/air are important in the dewetting process [147].

The dewetting of thin polystyrene films can also be used to produce patterns which may have further applications [148]. One method to produce these patterns is via light exposure of thin polymer films. Making use of the dehydrogenation and cross-linking of PS exposed to UV light thin PS films can be patterned. The areas of thin films exposed to light, cross-link and if the film is heated above T_g these areas of the film are unaffected. The regions of the film which were not exposed to light will dewet giving rise to the pattern on the photomask. Polymer blends of conjugated polymers with PS show a slowing of the dewetting process [149]. This was attributed to the stiffening of the conjugated polymer chains upon light exposure (i.e. an increase in R_g which has also been observed in solution [61]).

Both the dewetting [10, 150, 151] and stabilisation [152] of PS/C_{60} thin films have been observed alongside other morphologies [8, 9] and will be discussed next.

2.3.2 Polystyrene/C_{60} Thin Films

The study of PS/C_{60} thin films has attracted some attention in the past few years, one reason for this is its perceived simplicity over the semicrystalline P3HT/PCBM blends where a number of phases can co-exist. PS/C_{60} thin films on the other hand use an amorphous polymer where there is a fairly low miscibility (1-3 wt%) between the two components in the melt [6, 7].

Initial work by Barnes et al. [150] demonstrated the improved stability of 1.8 kg/mol PS/C_{60} over PS thin films after thermal annealing above T_g. Low mass fractions of 1 wt% C_{60} were shown to provide this stability by a preferential attraction of C_{60} to the substrate interface. Two reasons for this stabilisation were given: "equilibrium stabilisation" or a "long term kinetic inhibition'. A 5 nm enrichment layer of C_{60} at the film-substrate interface was observed with neutron reflectivity, this layer was thought to be influenced by the non-equilibrium conditions during the spin coating process and is responsible for suppressing the dewetting process. The surface energies of the individual components are 48.1 and 35 mN/m for C_{60} [153] and PS respectively. The substrate surface energy was not provided by the authors, however using a similar surface treatment it has been given as 72 mN/m [152]. Thus, one would expect C_{60} to be preferentially attracted to the substrate over PS.

Holmes et al. [151] also demonstrated stabilisation on 75 kg/mol PS/C_{60} thin films with 3 wt% C_{60} which were solvent annealed with toluene. A 2 nm C_{60} rich layer which was present prior to solvent annealing was determined to be the cause of stabilisation with a potential fractal-like structure. Further work by the same group [10] used a film flipping method to demonstrate the stability of PS/C_{60} films. A PS/C_{60} film was cast on to a freshly cleaved mica surface which was then either (a) directly transferred to a hydrophobic substrate or (b) flipped so that what was the top of the thin film was at the bottom and in contact with the hydrophobic substrate. As the 2 nm C_{60} rich layer was present in the as cast films [151] it was assumed in Ref. 10 that this layer was present when spin coating onto the mica substrate. Dewetting of the film was not observed after transferring, using method (a) to a silicon substrate and solvent annealing, however was observed on the silanized, hydrophobic surface. With method (b) the fullerenes were not able to disperse homogeneously upon annealing under a toluene atmosphere, or diffuse to the substrate interface and so dewetting was observed on both substrates.

Refs. 10, 150 and 151 used neutron reflectivity to confirm the presence of C_{60} at the substrate interface. The neutron scattering length density (SLD) used to confirm the presence of C_{60} at this interface was ~2-3×10^{-6} $Å^{-2}$. Commonly, silicon substrates have a thin (~10 nm) layer of SiO_2, which was not accounted for in the fitting of reflectivity data by the authors of Ref. 10, 150 and 151. Piranha etching was used to clean the silicon wafers before depositing the PS/C_{60} film, which would only remove any organic residues, there would still be SiO_2 on top of the Si, in order to remove SiO_2 etching with HF is necessary. The SLD of SiO_2 is 3.7-4.2×10^{-6} $Å^{-2}$ [vii] and therefore close to the reported SLD for the C_{60} enriched layer. It is highly likely

[vii] Calculated with NIST SLD calculator using densities of 2.33 and 2.65 g/cm^3, which are the densities of Si and SiO_2 respectively. A range was given as the SiO_2 is likely to be amorphous and therefore less dense than the

that perceived C_{60} surface enrichment was in fact a SiO_2 layer. Using a 5 wt% C_{60} loading, Wong [154] demonstrated that the C_{60}/substrate attraction was not as significant as seen in Ref. 150 and a continuous 2 nm C_{60} rich layer was not observed. A higher C_{60} loading was used compared to Ref. 150 however one would still expect to observe C_{60} surface segregation. Ref. 154 also reports that the results in Ref. 150 used a modified sample preparation method, with a 'waiting time' from depositing the solution to beginning the spin casting process.

The work on PS/C_{60} thin films was expanded by Wong and Cabral [8, 9] who reported a spinodal clustering process in thin PS/C_{60} films [8] containing 5 wt% C_{60}. The PS M_w was higher (270 kg/mol) than used in Refs. 10, 150 and 151, this slowed the dewetting of the thin film. Thus, Wong and Cabral [8] were able to study the kinetic interplay between C_{60} association and dewetting as the fullerene association became faster than dewetting. The structure of these films was investigated with regard to the dominant length scale, λ^*, with the initial dominant length scale denoted λ_0, and the size and number of individual clusters. A film thickness dependency was found, as λ_0 was linear with respect to film thickness. Thinner films were found to have a smaller λ^* with slower coarsening kinetics. A PS M_w dependence was also noted, as lower M_w PS films would dewet if neat; this was suppressed upon the addition of C_{60} as seen in previous studies [10, 150, 151]. An interesting morphology developed at higher M_w with a structure appearing similar to that observed with spinodal decomposition and was designated with the term 'spinodal clustering' [8]. Two effects were thought to be relevant for this morphology: PS/C_{60} miscibility and C_{60}/substrate attraction. The attraction is dependent on the polymer M_w as a gel matrix forms which could slow down the attraction kinetics [151]. Further work [9] investigated film morphology with respect to C_{60} loading: the neat PS film and 1% C_{60} film remained stable, with the 2% C_{60} film initially forming a nucleated structure and after 48 hours annealing developing into a spinodal pattern. The highest loading C_{60} film, at 5%, formed a spinodal clustering pattern as had been observed previously after a few minutes. This suggested a common mechanism starting with nucleation and growth. AFM topography measurements indicated an initial roughening of the top surface after which the process slowed and steady state was reached. A temperature dependence of the thin films was also noted where annealing at 145 °C displayed a slow nucleation process, whereas heating at 175 °C showed a spinodal clustering pattern after 1 hour. Spinodal clustering has also been shown to exist in other polymer matrices [154, 155]. Using the previous work on C_{60} photo-polymerisation and oxidation [112–114, 119] it was shown that the light exposure of PS/C_{60} thin films stabilised the nanocomposite layer [152]. The environmental conditions were not reported in Refs. 10, 150 and 151 and so it is possible that the stability observed was due to light exposure.

reported value. For completion, the SLD of Si is 2.07×10^{-6} Å^{-2}.

2.3.3 Surface segregation

The surface segregation of fullerenes (and nanoparticles in general) is very important to understand and control as this will impact the performance for any particular application, for example power conversion efficiency in organic solar cells. As was discussed in Section 2.3.2 there is thought to be, in some circumstances, a preferential attraction for C_{60} to the substrate.

A polymer/fullerene system where this has been widely studied in recent years due to its OSC relevance is P3HT/PCBM. The segregation of the fullerene (PCBM) to either the top or bottom electrode interface will directly effect the charge transport of excited electrons within the device and thus the device efficiency. All of the studies discussed below have used samples where one interface is open to air (or nitrogen) this is not a realistic situation as has been noted [156]. Some have found PCBM segregation to both interfaces [157], PCBM enrichment at the substrate interface [156, 158], P3HT segregation to both interfaces [159] or P3HT enrichment at the substrate interface [158–160]. These are all carried out on a number of different substrates: Si [156], SiO_2 [157–159], ITO [viii] [160], PEDOT:PSS [ix] [159], PTT [x]:Nafion [159] and OTS [xi] [158], HMDS [xii] [157].

These apparently contrasting reports on surface segregation can be understood by a comparison of surface energies (γ) of the substrates (see Table 2.1) and those of P3HT (26.9 mN/m) and PCBM (37.8 mN/m) [158]. In a simplistic 'ideal' situation, there would be P3HT enrichment at the substrate interface, as the incoming light is absorbed by the polymer which then transfers excited electrons to the PCBM towards the top electrode. P3HT substrate attraction on the whole was observed on substrates which had surface energies from 23-44 mN/m. PCBM enrichment has been reported for substrates with surface energies from 45-72 mN/m. The only contrasting result is on SiO_2 where both P3HT [159] and PCBM [158] enrichment at the substrate interface have been reported by the same group. There is clearly a very fine difference between whether P3HT enrichment (with PEDOT:PSS at 45 mN/m) or PCBM enrichment occurs (with HMDS at 44 mN/m). Another factor which was not reported for most of the studies was the P3HT M_w which is expected to have a large effect on the phase separation of the two components and crystallisation of PCBM. Others have claimed that interfacial segregation does not matter at all and has no bearing on device performance [161]. Surface directed spinodal decomposition, previously seen in thin films of hydrogenous/deuterated mixtures of poly(ethylenepropylene) [162], has also been observed for P3HT/PCBM thin films [163] on a ZnO substrate.

[viii] Indium tin oxide
[ix] Poly(3,4-ethylenedioxythiophene):Polystyrene sulfonate
[x] poly(thienothiophene)
[xi] octyltrichlorosilane
[xii] hexamethyldisilazane

Table 2.1: Surface energies of the substrates used in Refs. 156–160.

Substrate	Surface energy/mN/m
Si	57
SiO_2	72
ITO	24
PEDOT:PSS	45
PTT:Nafion	23
OTS	24
HMDS	44

2.3.4 Summary

The mechanism for thin polymer film dewetting is established [8, 143–146] with both the substrate and air interfaces playing some part in the process [147]. Light exposure of PS thin films has been shown to suppress dewetting [148] and slows the dewetting of conjugated polymers [149] via different mechanisms.

The addition of fullerenes to thin polymer films has been shown to slow down or suppress dewetting which is highly depending on polymer M_w, C_{60} loading and annealing temperature [8, 9, 150, 151]. Light exposure of PS/C_{60} thin films can also suppress dewetting [152].

The surface segregation and preferential attraction of the components in thin polymer/fullerene films has been shown to be highly dependent on the surface energy of the substrate. Although these studies are of some use, the annealing of OSC devices usually takes place after the top electrode is deposited and thus there is a thin, vertically confined film, whereas all of the studies presented here are open to atmosphere. This has not been acknowledged by many of the authors [156] and there are many additional challenges associated in studying buried interfaces.

2.4 Applications of polymer nanocomposites

There are a wide variety of applications for polymer nanocomposites where there are significant advantages over traditional composites, as well as applications which may otherwise not have been possible. Some of these include: OSCs [2], membranes [140], chemical sensors [151], self healing networks [164], biological imaging [165], drug release [166], mechanical reinforcement [167] and flame retardants [168]. Some of these applications will be reviewed below alongside desirable qualities for each use.

2.4.1 Mechanical Reinforcement

A major application for polymer nanocomposites is mechanical reinforcement. At the same volume fraction of either micro- or nano-particles, the mean particle-particle separation is three

orders of magnitude lower with nanoparticles alongside six orders of magnitude increase in interfacial area and nine order of magnitude increase in number density. Thus, there will be implications on the physical properties [169]. It has been shown that polymer composites with nanoparticle additives have a higher Young's modulus than those with micron sized additives with the same molecular composition [170, 171].

Studies have shown that the processing and subsequent dispersion of nanoparticles within the polymer matrix affect the mechanical properties such as the modulus and elongation at break of nanocomposites [172]. Moll et al. [173] have shown for polymer grafted silica particles, a percolated network of particles is desirable for stress propagation whereas a well-dispersed network gave the highest reinforcement.

The mechanical properties of a polymer nanocomposite can be tuned by selection of filler [169, 174], state of dispersion [172, 173] and size of filler [170, 171].

2.4.2 Active and Self Healing Materials

The range of applications for self healing materials seems almost limitless, from the oil and gas industry to aerospace and adhesives [175]. There are two types of self healing materials, those which are autonomic and non-autonomic [176]. Non-autonomic self healing materials require an external trigger (which may be associated with the devices operating conditions).

Experimental evidence for segregation of nanoparticles to cracks was established by Gupta et al. [177] using ~4 nm polymer coated CdSe/ZnS nanoparticles in a PMMA matrix. There is entropy-driven segregation of the nanoparticles to the polymer/air interface which could then be observed via fluorescence microscopy or TEM. Although no healing of the crack was reported here it was possible to detect the segregation of nanoparticles to the crack. Using the same nanoparticles as in Ref. 177, Lee et al. [164] investigated nanoparticle behaviour prior to crack formation. Crazes are micron-scale regions which form before cracks. These crazes determine the eventual strength and toughness of polymeric materials. A progression of craze formation was determined: precraze (nanoparticle alignment), premature craze (repulsion of nanoparticles from craze) and mature craze (entrapment of nanoparticles) [164].

2.4.3 Organic Solar Cells

Organic solar cells (OSCs) have offered much promise since photoinduced electron transfer from MEH-PPV to C_{60} was demonstrated [178]. In the proceeding years P3HT/PCBM has been a benchmark OSC system which has attracted much attention [1, 2]. The necessity for polymer nanocomposites in OSCs arises from this ability of the fullerene to 'remove' the excited electron from the polymer and transport it to an electrode. As was discussed before in Section 2.3.3, the vertical segregation of the polymer and fullerene phase is necessary. The 'ideal' morphology of OSCs is highly dependent on the crystallinity of the polymer and fullerene respectively [1] with current thinking, the morphology of P3HT/PCBM thin films consists of three phases: crystalline

P3HT, PCBM crystals in a pure P3HT matrix and an amorphous mixture of P3HT and PCBM. Other possible phases are amorphous phases of the pure components.

The optimum morphology for OSCs is unknown, [1] and this is not the only limiting factor for optimising performance. Other factors which would need to be considered for improving OSC performance are energy level alignment between the polymer, fullerene and respective electrodes, the flexibility of the thin film if OSCs are to be processed via roll-to-roll coating, and long-term stability [2].

Given these aspects of OSCs which require improvement part of the answer lies in the control over the morphology of the final product to provide a three phase system (for P3HT/PCBM) [1] which is stable and provides high efficiencies [2].

2.4.4 Summary

Given the wide variety of applications for polymer nanocomposites, either in the bulk or thin films, there is a necessity for well-controlled morphologies, such as a percolated network for enhanced mechanical properties [173], dispersed in a polymer matrix for self healing [164] or reinforcement [173] and a complex, potentially three phase, thin film for OSCs [1].

2.5 Processing Methods

In order to achieve the complex morphologies which seem necessary for efficient OSC device performance [1] various processing methods have been attempted and developed to achieve controlled morphologies. Two common methods are nucleating agents [179, 180] and solvent mixtures/additives [181–183].

2.5.1 Nucleating Agents

Due to the necessity for controlled micro and nanostructure of OSCs with crystalline polymer and fullerene phases, nucleating agents have been employed. Treat et al. [179] used two nucleating agents: DMDBS [xiii] and BTA [xiv], originally designed for isotactic polypropylene, to nucleate the crystallisation of P3HT, other poly-(alkylthiophenes), PCBM and TIPS [xv] pentacene. A very small fraction of either DMDBS or BTA (0.1-1 wt%) was necessary to induce crystallisation of the polymer. There were significant improvements to device performance upon addition of either nucleating agent.

A criticism which could be given to the work in Ref. 179 is that the nucleating agents are not active electronic components. Richards et al. [180] investigated mixtures of P3HT/PCBM/C_{60} for OSCs. There was an increase in PCBM crystal density with an associated decrease in crystal

[xiii] 1,3:2,4-bis(3,4-dimethylbenzylidene)sorbitol
[xiv] tris-tert-butyl-1,3,5-benzenetrisamide
[xv] 6,13-bis(triisopropyl-silylethynyl)

size indicating that the C_{60} molecules were used as nucleation sites. Device lifetime was also extended for those containing C_{60}. Others [184] have fabricated devices with a mixture of C_{60} and C_{70} however a morphological study was not conducted, the authors suggested there could be improved thermal stability.

2.5.2 Solvent Mixtures and Additives

The use of solvent mixtures and additives is now a standard processing route for high performance solar cells since the demonstration of the addition of diiodooctane (DIO) to chlorobenzene (CB) when processing PTB7 [xvi] and $PC_{71}BM$ [xvii] to improve OSC device efficiency [181].

Solvent mixtures have been used for P3HT/C_{70} thin films a using CB/heptane solvent mixture [182] and additives on Si-PDTBT [xviii]/PCBM thin films cast from a chlorobenzne/1-chloronaphthalene mixture [183] have previously shown to suppress fullerene phase separation.

Further investigations were carried out by Hammond et al. [185] and Collins et al. [186] on PTB7/$PC_{71}BM$ (and by Liu et al. [187] on PTB7/PCBM). Both reported a decrease in $PC_{71}BM$ domain size and an associated increase in device efficiency (as was found in Ref. 181). A mechanism determining the effect of DIO on morphology was given by Lou et al. [188]. They proposed that DIO was a better solvent for $PC_{71}BM$ than for PTB7 and so selectively dissolved the $PC_{71}BM$. Given the higher boiling point of DIO over chlorobenzene (vapour pressure data is unavailable for DIO), once the chlorobenzene had evaporated during the spin casting process, DIO remained in the film and the $PC_{71}BM$ remained solvated. $PC_{71}BM$ was then able to intercalate with the PTB7 causing smaller $PC_{71}BM$ aggregates to form and thus improved electronic properties of the OSC.

2.6 Overview and Problem Statement

There is a wide range of literature on polymer nanocomposites with fundamental studies focussing on nanoparticle effects on polymer chain dimensions in solution [36–39] and in the melt [101, 106–110, 126]. The studies on polymer nanocomposite solutions follow some of the theoretical predictions within the protein-limit of phase separation, colloid aggregation and a decrease in chain dimensions [33–35]. The dispersion of nanoparticles within polymer matrices is known to effect their properties [173]. There are some gaps within the literature which have been identified as areas for further study.

The majority of polymer nanocomposites, either as bulk samples [6, 7, 106–110, 126] or thin films [8–10, 150, 151, 185, 186], involve a solution processing step. This stage of the process has been very much overlooked with few studies linking solution conformation with bulk or thin film

[xvi] thieno[3,4-b]thiophene-*alt*-benzodithiophene copolymer
[xvii] [6,6]-phenyl-C71-butyric acid methyl ester
[xviii] poly[(4,4-didodecyldithieno[3,2-b:20,30-d]silole)-2,6-diyl-alt-(2,1,3-benzothiadiazole)-4,7-diyl]

morphology [182]. There are also discrepancies in the miscibility for PS/C_{60} mixtures in the bulk and thin films with 1-3 wt% C_{60} in the bulk [6, 7] and ≤1 wt% in thin films [9].

Although the behaviour of C_{60} exposed to light in the solid state has been extensively studied [112–114, 119], there are contradictory reports within the literature for C_{60}/solvent light exposure [77–79]. Whilst others reported C_{60} aggregation in neat solvent or solvent mixtures [83–88]. Often those who report aggregation do not fully report the solution storage conditions.

Studies on PS/C_{60} thin films demonstrated dewetting suppression or 'spinodal clustering' [8–10, 150, 151] which is dependent on a range of factors: PS M_w, annealing temperature, film thickness and C_{60} loading. The well-controlled and established morphologies which are observed on the micron scale make this an ideal model system to study.

This thesis examines, in detail, a number of factors impacting bulk and thin film morphology of fullerene-based polymer nanocomposites: (i) the effect of C_{60} addition to polymer chain dimensions in the dilute to semi-dilute regime, (ii) C_{60} and PCBM miscibility in PS/solvent solutions, (iii) impact of C_{60} aggregates on as cast and annealed thin film morphology, (iv) C_{60}/toluene and PCBM/toluene solution light exposure and (v) subsequent effect on thin film morphology.

3 Experimental Techniques

In this section details of the experimental techniques used are provided. Static and dynamic light and small angle neutron scattering were the primary techniques used, alongside optical and atomic force microscopy. Other analytical techniques are summarised at the end. The specifics for particular experiments are given in the relevant chapter.

3.1 Scattering Techniques

3.1.1 Light Scattering

Dynamic Light Scattering

Dynamic Light Scattering (DLS) is a technique which has been widely used to characterise polymers in solution, including polystyrene, the most widely studied [4, 5]. It provides the diffusion coefficient for translational diffusion D. Assuming that the polymer studied is in the dilute regime and is an ideal chain, then Equation 3.1 can be applied to extract R_h. Where k_B, T and η are Boltzmann's constant [1.38×10^{-23} $m^2kgs^{-2}K^{-1}$], absolute temperature [K] and solvent viscosity [Pa.s] respectively.

$$R_h = \frac{k_B T}{6\pi\eta D_0} \tag{3.1}$$

The intensity-intensity time correlation function, $g^{(2)}(q,t)$, of fluctuations in the scattered electric field in time, can arise from translational, vibrational or rotational motion and is equal to: $\frac{\langle I(t)I(t+\tau)\rangle}{\langle I(t)^2\rangle}$. This is then transformed into the field correlation function, $g^{(1)}(q,t)$, by the Siegert relation [189]: $g^{(2)}(q,t) = 1 + \beta g^{(1)}(q,t)^2$ which assumes that the scattered electric field is a stationary Gaussian random process. Here β is an instrument parameter and q [m^{-1}] is the scattering vector, given by Equation 3.2, where n, λ and θ are the refractive index of the solvent, laser wavelength [m] and scattering angle [radians] respectively.

$$q = \frac{4\pi n}{\lambda}\sin\frac{\theta}{2} \tag{3.2}$$

Once the field correlation function of the system being studied is known, there are three commonly used methods to determine the diffusion coefficient: (i) cumulant analysis , (ii) sum of exponentials and (iii) CONTIN.

If the correlation function has a single exponential decay, then the cumulant analysis [190]

is the simplest to use, a plot of $\ln(g^{(1)}(t))$ versus relaxation time, t, can for short times be described by a function of the form:

$$\ln(g^{(1)}(q,t)) = G - \Gamma(q,c)t + \frac{\mu_2}{2\Gamma^2(q,c)}t^2 \tag{3.3}$$

where G is a constant and $\Gamma(q,c)$ is the mean inverse relaxation time of diffusive modes with the z-averaged translational diffusion coefficient $D(q,c)$=$\Gamma(q,c)/q^2$ and c is the mass concentration of the solute. The quantity $\mu^2/\Gamma^2(q,c)$ corresponds to the normalized variance of the intensity-weighted distribution of diffusion coefficients. Linear extrapolation of $D(q,c)$ toward $q^2 \to 0$ and $c \to 0$ yields the z-averaged diffusion coefficient at zero scattering angle and infinite dilution, D_0. This translational diffusion coefficient can be transformed into a mean effective hydrodynamic radius R_h of the particles via Equation 3.1. A typical correlation function and resulting cumulant analysis is shown in Figure 3.1a.

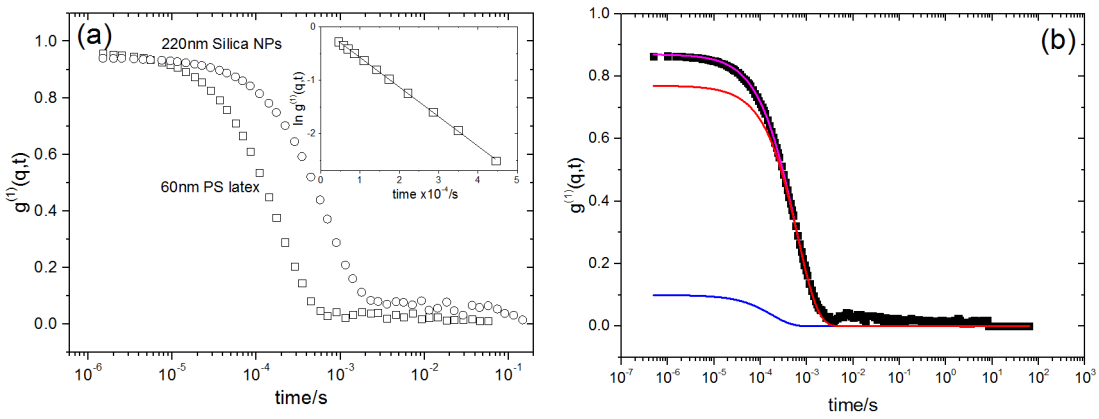


Figure 3.1: (a) Typical correlation functions, obtained using a Malvern Nano-S, for a single species in solution, 60 nm diameter PS latex (□) and 220 nm diameter silica NPs (○). Inset shows cumulant fit for 60 nm PS latex particles, the gradient of the straight line fit can give D_0 and thus an R_h of 38 nm. (b) Correlation function for a mixture of two nanoparticles, 60 nm diameter PS latex and 220 nm diameter silica NPs. The correlation function can be fit using Equation 3.4 (—). The individual additive contributions are for the latex particles (—) and silica NPs (—).

If there are multiple decays, arising from multiple size populations, then a sum of exponentials:

$$g^{(1)}(q,t) = \sum_{i=1}^{N} a_i(q)\exp(-\Gamma_i(q)t) \tag{3.4}$$

is a suitable method to fit the data, and is shown in Figure 3.1b. In Equation 3.4, each coefficient $a_i(q)$ represents amplitude of the respective $\Gamma_i(q)$, which can be illustrated by a plot of $a_i(q)$

versus $\Gamma_i(q)$. For large numbers of exponentials (usually N ≥ 50), Equation 3.4 can be established by means of the CONTIN analysis [191], which may, on the one hand, give detailed information on the shape of the size distribution of a sample, but on the other hand evaluation of the coefficients $a_i(q)$ and $\Gamma_i(q)$ may suffer from artefacts. For the case of two or three well-separated modes, DLS data can be adequately modeled with double- or triple-exponentials (N = 2 or 3). This allocates one exponential per mode and hence allows for a statistically robust estimate of the z-averaged particle size and of the corresponding partial scattering intensity of the respective mode.

Static Light Scattering

Static Light Scattering can provide information on R_g, M_w and the second virial coefficient, A_2. The information from SLS is a structure factor, $S(q)$. Using Equation 3.5, the excess Rayleigh ratio of the solute is found, where $S_{sample}(q)$ and $S_{solvent}(q)$ are the scattering signals of the sample and of the solvent and $S_{standard}(q)$ and $R_{standard}$ are the scattering signal and the known Rayleigh ratio of the standard, usually toluene, $R_{toluene,\ \lambda=633\ \mathrm{nm}} = 1.35 \times 10^{-3}\ \mathrm{m}^{-1}$ and $R_{toluene,\ \lambda=532\ \mathrm{nm}} = 2.4 \times 10^{-3}\ \mathrm{m}^{-1}$.

$$R(q) = \frac{S_{sample}(q) - S_{solvent}(q)}{S_{standard}(q)} R_{standard} \tag{3.5}$$

To find the R_g of solute(s), either Zimm's approximation [192] or Guinier's approximation which is only valid for $qR_g < 1$ [89] can be used. If there is a low angular dependency to the scattering, then Equations 3.6 & 3.7 are used.

$$\frac{1}{R(q)} = \frac{1}{R_{q=0}} \left(1 + \frac{q^2 R_g^2}{3} \right) \tag{3.6}$$

$$\frac{Kc}{R(q)} = \frac{1}{M_w} + \frac{R_g^2 q^2}{3M_w} + 2A_2 c \tag{3.7}$$

$$K = \frac{4\pi^2 n^2}{N_A \lambda^4} \left(\frac{dn}{dc} \right)^2 \tag{3.8}$$

$$\ln R(q) = \ln R_{q=0} - \frac{q^2 R_g^2}{3} \tag{3.9}$$

Using Equation 3.6, R_g^2 of the dissolved particles and the Rayleigh ratio at zero scattering angle, $R_{q=0}$, can be determined by a linear fit to a plot of $1/R_{(q)}$ versus q^2. Equation 3.6 is valid and independent of the particle shape at $qR_g \leq 1$. Additionally, the polymer M_w and A_2 can also be found using Equation 3.7. Contrast factor, K, is defined in Equation 3.8 where n, N_A, λ and $\frac{dn}{dc}$ are the refractive index of the solvent, Avogadro's number, laser wavelength and refractive index increment of the polymer respectively, values and units are given in Table 3.1.

For data which has a strong angular dependence, Zimm's approximation is no longer valid as the large slopes and intercepts close to zero create large uncertainties in finding R_g. Thus, Guinier's approximation [89] (Equation 3.9) is used as an alternative to Equation 3.6 in order to extract R_g from strongly angular dependent scattering curves.

Table 3.1: Summary of constants used in Equations 3.6 to 3.8

Symbol	Value	Unit
n	1.496	-
N_A	6.02×10^{23}	mol^{-1}
$\frac{dn}{dc}$	0.000105	mLmg^{-1}
T	298	K
K	1.1×10^{-17}	$\frac{\mathrm{m}^2\mathrm{mol}}{\mathrm{mg}^2}$

A benefit of simultaneous static and dynamic light scattering, is being able to deconvolute the SLS signal as the partial scattering intensity $R_i(q)$ of mode Γ_i is proportional to the coefficient a_i:

$$R_i(q) = \frac{a_i}{\sum_{i=1}^{N} a_i} R(q) \tag{3.10}$$

If the subdivision into different modes is significant, each $R_i(q)$ can be evaluated individually by means of Equation 3.6 or 3.9 [193].

For C_{60} clusters the FractalModel in SasView v2.2.0 [194] was used to fit the data. This model was developed by Teixeira [90] for small angle neutron scattering therefore there are terms within the model which are not necessary for the treatment of static light scattering data, nevertheless the model allows one to fit scattering from fractal-like aggregates which are composed of several, smaller spherical particles.

$$I(q) = \Phi P(q) S(q) \tag{3.11}$$

$$P(q) = V(\rho_{particle} - \rho_{solvent})^2 \times [3\sin(qR_0) - qR_0\cos(qR_0)/(qR_0)^3]^2 \tag{3.12}$$

$$S(q) = 1 + \frac{d_f \Gamma(d_f - 1)}{[1 + 1/(q\xi)^2]^{(d_f-1)/2}} \frac{\sin[(d_f - 1)\tan^{-1}(q\xi)]}{(qR_0)^{d_f}} \tag{3.13}$$

$$R_g^2 = d_f(d_f - 1)\xi^2/2 \tag{3.14}$$

where $I(q)$ [cm^{-1}], Φ, V [cm^3], ρ [cm^{-2}], d_f, ξ [cm] are the coherent scattering intensity, number density of scatterers, volume of a single sphere with a radius R_0 [cm], scattering length density of the particle and solvent, fractal dimension and correlation length respectively. ξ is similar to that seen in the Ornstein-Zernike treatment, and is only qualitative with its meaning is dependent on any particular situation.

Instruments

Three different light scattering systems are used in this thesis: Malvern Nano-S (DLS), CGS-3/MD-8 (DLS and SLS) and a SOFICA (SLS), all three used a HeNe laser (λ = 633 nm). The Malvern Nano-S (Malvern Instruments Ltd, Malvern, UK) has a fixed detector at 173°, corresponding to a q of 2.96×10^{-2} nm^{-1} when using toluene as the solvent. All experiments were performed in sealable rectangular quartz cuvettes (Hellma, Müllheim, Germany). The CGS-3/MD-8 Compact Goniometer System (ALV, Langen, Germany) is equipped with an array of eight detectors, where the angle between adjacent detectors is 8°. Each detector comprises an avalanche photodiode (APD) and a photocorrelator, enabling the simultaneous measurement of static intensity and the intensity-intensity time correlation function. The array of detectors also enables the simultaneous recording of a 56° range with a total angular range from $\theta_{\min}$ of 20° to $\theta_{\max}$ of 136°, corresponding to a q range of 5.1×10^{-3}< q < 2.7×10^{-2} nm^{-1}. Cylindrical quartz cuvettes (Hellma) with a diameter of 10 mm are used as scattering cells. Prior to any measurement with the ALV system, cuvettes were cleaned of dust by continuously injecting freshly distilled acetone from below for 5 min.

The SOFICA (Societé Francaise d'Instrumentes de Contröle et d'Analyses, Le Mesnil Saint-Denis, S. et 0., France) photometer, with modifications made by SLS Systemtechnik (G. Baur, Denzlingen, Germany) has a θ range of 27 to 105°, corresponding to a q range of 7.1 to 23.7 ×10^{-3} nm^{-1}. In both the SOFICA and CGS-3/MD-8 10mm diameter cylindrical quartz cells (Hellma) with a stopper to prevent evaporation are used. The photomultiplier (PM) tube is calibrated to a toluene (puriss. p.a. ≥ 99.7%, Sigma Aldrich) standard. An important difference between the ALV system and the SOFICA is the detection method, the ALV uses an APD whereas the SOFICA uses a PM tube, which gives the SOFICA a much higher sensitively when characterising low scattering or high absorbing samples.

3.1.2 Small Angle Neutron Scattering

Small angle neutron scattering (SANS) was employed to probe polymer conformation, fullerene clustering and composition fluctuations. As with all neutron scattering and reflectivity techniques, SANS requires a contrast in the scattering length density (SLD or ρ) of the species being studied. A common tool to provide contrast is via deuteration of one component, or part of one component. SLD [nm^{-2}] is calculated by $\frac{\rho N_A}{M}\Sigma b_i n_i \times 10^{-27}$ where b_i, n_i, M ρ are atomic scattering length of atom i [fm], number of i atoms, monomer mass [g/mol] and density [g/cm^3]

respectively. It should be noted that b has no trend with atomic number [102]. A summary of SLD's for components used in the SANS experiments is given in Table 3.2

Component	SLD ($\times 10^{-4}$ nm^{-2})
C_{60}	5.74
PS-h	1.41
PS-d	6.47
Tol-h	0.94
Tol-d	5.66

Table 3.2: Summary of SLD's of components used in this investigation

A typical q-range accessible in SANS is 0.05 to 5 nm^{-1}, corresponding to a length scale from 120 to 1.2 nm. However, this range can not be accessed in a single measurement and may often require changing sample-detector distance (L_{sd}) or the wavelength of neutrons being used (depending on the type of source). ISIS (Didcot, UK) is a pulsed neutron source, and produces a range of neutron wavelengths, on the other hand, ILL (Grenoble, France) is a reactor source and so L_{sd} is changed to access a wide q range. Equation 3.2 can be approximated to Equation 3.15 due to the low θ used. r_{det} is the radial distance at which neutrons impact the detector.

$$q \approx \frac{4\pi}{\lambda} \sin \frac{r_{det}}{L_{sd}} \tag{3.15}$$

The scattered signal from SANS consists of a coherent (I_{coh}) and incoherent (I_{inc}) portion, the incoherent portion must be subtracted from the total scattered intensity. Once I_{inc} has been subtracted the resulting data can be fit using models for structure ($S(q)$) and form ($P(q)$) factors. Typical SANS for two types of spheres and a Gaussian coil is shown in Figure 3.2. Some common form factors are summarised in Table 3.3. Common shapes also have characteristic power laws, summarised in Table 3.4.

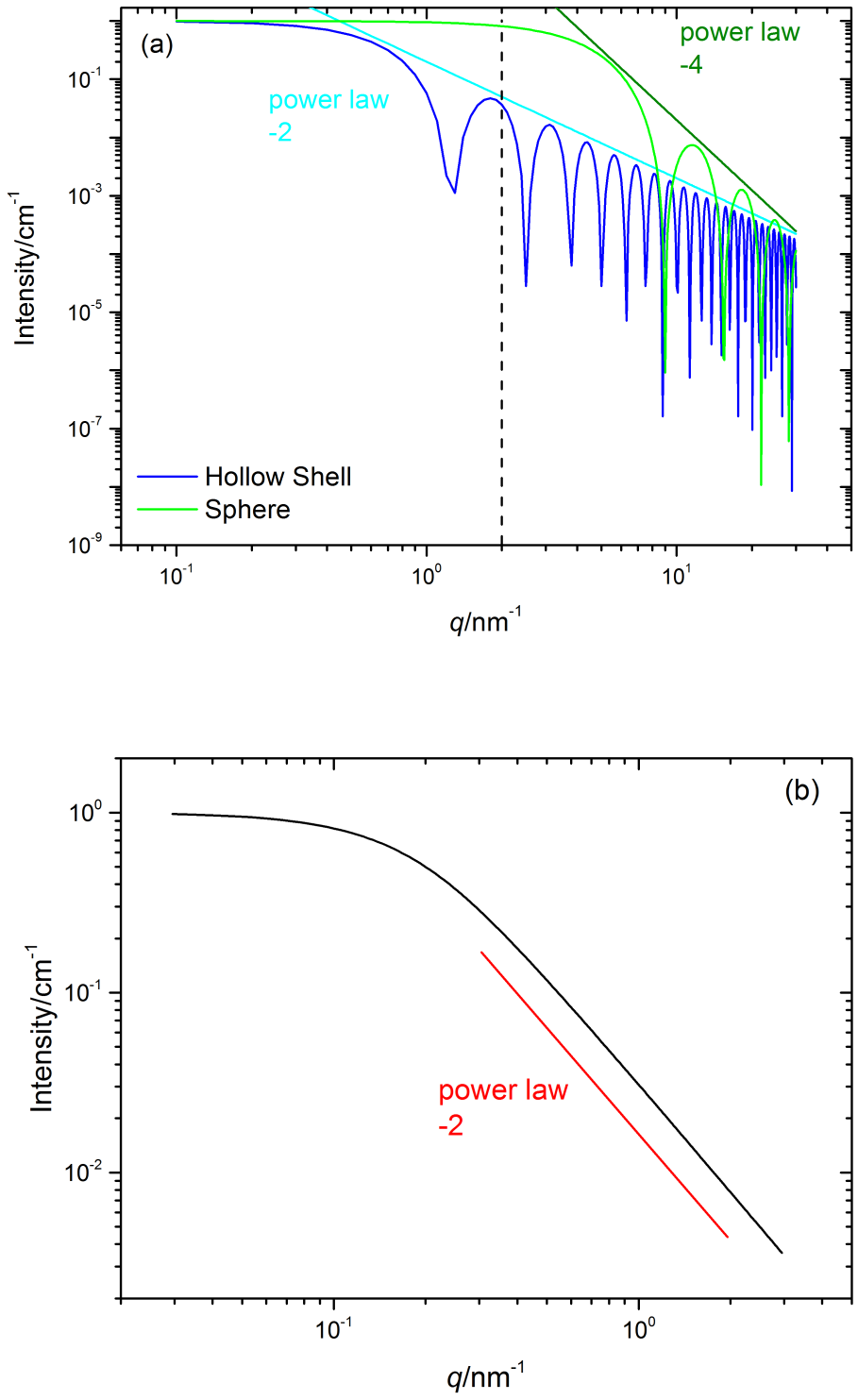


Figure 3.2: Model SANS data for (a) sphere and hollow sphere with a shell of negligible thickness with radius of 0.5 nm, dashed line corresponds to 1/radius, and (b) ideal Gaussian polymer coil, R_g of 8 nm with power laws of -4 and -2.

Shape	Form Factor ($P(q)$)
Polymer with Excluded Volume	$\frac{1}{\nu U^{1/2\nu}}\gamma\left(\frac{1}{2\nu}, U\right) - \frac{1}{\nu U^{1/\nu}}\gamma\left(\frac{1}{\nu}, U\right)$
Polymer coil in θ solvent	$\frac{2(\exp(-q^2R_g^2)+q^2R_g^2-1)}{(q^2R_g^2)^2}$
Polydisperse Gaussian chain	$\frac{2}{x^2}\left[\frac{h}{h+\frac{q^2R_g^2}{1+2/h}} - 1 + x\right]$
Correlation Length	$\frac{B}{1+(q\xi)^2}$
Hard Sphere	$\frac{9(\sin qR_g - qR_g\cos qR_g)^2}{(qR_g)^6}$
Hollow Spherical Shell	$(\frac{\sin qR}{qR})^2$
Porod Scattering	$2\pi\Delta\rho^2 S_V q^{-4}$

Table 3.3: Summary of form factors, $P(Q)$, and their corresponding shapes. The variables the polymer with excluded volume model are: excluded volume parameter, ν, $U = \frac{q^2a^2n^{2\nu}}{6}$, where a is the statistical segment length and n is the number of steps, γ is an incomplete gamma function so that $\gamma = \int_0^U dt \exp(-t)t^{x-1}$. For the polydisperse Gaussian chain: $x = \frac{R_g^2q^2}{1+2/h}$, here $h = \frac{M_w}{M_n}$ and for Porod scattering S_V is the specific surface area or surface to volume ratio [102, 195, 196].

For the SANS data presented in Section 4.4, background subtracted SANS data was fit using SasView (v2.2.0) [194]. In the dilute regime, PS chains were fit using the PolymerExclVol model (shown in Table 3.3) [195]. A detailed explanation of which can be found in Ref 195. For semidilute solutions, the CorrLength model was used, as shown in Equation 3.16. This combines the Ornstein-Zernicke (OZ) form alongside Aq^{-4}, where $A = 2\pi\Delta\rho^2 S_V q^{-4}$. A typical scattering profile from a deuterated PS/C_{60}/hydrogenous toluene mixture is shown in Figure 3.3, which demonstrates that an additive contribution is suitable as the scattering contributions for each component occurs in well-separated q regimes. The form factor for a solvent in a polymer/solvent mixture can be set to 1 and is commonly done so in literature [197].

Shape	Power Law (α)
1D rod	1
Polymer coil in good solvent	5/3
Polymer coil in θ solvent or 2D structure	2
Hollow Spherical Shell	2
Polymer coil in bad solvent	3
Hard Sphere, sharp interfaces	4

Table 3.4: Summary of typical power laws, $I \propto q^{-\alpha}$ [102].

$$P(q) = Aq^{-4} + \frac{B}{1 + (q\xi)^2} \tag{3.16}$$

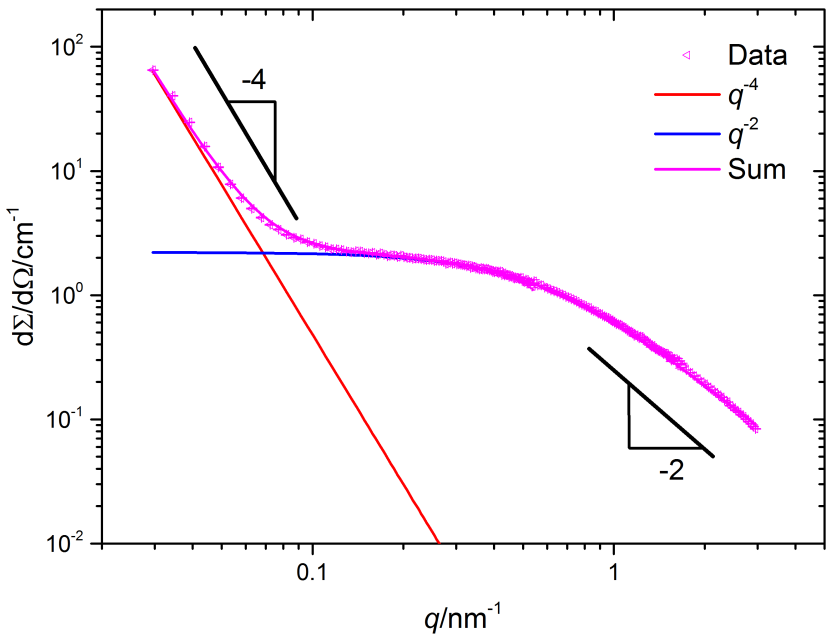


Figure 3.3: Coherent SANS data for a 9.5 wt% 1 Mg/mol deuterated PS and 0.5 wt% C_{60} solution in deuterated toluene (◂). A form factor with q^{-4} (—), an OZ form factor (—) and a sum of the two (—) are shown.

SANS experiments were carried out in rectangular or banjo Hellma cells (1, 2 or 5 mm depending on the volume of deuterated component) at LOQ (ISIS, Didcot), D11 and D22 (ILL, Grenoble) with q ranges of 0.09-4.85 nm^{-1} (LOQ), 0.013-3 nm^{-1} (D11) and 0.0296-3 nm^{-1} (D22) respectively.

3.2 Thin Films

3.2.1 Thin film preparation

For the thin films prepared in Sections 5.2 and 6.2 the relevant solution was prepared, a silicon < 100 > wafer (Compart Tech) was cut to 2 cm squares, blown with 1.2 μm filtered N_2 gas, and exposed to UV irradiation with a Ultraviolet UV Ozone Cleaner (Novascan) for 15 minutes to remove organic residues and provide a uniform surface energy. The wafer was placed onto the chuck of the spin coater (WS400Ez-6NPP-LITE, Laurell Technologies Corporation, PA, USA), the vacuum pulled and a stream of 1.2 μm filtered N_2 gas used to clean dust off the wafer. 100 μL of unfiltered solution was placed onto the wafer and the wafer spun at the necessary rpm for two minutes. Film thickness was measured with a UV-visible interferometer (Filmetrics, F20-UV) calibrated with a Si wafer standard prior to measurements. All thicknesses reported are ±4 nm.

3.2.2 Optical Microscopy and Image Analysis

Thin polymer composite films were imaged with an Olympus BX41M-LED reflectance microscope equipped with a AVT GigE GX1050C camera. *In situ* annealing experiments were carried out in a Linkam THMS600 at the required temperature and desired time. Image analysis was carried out using ImageJ (v1.46r). Depending on the desired analysis two different routes were necessary and are summarised in Figure 3.4. Route 1 gave cluster dimensions, C_{60} rich area fraction (A_f) and number of surface features and route 2 gives characteristic length scale (λ^*) between C_{60}-rich regions. Both routes required the RGB signals to be split. For route 1 (c) the brightness and contrast were varied, and (d) the image was made into a binary format, a uniformly lit area measuring 100 μm × 100 μm was selected and the particle analysis tool employed. For route 2 (e-h) once the colour channels had been split, (g) the image was thresholded to produce a binary image, (h) the holes were filled and a fast Fourier transform was carried out, as seen in the inset of (h). A radial profile was used to extract the q^* peak. q calibration was carried out using a standard diffraction grating.

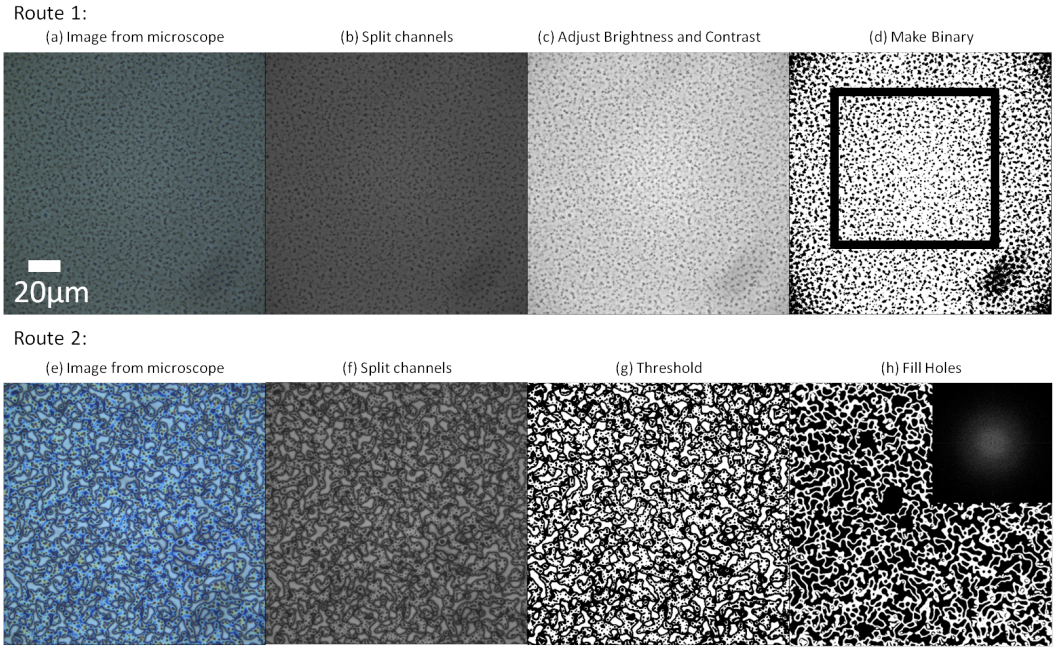


Figure 3.4: Optical Microscopy image processing with Route 1 (a-d) giving cluster dimensions, area fraction (A_f) and number of surface features and Route 2 (e-h) giving characteristic length scale (λ^*) respectively.

3.2.3 Atomic Force Microscopy

Atomic Force Microscopy (AFM) (Innova, Veeco) is employed in tapping mode to view nanoscale structures in thin polymer composite films. Images were processed using Gwyddion (v2.31). Raw data from the AFM was imported into Gwyddion, levelled by mean plane subtraction, polynomial background removed and lines corrected by matching height median. The minimum height for images was set to zero. AFM height calibration was carried out on a height calibration standard, shown in Figure 3.5. With typical, un-optimised, scanning conditions, topographic features within 10% of absolute height standard (200 nm) are found.

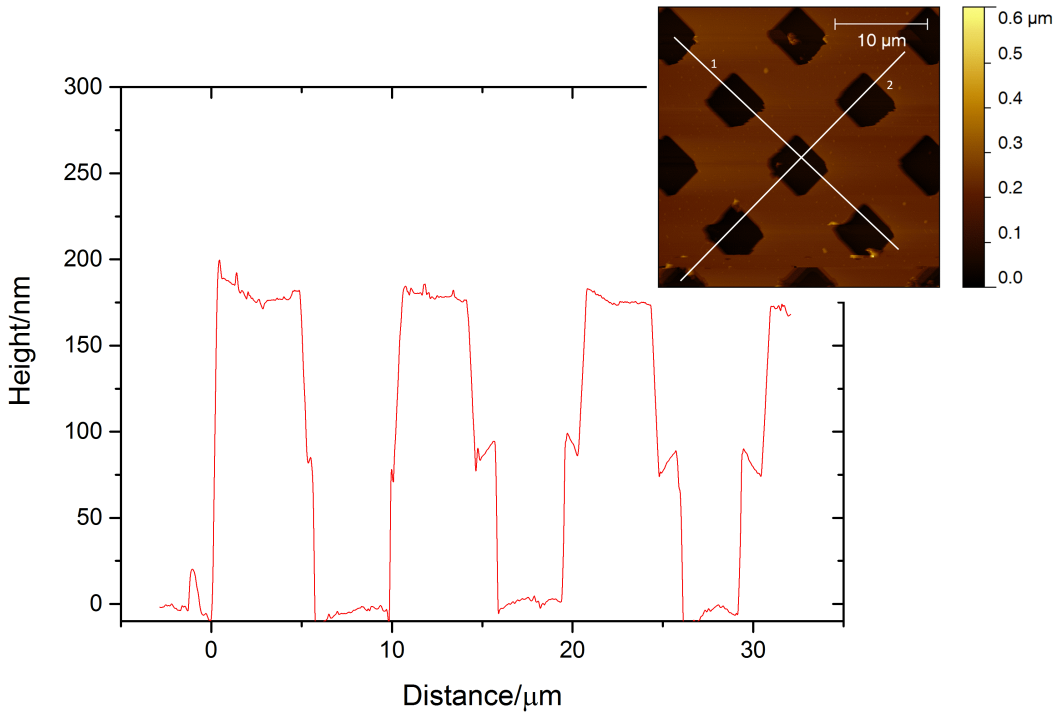


Figure 3.5: AFM step height standard linecuts, averaged from the two lines shown in inset image.

3.3 Rheology and Spectroscopy

Alongside reciprocal and real space imaging a number of other techniques were used. In Chapter 4 rheology and UV-visible spectroscopy are used. For determination of $C_{60}O_x$ clusters seen in Chapter 6, Nuclear Magnetic Resonance, Mass and Fourier Transform Infrared spectroscopies are employed.

3.3.1 Rheology

Rheology measurements were carried out using an Anton Paar stress controlled rheometer (Physica MCR 301) using a double gap geometry and a shear rate of 200 to 700 s^{-1}. This is used to find any differences in viscosity between toluene or C_{60}/toluene as the solvent in DLS measurements, as the calculation for R_h (see Equation 3.1) directly requires the viscosity of the solvent to be known.

3.3.2 UV-Visible Spectroscopy

To correct SLS measurements for the absorption of C_{60}, UV-Visible spectroscopy (Perkin Elmer Lambda 35) was necessary. Solutions of the relevant concentrations were placed in a sealed

quartz cuvette and a toluene cuvette was subtracted as background. The scan range was 300 to 900 nm.

3.3.3 Nuclear Magnetic Resonance

^{13}C Nuclear Magnetic Resonance was carried out on a Bruker AV500. Measurements were carried out at 300 K and 500 MHz.

3.3.4 Mass Spectroscopy

The presence of $C_{60}O_x$ in light induced fullerene clusters (Chapter 6) was determined by mass spectroscopy (MS). A Thermo Scientific LTQ Velos Pro was used. C_{60} was dissolved in toluene (Chromasolv, for HPLC ≥99.9%, Sigma Aldrich), after the relevant processing was carried out, the resulting solution was diluted with IPA (LC-MS grade, 99.90%, Fisher) to give solution:IPA of 4:1 and infused to an ion trap MS in negative ion mode using electrospray ionisation.

3.3.5 Fourier Transform Infrared Spectroscopy

Fourier transform infrared spectroscopy (FTIR) was also used to confirm the presence of $C_{60}O_x$. Pellets were made by adding 1 ml of solution to 250 mg KBr powder and were ground with a mortar and pestle. The solvent was evaporated under vacuum and the resulting solid mixture was ground further. The powder was pressed at 25 °C at 15 T for 40 minutes using an Atlas Manual Hydraulic Press. Spectra were obtained in transmission mode using a Bruker Tensor 27 FT-IR spectrometer equipped with a liquid nitrogen cooled MCT detector. 128 scans were collected with a spectral resolution of 4 cm^{-1} in the 418 to 6977 cm^{-1} range.

4 Conformation and interaction of polystyrene in dilute to semidilute polymer/fullerene solutions

4.1 Introduction

In this chapter the effect of C_{60} on the conformation of PS in a good solvent is evaluated. This is achieved by the use of static light scattering (SLS), dynamic light scattering (DLS) and small angle neutron scattering (SANS) to evaluate and quantify the phase, radius (R_g and R_h) and correlation length (ξ) of PS/C_{60}/toluene mixtures.

Four isopleths in this ternary system are studied, two in a dilute solution regime and two within the semidilute regime, these are summarised in Figure 4.1 and Table 4.1. Six molecular weights (20,000; 65,000; 79,000; 80,000; 100,000; and 1,000,000 $gmol^{-1}$ referred to hereafter as 20k, 65k, 79k, 80k, 100k and 1M) were used. PS concentrations ranged from 0.12 to 9.5wt%, C_{60} concentrations ranged from 0.005 to 0.96 wt%. This goes above and below the stated miscibility limit of C_{60} in toluene ($c_{C_{60}/tol}$) at 0.32 wt% [198]. All concentrations reported are for the whole of the ternary system.

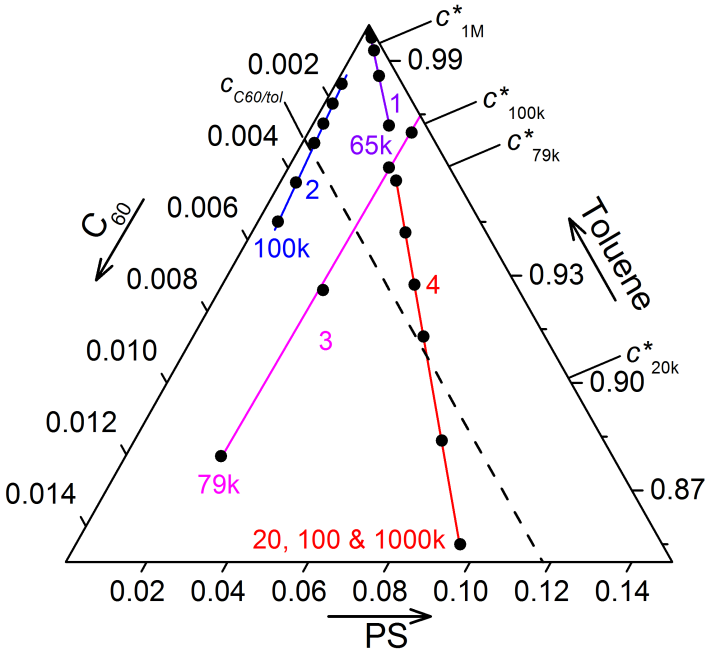


Figure 4.1: Ternary diagram showing the points where this system was studied. For the some of the molecular weights used c^* is given. Note that experiments on 65k were only in the dilute regime thus c^* is not shown. Isopleths 1-4 are marked out for clarity. The black dashed line represents the reported miscibility limit ($c_{C_{60}/tol}$) of C_{60} in toluene (0.32 wt%) [198].

Table 4.1: Summary of isopleths in this chapter, with polystyrene M_w, solution regime, objective of isopleth and technique used. Concentrations of individual samples can be found in Table 4.2.

Isopleth	M_w/kgmol^{-1}	Objective	Technique
1	65	$c < c^*$, C_{60}:PS = 0 & 0.05, $c_{C_{60}} < c_{C_{60}/tol}$	SLS, DLS
2	100 (▪)	$c < c^*$, C_{60}:PS = 0 & 1, $c_{C_{60}} < c_{C_{60}/tol} < c_{C_{60}}$	SANS
3	79 (◂)	$c \approx c^*$, $c_{C_{60}} < c_{C_{60}/tol} < c_{C_{60}}$	SANS
4	20 (▲); 100 (● or ▪); 1000 (◆)	$c \gtrsim c^*$, M_w, C_{60}:PS = 0 & 0.05, $c_{C_{60}} < c_{C_{60}/tol} < c_{C_{60}}$	SANS

4.2 Experimental

4.2.1 Materials

Hydrogenous polystyrene of molecular weights (M_w) 79 and 100 kg/mol with polydispersity indices (PDIs) of 1.05 and 1.06 respectively was obtained from Polymer Source and 65 kg/mol with a PDI of 1.1 from Polymer Laboratories Ltd. Deuterated polystyrene of M_w 20, 80, 100 and 1000 kg/mol with PDIs of 1.06, 1.05, 1.06 and 1.15 respectively were also from Polymer Source. Toluene (99.5%) was purchased from VWR, toluene-d8 used for SANS experiments was obtained from Goss Scientific and C_{60} (99% purity) from Mer Corp.

4.2.2 Sample Preparation

Sample compositions are detailed in Table 4.2. For simplicity, instead of preparing all samples separately, dilution or concentration series were carried out for isopleths 1, 2 and 4. This must be done with great care to avoid inadvertent precipitation of the solutes and prolonged redissolution of fullerene clusters.

Isopleth 1a: PS was dissolved with toluene and stirred overnight (~12 hours), at $3c^*$, this solution was diluted to the desired concentration, measured and subsequently diluted to the next concentration.

Isopleth 1b: As with Isopleth 1a except a solid mixture of PS and C_{60} at a ratio of 0.05 C_{60}:PS. The initial sample was prepared above $c_{C_{60}/tol}$. The presence of precipitated C_{60} is time dependent and very much depends on sample preparation. The dissolution pathway is shown in Figure 4.2. The experiments for Isopleth 1 used the ALV-CGS3/MD-8 system, described in Section 3.1.1.

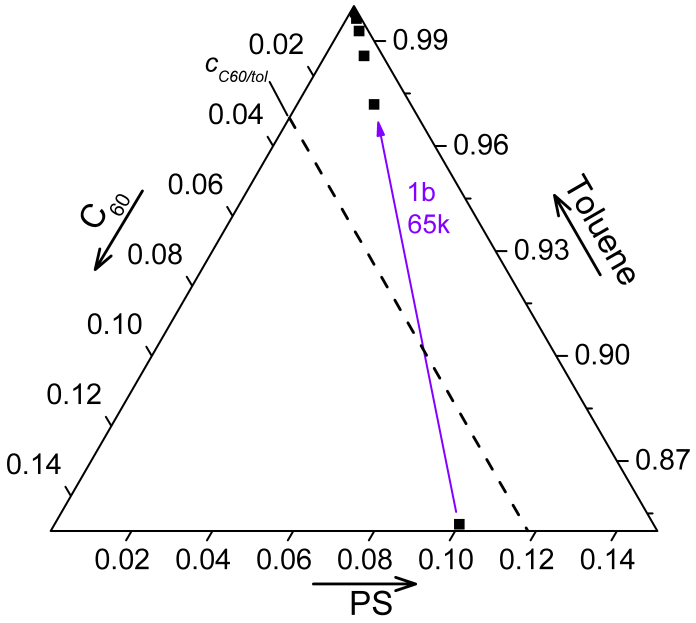


Figure 4.2: Ternary diagram of PS/C_{60}/toluene showing the initial concentrated state of the solution used for isopleth 1b. The black dashed line represents the miscibility limit in toluene (0.32 wt%) [198].

Isopleth 2a: Relevant mass of PS was weighed for each sample and toluene added. Samples were measured ~48 hours after dissolution.

Isopleth 2b: Solid mixture of PS and C_{60} was prepared and toluene added until the the most dilute concentration was reached, the solution was stirred overnight. An aliquot of the stock solution was taken and the solvent evaporated under nitrogen whilst the solution was being stirred. Samples were measured ~48-72 hours after preparation. The banjo cells used for SANS were wrapped in aluminium foil to minimise light exposure whilst in the beamline. (Empty cell used for SANS data reduction was also wrapped in aluminium foil).

Isopleth 3: Separate solutions of PS/toluene and C_{60}/toluene were prepared and stirred for an hour. The PS/toluene solution was then added to the C_{60}/toluene solution and stirred for another hour. The samples were measured ~5-10 hours after preparation.

Isopleth 4: Same as isopleth 2b.

All solutions were kept in the dark to avoid light exposure prior to measurement [152]. For consistency and future work the desired concentration is made directly as this minimises the time requried for solution preparation (e.g. via dilution or concentration series). Solutions for isopleth 1 were filtered with a 1.2 μm PTFE filter, all other solutions were unfiltered.

Isopleth	wt% C_{60}	wt% PS	C_{60}/PS	M_w/kgmol^{-1}
1a		0.12		
		0.25		
	0	0.49	0	
		0.97		
		1.93		65
1b	0.005	0.12		
	0.01	0.25		
	0.02	0.49	0.05	
	0.4	0.97		
	0.09	1.93		
2a		0.15		
		0.20		
	0	0.25	0	
		0.29		
		0.39		
		0.52		100
2b	0.15	0.15		
	0.20	0.20		
	0.25	0.25	1	
	0.30	0.30		
	0.40	0.39		
	0.50	0.49		
3	0	2.07	0	
	0.04	2.56	0.02	
	0.15	2.49	0.06	79
	0.48	2.56	0.19	
	0.97	2.37	0.41	
4/20k-d	0.15	2.82		
	0.20	3.76		
	0.25	4.71	0.05	20
	0.30	5.65		
	0.40	7.55		
	0.50	9.43		
4/100k-d	0.15	2.86		
	0.20	3.80		
	0.25	4.75	0.05	100
	0.30	5.73		
	0.40	7.62		
	0.50	9.53		

4/100-h	0.15	2.86	0.05	100
	0.20	3.83		
	0.25	4.78		
	0.30	5.71		
	0.40	7.62		
	0.50	9.55		
4/1M-d	0.15	2.86	0.05	1000
	0.20	3.80		
	0.25	4.77		
	0.30	5.73		
	0.40	7.63		
	0.50	9.51		

Table 4.2: Summary of isopleths investigated, all concentrations (c_i) in the system are reported by the ratio of the mass of component i to the total mass of the solution (mass fraction of total ternary mass), ratio C_{60}:PS and polystyrene molecular weight.

4.2.3 Data Analysis

For clarity, the equations introduced in Section 3, which are necessary in the analysis of the data presented, are reproduced here. Equation 3.4[i] was used for dynamic light scattering, Equations 3.6, 3.7, 3.8 and 3.9 for static light scattering and Equation 3.16 for small angle neutron scattering, alongside the polymer excluded volume model [195].

$$g^{(1)}(q,t) = \sum_{i=1}^{N} a_i(q) \exp(-\Gamma_i(q)t) \tag{3.4}$$

$$\frac{1}{R(q)} = \frac{1}{R_{q=0}}\left(1 + \frac{q^2 R_g^2}{3}\right) \tag{3.6}$$

$$\frac{Kc}{R(q)} = \frac{1}{M_w} + \frac{R_g^2 q^2}{3M_w} + 2A_2 c \tag{3.7}$$

$$K = \frac{4\pi^2 n^2}{N_A \lambda^4}\left(\frac{dn}{dc}\right)^2 \tag{3.8}$$

$$\ln R(q) = \ln R_{q=0} - \frac{q^2 R_g^2}{3} \tag{3.9}$$

$$P(q) = Aq^{-4} + \frac{B}{1 + (q\xi)^2} \tag{3.16}$$

[i] $\Gamma(q,c)$ is the mean inverse relaxation time of diffusive modes with the z-averaged translational diffusion coefficient $D(q)$=$\Gamma(q,c)/q^2$. Where, $D = \frac{k_B T}{6\pi\eta R_h}$.

Table 4.3: Summary of constants used in Equations 3.4 to 3.8

Symbol	Value	Unit
n	1.496	-
N_A	6.02×10^{23}	mol^{-1}
$\frac{dn}{dc}$	0.000105	mLmg^{-1}
k_B	1.38×10^{-23}	$\text{m}^2\text{kgs}^{-2}\text{K}^{-1}$
η	0.56	mPa.s
T	298	K
K	1.1×10^{-5}	$\frac{\text{mL.mol}}{\text{m}^4\text{mg}}$

4.3 Preliminary Control Experiments

Prior to carrying out the main body of the work presented in this chapter, a number of preliminary and control experiments were carried out. This involved UV-Vis Spectroscopy, necessary to correct SLS data due to C_{60} light absorption, rheology for DLS, alongside initial SANS and DLS control studies.

4.3.1 UV-Visible Spectroscopy

To correct for C_{60} absorbance in SLS experiments, UV-Vis spectroscopy was necessary so that a transmission correction could be made. Using $1 - I_{Abs} = I_{Trans}$, the transmission was calculated which was scaled with the transmission of toluene (0.97), via $\frac{T_{solvent}}{T_{sample}}$. The measured $S_{sample}(q)$ was then multiplied with the transmission correction. A concentration series of C_{60}/toluene via UV-vis is shown in Figure 4.3.

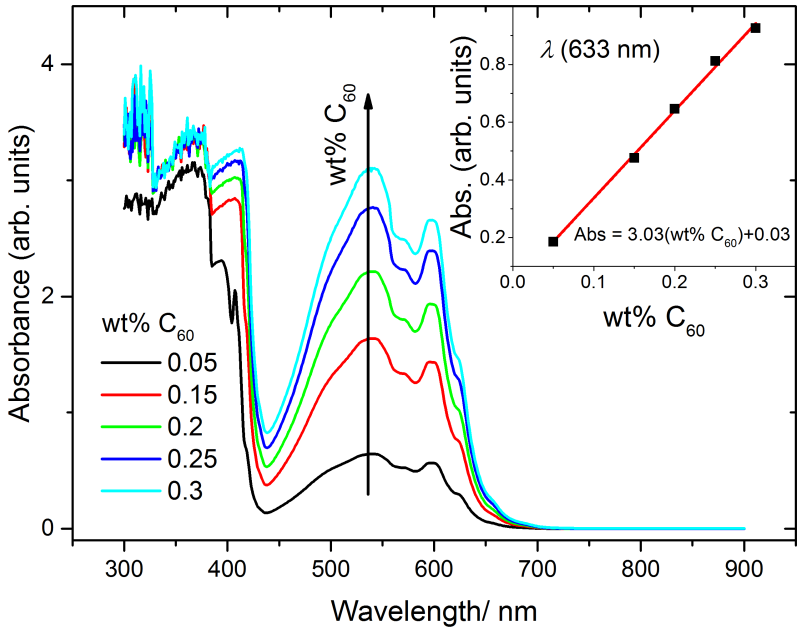


Figure 4.3: UV-Vis spectra as a function of C_{60} loading. Inset shows increasing absorbance at $\lambda = 633$ nm as a function of C_{60} loading.

4.3.2 Static Light Scattering

A typical C_{60}/toluene solution was scattered from to ensure that no structural features are present and a dispersed solution is achieved. The variation observed in scattering intensity is due to the individual detector sensitivities rather than any possible structural features in the sample. This effect becomes magnified in low scattering samples, as opposed to PS/toluene solutions.

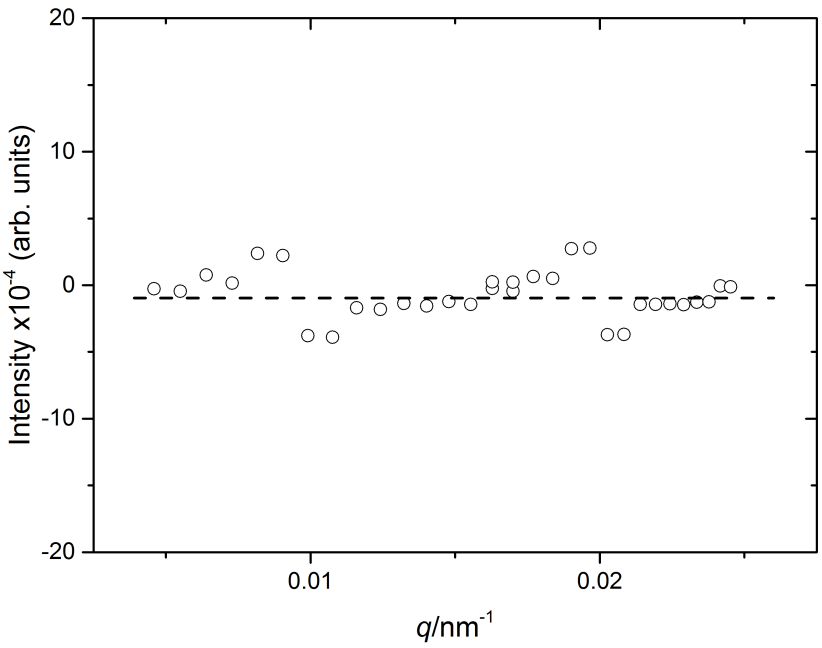


Figure 4.4: Static Light scattering results from a 0.2 wt% C_{60}/toluene solution. Dashed line is drawn as a guide to the eye.

4.3.3 Rheology

To calculate R_h, via Equation 3.1, it is necessary to know the viscosity (η). Therefore it is necessary to know the viscosity of C_{60}/toluene solutions as the addition of C_{60} could have an impact on viscosity and thus a resulting effect on R_h. As can be seen in Figure 4.5 there is no observed change in C_{60} viscosity within error with C_{60} concentration. Thus, for calculating R_h or D, the viscosity of toluene was used.

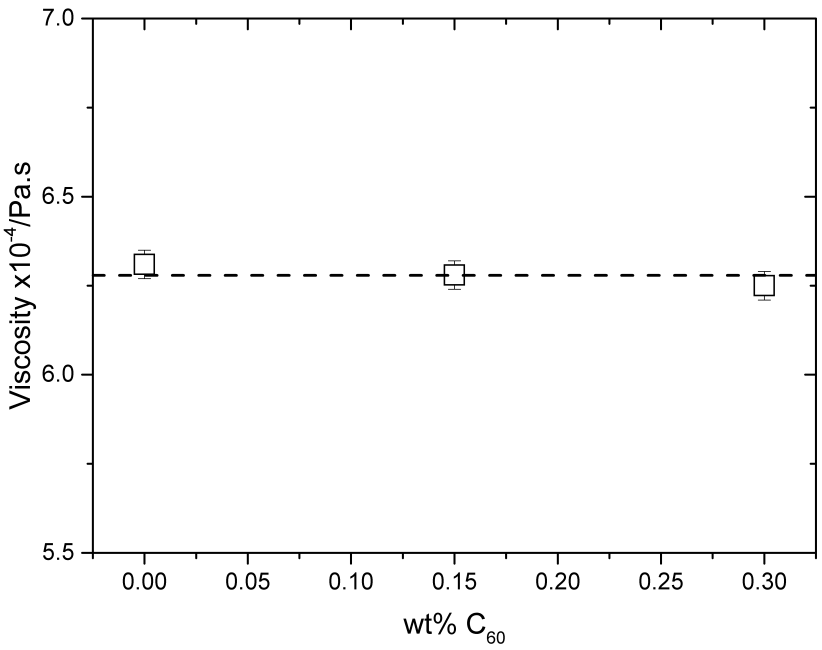


Figure 4.5: Viscosity of C_{60}/toluene solutions as a function of fullerene concentration. There is no change in viscosity with fullerene addition within measurement error.

4.3.4 Dynamic Light Scattering

Dynamic light scattering was carried out, as seen in Figure 4.6 on C_{60}/toluene solutions in order to assess whether a contribution from fullerenes or the solvent, toluene, could be observed. There is a very weak correlation signal which does not appear to be a clear correlation decay corresponding to individual fullerenes.

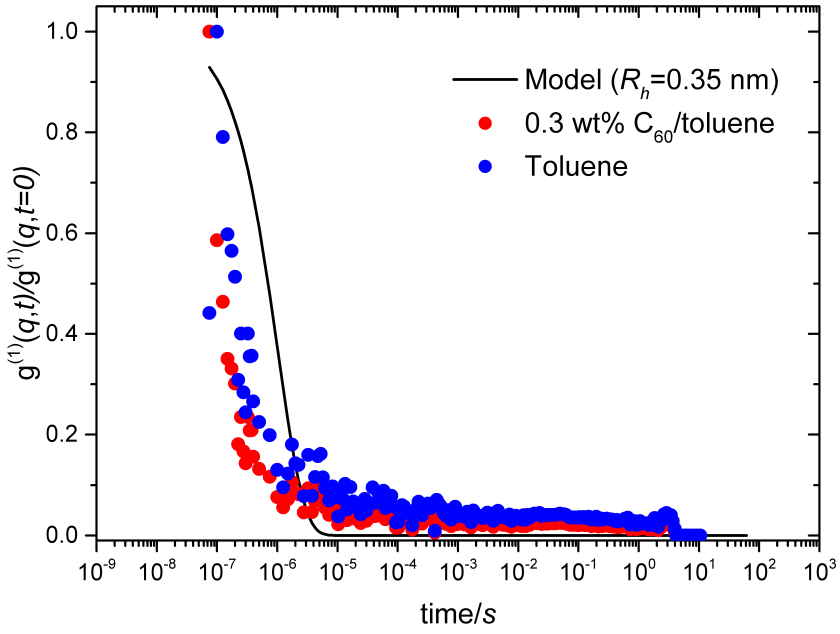


Figure 4.6: Correlation function for 0.3 wt% C_{60} in toluene (•) and neat toluene (•) with a model for a particle with R_h of 0.35 nm measured at 173° corresponding to q=2.96×10^{-2} nm^{-1}. There is no clear decay occurring for this size regime and given the similarity between the C_{60}/toluene solution and toluene and it is not possible to observe individual fullerene molecules on the Malvern Nano-S DLS system.

4.3.5 Small Angle Neutron Scattering

Prior to PS/C_{60}/toluene mixtures, SANS was carried out on C_{60}/tol-h solutions. As can be seen in Figure 4.7 there is no angular dependent scattering originating from C_{60} in toluene, from 0.1 to 2 wt% in solution, in the SANS q range used. Alongside the DLS and SLS experiments on C_{60}/toluene solutions, it can be confirmed that there are no C_{60} aggregates within a freshly prepared C_{60}/toluene solution.

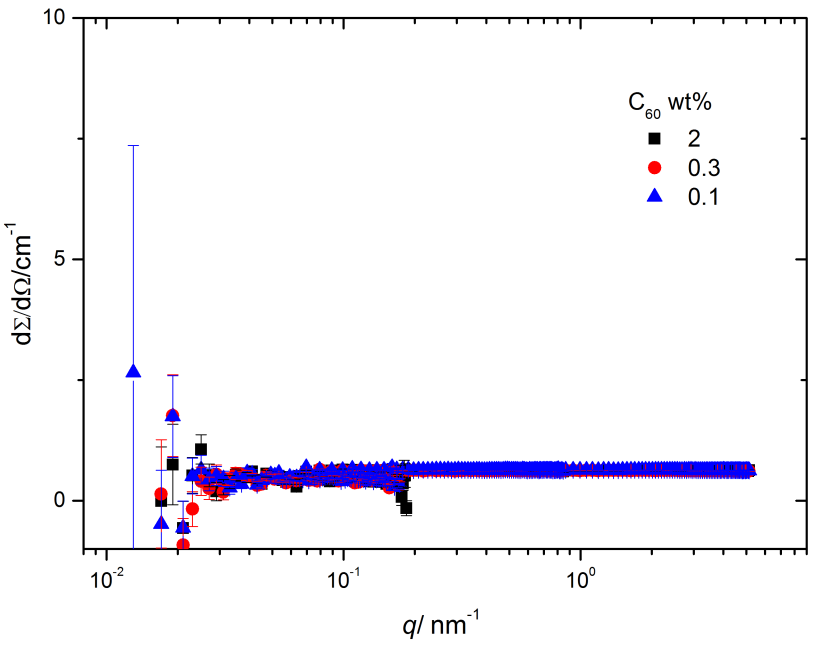


Figure 4.7: Total Scattering Intensity from SANS for C_{60}/toluene solutions as a function of C_{60} concentration ranging from 0.1 to 2 wt%.

A contrast variation experiment was also carried out, using 2.5 wt% 79k PS-h or 80k PS-d (as necessary) with 0.14 wt% C_{60}. This allowed determination of the optimum system with which to observe either C_{60} aggregates or polymer conformation. C_{60} has a similar SLD to deuterated toluene and so in a blend with PS-h, the C_{60} would appear 'invisible' and only the scattering from the PS chains would be observed. Using this rationale, four contrasts were tested: (A) PS-d/C_{60}/tol-h, (B) PS-h/C_{60}/tol-d, (D) PS-h/C_{60}/tol-h and (E) PS-h/C_{60}/tol-d/tol-h (Contrast C will be introduced later). Contrast A allowed the observation of both the polymer and C_{60} at the expense of a high incoherent background and in Contrast B only the scattering from PS-h in a blend with C_{60} and tol-d is observed. In Contrast D only scattering contributions from C_{60} in a PS/toluene mixture would be seen and the other, Contrast E allowed the observation of PS chains and C_{60} in a background of tol-d and tol-h so that scattering contributions would arise from both solutes. As can be clearly seen from Figure 4.8 there is no C_{60} scattering from Contrast D and there is only a slight contribution from the polymer chain in Contrast E. Contrast E also has the added difficulty of accurately controlling the background contribution from a hydrogenous/deuterated solvent mixture. Thus Contrasts A and B were selected for future experiments.

Component	SLD ($\times 10^{-4}$ nm^{-2})
C_{60}	5.74
PS-h	1.41
PS-d	6.47
Tol-h	0.94
Tol-d	5.66

Reproduced Table 3.2: Summary of SLD's of components used in this investigation

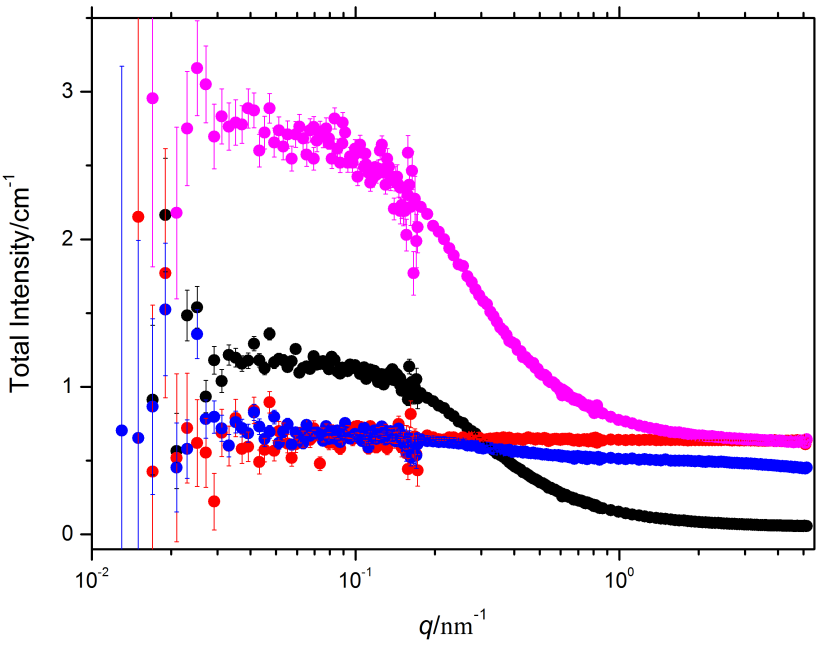


Figure 4.8: Total Scattering Intensity from SANS for various PS/C_{60}/toluene solutions with a concentration of 2.5 wt% 79k PS-h or 80k PS-d (as necessary) with 0.14 wt% C_{60}, using different SLD contrasts. (A) PS-d/C_{60}/tol-h (•), (B) PS-h/C_{60}/tol-d (•), (D) PS-h/C_{60}/tol-h (•) and (E) PS-h/C_{60}/tol-d/tol-h (•).

Following these preliminary SANS experiments, three SLD contrasts were employed to ascertain the effect of C_{60} scattering in the data obtained, these are summarised in Figure 4.9. Contrast A and B, and Contrast C in which the R_g of only the PS-h in a matrix of PS-d, Tol-d and C_{60} will scatter, enabling the effect of C_{60} addition on R_g in the semidilute regime to be ascertained.

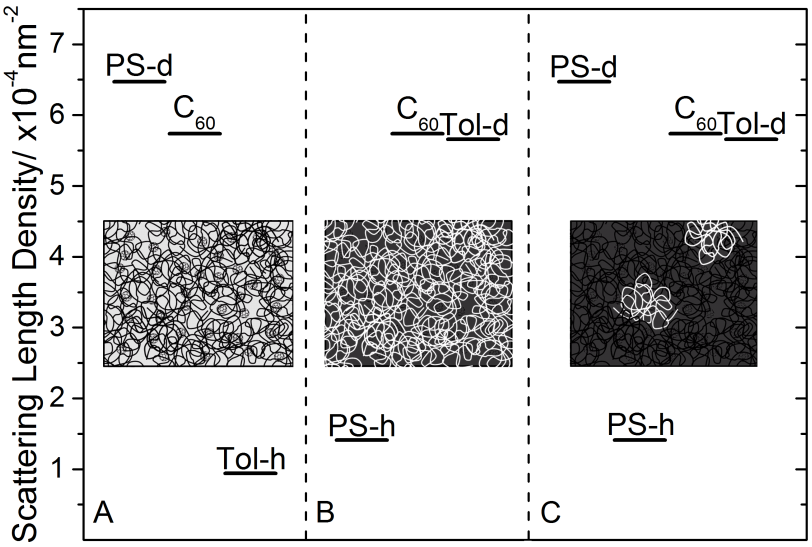


Figure 4.9: Graphic of the three SLD contrasts used. Contrast A uses deuterated PS (PS-d) and C_{60} with hydrogenous toluene (tol-h) (20k, 100k & 1M PS), so that the fullerene and polymer contributions can be observed. Contrast B uses hydrogenous PS (PS-h) and C_{60} in deuterated toluene (tol-d) (79k & 100k), here only the polymer contribution to the scattering is observed. Contrast C uses a mixture of PS-h and PS-d (100k) , thus the R_g of single chain PS in a semidilute regime can be found.

4.4 Results and Discussion

Initially, the PS conformation in the dilute solution regime, where $c << c^*$, corresponding to isopleths 1 and 2 is discussed. Isopleth 1 traverses varying toluene concentrations at a constant ratio of C_{60}:PS of 0.05. Zimm analysis of the SLS data was carried out for the PS/toluene, shown in Figure 4.10a. A q range of (5.1 to 27)$\times 10^{-3}$ nm^{-1} was used to linearly extrapolate to q = 0, yielding a c = 0 intercept of 0.0163±0.003, and therefore a M_w of 61.3±1.2 kg/mol, which is close to the expected 65 kg/mol, (Figure 4.10b, •). This M_w was chosen as there is no angular dependence from the PS in this q range. For isopleth 1, there was a clear increase in scattering intensity for solutions containing higher loadings of C_{60} (0.04 and 0.09 wt%). Guinier analysis, shown in Figure 4.10d, indicates scattering from a component with R_C in the region of 100-200 nm after 12 hours of solution preparation. C_{60} aggregation below $c_{C_{60}/tol}$ is examined in more detail in Chapter 5. Extrapolation of the data shown in Figure 4.10c to c = 0 is also shown in Figure 4.10b. This results in the same value at the intercept and therefore same M_w. However the gradient of the slope is clearly different. The A_2 calculated for PS/toluene is 0.008

cm^3molg^{-2}, in good agreement with the literature [5]. The change in gradient upon C_{60} addition, shown in Figure 4.10b, can be due to two factors: changes in A_2 and $\frac{dn}{dc}$ of C_{60}/toluene. Since A_2 is a binary interaction parameter relating to the interaction of PS and toluene, and polymer dimensions remain unchanged with C_{60} addition (see isopleths 2-4), it could be expected that the observed change in slope is due to changes in $\frac{dn}{dc}$ of C_{60}/toluene. Measurements of $\frac{dn}{dc}$ with C_{60} are, however, complex. For the experiments presented here, in order to measure $\frac{dn}{dc}$ accurately, it is not a simple case of adding C_{60} to toluene or even a PS/toluene solution, as the concentration of PS in the solution surrounding the C_{60} molecules is increasing, this could be due to volume exclusion and other possible reasons. C_{60} at a constant chemical potential of PS in toluene is necessary. This is difficult to achieve as dialysis of a C_{60}/PS/toluene solution against PS/toluene would be necessary with identical PS concentrations on both sides of the membrane at the end of the dialysis. This would require a dialysing wall permeable to the polymer but impermeable to C_{60}. These measurements were outside the scope of this work and therefore not considered. A third factor considered was the light absorption of C_{60}, however transmission measurements were carried out and this was corrected for.

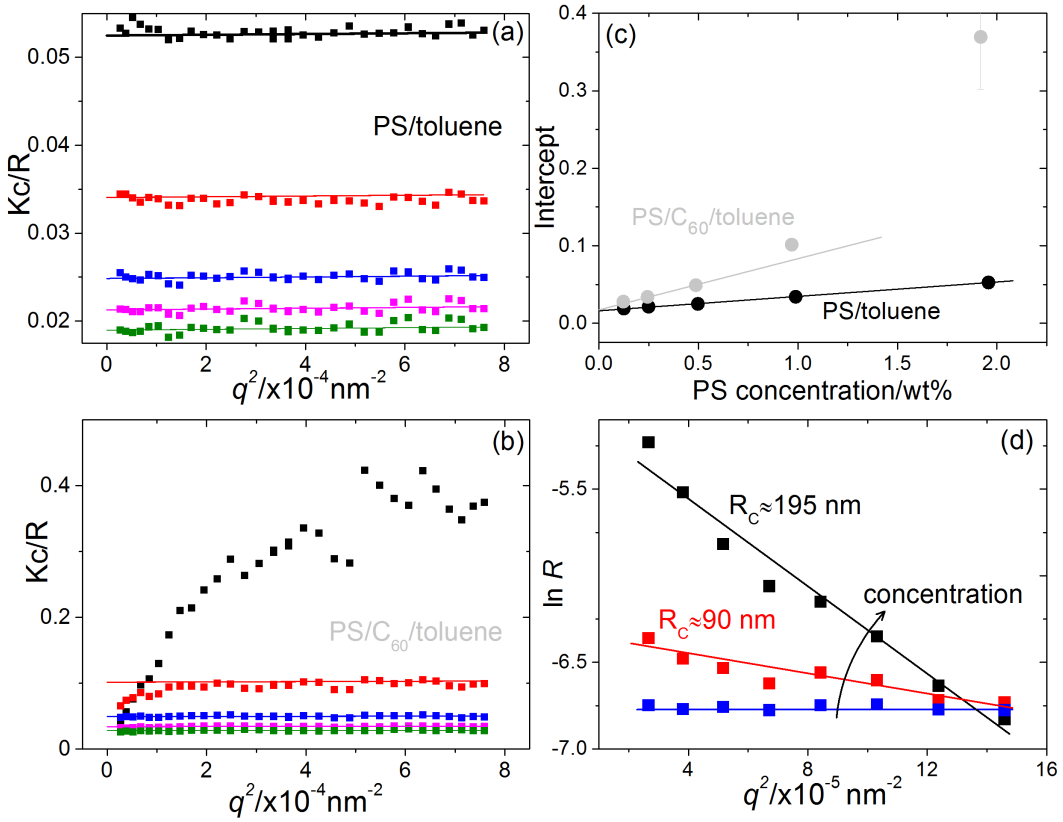


Figure 4.10: Zimm analysis of Static Light Scattering from isopleth 1 of (a) 65k PS/toluene and (c) PS/C_{60}/toluene with C_{60}:PS of 0.05. PS concentrations = 1.93 (■), 0.97 (●), 0.49 (▲), 0.25 (▼) and 0.12 wt% (◆). (b) shows the extrapolation of the intercepts from (a) and (c) for PS/C_{60}/toluene (■) PS/toluene (●) to zero concentration. For the higher concentrations of C_{60} only the high q portion of the data was extrapolated to zero. The intercept at zero concentration gives $1/M_w$, which for PS with and without C_{60} is 61.3 kgmol^{-1}. This is close to the expected 65 kgmol^{-1}. (d) Guinier plot of low q scattering. R_C of 195±25 nm and 90±10 nm could be fitted for PS concentrations of 1.93 and 0.97 wt% respectively. This is likely to arise from C_{60} aggregation taking place below $c_{C_{60}/tol}$ of 0.32 wt%.

Selected DLS data for the same q range is shown in Figure 4.11 for PS/C_{60}/toluene with fitted correlation functions from Equation 3.4 where i was varied from 1 to 3 depending on the number of decays observed. A component corresponding to individual C_{60} molecules cannot be reliably extracted. The correlation function for the ternary blend with the highest PS concentration (1.9 wt% PS and 0.09 wt% C_{60}) shows a clear second decay corresponding to a peak at 200 nm via CONTIN analysis. This signal is associated with the same aggregates observed using SLS. The $R_h^{C_{60}}$ is in good agreement with the R_C estimate from the Guinier plots (Figure 4.10d). There appears to be a decrease in C_{60} miscibility in toluene upon the addition of PS. This

phenomenon is studied further in Chapter 5. Extrapolation to zero q and zero concentration for the diffusion coefficient are shown for PS/toluene and PS/C_{60}/toluene in Figure 4.12c. For both sets of data the same diffusion coefficient is found, at 6.08×10^{-7} cm^2s^{-1}, which is close to the value found using the relationship given by Huber et al. [4] Using the fitted value of D_0, R_h^{PS} can be calculated to be 6.45 nm using Equation 3.1. It should be noted here that the viscosity (seen in Figure 4.5) for solutions containing 0 to 0.3 wt% C_{60} in toluene and was constant within experimental uncertainty. Thus, there is no change in D_0 and therefore R_h^{PS} upon the addition of C_{60}.

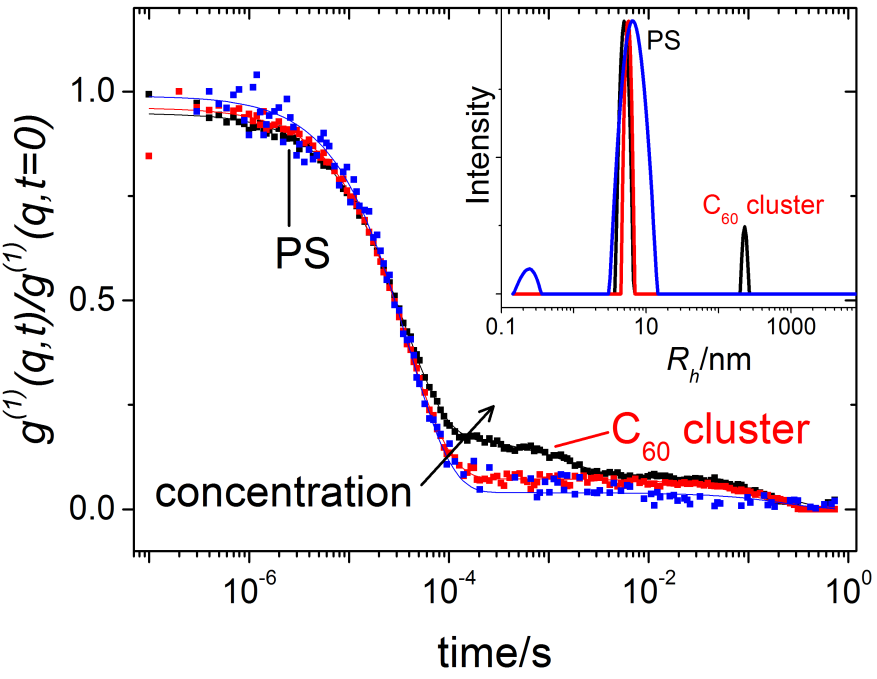


Figure 4.11: Dynamic Light Scattering of PS/C_{60}/toluene (C_{60}:PS of 0.05) from isopleth 1, $\theta = 80°$ ($q = 0.019$ nm^{-1}), at three concentrations, 1.9 (■), 0.49 (■) and 0.12 wt% PS (■). Solid lines are fits to the data using Eq 3.4. Inset shows the result of a CONTIN analysis for the three concentrations. A second decay emerges for 1.9wt% PS, with an $R_h^{Cluster}$ in the region of 200 nm, following 12 hours of sample preparation.

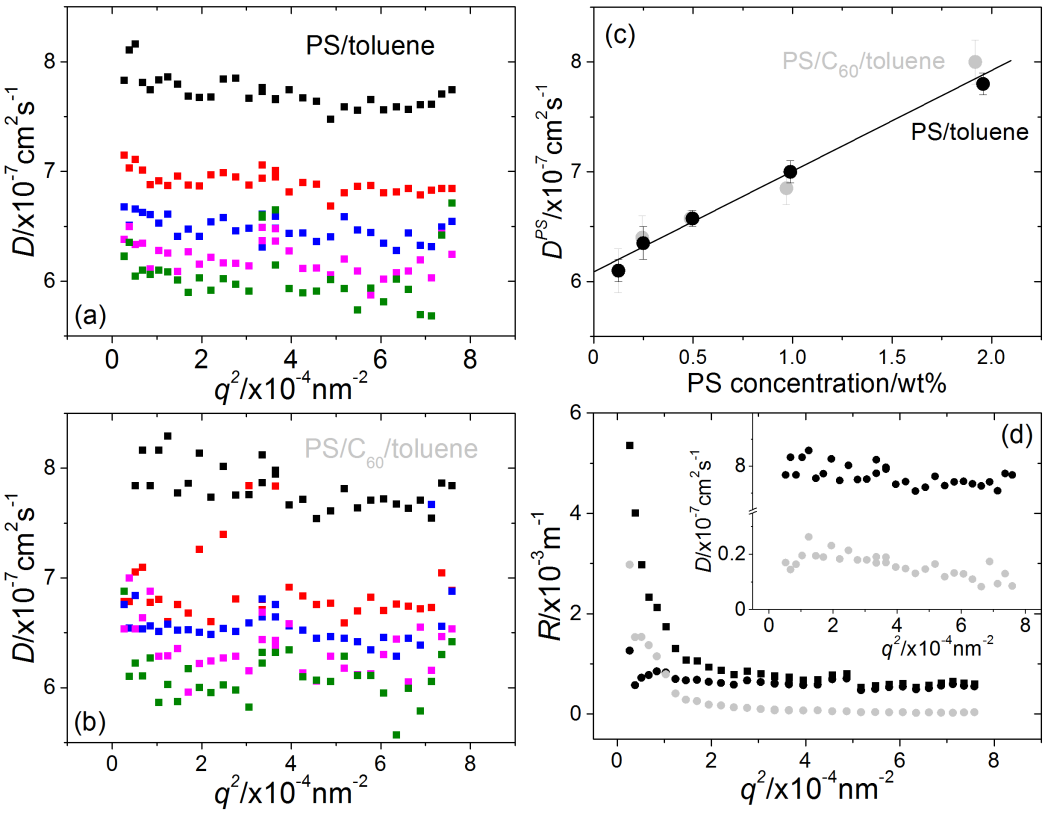


Figure 4.12: (a) and (b) show fitted diffusion coefficient of the fast mode of the multiexponential fit (Equation 3.4) from DLS across the accessible q range for (a) PS/toluene and (b) PS/C_{60}/toluene (b); PS = 1.93 (▪), 0.97 (●), 0.49 (▲), 0.25 (▼) and 0.12 wt% (◆). (c) shows the extrapolation to zero concentration for isopleth 1 showing PS/toluene (▪) and PS/C_{60}/toluene with C_{60}:PS of 0.05 (●). As shown by the black line, there is no difference in the diffusion coefficient either with or without C_{60}. This corresponds to an R_h of 6.45 nm. (d) demonstrates the procedure described by Kanai and Muthukumar [193] where the values fitted for a_i in Equation 3.4 can inform the origin of the intensity of scattering in SLS. Here, this is shown for 1.93 wt% PS and 0.09 wt% C_{60}. Total intensity (▪) was split into single PS chains (●) and C_{60} aggregates (●). The diffusion coefficient via DLS is shown in the inset, demonstrating the bimodal distribution and hence the scattering intensity arising from two contributions. This confirms that the increase in scattering intensity at low q is from C_{60} aggregates.

Following a procedure detailed in Ref. 193, the values of a_1 and a_2 fit using Equation 3.4 can be used to deconvolute the SLS intensity contribution from the two species in solution, in this case PS and C_{60} and was described with Equation 3.10. This can be see in Figure 4.12d where a q independent signal is found for the single PS chains and a strong q dependance is present for

the signal arising from C_{60} clusters. Thus it is possible to conclude that C_{60} aggregates of 100-200 nm are present in PS/C_{60}/toluene blends of relatively high PS concentrations indicate that such systems comprise of aggregated C_{60}, individual fullerene molecules, individual PS chains and toluene. Prior to the addition of PS, the C_{60}/toluene solutions are below $c_{C_{60}/tol}$ and so aggregates should not be expected and are indeed not observed experimentally by either SLS or DLS, as shown in Figures 4.4 and 4.6. Two of the expected outcomes from a system in the PL are a decrease in R_g^{PS} and R_h^{PS} and C_{60} aggregation, only the latter is observed. Experimentally, it is often necessary for higher colloidal particle loadings to be present in the solution for a decrease in polymer chain dimensions to be observed [36], therefore higher concentrations of C_{60} are needed. Due to experimental limitations higher concentrations of C_{60} cannot be reliably measured via light scattering techniques, thus there is no light scattering data presented for C_{60} above $c_{C_{60}/tol}$. Due to the inability to measure above $c_{C_{60}/tol}$ and to extract a reliable A_2, SANS was employed as the technique to study PS/C_{60}/toluene mixtures above $c_{C_{60}/tol}$.

SANS data from isopleth 2 (C_{60}:PS=1) is shown in Figure 4.13. Contrast A (PS-d, C_{60} and Tol-h) was chosen, such that scattering is dominated by contributions from PS and C_{60} at the expense of a larger incoherent background from tol-h. Along this isopleth, there is a clear increase in scattering intensity at low values of q from 0.03 to 0.1 nm^{-1}, as the concentration of solids increases. Based on the results from the contrast variation experiment discussed later, the low q upturn at 0.3-0.5 wt% PS can be attributed to C_{60}. As mentioned previously, the PolymerExclVol model in SasView [195] was used to fit the polymer coherent scattering contribution, with an additional Porod term (Aq^{-4}). The high q scaling exponent is expected to be 5/3 for the conformation of a polymer in a good solvent, as is seen in Figure 4.13b for PS/toluene, and 2 for a Gaussian coil. Here, the exponent ranges from 1.66 to 1.85 for the PS/C_{60}/toluene samples investigated and is rather sensitive to the background subtraction (which uses an ideal mixing assumption). This is in agreement with the expanded coil conformation expected for PS in a good solvent. Additionally there is no change in R_g for the samples investigated within error when compared 100k PS/toluene (hollow symbols in the inset of Figure 4.13a). The Flory-Huggins interaction parameter, χ, was also found for the solutions in isopleth 2, 0.44 to 0.48, these values are within those previously found in literature for PS/toluene. [ii] [199] Thus, it has been clearly demonstrated with the use of SLS, DLS and SANS, that there is no change in PS R_h, R_g and χ upon the addition of up to 0.4 wt% C_{60} in the dilute regime in toluene when compared to PS/toluene.

[ii] χ was found using the RPA [14], the form factor for a solvent in this instance, was set to unity as is commonly done so in literature [197]

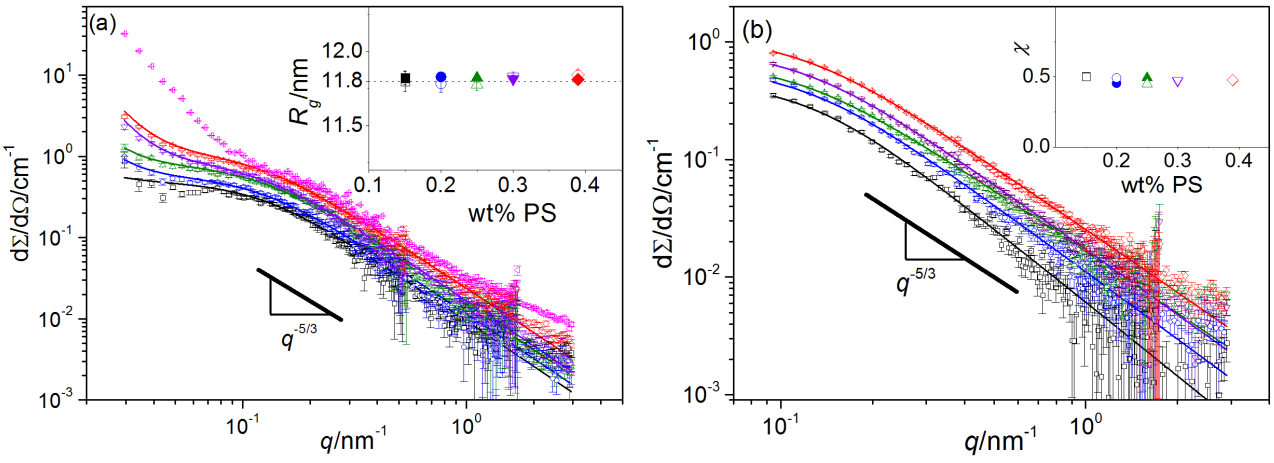


Figure 4.13: Coherent scattering intensity from small angle neutron scattering for (a) 100k PS/C_{60}/toluene, where C_{60}:PS=1 and (b) 100k PS/toluene. PS = 0.15 (■), 0.2 (●), 0.25 (▲), 0.3 (▼), 0.4 (◆) and 0.5 wt% (◀) . The inset in (a) shows fitted R_g and in (b) χ for C_{60}/PS/toluene (filled symbols) and PS/toluene (hollow symbols), the dashed line in (a) is a guide to the eye and is calculated using R_g=0.0125$M_w^{0.595}$ [4].

Next, the semidilute regime is studied, this is where the concentration of polymer is close to c^*. Along isopleth 3 (constant concentration PS = 2.40±0.15 wt% and C_{60} from 0 to 0.96 wt%), the concentration of C_{60} eventually exceeds $c_{C_{60}/tol}$ and fullerenes visibly precipitate. It has been previously found that high colloidal loadings can result in changes to polymer chain dimensions in solution [36]. Contrast B was used in this case (PS-h, C_{60}, tol-d) so that potentially small changes in PS conformation could be investigated. A result of Contrast B is that the low q scattering, previously observed in Figure 4.13 is not observed due to C_{60} and tol-d contrast matching, corroborating the assignment to C_{60} clusters. The data was analysed using the Ornstein-Zernicke scattering function given in Equation 3.16. Figure 4.14 clearly shows that all data superposes at loadings of C_{60} both above and below $c_{C_{60}/tol}$ (0.32 wt%). Indeed, the correlation length ξ fitted for all the solutions in isopleth 3 ranged from 3.44 to 3.54 nm, and therefore remains constant within measurement uncertainty.

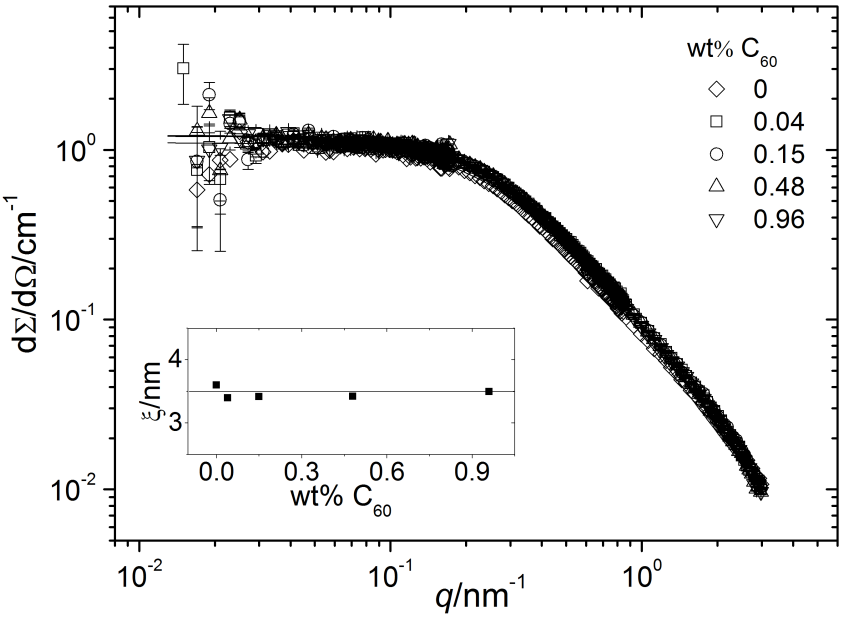


Figure 4.14: Coherent scattering intensity from small angle neutron scattering for 79k PS on isopleth 3 (constant concentration of 2.40±0.15 wt% PS with C_{60} loadings from 0 to 0.96 wt%) using contrast B. No contribution from the C_{60} is observed due to contrast matching and was in order to parse out small differences in ξ, however the data clearly shows there is no change in correlation length, ξ, from PS/toluene to PS/C_{60}/toluene at 0.96 wt% C_{60}. ξ ranges from 3.44 to 3.54 nm in the fits (solid lines) shown.

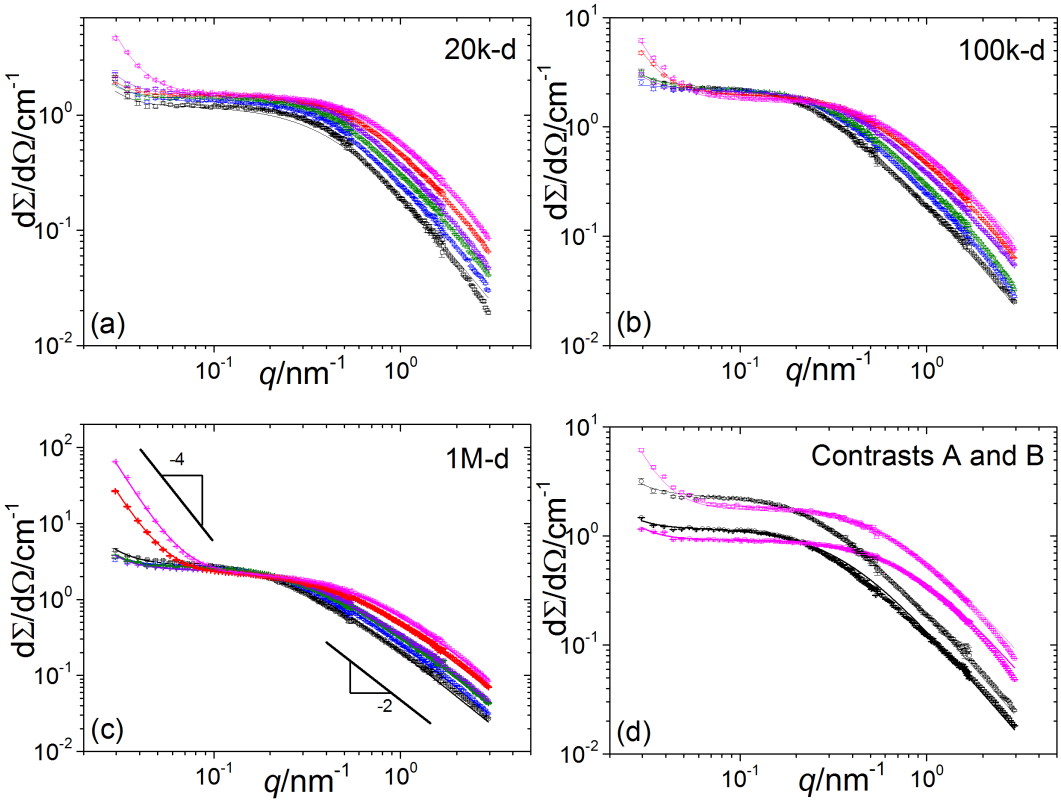


Figure 4.15: Coherent scattering intensity from small angle neutron scattering for isopleth 4 (C_{60}:PS = 0.05). (a-c) Use contrast A (PS-d, C_{60} and tol-h); C_{60} = 0.15 (■), 0.2 (●), 0.25 (▲), 0.3 (▼), 0.4 (◆) and 0.5 wt% (◀). (d) Is a comparison for contrast A (Circles) and B (Squares) (PS-h, C_{60} and Tol-d) to demonstrate the low q upturn was due to scattering contributions from C_{60}.

Isopleth 4 exceeds $c_{C_{60}/tol}$ and, in order to elucidate the C_{60} scattering contribution, contrast A was used. This enables any aggregation, seen previously with SLS and DLS in dilute systems, to be observed in the semidilute regime. Previous literature has suggested that up to 1 [6] or 3 wt% [7] C_{60} is miscible in PS melts and 1 wt% in thin PS/C_{60} films [9]. In solution, depending on the relative component miscibility it could be expected that either (i) PS suppresses C_{60} aggregation due to improved solvent quality or (ii) unfavourable interactions result in polymer:fullerene phase separation in solution. Figure 4.15a-c shows the background subtracted and fitted data for the three molecular weights (20k, 100k and 1M). There is a clear M_w dependence in the low q scattering intensity, increasing from 20k to 1M. Figure 4.15d compares the coherent scattering signal from contrast A and B at fixed M_w (100k). Using contrast B, only a small upturn can be seen, which gave a clear indication that the upturn seen with contrast A, was indeed from the C_{60}. The SANS data was fit using Equation 3.16 where the magnitude of weighting factor

A was unambiguously attributed to C_{60} and is used a qualitative indicator of the magnitude of fullerene aggregation. A scaling of -4 indicates sharp interfaces. The extent of forward scattering is related to the miscibility of C_{60}. Figure 4.16a plots weighting factor, A, as a function of wt% C_{60}. There is a clear M_w dependence, highlighted in Figure 4.16b, and isopleth 4/1M PS exhibits the greatest A at constant mass fraction. A for the dilute 100k PS from isopleth 2 is also included in Figure 4.16a, and takes similar values for 100k PS regardless of whether in the dilute (▪) or semidilute (●) regime. Using $A = 2\pi\Delta\rho^2 S_V$, the surface to volume ratio S_V of the C_{60} clusters can be calculated. Figure 4.16c plots S_V data as a function of C_{60} wt%. The value for $\Delta\rho^2$ used for contrast A was calculated from $(\rho_{C_{60}} - \rho_{Tol-h})^2$ and for contrast B from $(\rho_{C_{60}} - \rho_{PS-h})^2$.

C_{60} cluster dimensions, shape or number cannot be extracted from the SANS data in this q range. However, SLS and DLS data on the addition of PS in the dilute regime induced C_{60} aggregation of 100-200 nm. It is thus likely that these solutions comprise dispersed fullerenes, as well as clusters which would be classed as being in the CL however, the system is not actually in the CL as there would be significantly more dispersed C_{60} molecules than in aggregates. According to the Asakura-Oosawa model [28, 29], the depletion layer around colloidal particles is governed by the polymer R_g. Thus as R_g increases from 4.5 to 46 nm, corresponding to M_w from 20k to 1M, the depletion layer around the C_{60} aggregates should increase accordingly. It is noted that the Asakura-Oosawa model is only valid within the dilute solution regime, but serves as a useful guide to the data presented here. Thus with a higher M_w, one can expect that the C_{60} aggregates will experience a greater anisotropic osmotic pressure gradient, resulting in an increase in the number of aggregates formed. Fullerene aggregation, as measured by the forward scattering intensity, thus appears to increase with increasing polymer M_w, in the semidilute regime. This result is surprising, as above c^* a M_w effect on solution conformation is not expected. This could however be related to the very broad crossover between dilute and semidilute regimes, which in turn may impact the degree of solution homogeneity for the various polymer M_w. Evidently, the larger the M_w at constant mass fraction, the further away the solution is from the crossover definition.

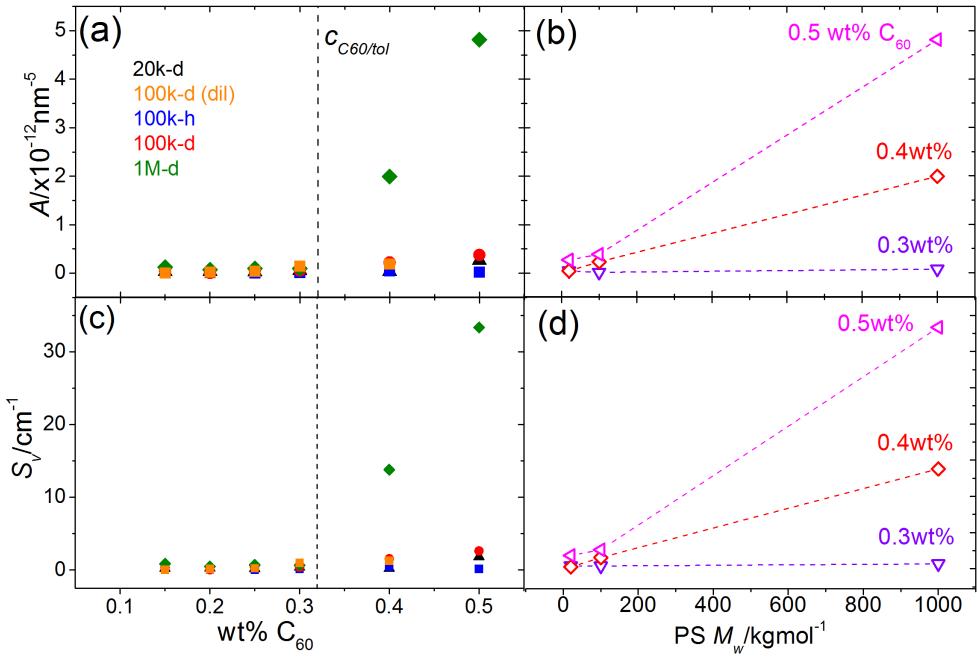


Figure 4.16: (a-b) Weighting factor, A, and (c-d) S_V for the three molecular weights (20k, 100k and 1M) studied on isopleth 1 and 5. For (a) and (c) the dashed black line indicates $c_{C_{60}/tol}$ (0.32 wt%) as determined by Ruoff et al. [198]. The values for A from the dilute 100k-d PS (100k-d dil) seen in isopleth 1 is also included. The data for 100k-h is included as a baseline for which the C_{60} aggregation is not observed due to contrast matching. (b) and (d) A and S_V as function of M_w for isopleth 4, at C_{60} = 0.3 ($\triangledown$), 0.4 ($\diamond$) and 0.5 ($\triangleleft$) wt%.

The fitted ξ, shown in Figure 4.17a, agree almost perfectly, with values obtained in the literature by King et al. [20] and Hamada et al. [21] for PS/toluene solutions. The lower M_w 20k PS deviates from the scaling law of -0.77 unlike 100k and 1M; this is expected since the concentrations studied are lower than c^* for this M_w. Similarly to the dilute regime, there is no effect on the polymer conformation in the semidilute regime below and above $c_{C_{60}/tol}$. The fitted ξ for isopleths 3 and 4 also fall onto a master curve with the correlation length reduced by a constant R_g, calculated using R_g[nm]=1.25×10^{-5}$M_w^{0.595}$ [4], and concentration reduced by c^*, shown in Figure 4.17b. The data fall onto a single line, described by $(1+\beta c/c^*)^{\alpha}$, where α=-0.77, the expected exponent for semidilute polymer solutions in a good solvent [19–21].

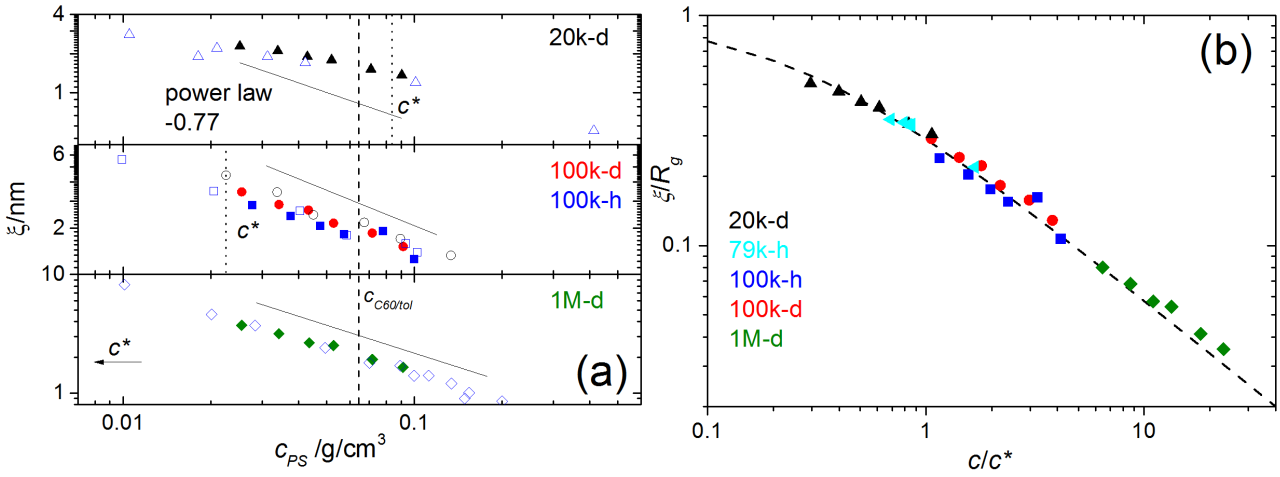


Figure 4.17: (a) Fitted correlation length ξ against PS concentration in the overall PS/C_{60}/toluene solution for isopleth 4 (C_{60}:PS = 0.05) for the three M_w studied (filled symbols). The hollow symbols are literature data from King et al. [20] (100 kg/mol, black) and Hamada et al. [21] (17.5, 110 and 900 kg/mol, blue). Dashed lines indicate c^* for the 20k and 100k. c^* for 1M is not on this scale, as indicated by the arrow. (b) Reduced correlation length ξ/R_g of data from both isopleth 3 and 4 in the semidilute regime, covering a regime of C_{60}:PS from 0 to 0.41 and C_{60} loading from 0 to 0.96 wt% plotted against reduced concentration c/c^*. A line of best fit of the form $(1+\beta c/c^*)^{\alpha}$, where β=4 and α=-0.77 [200]. R_g was calculated using R_g[nm]=$1.25\times10^{-5}M_w^{0.595}$.

A third contrast matching experiment was carried out, using contrast C (a mixture of PS-h, PS-d, C_{60} and tol-d) at either end of isopleth 4/100k with a low concentration of PS-h (0.11±0.003 wt%) and thus allowing the direct determination of single chain polymer conformation in semidilute solutions ($c_{PS-h}+c_{PS-d}\gtrsim c^*$). This contrast examines possible R_g changes upon C_{60} addition in this semidilute regime. As found in Figure 4.18, no R_g change is observed upon addition of 0.15 and 0.5 wt% C_{60}. The values of the fitted R_g agree with those of King et al. [20] and Daoud et al. [201] who found a decrease in R_g of PS in toluene with concentration in the semidilute regime.

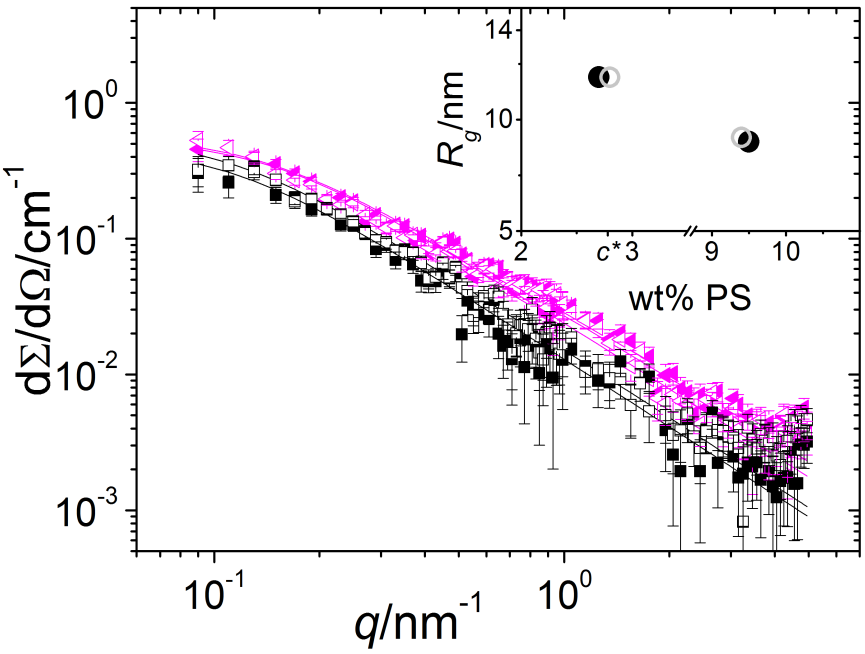


Figure 4.18: Contrast C used to evaluate effect of C_{60} on single chains taken at either end of isopleth 4 (0.15 and 0.5wt% C_{60}). All samples contained 0.11±0.003wt% PS-h. Solid lines are fits to the data using the PolymerExclVolume model in SasView [194]. Inset shows fitted R_g with total concentration of PS (hydrogenous and deuterated) for PS-h/PS-d/tol-d (•) and C_{60}/PS-h/PS-d/tol-d (○) in the semidilute regime, confirming there is no change in R_g upon the addition of C_{60}.

4.5 Conclusions

In summary, the conformation and interactions of polystyrene, and the dispersion of C_{60}, in ternary solutions with toluene have been investigated. Given the reported limited miscibility of C_{60} in pure toluene (0.32 wt%), fullerene concentrations between 0-0.96 wt% were studied. The R_h and R_g for PS in dilute solutions (isopleths 1 and 2) are unchanged upon addition of C_{60}; further there is no change in the solvent quality experienced by the individual PS chains in the concentration range measured for PS (0.12 to 1.93 wt%) and C_{60} (0.005 to 0.5 wt%). The R_g measured is the expected value using the relationship provided by Huber et al. [4], R_g[nm]=$0.0125M_w^{0.595}$. The correlation length ξ in PS/C_{60}/toluene solutions, for which PS is in the semidilute regime (isopleths 3 and 4) agree well with those obtained by King et al. [20] and Hamada et al. [21] This demonstrates that there is no change in PS/toluene solution conformation when C_{60} is added to the system. Using contrast matching it has been shown that the R_g of individual chains in a semidilute solutions follows the expected trend shown previously

by King et al. [20] and Daoud et al. [201] The reduced correlation length falls onto a master curve with concentration with power law of -0.77 regardless of C_{60} addition up to 0.96 wt%. These findings are not inconsistent with previous observations [36–39] of a decrease in PS chain dimensions with colloid addition as it is possible that the low solubility limit of C_{60} prevents reaching high enough concentrations ($\gtrsim$8 wt%) to induce coil shrinkage by depletion in the PL.

The addition of PS to C_{60}/toluene is found to reduce the fullerene miscibility and induce C_{60} aggregation, as shown in Figures 4.10 and 4.11. This is interpreted as due to a reduction in volume available to C_{60} molecules in toluene by addition of the polymer, thus increasing its effective concentration towards $c_{C_{60}/tol}$ (0.32 wt%); $c_{C_{60}/tol}$ is clearly decreased by the addition of PS in particular for higher M_w. The Porod exponent of 4 suggests the formation of compact clusters with sharp interfaces.

There is a clear increase in the scattering intensity at low q from SANS when the C_{60} wt% is higher than $c_{C_{60}/tol}$. A from this scattering contribution is M_w dependent, where the higher M_w (1M) results in a higher A. In conclusion increasing the M_w of PS results in the C_{60} aggregates experiencing a higher osmotic pressure associated with depletion interactions at lower concentrations than with a lower M_w (20k); upon increasing the size of the depletion layer with a higher M_w and, there is a reduction in available volume for C_{60}.

These results demonstrate, for the first time, the phase behaviour and chain conformation in model polymer solutions upon addition of C_{60} fullerenes. In the next chapter, the aggregation of C_{60} below its miscibility limit in dilute solution is investigated further, alongside the impact C_{60} aggregates can have on as cast and annealed thin nanocomposite films.

5 Polymer induced Fullerene Clustering: Impact on thin films

In the previous chapter C_{60} clustering upon the addition of 65k PS in the dilute solution regime was observed, as predicted by the so-called protein limit of polymer/colloid theory. In this chapter this effect is explored further with a range of molecular weights and polymer concentrations in the dilute regime ($c < c^*$).

As determined previously, PS/C_{60}/toluene mixtures exist in the PL. This is where $R_C < R_g^{poly}$. The expected outcomes of the components in this limit are: (i) aggregation of the small colloidal particle, (ii) collapse of the polymer chain (i.e. a decrease in R_h and/or R_g) and (iii) phase separation of the two components. These results have, for a variety of systems, been observed experimentally [36–40] and predicted theoretically [33–35] and is reported to follow the above three results.

5.1 Fullerene clusters in solution

5.1.1 Experimental

Samples for polymer induced fullerene aggregation were prepared by weighing out the necessary mass of each individual component prior to adding the required mass of toluene, the concentrations are summarised in Figure 5.1 and Table 5.1. The resulting PS/C_{60}/toluene solutions were stirred in the dark for 48 hours prior to measurement with the SOFICA or visual inspection. The longer stirring time, compared to the data shown in Chapter 4 allowed a state closer to equilibrium to be reached. Scattering data was corrected for transmission using the procedure described in 4.3.1. Three PS molecular weights were used: 18,000; 65,000 and 775,000 $gmol^{-1}$, referred to as 18k, 65k and 775k, with PDIs of 1.1, 1.1 and 1.3 respectively, GPC traces of the 18k and 775k PS can bee seen in Appendix 1, 65k PS was received from Polymer Laboratories Ltd. Unless otherwise indicated, all experiments with C_{60} used 65k PS. All solutions were stored in the dark and were only exposed to light for the duration of an experiment (approximately 3-5 minutes). The SOFICA is a better light scattering system to use for measurements where there is high absorbance as the photomultiplier tube is more sensitive than the avalanche photodiode used in the ALV. This meant higher fullerene concentrations could be reached, closer to $c_{C_{60}/tol}$.

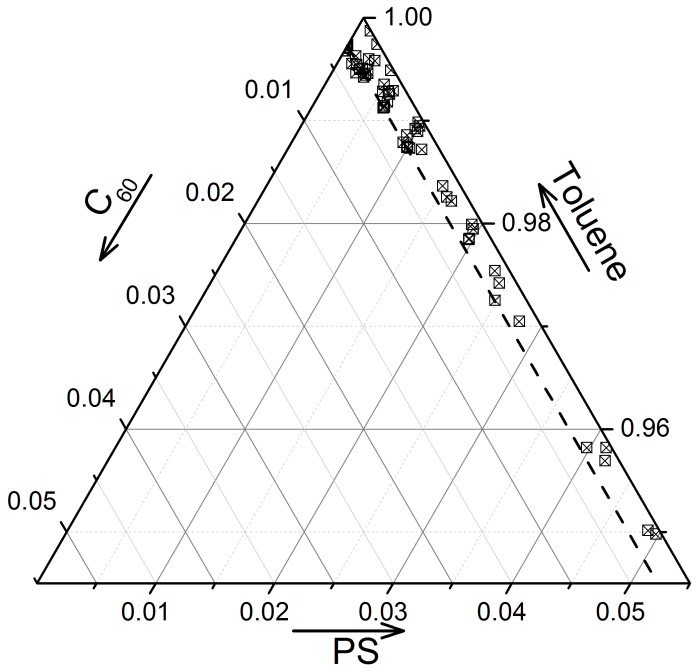


Figure 5.1: Ternary diagram with samples studied for 65k PS/C_{60}/toluene mixtures, showing $c_{C_{60}/tol}$ miscibility line (– – –).

wt% PS	wt% C_{60}	C_{60} loading	State
0.00	0.26	100.00	S
0.00	0.32	100.00	P
0.00	0.32	100.00	P
0.00	0.30	100.00	P
0.00	0.30	100.00	P
0.00	0.29	100.00	P
0.00	0.28	100.00	P
0.00	0.27	100.00	S
0.12	0.25	67.57	S
0.13	0.32	71.64	P
0.17	0.29	62.86	P
0.20	0.33	61.96	P
0.22	0.28	56.25	P
0.24	0.25	51.95	P
0.29	0.28	49.47	P
0.29	0.22	42.86	S
0.29	0.26	47.31	P
0.29	0.26	47.31	P
0.30	0.11	26.98	S
0.31	0.23	43.21	S
0.52	0.19	27.12	S
0.57	0.15	20.68	S
0.59	0.15	20.54	S
0.60	0.27	31.18	P
0.60	0.25	29.57	P
0.60	0.11	14.81	S
0.61	0.21	25.31	S
0.61	0.26	29.77	P
0.94	0.20	17.86	S
0.94	0.27	22.46	P
0.98	0.10	9.48	S
1.00	0.26	21.00	P
1.00	0.26	20.42	P
1.00	0.05	5.05	S
1.01	0.10	8.76	S
1.02	0.25	19.42	P
1.48	0.15	9.22	S
1.57	0.17	9.72	S
1.63	0.15	8.38	S
1.95	0.10	4.93	S
1.96	0.18	8.44	P
1.97	0.19	8.76	P

2.34	0.12	5.02	S
2.48	0.26	9.63	P
2.79	0.16	5.55	P
3.97	0.21	4.99	P
4.13	0.05	1.10	S
4.19	0.12	2.78	S
4.89	0.09	1.90	S
4.97	0.05	0.93	S

Table 5.1: Summary of PS/C_{60}/toluene mixtures investigated, all concentrations (c_i) in the system are reported by the ratio of the mass of component i to the total mass of the solution (mass fraction of total ternary mass), mass fraction of C_{60} and whether the system appeared stable (S) or precipitated (P) after two days of stirring.

5.1.2 C_{60} miscibility in toluene

Previously, C_{60} miscibility was taken to be the reported value of 0.32 wt% as reported by Ruoff et al. [198]. The error bar given in their work gives the lowest possible miscibility to be 0.29 wt%. The method by which solutions are prepared, however, may inadvertently induce solubility of C_{60} due to the heating and cooling steps carried out, alongside the relatively impure C_{60} used for the experiments compared to that used in this work.

Experiments here have demonstrated that solid C_{60} precipitates can be observed at 0.28 wt% and no precipitates are observed at 0.27 wt%. In order to achieve the reported miscibility of 0.32 wt% the solution had to be heated to 45 °C and cooled back down to 25 °C which appears to yield a (meta)stable solution. Thus for the work presented in this chapter, $c_{C_{60}/tol}$ is redefined to 0.27 wt% as this provides consistent results with the same sample preparation method. Images of C_{60} aggregates above $c_{C_{60}/tol}$ are shown in Figure 5.2.

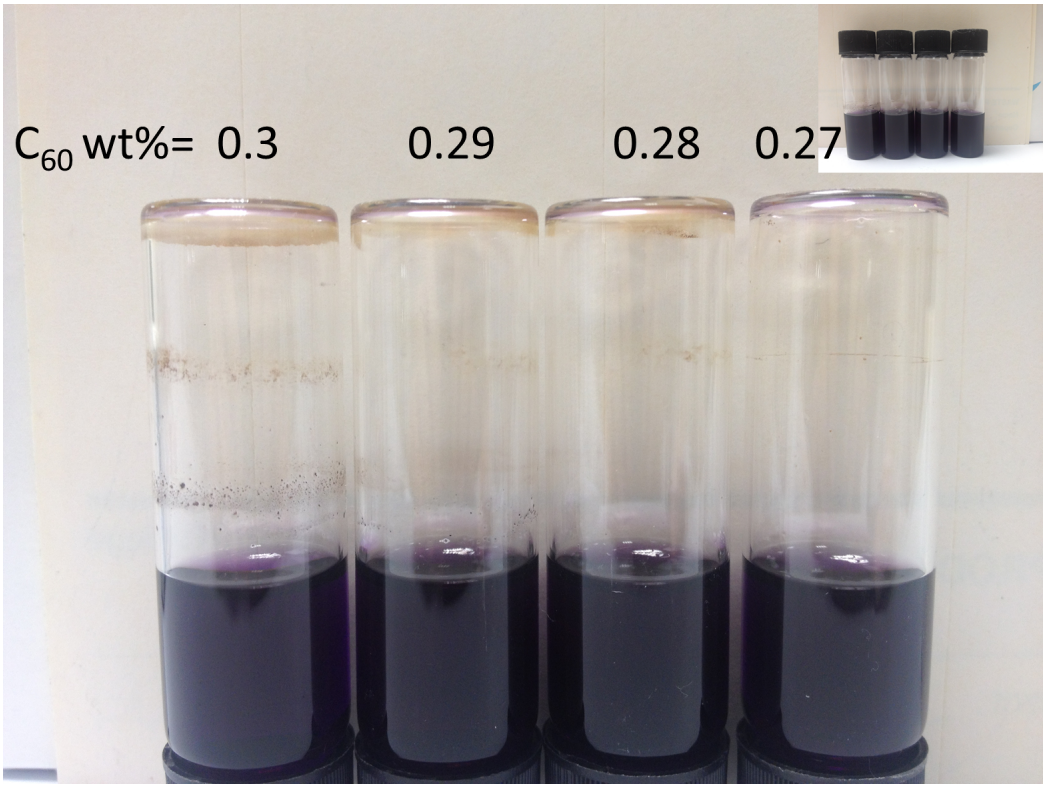


Figure 5.2: Images of C_{60}/toluene solutions (vials turned upside down to demonstrate C_{60} aggregates) close to the reported miscibility limit (0.32 wt%) [198]. Aggregates can clearly be observed between 0.3 and 0.28 wt%. No aggregates are seen at 0.27 wt% and so this is used as the new miscibility limit. Inset shows vials the right way around in the same order.

5.1.3 Results and Discussion

In experiments shown in Chapter 4, a wide C_{60} concentration range of 0 to 0.96 wt% was studied. Now the focus is on a narrower concentration range from 0.05 to 0.32 wt% C_{60}. As expected, given the results from Chapter 4, SLS demonstrated the presence of fullerene clusters below $c_{C_{60}/tol}$ in the dilute solution regime. For highly precipitated solutions it was possible to see C_{60} aggregates below $c_{C_{60}/tol}$ as as there were brown deposits along the sides and bottom of the vials in which solutions were stored as seen in Figure 5.3.

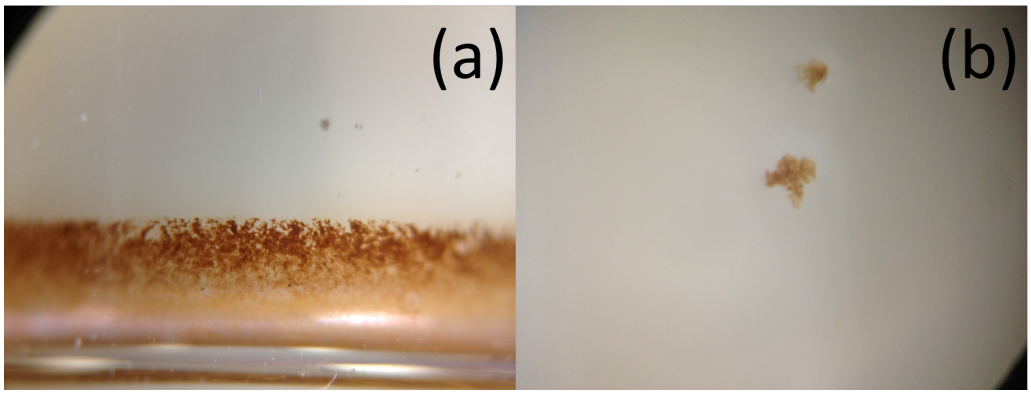


Figure 5.3: Images of macroscopic fullerene aggregates induced by polymer addition, from the (a) bottom of a vial and (b) wall of a vial. Image width is ≈1 cm.

Fullerene aggregation is studied as a function of C_{60} and PS concentration. C_{60} is shown to aggregate at concentrations below the newly defined $c_{C_{60}/tol}$ at 0.27 wt%. Aggregates are found to form at 0.26 wt% C_{60} with 0.3 wt% 65k PS (Figure 5.4a). There is an additional dependence of PS concentration on aggregation (Figure 5.4b). At a fixed C_{60} concentration of 0.25±0.01 wt%, as the polymer concentration increases, there is initially no aggregation, at 0 and 0.12 wt% PS, to aggregation taking place above 0.3 wt% 65k PS. The expected trend for R_C with PS concentration would be for R_C to increase with increasing PS concentration. This is observed in the inset for R_C but is not quite the expected trend, it is very likely that this is due either to the time dependance of C_{60} clusters (discussed later in this chapter) or an increase in the number of C_{60} clusters. There is a change in the onset of C_{60} aggregation with increasing PS concentration. As PS concentration increases, C_{60} begins to precipitate at a lower concentration. This is summarised in Figure 5.5. Also noted is that the PS hydrodynamic radius (R_h^{PS}) does not change, shown in Figure 5.6, demonstrating that the different sample preparation method has no effect on the PS chain dimensions.

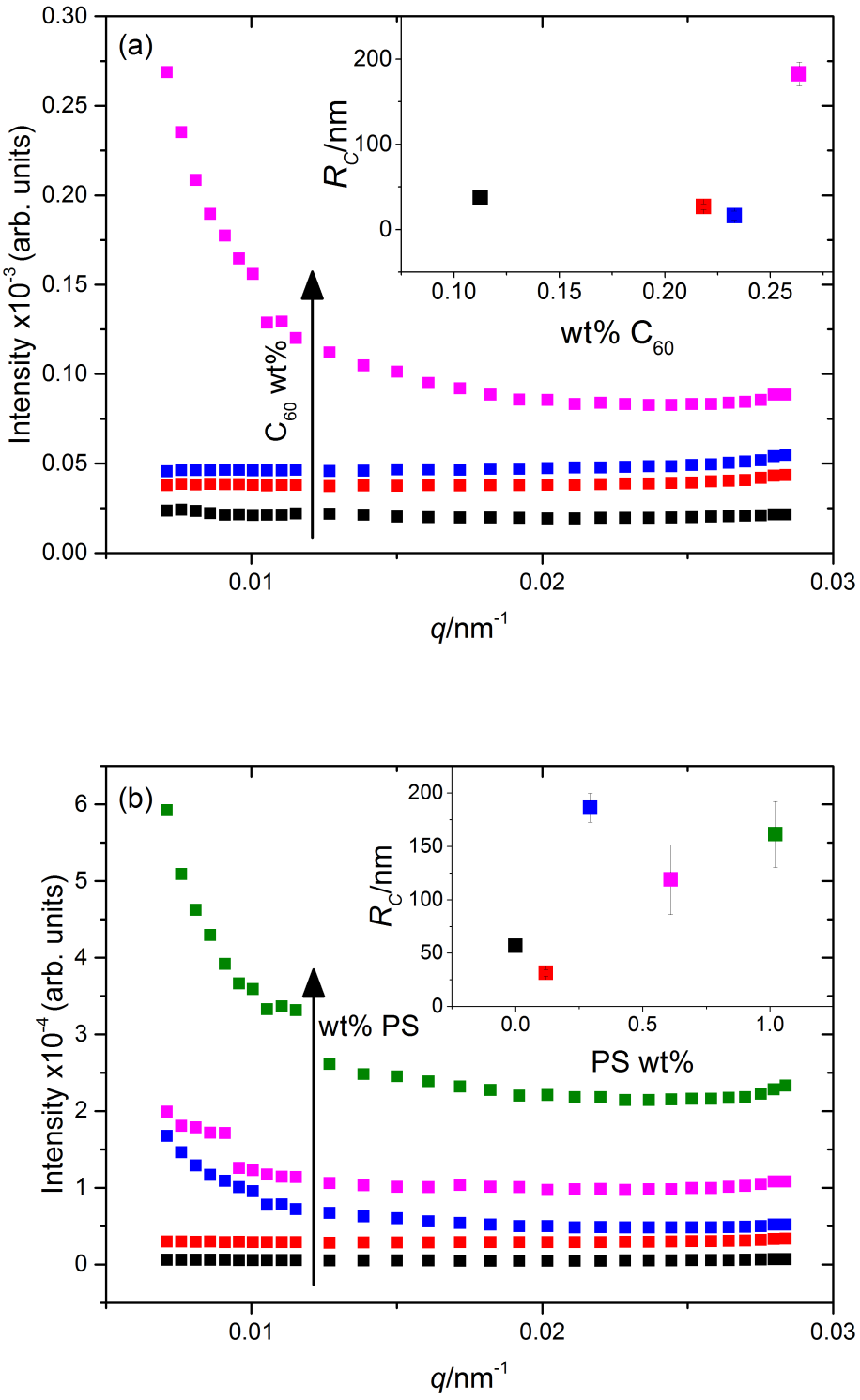


Figure 5.4: SLS data showing PS/C_{60}/toluene mixtures. (a) Constant PS concentration at 0.30±0.01 wt% with C_{60} from 0.11 to 0.26 wt%. Inset shows fitted R_C via Guinier analysis. There is a clear trend with C_{60} loading leading to a detectable R_C. (b) Fixed C_{60} concentration of 0.25±0.01 wt% and varying PS concentrations from 0 to 1.02 wt%. Inset shows R_C via Guinier analysis, there appears to be a trend for increasing PS concentrations having larger aggregate sizes. For both graphs the color in the inset refers to the same colour within the I vs q plots.

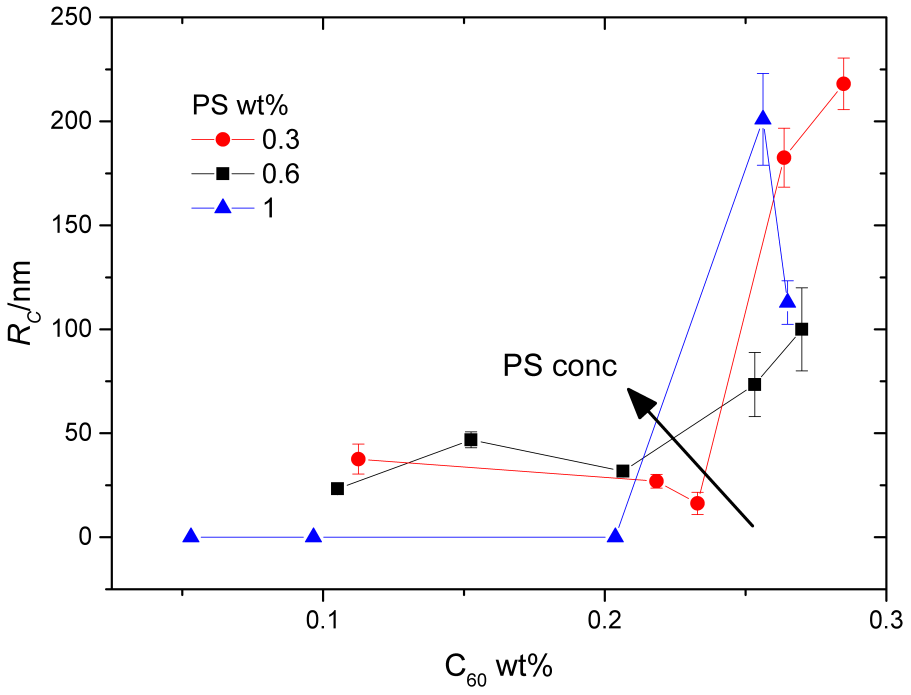


Figure 5.5: C_{60} R_C via Guinier analysis as a function of C_{60} loading and PS concentration. There is a trend of a decreasing miscibility limit with increasing PS concentration. Light scattering was carried out after 48 hours of solution stirring.

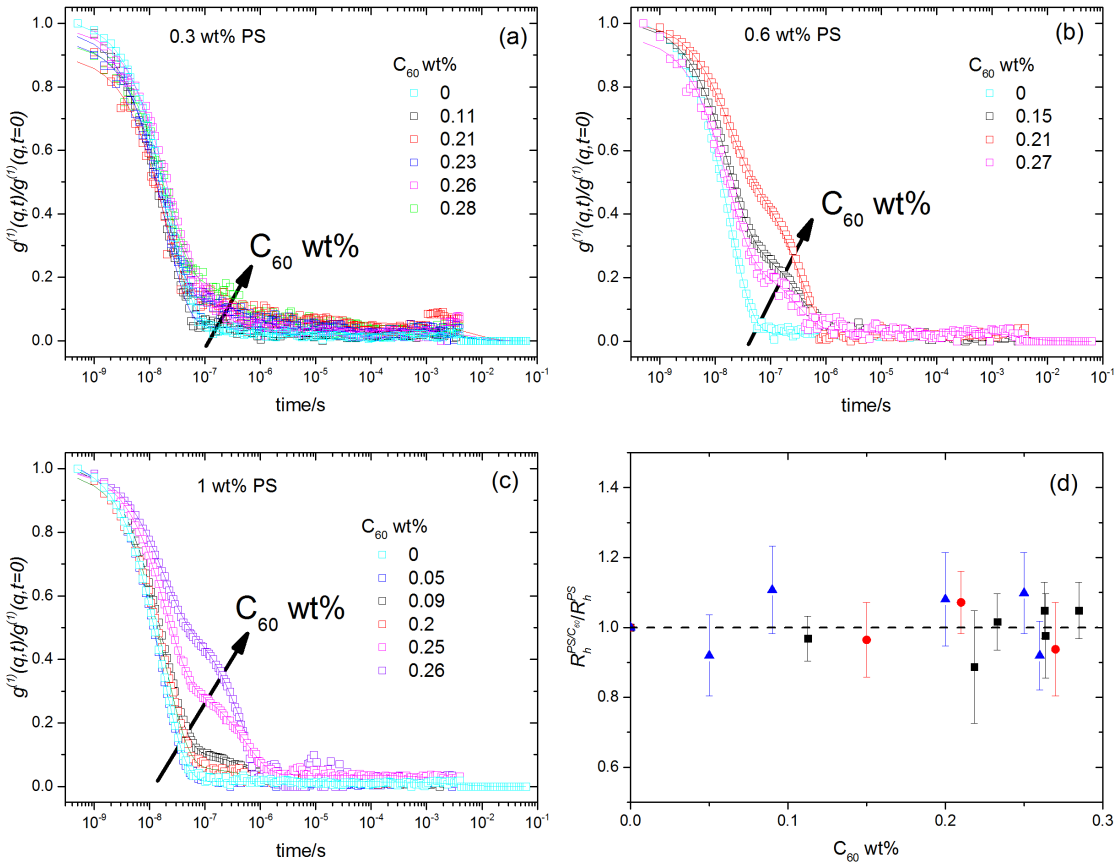


Figure 5.6: (a-c) DLS correlation functions at constant PS concentration at (a) 0.30±0.01 (■) (b) 0.6±0.1 (●) (c) 1.00±0.07 wt% (▲) with C_{60} from 0 to 0.28 wt%. (d) shows fitted R_h/R_h^{PS} via fits to Equation 3.4. There is no change in R_h^{PS} with C_{60} loading.

Further investigation with a wide range of concentrations in the dilute regime, using 65k PS lead to the formation of a ternary diagram seen in Figure 5.7. It is important to note that this is not an equilibrium phase diagram, but gives the state of the solution (stable or precipitated) after 48 hours the solution being stirred. PS/C_{60}/toluene solutions equilibrate slowly over a number of days when stored at 25 °C, additionally, any heating steps may force the solubilisation of C_{60} which would in fact place the system further from equilibrium, highlighting the kinetically trapped nature of these solutions.

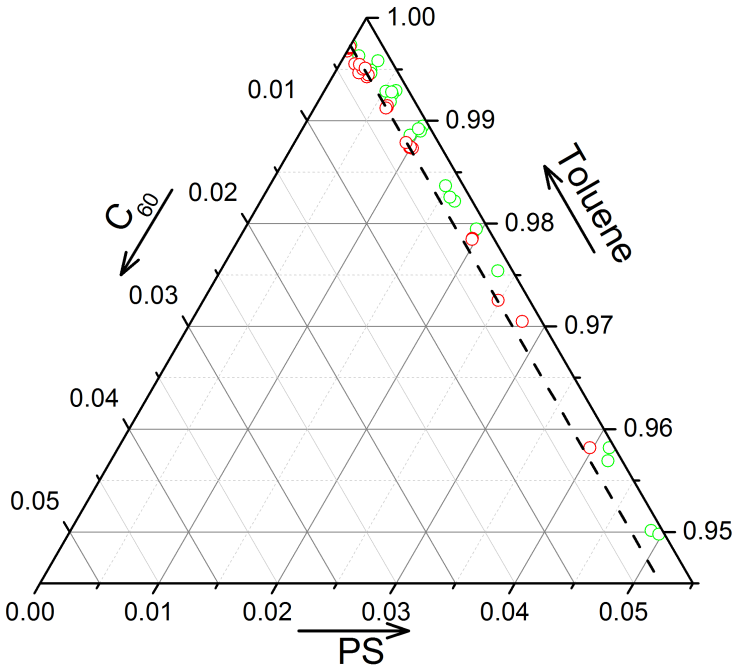


Figure 5.7: Ternary diagram of 65k PS/C_{60}/toluene showing homogenous (○) and precipitated (○) samples. $c_{C_{60}/tol}$ (– – –) is shown.

The time dependence of fullerene clusters was also investigated, in Figure 5.8. The scattering data shows an apparent decreasing to vanishing R_C, however in reality this is not the case. Over the time period studied, there was precipitation of C_{60} aggregates to the bottom of the scattering cuvette. Thus, the fullerene clusters were out of the q range, and out of the laser path within the instrument. This same trend was observed for 18k and 775k PS.

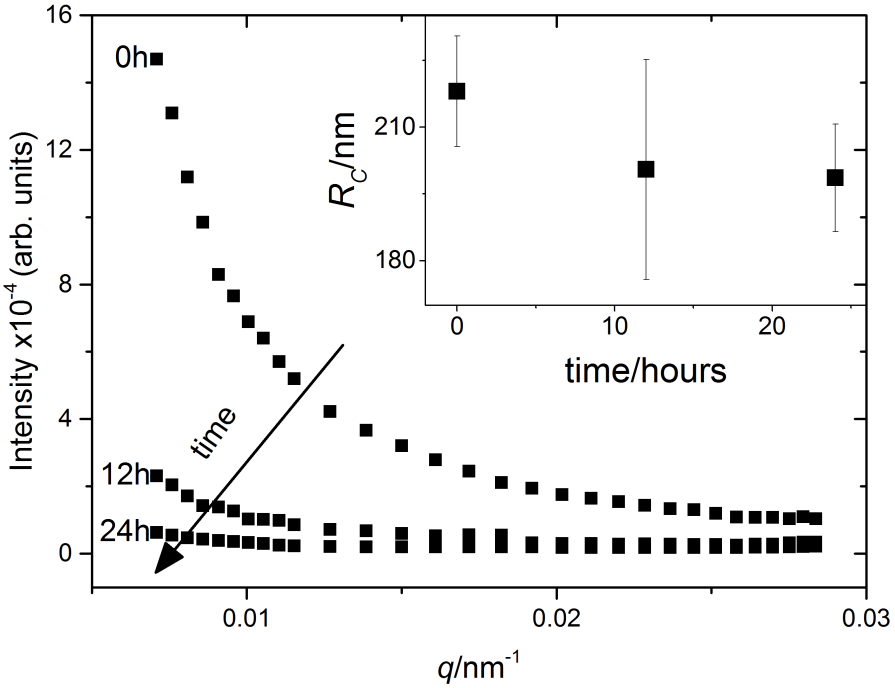


Figure 5.8: Time study of 0.29 wt% PS and 0.28 wt% C_{60} via SLS, the number of clusters observed within the solution decreases as they are forming micron scale precipitates at bottom of SLS cuvette and hence going out of the q range of the instrument.

To provide a basic framework with which to predict stability or precipitation, simple scaling calculations are carried out. Using the definition of the overlap concentration as the concentration at which the most number of polymer chains can fit into a certain volume prior to chains beginning to overlap, the most efficient packing structure of a face-centred cubic is assumed. This gives a packing efficiency of 74%. c^* is calculated according to $3M/4\pi N_A R_g^3$, where R_g[nm]=$0.0125M_w^{0.595}$ [4], giving the expected trend of higher M_w reaching c^* at lower concentrations, this is shown in Figure 5.9. It stands to reason, therefore, that at once all the possible space has been occupied, the remaining space can be occupied by C_{60}. Thus the concentration of C_{60} which is able to fill the remaining space (26%) is calculated. Given the miscibility of C_{60} at 100% free volume at 0.27 wt%, the concentration of C_{60} miscible at PS/toluene solution at c^* is 0.07 wt%. This agrees extremely and surprisingly well with the experimental data as shown by the gray line in Figure 5.10. There are four solutions studied above c^*. It is expected that there would be some finite miscibility of C_{60} in PS in the melt (1-3 wt%) as was observed in Refs. 6 and 7. Given the data acquired above c^*, there appears to only be 0.12 to 0.15 wt% C_{60} which is able to remain molecularly dissolved. It is very common for polymer nanocomposite melts to be processed from the solution state; either via drop casting (a slow drying of the

solution until all solvent is removed) [107–110, 126] or rapid precipitation (adding the solution drop-wise into a non-solvent for both solutes) [6, 7]. Assuming that there is no unexpected increase in miscibility in the melt, it is conceivable that the miscibility of C_{60} in a PS matrix is governed by the solution state (homogenous or precipitated). Given the boundary shown in Figure 5.10, preparing a solution in the homogenous (green) regime, the solution would eventually pass through the boundary with solvent removal. A miscibility of C_{60} in PS melts between 0.12 and 0.15 wt% is predicted from experiments and calculations, this value comes from assuming that as toluene is removed it is replaced by PS, and that there must be some finite miscibility of C_{60} in PS. Comparing these to the values (1 and 3 wt%) acquired previously in Refs. 6 and 7, they are an order of magnitude below those reported. Three possible effects are considered, M_w variations giving rise to different miscibilities, sample preparation technique and thermal annealing. According to the predictions of the simplistic model above, (and the data presented later in Figure 5.11) increasing M_w would lead to a decrease in C_{60} miscibility. Comparing this prediction to literature, Mackay et al. [7] demonstrate that there is no M_w dependence in the 63 to 393 $kgmol^{-1}$ range. The sample preparation technique assumed in the miscibility limit here is via drop casting (solvent evaporation) whereas within the literature rapid precipitation is used to achieve a dispersed nanocomposite blend. In order to quantify miscibility, the difference between miscibility and dispersion must be stated. Miscibility is true thermodynamic equilibrium state, whereas dispersion is a fine intermixing of two immiscible phases. Previous work by Wong and Cabral [9] has shown that a dispersed nanocomposite melt (as measured by X-Ray Diffraction and optical microscopy) of 1 wt% C_{60}/PS can, upon annealing at 180 °C, begin to crystallise. This indicates a phase separation and thus 1 wt% is above the miscibility threshold for C_{60} in a PS matrix.

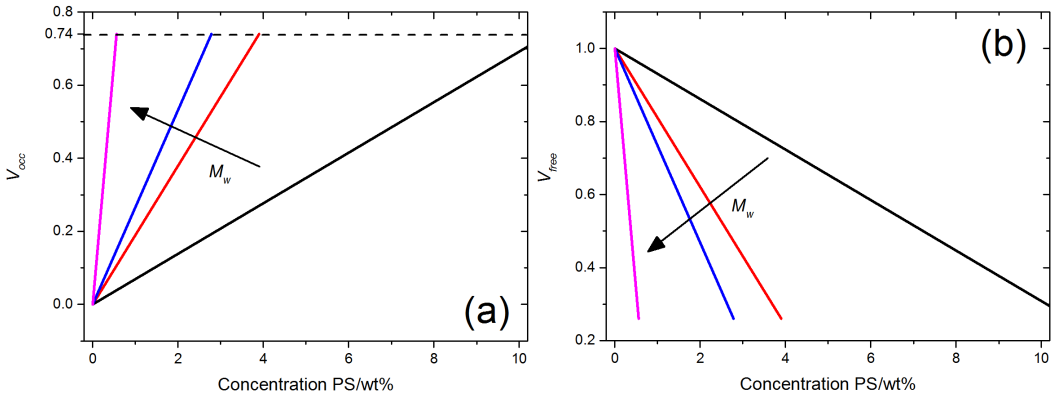


Figure 5.9: Scaling calculations for (a) occupied volume (V_{occ}) and (b) free volume (V_{free}) with four PS M_w shown. 18, 65, 100 and 775 kgmol^{-1}. Dashed line indicates the volume at which maximum packing efficiency is achieved i.e. c^*.

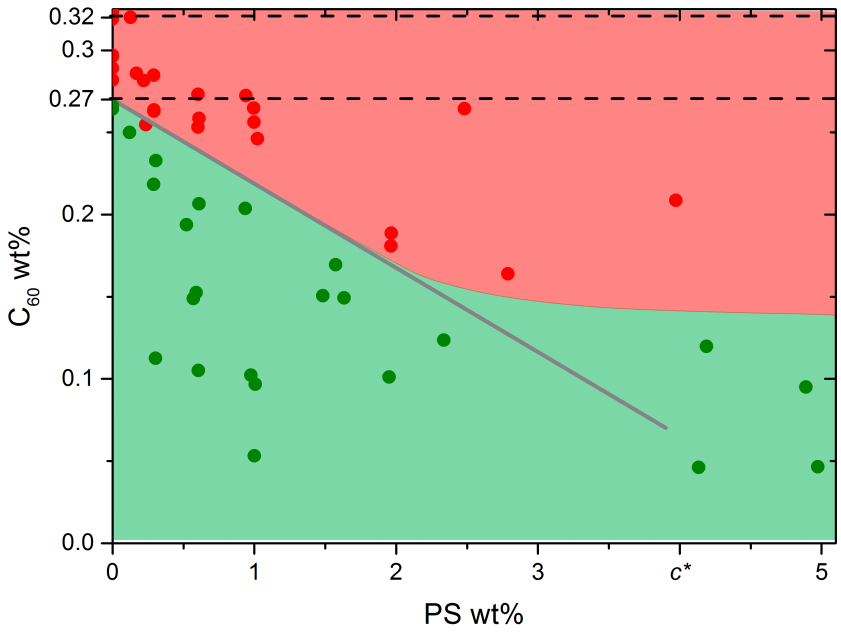


Figure 5.10: PS and C_{60} concentrations using data shown in Fig. 5.7 to magnify the effect of increasing PS concentration on C_{60} miscibility limit within PS/C_{60}/toluene mixtures. Homogenous (•) and precipitated (•) solutions are shown as before. $c_{C_{60}/tol}$ is shown at 0.27 wt% (– – –) as well as the published miscibility limit at 0.32 wt% [198]. The calculated miscibility limit (—) (described in the text) agrees well with the observed homogenous and precipitated phases, shown in green and red respectively. The plateau at ~0.15 wt% C_{60} indicates the finite miscibility of C_{60} in PS.

Using this model, two main conclusions are reached: (i) as PS loading, at a given M_w, increases, a larger volume is occupied by the PS and therefore less volume in solution is effectively available for the C_{60}. Thus, it is expected that, as the mass fraction of PS increases there is less and less volume for the C_{60} molecules, causing aggregation at lower mass fractions of C_{60}. This is observed experimentally with 0.3 to 1 wt% 65k PS (c^* = 3.9 wt%) and is shown in Figures 5.5 and 5.10 where from 0% to 2% PS, the line where C_{60} starts to precipitate falls from 0.27% to 0.17%. (ii) At higher M_ws C_{60} aggregation will occur at a lower mass fraction as a larger volume fraction is taken up by polymer chains of higher M_w, at the *same* polymer mass.. To test this potential effect the molecular weight effect on fullerene clusters was investigated.

The data collected for 18k and 775k PS broadly follow the trend from the calculations and are summarised in Figure 5.11a. On the whole, aggregated samples are above the solid line calculated from the model described above. This gives a very good indication that the model is a useful approximation to use of PS/C_{60}/toluene solutions. To fully test the applicability of

this model a more extensive range of PS M_w and mass fractions should be carried out. For the samples which showed C_{60} aggregates there is no change in the cluster size (Figure 5.11b), however there were noticeably more aggregates at the bottom of the cuvette containing 775k PS. According to the calculations above this is very much expected as at same mass fraction, there is more free volume available to the fullerenes with lower M_w, and so as M_w increases, there are more C_{60} aggregates.

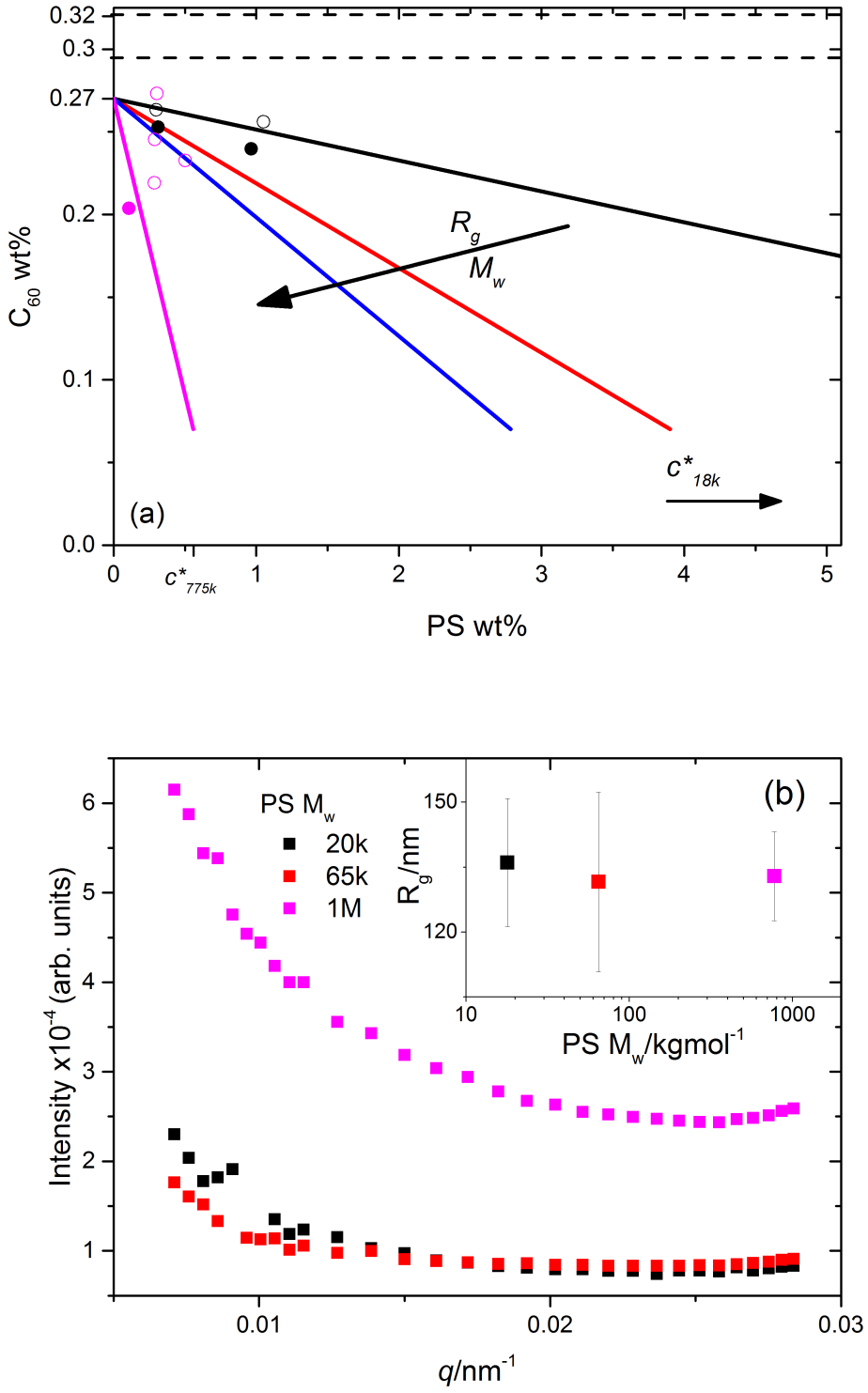


Figure 5.11: (a) Using the calculations described above, the modelled miscibility limit for C_{60}in PS/toluene is shown for 18, 65, 100 and 775 kgmol^{-1}. Homogenous (•) and aggregated samples (○) are indicated in the relevant colour. Note that experiments were only carried out using 18 and 775 kgmol^{-1} PS. (b) Static Light Scattering results at fixed concentration of PS/C_{60}/toluene at 0.3 wt% PS and 0.26 wt% C_{60} with varying PS M_w at 18k, 65k and 775k. Inset shows that there is no change in fullerene cluster size with M_w in dilute solutions.

Consolidating the results here on C_{60} aggregation with those presented in the previous chapter, it is clear that there are several factors which can affect the presence of C_{60} clusters in solution. The solution preparation method in this chapter was one where the desired concentration is reached directly as opposed to a dilution series, as was carried out in isopleth 1 described in Section 4.2.2. Here, it is shown that the point at which the miscibility threshold is achieved (0.12-0.15 wt% C_{60}) is higher than was previously found (~0.1 wt% C_{60}). This is a direct result of sample preparation, as the samples in isopleth 1 were taken from a region outside of $c_{C_{60}/tol}$ and diluted to a region inside $c_{C_{60}/tol}$ without enough time for the precipitated fullerenes to dissolve into the solution. Hence, the results presented here are more consistent and robust than those shown on C_{60} aggregation in Chapter 4. Nevertheless, the results demonstrating no change in the polymer chain dimensions (R_g or R_h) and mixture correlation length, ξ, are valid as confirmed by DLS on the same solutions shown in this chapter (Figure 5.6).

This section has demonstrated that the addition of PS to C_{60}/toluene solutions induces the following behaviour: (i) increasing PS wt% increases C_{60} aggregation, (ii) C_{60} aggregates are time dependent and grow larger over time, eventually settling to the bottom of an undisturbed solution vessel, (iii) at a fixed mass fraction, larger PS chains (i.e. increased M_w) decreases the miscibility limit of C_{60}.

Now that the properties of PS/C_{60}/toluene solutions are known from the perspective of the polymer and fullerene, the next step is to use this to evaluate the implications to thin film morphology, in both the as cast and annealed film state.

5.2 Fullerene clusters in thin films

Prior work by Wong and Cabral [8, 9] has demonstrated the molecular weight, thickness, concentration and time dependance of polystyrene fullerene thin films. Here, the state of the casting solution is varied to affect the as cast and annealed film morphology. In order to make a thin film of a certain thickness one may chose to prepare a dilute solution and, via spin coating, cast with lower rpm or a more concentrated solution at higher rpm. The first step for this study was to find a concentration range where the rpm could be varied to achieve films of the same thickness. After which films of comparable thicknesses are prepared from different solution concentrations which are either stable or have precipitated.

5.2.1 Preliminary Experiments

In order to achieve similar film thicknesses from the same PS concentration, it was necessary to find a PS concentration and rpm range in which this could be achieved. The initial thickness of annealed films can effect their final morphology and so it was important to obtain the same film thickness in order to compare annealed morphologies. This result is shown in Figure 5.12 where an effective range to vary film thickness with polymer concentration is found from 500 to 7000

rpm. It was not possible to form a visibly smooth film with s 5 wt% 65k PS/toluene solution at a 500 rpm.

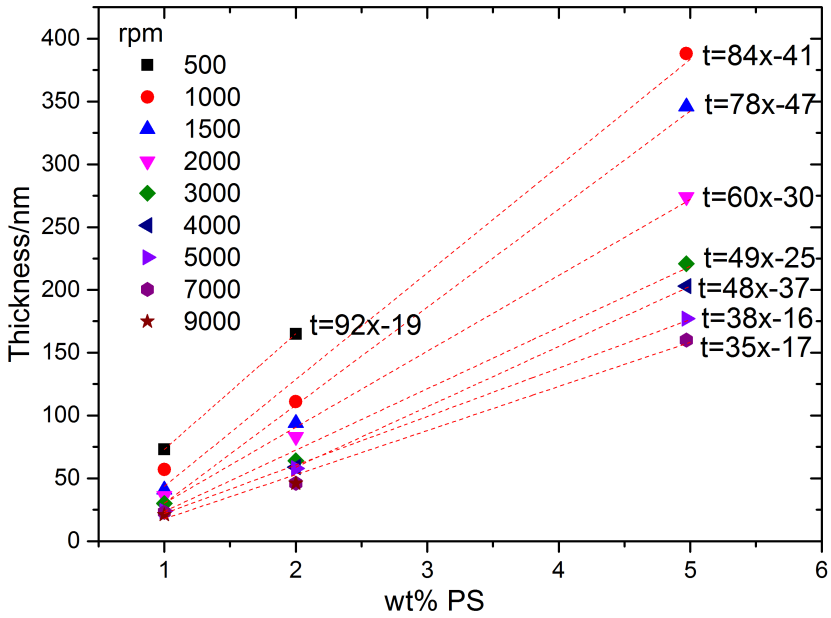


Figure 5.12: Calibration for varying PS concentration with spin coater rpm. Three PS concentrations are used: 1, 2 and 5 wt%. The equations are from lines of best fit and were used to achieve the similar film thicknesses from solutions starting at different concentrations.

From this result, there are limited thicknesses achievable at various C_{60} solids loading, which are shown in Figure 5.13b. If a homogenous 15 wt% C_{60} thin film is desired, the maximum film thickness possible is 100 nm. It is also possible to form homogenous 400 nm thick films with 2 wt% C_{60}. As for a minimum film thickness, difficulties arise from inhomogenous, patchy films forming and so references to the lower end of the film thickness scale are not made here. These findings are extremely important for the processing of thin nanocomposite polymer films from solutions as forming films from a precipitated solution may have drastic effects on film morphology and impact film properties such as device efficiency in OSCs.

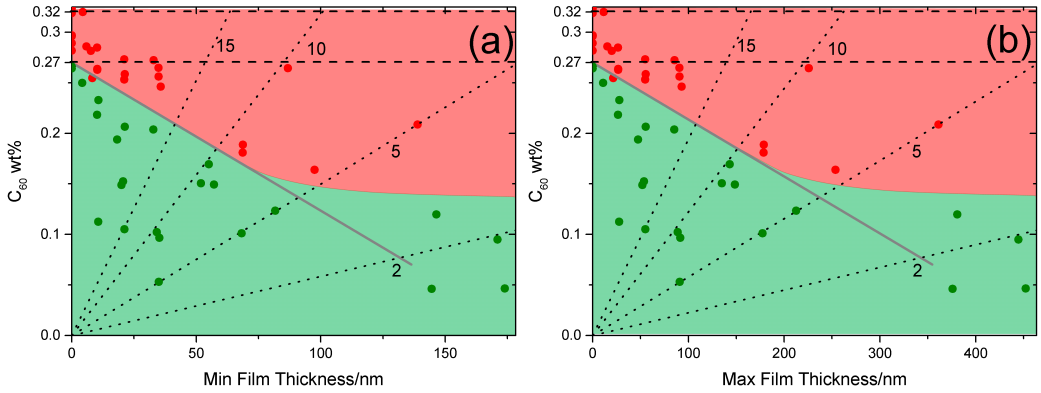


Figure 5.13: Demonstration of (a) minimum and (b) maximum film thickness' achievable from homogenous solutions with indications of C_{60} solid loading in the final film. This enables one to chose a PS concentration at which their desired C_{60} loading and film thickness can be met. Homogenous (•) and precipitated (•) solutions are shown as before. $c_{C_{60}/tol}$ is shown at 0.27 wt% (– – –) as well as the published miscibility limit at 0.32 wt% [198]. The calculated miscibility limit (—) (described in the text) agrees well with the observed homogenous and precipitated phases, shown in green and red respectively. Constant C_{60} solids mass fraction in the film are shown (⋯) with the mass % of C_{60}/PS noted.

5.2.2 Results and Discussion

Based on the results of solution state (stable or precipitated) and the ability to control film thickness within a given rpm range, it was possible of fabricate thin films with a constant thickness and C_{60} loading in the stable (green) and precipitated (red) phases. As indicated in Figure 5.14, five solutions were selected for the thin film study, three in a stable state and two in the precipitated state. It was possible, by controlled spin coating rpm, for the films to be a constant thickness (±3 nm) and as the solutions lie on the same isopleths (at 5 and 9 wt% C_{60} respectively) the films were in effect 'identical'. The films fabricated are summarised in Table 5.2.

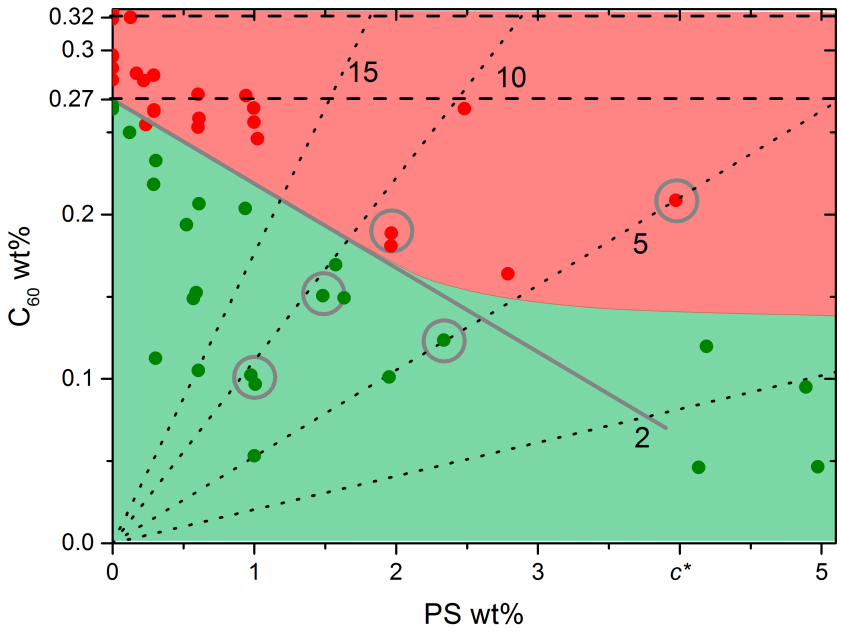


Figure 5.14: Reproduction of Figure 5.10 to highlight solutions used in the thin film study. Thin films were fabricated from the circled solutions and are summarised in Table 5.2. Homogenous (•) and precipitated (•) solutions are shown as before. Constant C_{60} solids mass fraction in the film are shown ($\cdots$) with the mass % of C_{60}/PS noted.

Solution Name	wt% PS	wt% C_{60}	C_{60} mass fraction/%	State	Film thickness (h) Range /nm
P1C01	1	0.1	9	S	53-58
P1.5C015	1.5	0.15	9	S	54-56
P2C02	2	0.2	9	P	56-62
P2.3C012	2.3	0.12	5	S	129-131
P4C021	4	0.21	5	P	130-132

Table 5.2: Summary of solutions used in the following thin films study. Given are solution name, starting solution concentrations parameters, C_{60} mass fraction (to PS), state, either stable (S) or precipitated (P), and film thickness (h) studied. For simplicity, in the following discussion samples P1C01, P1.5C015 and P2C02 are referred to as 60 nm films, and P2.3C012 and P4C021 as 130 nm.

The aggregation of C_{60} in solution is expected to have impact on thin film morphology, both in the as cast state and after a period of annealing. Initially, three films were made from solutions P1C01, P1.5C015 and P2C02 by using the appropriate spin speed (via Figure 5.12)

h=57±4 nm were produced, referred to as 60 nm films in the proceeding discussion. There are no micron sized aggregates visible for the films prepared from homogenous solutions in Figure 5.15a and b, whereas in Figure 5.15c, for P2C02, there are micron sized aggregates visible. This is indicative of the already aggregated state and visible precipitates in solution (as shown previously in Figure 5.3). Upon closer examination, via AFM, fullerene clusters, observed in solution with light scattering, with $R_C \approx$ 120±20 nm, are seen in the as cast films in Figure 5.15e and f. Line profiles of the AFM images are seen in Figure 5.15g-i. Both P1C01 and P1.5C015 are thought to be homogenous solutions, however, it appears from this that there are clusters within the as cast film of P1.5C015. The largest of these clusters that was observed had a radius of 25 nm. This would not be seen via a Guinier analysis of the SLS data and so the solutions were assumed to be homogenous. Some smaller clusters of approximately 12±2 nm were seen via AFM of P1C01. There are two possible reasons for this: (i) C_{60} far less soluble at all in PS/toluene solutions than previously thought or (ii) the clusters are formed during the spin coating process. As the solvent evaporates, the solution would pass through the previously determined miscibility limit (e.g. Figure 5.14) and would subsequently cause C_{60} to cluster, due to the rapid solvent evaporation only small clusters would be formed as opposed to those on the 100 nm length scale.

Given the aggregation state of C_{60} in the as cast films, two results could be expected upon annealing the films: (i) The same annealed film morphology is reached, via a different kinetic pathway, and/or (ii) the annealed film morphologies are different due to the sub-micron differences within the films. Additionally, one could expect that the two homogenous films (prepared from solutions P1C01 and P1.5C015) produce identical morphologies upon annealing. After annealing for 30 mins at 180 °C the morphologies of the films have observable differences on the micro (Figure 5.15j-l) and nano-scales (Figure 5.15m-o). P1.5C015 and P2C02 have similar morphologies with both imaging techniques. Optical microscopy shows numerous, but smaller clusters on the film fabricated from P1C01 compared to P1.5C015 and P2C02 with larger and fewer clusters.

Prior work conducted on PS/C_{60} films has focussed on a lower (≤5 wt%) C_{60} loadings within a composite thin film [8–10], thus for comparisons to be made with previous work, solutions were prepared from the stable (P2.3C012) and precipitated (P4C021) soutions, resulting in films with a 5 wt% C_{60} loading. The films prepared had a 5 wt% C_{60} and h=131±1 nm. As is seen from Figure 5.16 there are micron size clusters the film prepared from the precipitated state (Figure 5.16b) and slightly larger clusters on the nanoscale (Figure 5.16d) than compared to P2.3C012. Annealing the film prepared from the homogenous state gives morphologies (Figure 5.16e) very similar to those seen in Figure 7d of Ref. 9. Note that Ref 9 used a slightly lower temperature (175 °C) longer annealing time (60 mins) and higher M_w (270 kg/mol), hence identical topography and morphology should not be expected. Comparing the two films shown in Figure 5.16e-f, the differences between the morphology is clear. The film prepared from the homogenous solution (P2.3C012) has fewer and larger clusters compared to P4C021. These

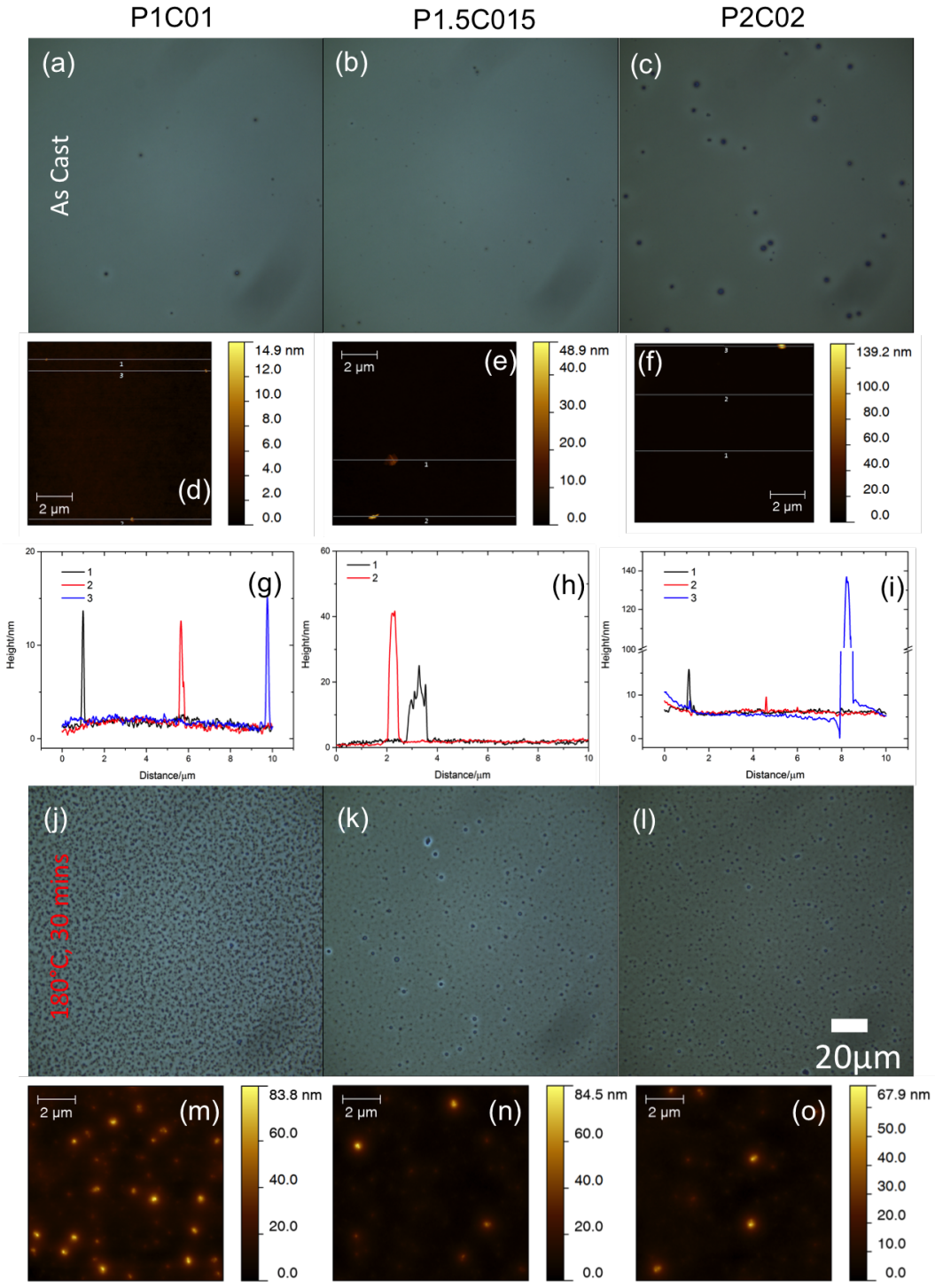


Figure 5.15: (a-c, j-l) Optical microscopy and (d-f, m-o) AFM images with line cuts (g-i) of the lines indicated in the as cast 60 nm films in d-f and (j-o) films annealed at 180 °C for 30 minutes. Left images are made from P1C01, centre from P1.5C015 and on the right from P2C02. From the as cast films, homogenous solutions, P1C01 and P1.5C015 appear similar the micron lengthscale. In the nanoscale, clusters on the order of 10 nm visible in all films, with 200 nm clusters seen in P2C02, corresponding to those seen via SLS. After annealing it is clear that there are significantly more clusters in the solution which was originally homogenous, whereas P1.5C015 appears very similar to P2C02 on the micron scale.

differences are also borne out in the AFM images, Figure 5.16g-h where the C_{60} clusters in the film are taller (700 nm) in P2.3C012 and are significantly less in number. Additionally, radial profiles of FFTs of the annealed films are shown in Figure 5.17. There is a clear peak in from P2.3C012 corresponding to a characteristic length scale, this is not seen for P4C021.

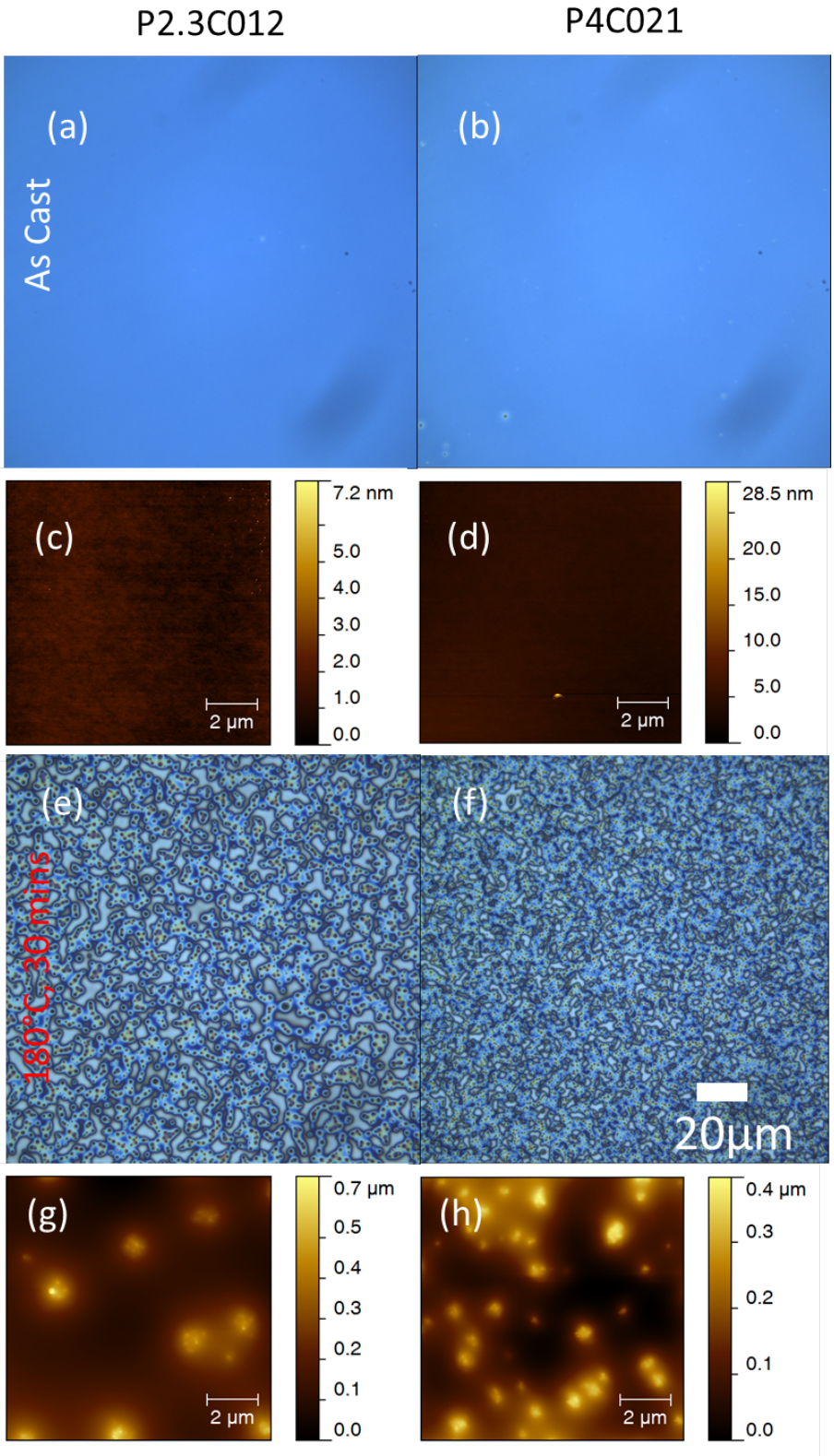


Figure 5.16: (a-b, e-f) Optical microscopy and (c-d, g-h) AFM images of (a-d) as cast 130 nm 5 wt% C_{60}/PS films and (e-g) films annealed at 180 °C for 30 minutes. As expected from the previously shown 9 wt% C_{60} films, the sample spun from the precipitated state (P4C021) has some micron scale aggregates.There is a clear difference between the two samples, with the homogenous solution giving a morphology with fewer, but larger clusters and the precipitated giving smaller, but numerous clusters.

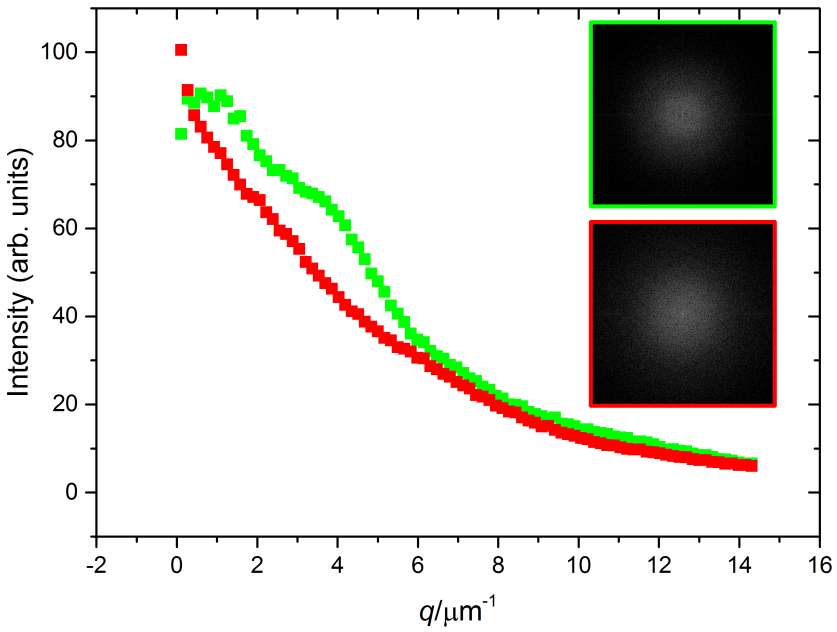


Figure 5.17: Radial profiles of films prepared from P2.3C012 (▪) and P4C021 (▪) after annealing at 180 °C for 30 minutes. Insets shows the FFT's of films from which the radial profiles are extracted. There is a clearly a structural peak present for the films fabricated from P2.3C012.

Solution Age

As was shown previously in Figure 5.8, there is a time dependence to cluster formation and size within solution, the clusters which are observed initially on the order of 100s nm form aggregates on the micron scale which settle to the bottom of a stationary vessel. Thus it is very likely the morphology of thin films would be highly dependent on the age of the solution from which it is cast. For the purposes of these results 'day 0' is considered to be after the solution had been prepared and stirred for 48 h, and so 'day 5' would be 5 days after the 48 h had elapsed. Between the thin films being cast there was minimal movement of the vial containing the solution. There is also no change, within error, of film thickness prepared from solutions of different ages. As a reminder, solutions were not filtered prior to casting films.

The evolution of film morphology is shown in Figure 5.18, the solution classed as homogenous (P1C01) has no change in morphology over the time period studied. The solution which was clearly in the aggregated regime (P2C02) shows a definite trend in morphology from a sparse clusters to a densely packed structure with 10s μm aggregates. The interesting result comes from the solution situated between the two limits, P1.5C015. In the solution state it was assumed to be a homogenous solution, however, there is an evolution in film morphology with time,

indicating the solution is not actually stable as was thought before.

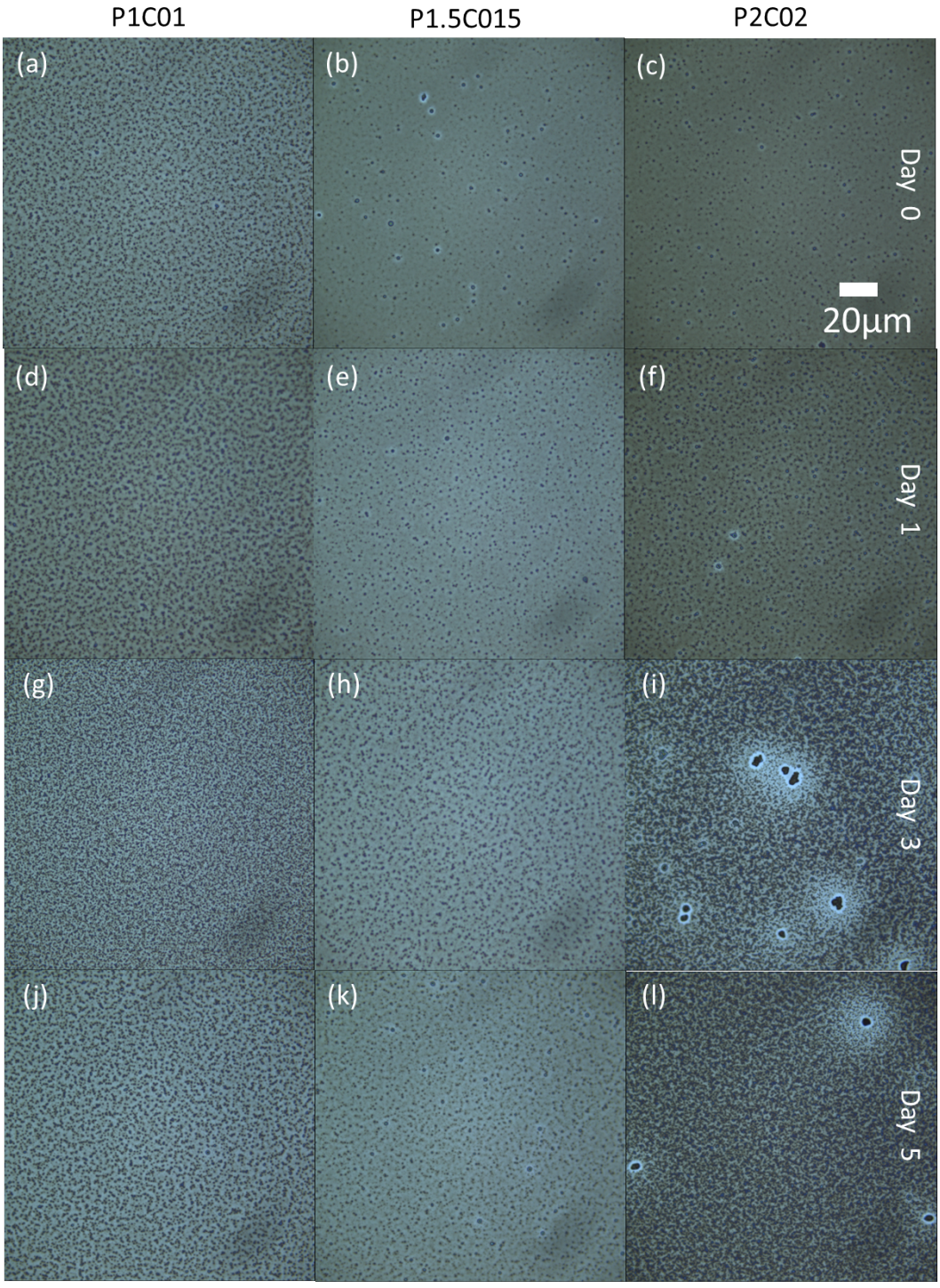


Figure 5.18: Optical Microscopy images of 9 wt% C_{60} loaded 60 nm thin films cast at different solution ages, from 0 to 5 days.

Image analysis of the OM images shown in Figure 5.18 yields the area fraction (A_f) of C_{60} rich regions, plotted in Figure 5.19. This displays the trend observed quantitatively. Films prepared from P1C01 show no change with solution age, whereas those prepared from both P1.5C015 and P2C02 show an increase in A_f of C_{60} rich regions, with the change in P2C02 much more significant than that seen in P1.5C015. The increase in A_f of C_{60} rich regions is very likely to arise from an increase in cluster size and number within the solution. Once they are transferred to the film, the growth of clusters within the film appear to be hindered by a decrease in diffusivity of the solution-formed aggregates. i.e. the aggregates from the solution are larger than individual C_{60} molecules and so will diffuse slowly through the film or they will be effectively frozen within the matrix and act as nucleation sites. Both of these situations will cause there be an increase in clusters in the film, but a decrease in their size.

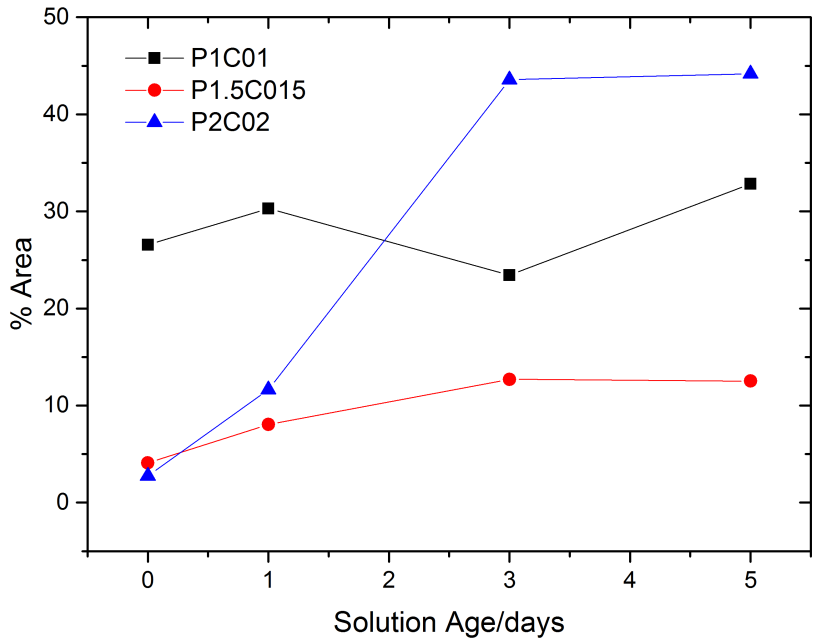


Figure 5.19: Area fraction of 9 wt% C_{60} loaded 60 nm thin films cast at different solution ages, from 0 to 5 days.

A inspection of look at the films prepared from the oldest solution studied (after 5 days of solution ageing) is seen in Figure 5.20, comparing the as cast and annealed state of the films. The film fabricated from the homogenous solution (P1C01) shows no micron scale aggregates, which are seen in films made from P1.5C015 and P2C02, giving further indication that P1.5C015 is not a homogenous solution. Significantly larger aggregates (10s μm) are seen in P2C02 than compared films cast at day 0, these are very likely to be the aggregates which are observed settling to the bottom of the solution storage vessel and that the micron sized clusters are

grown from the ~100 nm clusters. There are 10-30 nm aggregates observed in all three as cast films, however those seen in P2C02 are significant due to the consistent coverage over the film as opposed to the sporadic nature of the clusters seen in P1C01 or P1.5C015. Similar sized clusters can also be seen within the regions of Figure 5.20l which are seemingly C_{60} poor regions. These clusters are not observed in P1C01 and P1.5C015, this is seen from the linecuts in Figure 5.21. The diffusion coefficient of smaller aggregates is higher than that of larger aggregates and so it is very likely that whilst the smaller aggregates on P1C01 are able to diffuse through the polymer when annealed, the larger aggregates will be unable to diffuse, hence some of these aggregates are still present in the annealed film.

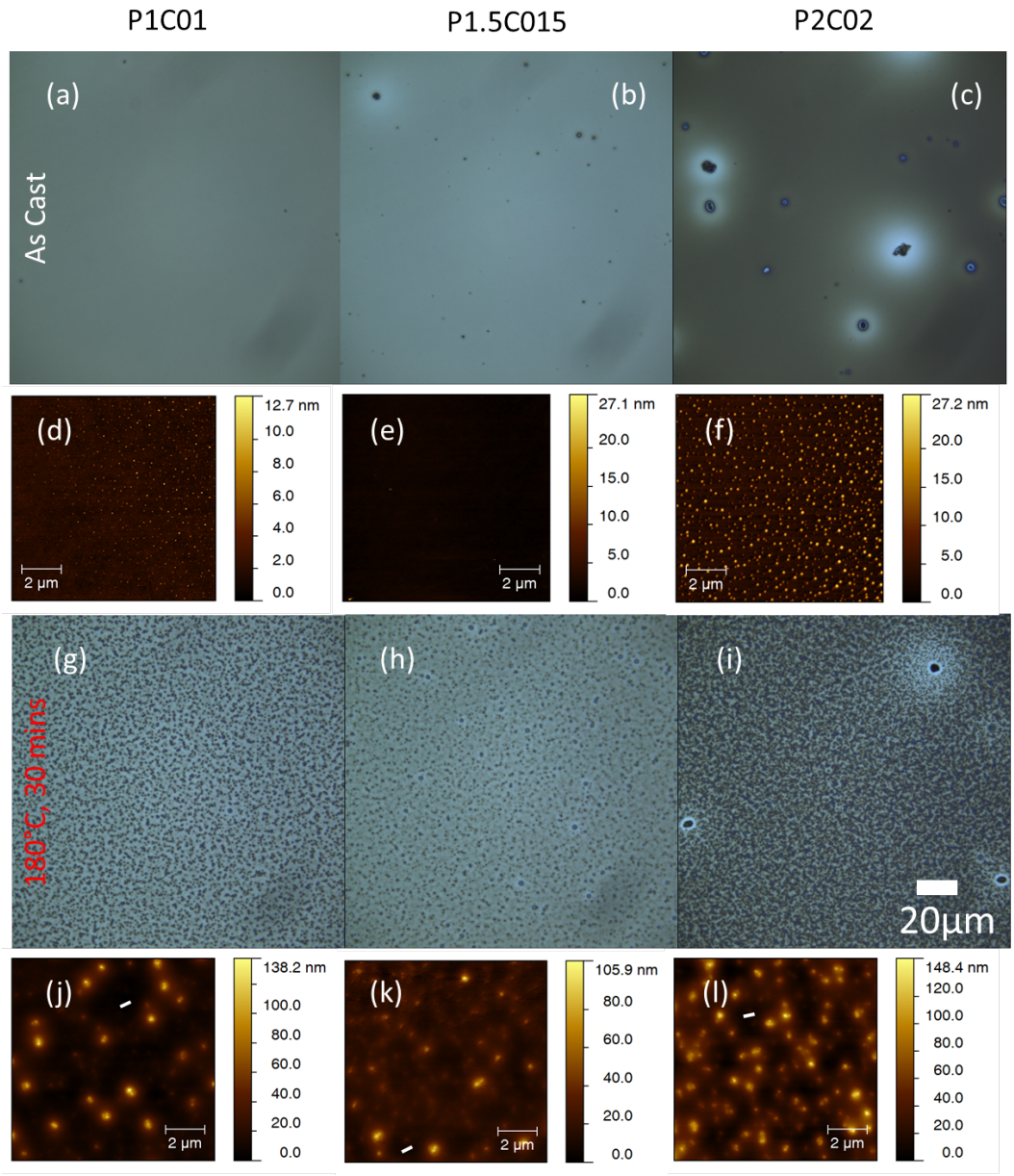


Figure 5.20: (a-c, g-i) OM and (d-f, j-l) AFM showing 9 wt% C_{60} at day 5 solution age 60 nm thin films in the (a-f) as cast state and (g-l) annealed at 180 °C for 30 minutes. White lines in j-l are line cuts used in Figure 5.21.

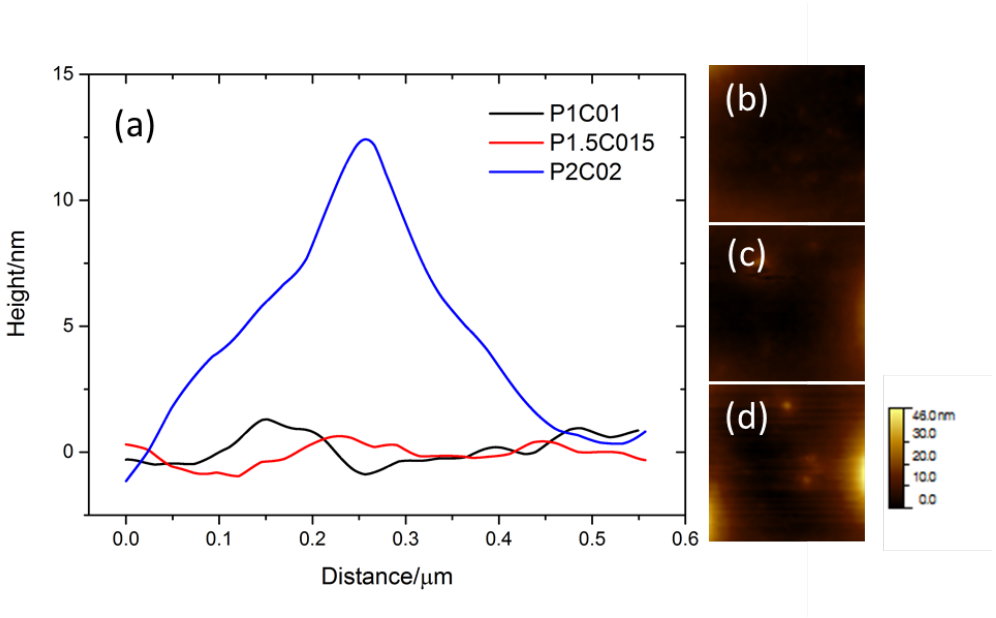


Figure 5.21: (a) Line cuts from AFM (Figures 5.20j-l) of 9 wt% C_{60} at day 5 solution age 60 nm thin films annealed at 180 °C for 30 minutes. (b-d) Cropped AFM images from Figures 5.20j-l zooming in on regions where line cuts were taken from. (b) P1C01, (c) P1.5C013 (d) P2C02. Small C_{60} clusters can be seen in the film prepared from P2C02 compared to P1C01 and P1.5C015.

A comparison at the two ends of the time study (day 0 and 5) shows a distinct morphological evolution over solution age on the nanoscale (as well as that previously discussed on the micro-scale) of the annealed films. As could be expected from the lack of evolution of films cast from P1C01 there is no discernible difference in the nanoscale. There are significantly more clusters seen with AFM in both P1.5C015 and P2C02 in the day 5 films compared to day 0.

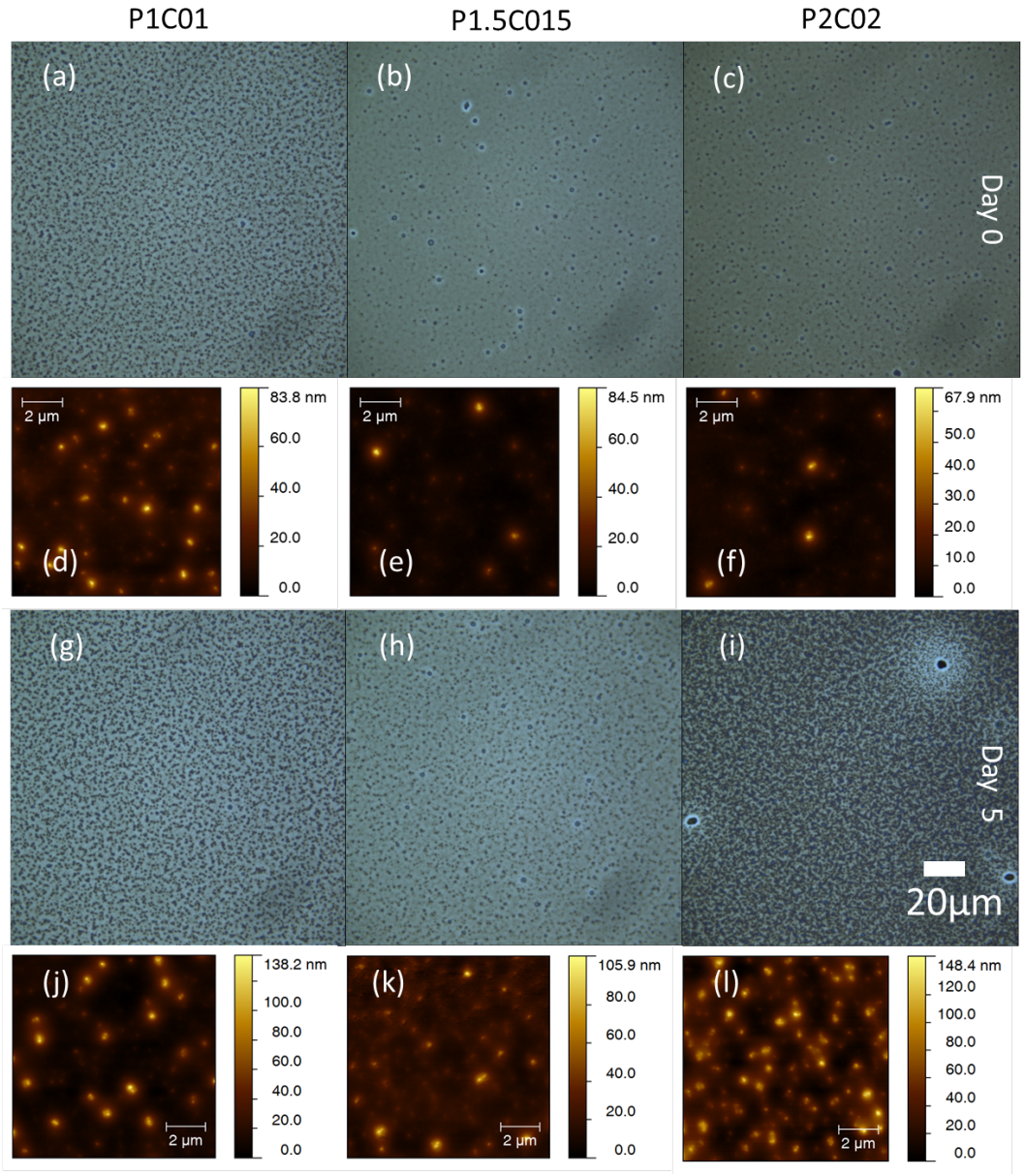


Figure 5.22: (a-c, g-i) Optical and (d-f, j-l) atomic force microscopy of 60 nm 9 wt% C_{60} films annealed at 180 °C for 30 minutes, comparing films cast from solutions at (a-f) day 0 and (g-l) day 5.

An ageing study was also carried out on the 5 wt% C_{60} films (using P2.3C12 and P4C021). Differences in film morphology can be observed in the films fabricated from P4C021 in the as cast state (Figure 5.23) with more clusters observed via AFM than for the precipitated (P4C021) solution which was aged for 5 days. The same films were annealed and are shown in Figure 5.24. There are slight changes in the morphology of films from P4C021 with solution age, with slightly larger and fewer clusters present. A comparison of the films from P2.3C012 and P4C021, gives

similar differences at day 5 as there were at day 0.

The volume fraction (V_f) of C_{60} within the film should ideally be identical in the film to that in solution. It is possible that due to the mechanism of spin coating more of one component could be lost compared to the other, i.e. more C_{60} could be removed in the initial step of spin coating compared to PS meaning the C_{60} loading in the thin film is less than in solution. Using a calculation described in Ref. 154, $V_f = y \times A_f x$, where y is a constant and x is the height ratio between the average cluster height and the as cast film. The value for y arises from the shape of the structures within the film, for a cone, $y = \frac{1}{3}$ and for an hemioblate $y = \frac{2}{3}$. For the films shown in Figure 5.22 the films prepared from solution P1C01 give $V_f \approx 7\%$, the expected V_f for a 9 wt% C_{60} film is 5.7%, P1.5C015 and P2C02 both gave lower V_f at 4%. The films fabricated from 5 wt% C_{60} solutions shown in Figure 5.23 the V_f values were 2.5% for P2.3C012 and 2.8% for P4C021 which is close to the expected V_f of 3%. Thus, for the majority of films, the mass of C_{60} in thin films is conserved, whereas for the 9 wt% C_{60} films fabricated from P1.5C015 and P2C02 there must be significant aggregation of C_{60} within solution resulting in a lower C_{60} mass in the films of 6-7 wt%. This indicates a decrease of ~3 wt% of C_{60} in the thin film and thus there is a decrease of ~0.006 wt% C_{60} in solution.

Solution Name	C_{60} wt%	Expected V_f	Actual V_f
P1C01	9	5.7	7
P1.5C015	9	5.7	4
P2C02	9	5.7	4
P2.3C012	5	3.1	2.5
P4C021	5	3.1	2.8

Table 5.3: Expected and actual volume fractions (V_f) for the films studied.

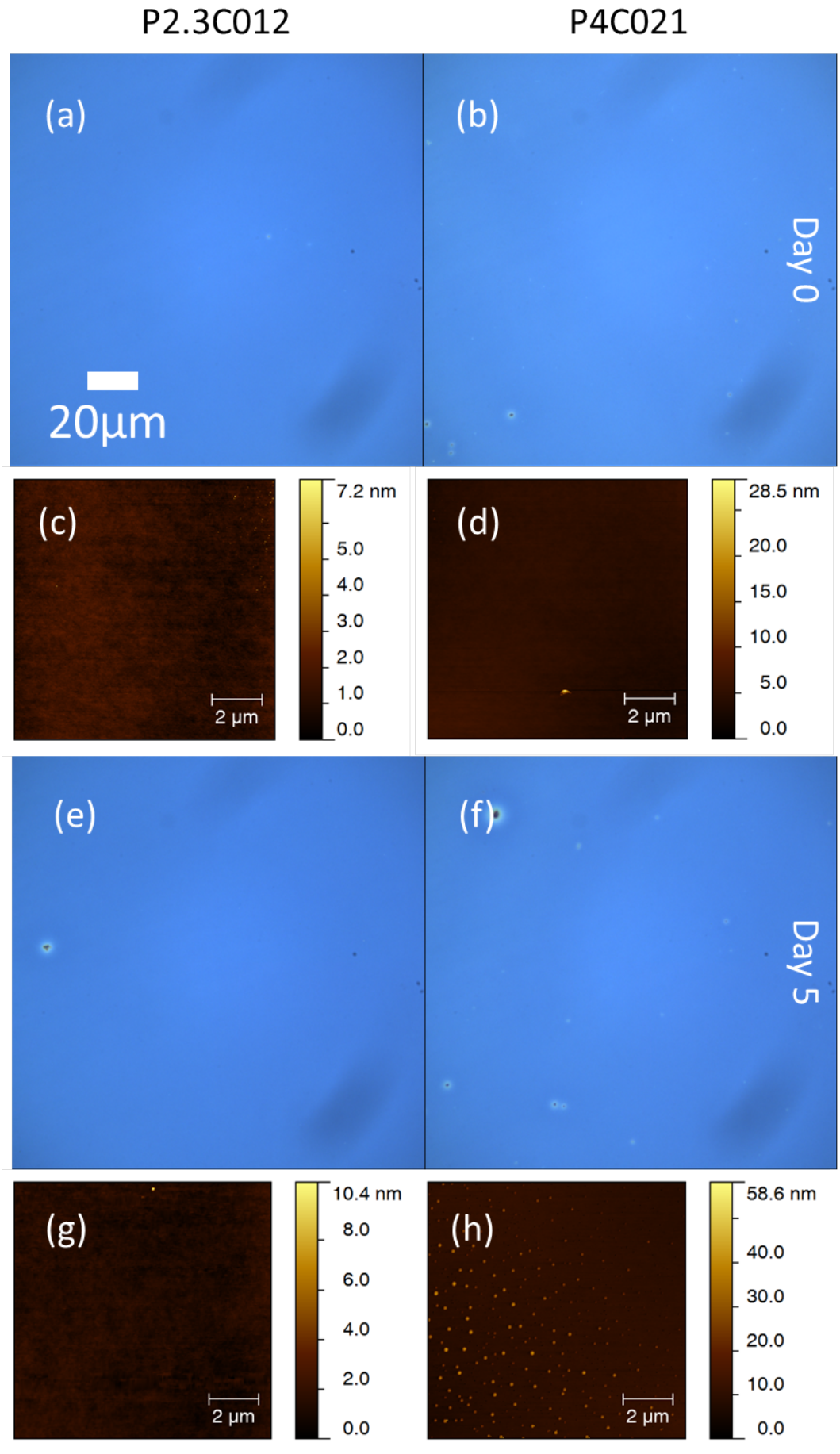


Figure 5.23: (a-b, e-f) Optical and (c-d, g,h) atomic force microscopy of as cast 5 wt% C_{60} 130 nm thin films at (a-d) day 0 and (e-h) day 5 of solution age.

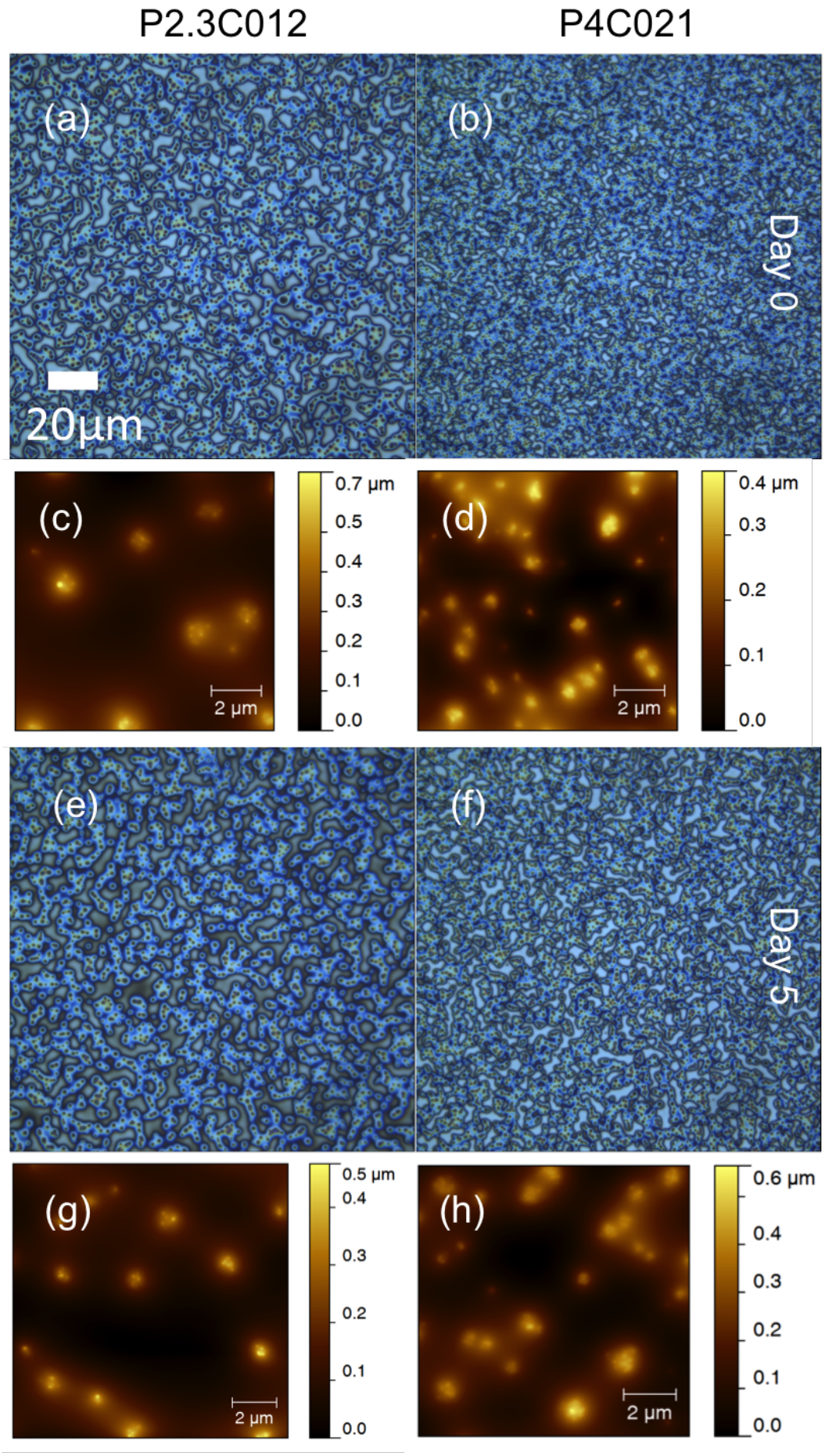


Figure 5.24: (a-b, e-f) Optical and (c-d, g,h) atomic force microscopy of 5 wt% C_{60} 130 nm thin films annealed at 180 °C for 30 minutes at (a-d) day 0 and (e-h) day 5 of solution age.

5.2.3 Mechanism

Previous work on PS/C_{60} thin films has outlined a mechanism by which a spinodal-like percolation occurs in 5 wt% C_{60} films [9]. Four stages were identified in this process: (i) nucleation, (ii) percolation, (iii) saturation and (iv) coarsening. The morphologies observed here are consistent with that mechanism for the 5 wt% C_{60} film fabricated from the homogenous solution (P2.3C012). However, given the change in morphology for those films fabricated from P4C021 with solution age, an alternate mechanism is proposed to account for the different morphologies from what should be identical films.

From the solution state, it is known that C_{60} clusters form via the addition of PS to a C_{60}/toluene solution to form a precipitated solution with R_C ranging from 50-200 nm and if a precipitated solution is left over time, clusters will aggregate to form larger aggregates with R_C on the order of 10s μm. It is worth noting that the clusters which form in solution (50-200 nm) are significantly larger than the film thickness (60 and 130 nm). Therefore, the aggregates which can be seen on the surface of films cast from a precipitated solution are those which are seen in solution via SLS. In addition, comparing P2C02 and P4C021, the C_{60} clusters in P4C021 are expected to be larger than in P2C02 as there is more PS present with the same C_{60} concentration. However, a second consideration needs to be taken into account. The viscosity of the PS/toluene solutions which the C_{60} clusters are dispersed in. As an approximation, the viscosity of the solution would double with twice the concentration of PS, therefore the clusters would diffuse slower within P4C021 than in P2C02. And so, after the initial solution preparation step, P4C021 would have a greater R_C, over time this would be overtaken by the clusters within P2C02 as they are in a less viscous medium and therefore able to aggregate faster.

Selective dissolution experiments were carried out for the day 0, 5 wt%, C_{60} films (P2.3C012 and P4C021) annealed at 180 °C for 30 minutes. The films, supported by a silicon wafer, were placed into THF for a few minutes, removed and gently dried with 1 μm filtered N_2 gas. THF is a good solvent for PS and a non-solvent for C_{60}[198]. As is seen in Figure 5.25 the clusters observed prior to dissolution in a and b are seen after dissolution in e and f. This indicates the clusters are anchored to the silicon substrate surface and that the C_{60} rich regions in both films have a layer of PS on top of a 'pile' of C_{60}. Comparing Figure 5.25g and h with i and j, the distribution of C_{60} appears similar before and after dissolution, indicating that there have been no changes to the C_{60} in the dissolution process. The 10 μm line cuts in Figure 5.25e and f are shown in Figure 5.26, this provides an important insight into the impact of C_{60} clusters from solution to thin film morphology. Away from the C_{60} rich regions, P2.3C012 is relatively flat with some peaks observed on the order of 10 nm, in stark contrast, P4C021 shows clusters which are 40-100 nm in height and width. The 5 μm line cuts compare the relative thickness' of P2.3C012 and P4C021, to demonstrate that the thickness of the film is relatively unchanged upon annealing, with the distance between the top of C_{60} in selectively dissolved films and those prior to dissolution is approximately equal to the thickness measured via interferometry. Note that identical areas on the same films are not used and instead comparable regions are selected.

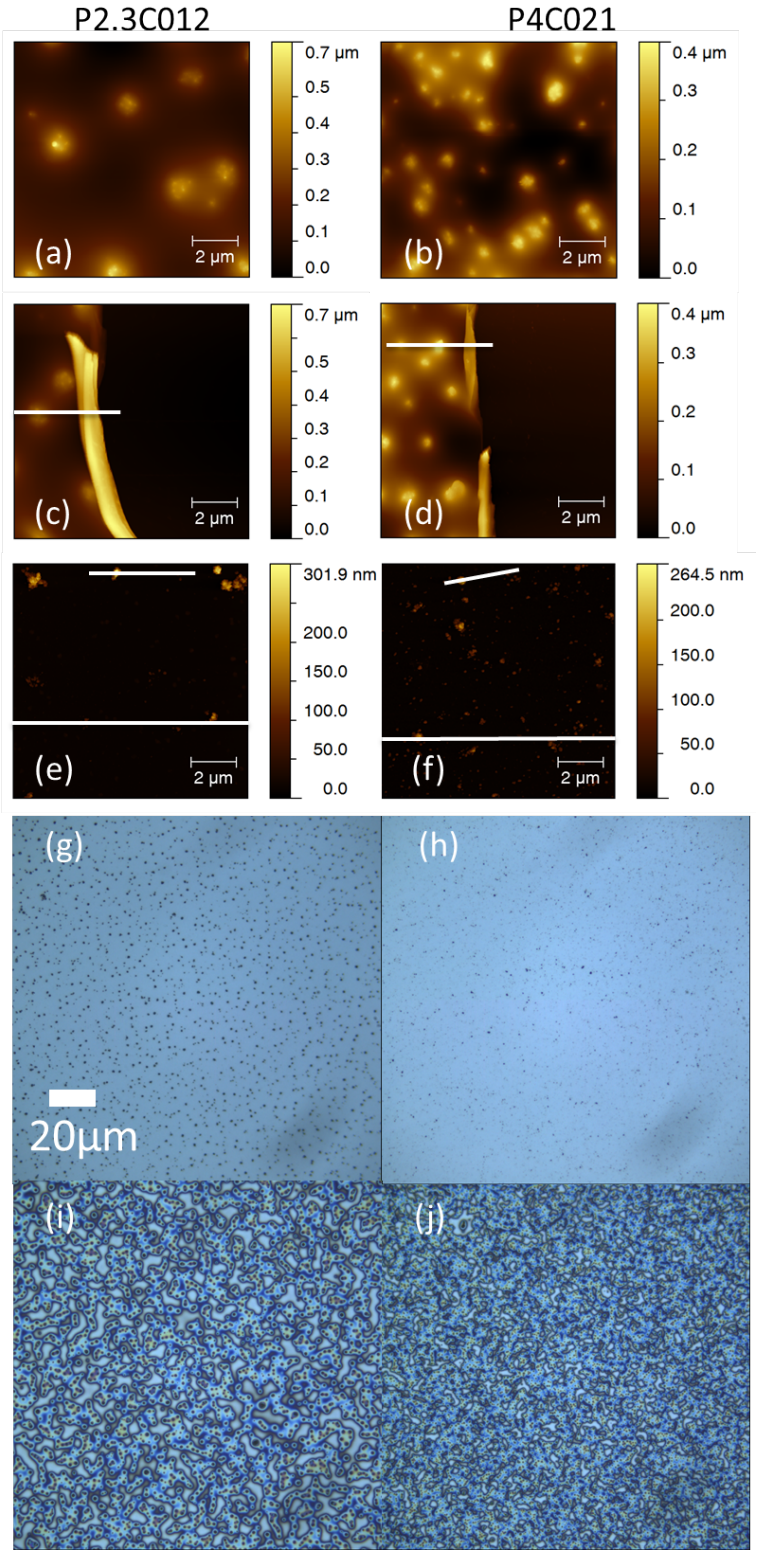


Figure 5.25: (a-f) AFM images of (a-b) 5 wt% C_{60} films annealed at 180 °C for 30 minutes and (c-d) a scratch in the film surface for thickness measurement. (e-h) THF dissolution experiment to show the micron-sized clusters observed via OM consist of 200 nm clusters. (i-j) OM images prior to dissolution for comparison. White lines in c-f are line cuts for height profiles in Figure 5.26.

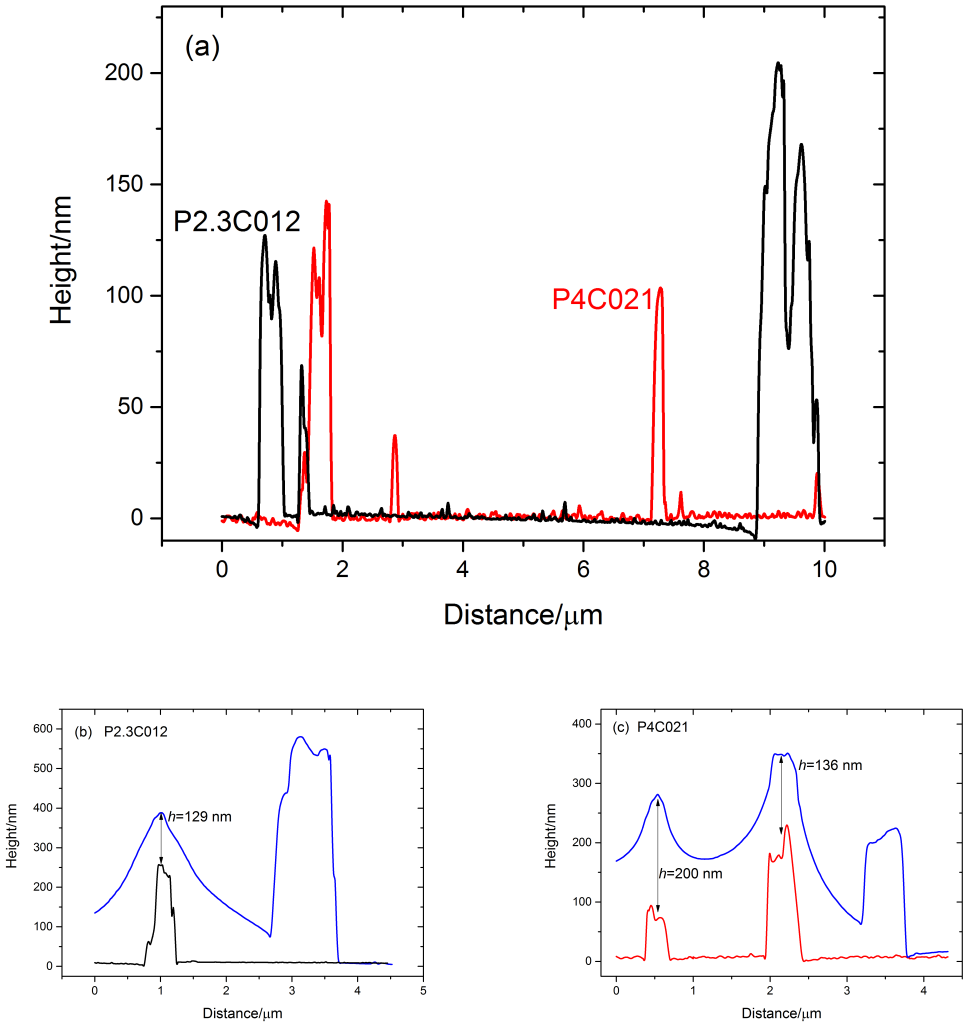


Figure 5.26: Line cuts from AFM (a) of Figures 5.25e-f of 5 wt% C_{60} after the PS was washed off with THF. (b-c) 5 μm line cuts from Figures 5.25c-f to demonstrate there is no change PS thickness after annealing.

The previous mechanism [9] included an initial nucleation step, however, in the films which contain C_{60} clusters from the solution it is very likely that the clusters from solution act as nucleation sites within the film. This of course would impact on the growth of the clusters within the film. First, the 9 wt% films are considered (P1C01, P1.5C015 and P2C02). After annealing, there are fewer and larger clusters present in films prepared from P1.5C015 and P2C02 compared to P1C01. Over time (with solution age) there are then smaller and more clusters (this is seen most clearly with P1.5C015). It appears as though the clusters present in the solution and subsequently in the film are small enough to be able to diffuse in the PS matrix and form nucleation sites when a number of clusters meet. Conversely, in the day 5

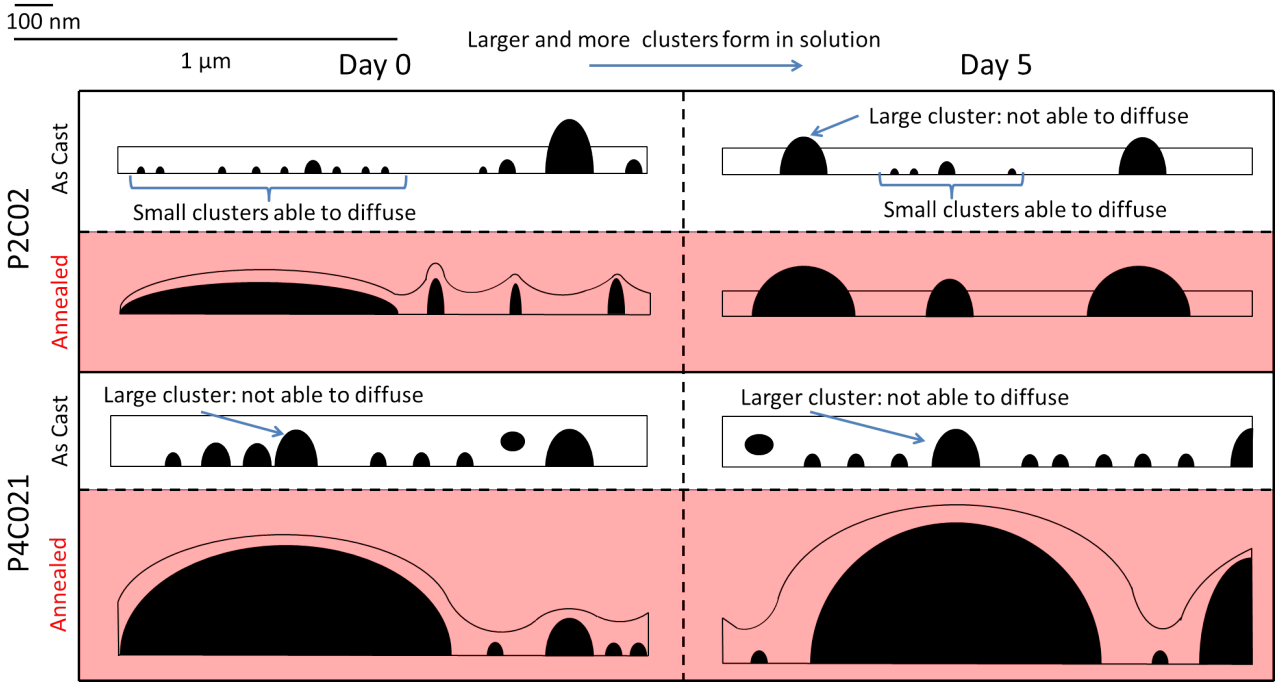
films, the clusters in solution are much larger (some on the micron scale) and so are ready to be used as nucleation sites, however due to there being more nucleation sites, the C_{60} rich regions are smaller than in the day 0 film. The mechanism proposed here would also indicate that the morphology formed in P4C012 is in effect a random process depending on the casting technique (in this case spin coating) and the morphology is reliant on where the C_{60} clusters land on the substrate. This is shown by the radial profiles of the two 5 wt% films (Figure 5.17) where a q^* peak is seen for the sample prepared from a homogenous solution and not seen for the samples prepared from P4C012.

As described above, the solution P4C021 will have larger clusters than P2C02, thus as these are transferred to the film. These clusters appear to be too large to diffuse through the PS matrix and so, as with P2C02 at day 5, act as nucleation sites for molecularly dispersed C_{60}, or smaller clusters to grow on to. These clusters are observed clearly in Figure 5.26 and so, as a lower limit, clusters of ~100 nm will act as the nucleation sites as they diffuse significantly slower through the film than molecular C_{60}. Comparing P4C021 at day 0 to the day 5 film, the C_{60} clusters in solution would have grown larger, and even less able to diffuse within matrix. Thus there are fewer and larger clusters observed within the day 5 film.

This mechanism accounts for the difference in the trends shown between the two sets of thin films. The difference being P2C02 from day 0 to day 5 has more and smaller C_{60} rich regions in the film whereas P4C021 showed fewer and larger C_{60} rich regions at day 5 compared to day 0. This is due to the factors outlined above: (i) increased viscosity of PS/toluene in P4C021 modifying the aggregation rate of the C_{60} clusters in solution and (ii) competition between diffusion and nucleation. For P2C02 the ~100 nm C_{60} clusters over time have formed clusters which are 10s μm which has been possible due to the lower solution viscosity. Whereas with P4C021 the clusters in both cases (day 0 and day 5) are large enough to be unable to diffuse within the PS matrix.

These findings are summaried in Scheme 5.1. The morphology of thin films prepared from precipitated solutions is highly dependent on the competition between diffusion of smaller clusters with the nucleation sites provided by the larger clusters (~100 nm). If a solution contains clusters which are larger than 100 nm, then nucleation sites will form for individual fullerenes to be attracted to. Conversely if a solution contains clusters, but they are still relatively small they are able to diffuse within the film and form nucleation sites themselves. It is also relevant to note that the micron sized clusters within the annealed films have a 'raspberry' structure, similar to that observed in previous work [8, 154].

To confirm this mechanism as that responsible for the differences in morphology between homogenous and precipitated films, 5 wt% C_{60} films prepared at day 0 were annealed at 140 °C for 2.5 hours. It is expected that the film prepared from P4C021 will have significantly more nucleation sites than one prepared from P2.3C012 as the clusters from solution provide nucleation sites for the molecularly dispersed C_{60} to grow on to. This is seen experimentally as there are more clusters in Figure 5.27d than c, confirming that the clusters formed in solution



Scheme 5.1: Schematic depicting presence of fullerene clusters within a PS thin film, showing differences within cluster formation depending on the casting solution. The clusters with a width of ~1 μm have previously been shown to have a 'raspberry' structure (i.e. a compact cluster composed of ~100 nm clusters) [8] but this is not depicted in the schematic for simplicity.

behave as nucleation sites within the PS matrix.

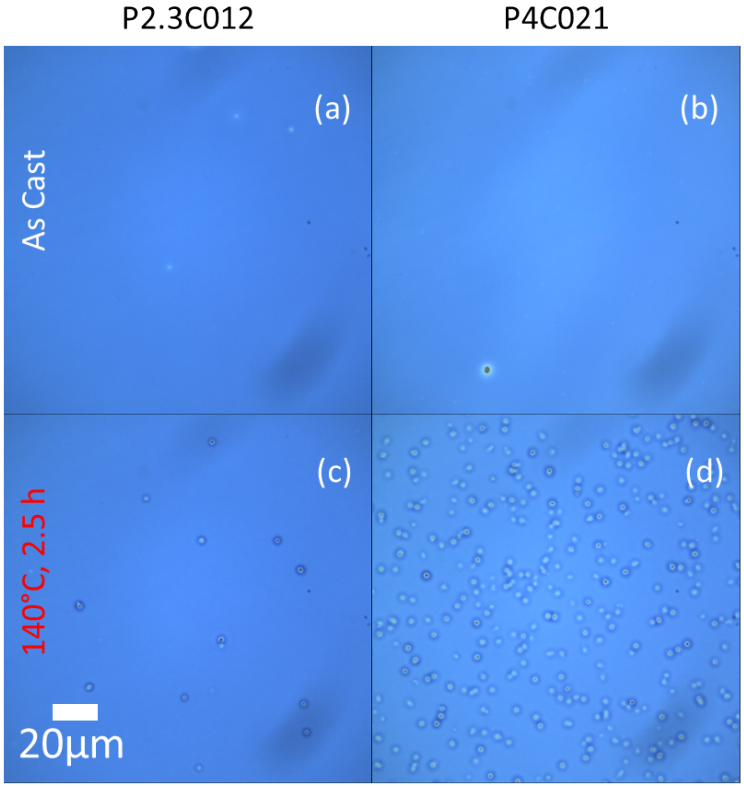


Figure 5.27: Optical microscopy of 130 nm films (a-b) as cast and (c-d) annealed at 140 °C for 2.5 hours. There is a clear difference between the two samples, with the precipitated solution giving a morphology with more clusters.

5.3 Bulk Samples

A cause of alternate morphologies arising from thin films could be due to the fast drying times of the processing technique used (spin coating), therefore, using the same solutions, bulk samples were fabricated via a solvent drying method (drop casting). The samples were prepared by taking a 1 cm^2 <100> Si substrate and dropping 100 μL of the required solution onto the substrate. The samples were then left in the dark at either 60 °C for 30 mins or 25 °C for 24-48 hours to evaporate the solvent, toluene. Figure 5.28a-d show the as cast state of the two samples prepared at 60 °C. Comparing the number density of the as cast films in Figure 5.29, it is clear that there are a significant number of larger clusters in the sample prepared from P4C021. Annealing this film led to an increase in the number of large C_{60} aggregates on the surface of the film. The morphology of the annealed sample prepared from P2.3C012 is extremely interesting (Figure 5.28e), the structure of the clusters is completely different to the compact structures seen in Figure 5.28f. Similar open stringy structures, as in Figure 5.28e have been observed for systems which are deep into a phase separated region [202], which is the region in which the

PS/C_{60} samples are likely to be. Due to the differences in drying time of spin coating to drop casting, the open stringy structures clearly need time to develop and the fast quench of spin coating does not allow for these to form.

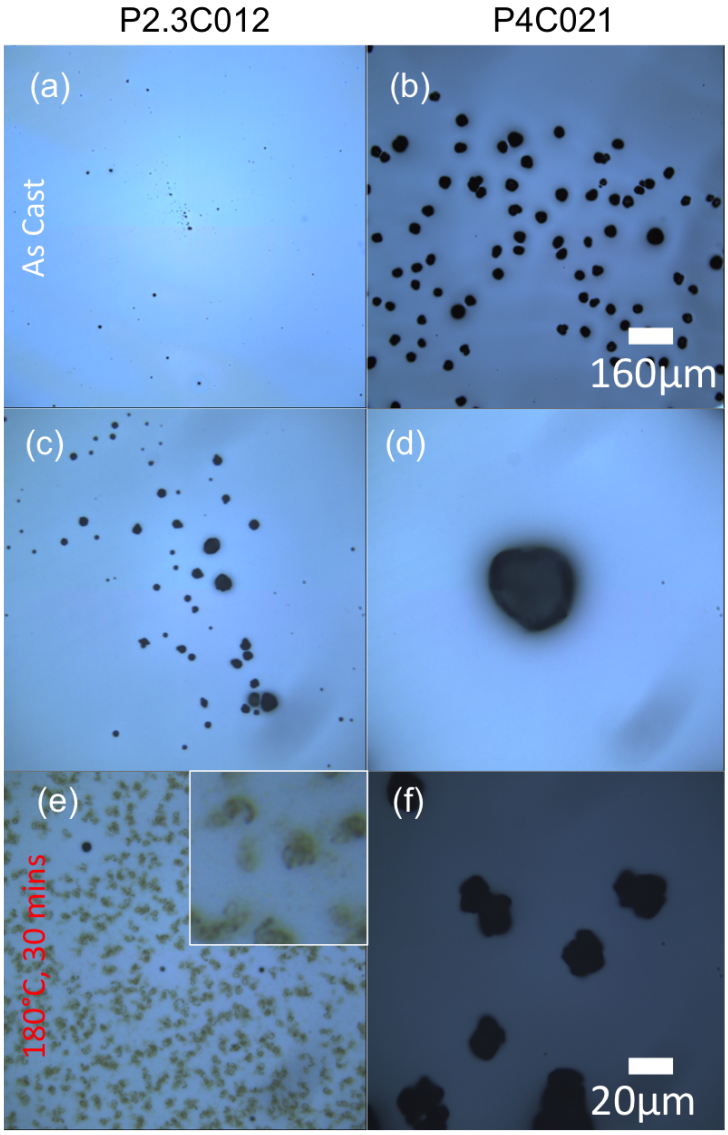


Figure 5.28: Optical microscopy of drop cast films on silicon substrates (a-d) as cast and (e-f) annealed at 180 °C for 30 mins. There is a clear difference between the two samples, with the sample prepared from the homogenous solution giving a vastly different morphology than that from the precipitated solution. The image width of the inset in (e) is 10 μm.

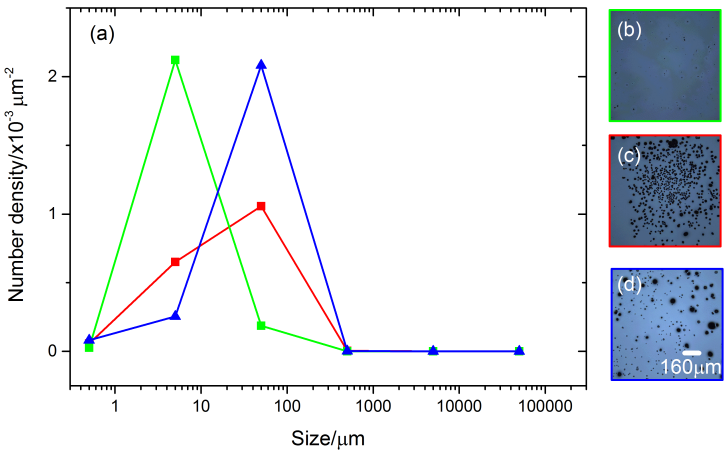


Figure 5.29: (a) Number density of 4-7 representative images of the as cast drop cast samples shown in Figure 5.28a-d and f. Due to the morphology shown in Figure 5.28e consistent, representative image analysis proved difficult. Typical images are shown in (b-d) of (b) as cast from P2.3C012, (c) as cast from P4C021 and (d) annealed from P4C021.

There is a possibility that drying the samples at a slightly elevated temperature induced C_{60} nucleation sites which could account for the differences in morphology. Samples prepared at 25 °C took significantly longer to dry showed a similar morphology to those prepared at 60 °C in the as cast and annealed state. This highlights an aspect of the polymer nanocomposite melt literature which has been seemingly untouched and could explain much of the disparity in results obtained with respect to miscibility and polymer chain dimensions.

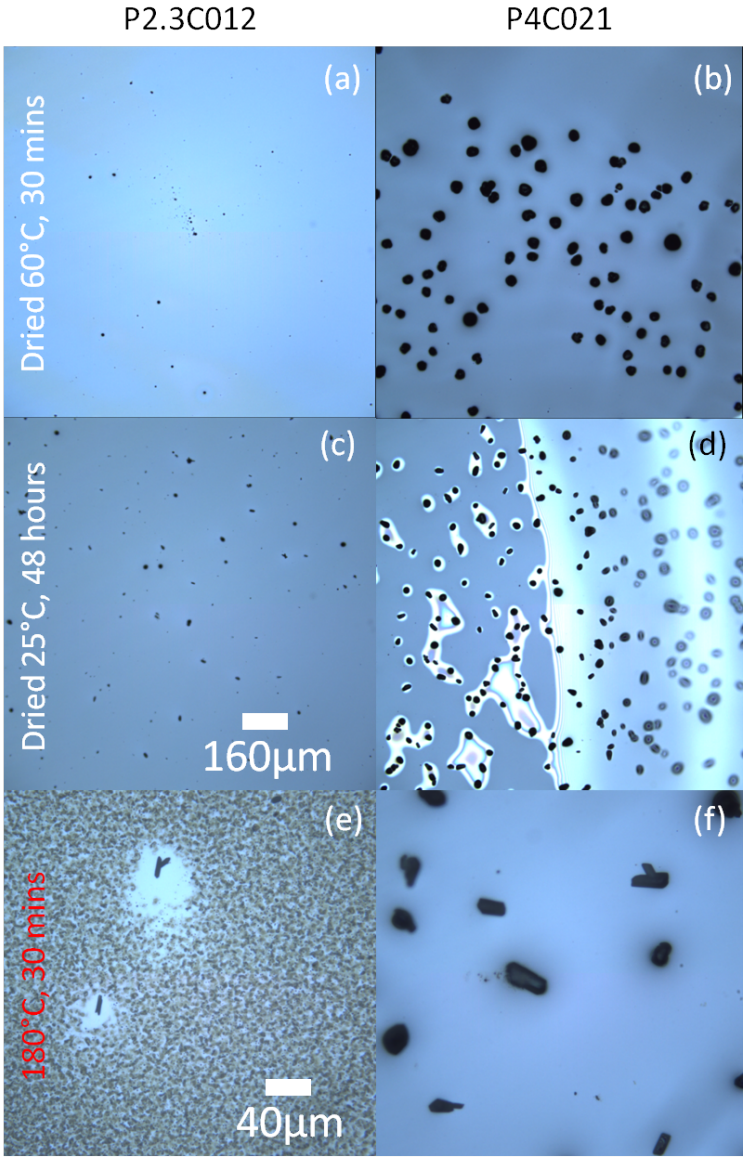


Figure 5.30: Optical microscopy of drop cast films on silicon substrates (a-b) cast at 60 °C, dried within 30 minutes, (c-d) cast at 25 °C, dried over 24-48 hours and (e-f) samples shown in (c-d) annealed at 180 °C for 30 mins. There is a clear difference between the two samples, with the sample prepared from the homogenous solution (a, c, e) giving a vastly different morphology than that from the precipitated solution (b, d, f). The scale bar in (c) applies to (a-d) and the scale bar in (e) applies to (e-f).

5.4 Other systems studied

To expand this work towards organic solar cells (OSCs) and a system capable of higher fullerene loadings, two systems containing PCBM were studied. The systems studied were prepared with chlorobenzene (CB) and toluene. CB is a common solvent for use with PCBM in OSC device

fabrication. For the two systems considered, the miscibility limit reported in literature was not found to be consistent with the results presented here. The reported miscibility limit of PCBM in toluene ($c_{PCBM/tol}$) is 1.76 wt% and for PCBM in CB ($c_{PCBM/CB}$) is 5 wt% [203]. The method by which these values are obtained involves preparing a concentrated solution, centrifugation, dilution and then UV-Vis spectroscopy. Using the same method as the PS/C_{60}/toluene solutions in Section 5.1.1, the miscibility limit $c_{PCBM/tol}$ is 0.9 wt% and $c_{PCBM/CB}$ is 2.6 wt%. Using the concepts learnt from PS/C_{60}/toluene, the highest M_w of 775k PS was selected as this appeared to be the most effective at precipitating fullerene aggregates.

Static light scattering was attempted for PCBM/CB (○) and PS/PCBM/chlorobenzene solutions (○), however the data was very inconclusive and is shown in Fig 5.31. There is what appears to be a peak developing at the high-q limit of SLS. Small angle X-ray scattering (I22, Diamond) was used as a technique to attempt to capture this q-range and retain the scattering from both polymer and fullerene however this was unsuccessful as the low-q limit of SAXS did not overlap with SLS. Therefore samples were visually inspected for PCBM precipitation. This resulted in an underestimate of PCBM miscibility as nanoscopic aggregates which may be present will not be detected with this method.

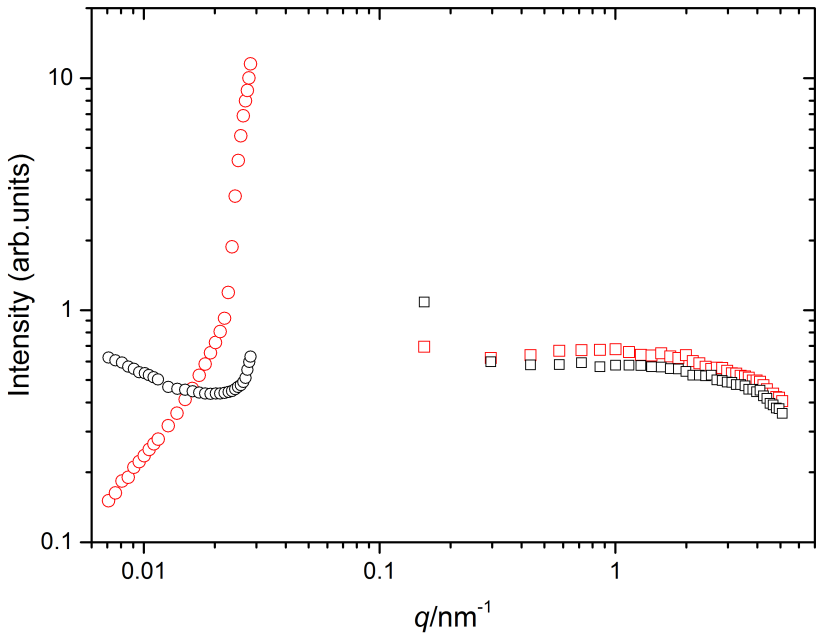


Figure 5.31: Scattering data for 0.63 wt% PCBM/CB and 2 wt% 775k PS/0.56 wt% PCBM/CB using (○) SLS and (□) SAXS, which in the configuration used did not have an overlap with SLS.

From a mixture of PCBM/775k PS/toluene, PCBM aggregation was observed below its mis-

cibility limit at 0.9 wt%. The miscibility of PCBM in toluene is comparable to that of C_{60} in toluene, and thus, it is likely the mechanism behind the aggregation of this system in the protein limit is the same as that with PS/C_{60}/toluene mixtures. The aggregated (red) and homogenous (green) regimes are highlighted in Figure 5.32.

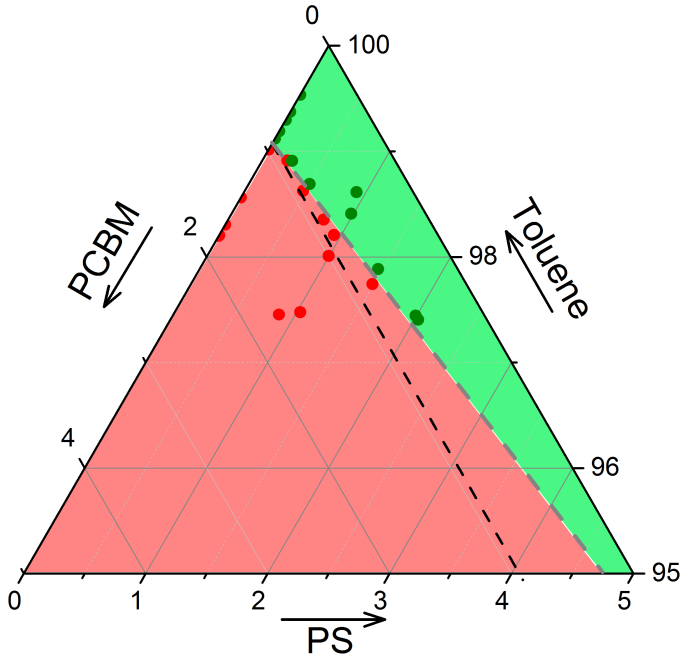


Figure 5.32: Ternary diagram of 775k PS/PCBM/Tol. Homogenous (•) and precipitated (•) are shown alongside the miscibility limit of PCBM in toluene ($c_{PCBM/Tol}$) at 0.9 wt% (– – –). (– – –) indicates miscibility of PCBM in 775k PS/toluene. Exact concentrations of solutions used are shown in Table 5.4.

wt% PS	wt% PCBM	State
0.00	0.47	S
0.00	0.63	S
0.00	0.70	S
0.00	0.81	S
0.00	0.88	S
0.00	0.99	P
0.00	1.44	P
0.00	1.70	P
0.00	1.79	P
0.00	1.80	P
0.21	0.88	P
0.25	0.84	S
0.48	0.90	P
0.50	0.81	S
0.78	0.86	P
0.87	1.68	P
0.92	0.46	S
0.98	0.61	S
0.94	0.85	P
1.00	0.99	P
1.03	1.50	P
1.46	0.65	S
1.49	0.77	P
1.99	0.56	S
2.03	0.56	S

Table 5.4: Summary of 775k PS/PCBM/toluene mixtures investigated, all concentrations (c_i) in the system are reported by the ratio of the mass of component i to the total mass of the solution (mass fraction of total ternary mass), and and whether the system appeared stable (S) or aggregated (A) after two days of stirring.

Converse to 775k PS/PCBM/toluene there appears to be no aggregation of PCBM in 775k PS/PCBM/CB below $c_{PCBM/CB}$, as shown in Figure 5.33. This is unexpected from polymer/colloid theory in the protein-limit.

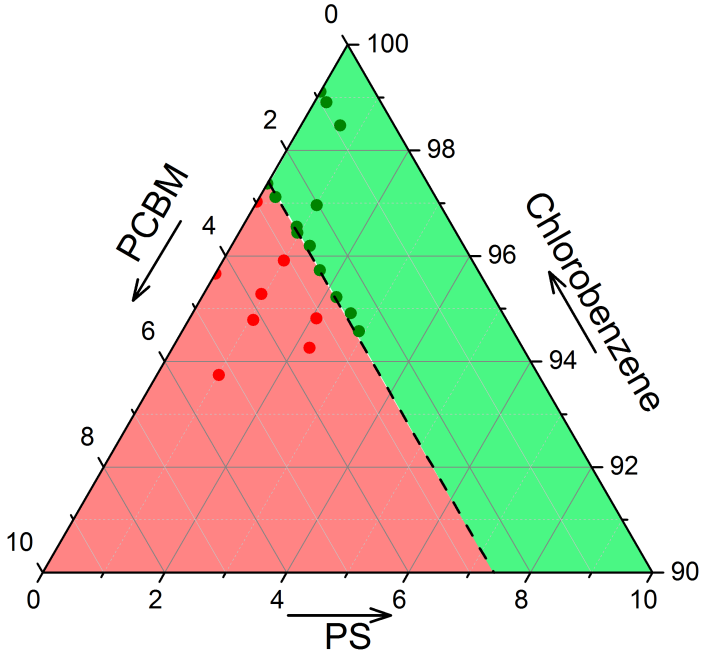


Figure 5.33: Ternary diagram of 775k PS/PCBM/CB. Homogenous (•) and precipitated (•) are shown alongside the miscibility limit of PCBM in CB ($c_{PCBM/CB}$) of 2.6 wt% (– – –). Exact concentrations of solutions used are shown in Table refsec:App3 .

wt% PS	wt% PCBM	State
0.00	0.89	S
0.00	2.63	S
0.00	2.98	P
0.00	4.34	P
0.20	0.89	S
0.26	2.62	S
0.64	0.89	S
0.89	2.56	S
0.96	2.61	S
1.00	3.09	P
0.94	3.78	P
1.02	2.03	S
1.06	4.16	P
1.02	5.24	P
1.29	2.52	S
1.68	2.59	S
2.08	3.11	P
2.21	2.58	S

2.25	3.49	P
2.60	2.49	S
2.90	2.53	S

Table 5.5: Summary of 775k PS/PCBM/chlorobenzene mixtures investigated, all concentrations (c_i) in the system are reported by the ratio of the mass of component i to the total mass of the solution (mass fraction of total ternary mass), and whether the system appeared stable (S) or aggregated (A) after two days of stirring.

To consolidate the findings of fullerene aggregation in PS/C_{60}/toluene and PS/PCBM/toluene, along with no observable aggregation in PS/PCBM/CB, Hansen Solubility Parameters (HSPs) are considered. These parameters are well-known for commonly used polymers, such as polystyrene, but unfortunately very little work has been done for PCBM in various solvents. The work of Machui et al. [203] has given different miscibility limits than those found here, and so it is highly likely that if the miscibility limits reported are inaccurate, then the HSPs reported are also inaccurate, nevertheless the trend in the parameters is correct and they serve well as a guide for the following discussion. The HSPs for the solutes and solvents used are tabulated in Table 5.6. The relative energy difference (RED) is calculated using Equation 1.10 and is also tabulated. As a reminder, if RED>1 then interactions are unfavourable, for RED=1 there there is partial dissolution and if RED<1 then the solute will dissolve.

	HSP/MPa$^{1/2}$				RED	
Component	δ_D	δ_P	δ_H	Ro/MPa$^{1/2}$	Toluene	CB
Polystyrene	21.28	5.75	4.30	12.7	0.65	0.42
C_{60}	19.7	2.9	2.7	3.9	0.97	0.54
PCBM	19.5	3.4	7.2	6.7	<0.97	<0.54
	(17.9-21)	(0.4-7.4)	(6-8.4)	(4.4-8.9)	(0.49-2.41)	(0.73-1.85)
Toluene	18	1.4	2.0	-	-	-
Chlorobenzene	19	4.3	2.0	-	-	-

Table 5.6: Summary of Hansen Solubility Parameters (HSPs) for components used, interaction radius (Ro) given for solutes and relative energy difference (RED) between solute/solvent pairs. A range of values is given for PCBM, with the centre of the range given for the HSPs and Ro, as there is no definite value in the literature [203, 204]. Shaded values are discussed within the text.

From the RED, it is immediately clear that polystyrene is more soluble in both solvents than either C_{60} or PCBM. If the HSPs given in the literature were used to calculate the RED, it would appear as though C_{60} is more soluble in CB than PCBM, however this is not seen experimentally in their relative miscibility limits of 0.63 wt% for C_{60}/CB and 2.6 wt% for PCBM/CB. Thus it is likely that the RED for PCBM/CB is <0.54 (as indicated in Table 5.6). This is not seen in the RED calculated from literature values which ranges from 0.73 to 1.85. The same

argument applies to PCBM/toluene and the RED is likely to be <0.97 (also indicated in Table 5.6). It is highly likely that the literature values for the HSPs are inaccurate due to the lack of research in this area. Broadly, it is expected that if there is a small difference between the RED, $\left|\mathrm{RED}_{\mathrm{fullerene/solvent}} - \mathrm{RED}_{\mathrm{PS/solvent}}\right| \approx$ small ($\ll 1$), then there will be a miscible system and if the difference is large, $\left|\mathrm{RED}_{\mathrm{fullerene/solvent}} - \mathrm{RED}_{\mathrm{PS/solvent}}\right| \approx$ large ($\lesssim 1$), then there is solute immiscibility. A similar rationale has been provided for ternary polymer blends [205], in this case all binary blends were miscible, but there was a $\Delta\chi$ effect from asymmetric binary interactions which resulted in the ternary blends being immiscible.

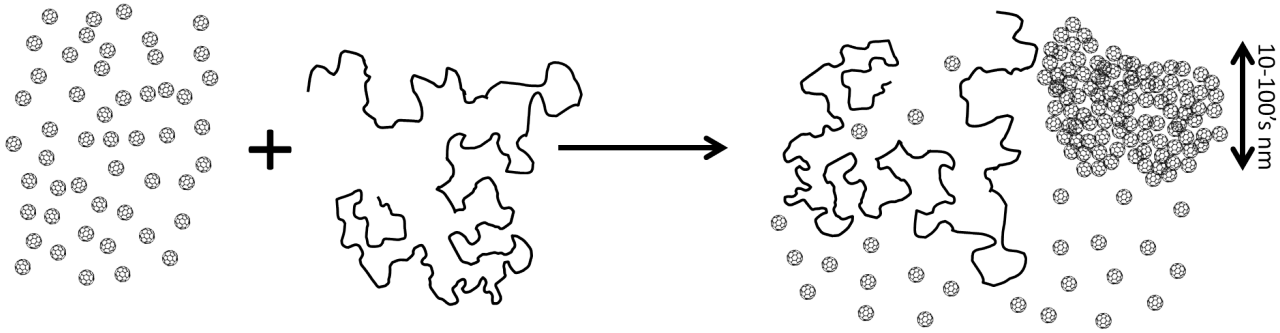
Therefore as a general concept, if aggregation of the fullerene is desired, then an asymmetric solvent can be chosen (i.e. one where there is a significant preference of polymer dissolution over fullerene), if aggregation is undesirable then a symmetric solvent can be employed. Comparing to the work of Jouault et al. [128] where the solvent used was found to alter the dispersion state of bulk poly(2-vinylpyridine)/silica nanocomposites, the nature of the silica/solvent interaction was not considered to be a significant contribution to the dispersion of silica NPs. These results demonstrate the importance of this factor. An aspect not explored in detail here is the miscibility of the two solutes within each other. e.g. PS/C_{60} (1-3 wt% [6, 7]) and PS/PCBM.

5.5 Conclusions

This chapter has clearly demonstrated that the addition of PS to C_{60}/toluene solutions decreases the miscibility of C_{60} in a mixture of C_{60}/PS/toluene, forming aggregates on the order of 100 nm, this is depicted in Scheme 5.2. The C_{60} clusters proceed to grow to the micron scale over the course of 24 hours and settle at the bottom of a stationary vessel when left undisturbed, highlighting the kinetically trapped nature of these systems. A simple model based on the space filled by PS chains at the overlap concentration, c^*, fits the experimental data very well after 48 h of dissolution, however it is reasonable to assume that there would be some finite miscibility of C_{60} in PS in the melt which is here estimated to be 0.12 - 0.15 wt% from samples prepared from the solution state.

The experiments have demonstrated that there is a limited thickness range in which certain concentration C_{60}/PS thin films can be fabricated, 2 wt% C_{60} loaded films can reach ≃400 nm whereas higher loadings of 15 wt% are limited to 100 nm films, if preparation from a stable casting solution is desired. This link has previously not been made, i.e. the stability and homogeneity of solution will have an effect on the thin film morphology and the correlation between the desired fullerene loading and maximum film thickness achievable. There is a thickness dependence to OSC device efficiency [2] and film homogeneity would also have an impact on the efficiency and consistency.

Within the thin films fabricated here, two size regimes are found in the as cast state: 10s nm clusters which are thought to arise from the rapid solvent evaporation in the spin casting stage as the solution must, at some point, pass into a phase separated region causing small clusters



Scheme 5.2: Schematic depicting presence of fullerene clusters (10-100's nm) alongside individual C_{60} molecules and undisturbed polystyrene chains. Fullerene agglomeration occurs for sufficiently large polymer concentration in solution, and increases for larger polymer M_w at constant mass fraction.

to form; 100-300 nm clusters are in the same size regime as seen via SLS and therefore it is not unreasonable to assume that these clusters observed in the film are in fact the same as those observed in solution. Upon annealing there are different morphologies obtained depending on the aggregation state of C_{60} within the casting solution. It is possible to conclude that the solution state does affect the as cast film formation. There are grave implications here for the processing of thin nanocomposite films. Given the restricted C_{60} concentration achievable in a PS/C_{60}/toluene mixture, there are limits to the film thickness and C_{60} loading in thin films.

A mechanism for the different morphology of films prepared from a precipitated state has been proposed. Solutions in the homogenous regime give reproducible films over a number of days. Upon annealing films fabricated from solutions which were in the precipitated state at 9 wt% C_{60} give more but fewer clusters, with the opposite trend taking place at 5 wt%. These opposing trends can be rationalised by the same mechanism which relates to the C_{60} clusters in solution. If the clusters in solution are above a critical size (~100 nm) they will not diffuse through the polymer matrix and instead behave as nucleation sites for molecularly dispersed C_{60} to be attracted towards. The change in film morphology with starting regime and over solution age provides an alternate handle on tuning thin film morphology compared to the commonly used film thickness, annealing temperature and solids ratio.

A distinct difference was observed in the morphologies of the as cast and annealed state of bulk samples prepared via drop casting from homogenous and precipitated solutions. Characteristically larger C_{60} clusters can be observed in the sample prepared form the precipitated solution compared to the homogenous solution and grown in number upon annealing.

In addition of mixtures of PS/C_{60}/toluene, PCBM was also studied in toluene and chlorobenzene. PCBM aggregation was observed in toluene and not in chlorobenzene. Given the relative miscibility of PCBM in both these solvents (a lower solubility in toluene than chlorobenzene), it is very likely that a leading effect as to whether aggregation will occur is the interactions between fullerene/solvent and polymer/fullerene. That is to say, if the fullerene is relatively immiscible

in the solvent, the addition of another component in which it has low miscibility, will lead to aggregation, e.g. in the cases of PS/C_{60}/toluene and PS/PCBM/toluene. However, in the situation where there is a higher miscibility threshold between fullerene and solvent, aggregation will not occur, and this is seen in PS/PCBM/chlorobenzene.

6 Pre-processed fullerene solutions impact on polymer composite thin films

In this chapter, the light exposure of C_{60} and PCBM in solution and resulting impact on thin film morphology is studied. Recent work [8, 9] on polymer:fullerene thin films has demonstrated the dependance of dewetting and 'spinodal clustering' phenomena on polymer molecular weight (M_w) and annealing temperature. Photo -polymerisation and -oxidation have been demonstrated for C_{60} fullerenes and their derivatives in the solid state [112]. The process has been extensively studied and is now relatively well understood [112–114]. Additionally, the exposure of polymer:fullerene thin films to a high intensity white light source have shown to improve OSC device stability [152].

Three outcomes have been reported for the light exposure of C_{60} solutions: (i) degradation of the fullerene cage (photolysis) induced by UV radiation in hexane, [77, 78] and confirmed by mass, UV, NMR and IR spectroscopies, eventually leading to the formation of a brown deposit which could not be re-dissolved. (ii) fullerene photo-polymerisation and (iii) photo-oxidation upon exposure to UV radiation has been investigated in a variety of chlorinated and saturated hydrocarbon solvents under inert atmosphere [79]. Under ambient conditions photo-oxidation was found to occur in saturated hydrocarbon solvents (including cyclohexane) while fullerene photo-polymerisation was reported to occur in chlorinated solvents. The formation of a brown deposit was then rationalised as fullerene "polymer".

Aggregation of fullerenes in benzene solution over a 40-90 day period was reported by Ying et al. [83, 84] using static and dynamic light scattering. An increase in scattering intensity (I_0) over time was found, which reversed upon shaking the solution by hand. The laser wavelength, 790 nm (and power of 30 mW), was chosen to be sufficiently away from the UV region in which degradation or polymerisation had been reported to occur; oxidation was, however, not discussed although it is expected to occur close to this wavelength range [206]. Solution storage between measurements was not discussed but the formation of an insoluble brown residue was also observed during their experiment. All solution concentrations in the above studies were below the reported solubility limits [198]. Mixed solvent systems containing toluene and acetonitrile [86] or water electrolyte solutions [88] have also been found to cause C_{60} cluster formation and crystallisation with various crystal symmetries [124].

Effect	Observation(s)	Solvent(s)	Experimental Techniques	Light Source	Reference(s)
Degradation	Brown deposit	Hexane	UV, NMR & IR	308 nm XeCl-excimer laser/UV lamp	77, 78
Polymerisation	Brown deposit	Chlorinated solvents	UV & IR	125 W Hg lamp	79
Oxidation	No brown deposit reported	Saturated hydrocarbons	UV & IR	125 W Hg lamp	79
Aggregation	Reversible aggregation, brown deposit	Benzene	DLS & SLS	790 nm	83, 84

Table 6.1: Summary of light induced degradation, polymerisation and oxidation of C_{60}/solvent systems as well as aggregation reported in literature [77–79, 83, 84].

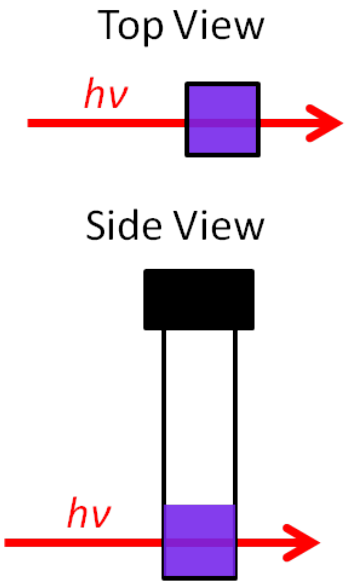
The mechanism for C_{60} oxidation has previously been described [206, 207]. Briefly, the incoming photon excites an electron in the C_{60} to the first excited state. Internal conversion and intersystem crossing form the triplet excited state. In the presence of oxygen, triplet energy transfer occurs and produces singlet oxygen. The simultaneous presence of triplet excited state C_{60} and singlet oxygen produces fullerene oxide.

The two extreme cluster-cluster aggregation mechanisms were discussed in Section 1.7. Namely, reaction-limited cluster aggregation (RLCA) and diffusion-limited cluster aggregation (DLCA). The fractal power law (d_f), found from $I = q^{-d_f}$ distinguishes the two regimes as both cluster types have differing structures. RLCA results in more compact clusters compared to DLCA, shown by their fractal dimensions: $d_f \simeq 2.1$ for RLCA and $d_f \simeq 1.8$ for DLCA. The growth kinetics for each regime are also unique. RLCA has exponential kinetics and in contrast, DLCA is linear in time [49]. These characteristic traits can be probed with static and dynamic light scattering. Monomer-cluster aggregation models were also discussed with the Eden (reaction-limited) [45] and Witten-Sander (diffusion-limited) models [56]. Both have a higher d_f than their respective cluster-cluster aggregation models, and thus form more dense structures. A 'poisoned' Eden model [43, 46] has also been proposed. In this model the sites where aggregation can take place is also limited. The following experiments determine the mechanism for fullerene aggregation upon light exposure and growth of clusters after light exposure.

6.1 Fullerene oxidation and clustering in solution

6.1.1 Experimental

For the light induced clustering, C_{60} fullerenes (99%, MER Corp) were dissolved in toluene (99.5%, Sigma Aldrich) and were exposed to a laser light source (λ =633 nm) in a sealed, rectangular quartz cuvette (Hellma), this is depicted in Scheme 6.1. Prior to experiments the C_{60}/toluene solution was passed through a 220 nm PTFE filter (VWR) to remove large particulates and undissolved matter. Dynamic Light Scattering (DLS) was performed using a Malvern Nano-S with a fixed angle detector at 173° in the same cuvette. All solution based studies were carried out at 25 °C unless otherwise indicated. As there were 2-3 clear decay modes, Equations 3.1 and 3.4 were used to fit the DLS correlation functions. Equation 3.4 is reproduced below. $\Gamma_i(q)$ is the mean inverse relaxation time of the i^{th} diffusive mode with the z-averaged translational diffusion coefficient $D(q)_i$=$\Gamma_i(q)/q^2$. Where, $D = \frac{k_B T}{6\pi\eta R_h}$.



Scheme 6.1: Schematic of laser light exposure set up, the laser was passed through the centre of the solution.

$$g^{(1)}(q,t) = \sum_{i=1}^{N} a_i(q) \exp(-\Gamma_i(q)t) \tag{3.4}$$

Anhydrous toluene was prepared via refluxing toluene (99.5% VWR) over benzophenone and metallic sodium, after which the solvent went through a freeze-pump-thaw cycle three times with liquid nitrogen and stored under nitrogen. Karl Fischer titration showed the anhydrous toluene had <1 ppm water. The C_{60}/anhydrous toluene solution was prepared in a glovebox under nitrogen, with care taken to ensure no other contaminants were present in the final sample.

Oxygenated toluene was made by bubbling O_2 gas into toluene for 3 h. The necessary mass of C_{60} was weighed out and the toluene was added. The solution was then stirred under an O_2 atmosphere.

The molecular geometry of $C_{60}O_x$ and pairwise dipole interactions were calculated using two different methods. In the first, molecular geometry of a $C_{60}O$ molecule was energy minimised using B3LYP/6-31g*. A single point calculation was carried out upon the optimised structure, using CAM-B3LYP/6-31+g*, from which partial atomic charges were extracted using an ESP population analysis [208]. This functional has been shown to well reproduce experimental charge distributions for conjugated molecules [209]. The Coulomb energy resulting from the interaction between these charges on neighbouring molecules was calculated as a function of molecular separation along the vector joining the centre of the cage to the oxygen atom. In order to determine the impact of induced dipoles on the energetic landscape, a second approach was taken, in which single point calculations were carried out including a pair of $C_{60}O$ molecules using CAM-B3LYP/6-31+g*, as a function of closest atomic approach. Partial charges were again extracted using an ESP population analysis, and the Coulomb interaction calculated in a similar manner.

6.1.2 Fitting DLS Correlation Functions

As summarised in Table 6.2, in order to allow reproducible fitting of the three decay modes, the initial decay ($\Gamma_1(q)$), could not be assigned to individual fullerenes, as this decay was also present in neat toluene, for consistency this was fixed to give $R_{h,1}$=0.05±0.01 nm. The second decay ($\Gamma_2(q)$) was assigned to clusters which formed on the order of 100s nm and the final decay ($\Gamma_3(q)$) was fixed to give $R_{h,3}$ on the order of 10s μm, along with their respective amplitudes, a_1, a_2 and a_3. A full correction function giving the R_h of individual fullerenes can not be measured on the Malvern Nano-S as the measurement angle and correlator times do not allow for it (as shown in Figure 4.6), however this has been measured previously [75]. It is common for slow decay times measured via DLS on the order of several microns to be accounted for as contaminants, however due to the trend observed over exposure time, and via transmission optical microscopy (Olympus BX71) they are treated as larger C_{60} clusters. It should be noted here that it is not possible to acquire a more precise size of the large clusters as they are non-Brownian. Various techniques were used to gain a more accurate representation of the large cluster size distribution such as optical profilometry (OP), scanning electron microscopy (SEM), and a particle size analyser. OP and SEM suffered from the same problems, the sample is required to be in the solid state, and during the drying process (e.g. via spin casting) as the solvent evaporates, the C_{60} within the solution will begin to the cluster regardless of its oxidation state and so the results from these two techniques were unreliable. A particle size analyser although suitable due to it being in the solvent state had other problems which made it an unsuitable measurement technique. A large volume of solution was required (~150 mL) and the measurement required agitation of the solution in order for the measurement to occur which, as is shown in Figure 6.3a is undesirable

for cluster size measurements.

Mode	Contribution	R_h Regime/nm	Attributed to
1^{st}	a_1	0.05±0.01	Solvent
2^{nd}	a_2	50-200	Clusters
3^{rd}	a_3	10,000-90,000	Large Clusters

Table 6.2: Summary of fitting parameters, size regimes and species.

6.1.3 Results and discussion

As discussed earlier, there are three possible outcomes of light exposure to C_{60} in solution: degradation [77, 78], polymerisation [79] and aggregation [83, 84]. The first two are changes in the chemical species which generally occur upon UV irradiation. Via MS, FTIR spectroscopy and NMR [i] (Figure 6.1a, b A2 and A3) it is clear that there are $C_{60}O_x$ molecules formed. MS shows a main peak at 720, with peaks at 736, 752 and 768, corresponding to $C_{60}O$, $C_{60}O_2$ and $C_{60}O_3$ respectively. This indicates the C_{60} molecules are being oxidised. It is not possible by this technique alone to determine whether oxidation is via an epoxide or carbonyl bonds. Therefore FTIR and NMR were employed to probe the type of oxidation. NMR spectra of C_{60}/toluene shows a peak at δ 142 ppm, the peaks observed at δ 21, 125, 128, 129 and 137 ppm are all due to the solvent (toluene). For the light exposed C_{60}/toluene solution, there is an additional peak observed at δ 49 ppm, which corresponds to epoxide formation. Carbonyl groups would appear in the δ 180-220 ppm region. A ratio of peaks gives 0.7% epoxide formation, giving an overall solution concentration of 0.0021 wt% $C_{60}O_x$/toluene. In order to confirm the results from MS and NMR, FTIR spectroscopy was also conducted. Due to the low concentration of $C_{60}O_x$ after 21 hours of exposure, a significantly longer exposure time of 2 weeks was employed for FTIR spectroscopy samples in order to increase the concentration of fullerene epoxide. Upon light exposure peaks were observed at 806, 1018, 1095, 1261 and 1459 cm^{-1} which have been previously assigned to fullerene epoxide formation, either for $C_{60}O$ or $C_{60}O_3$ as indicated on Figure 6.1b [82, 210, 211]. The mechanism for photo-induced C_{60} oxidation has been described previously [206, 207], it is briefly summarised here. An incoming photon (λ=633 nm, 1.8 eV) excites an electron in the C_{60} to the first excited state, followed by internal conversion and intersystem crossing to form a triplet excited state; in the presence of oxygen, triplet energy transfer occurs and produces singlet oxygen; the simultaneous presence of triplet excited state C_{60} and singlet oxygen then produces fullerene oxide. Given the previously stated potential outcomes of degradation, polymerisation and oxidation it is possible to rule out degradation and polymerisation. No significant peaks below 720 were observed in the C_{60}/toluene solution exposed to light via MS, ruling out degradation. With FTIR spectroscopy no peaks corresponding to previously observed

[i] Mass and FTIR spectroscopies were carried out in collaboration with Aaron J. Borg and Dr Kirsty F. Gibson respectively. NMR was conducted by Peter Haycock.

C_{60} polymerisation in the solid state [112] were observed, these were expected in the 480 to 800 cm^{-1} range. Whilst spectroscopy cannot detect cluster formation, it does provide definitive evidence for fullerene epoxide formation. Therefore, it is possible to state that the exposure of fullerene to light (λ=633 nm, power=4 mW) in toluene results in fullerene epoxide formation.

The aggregation of C_{60} and $C_{60}O_x$ in toluene upon light exposure was investigated via DLS. A comparison of a freshly prepared and control solution of two week old 0.3 wt% C_{60}/toluene solution stored in the dark is shown in Figure 6.1c. Both aged (•) and freshly prepared (▪) exhibit similar scattering profiles, distinct from the multi-step decay functions, seen in Fig 6.1d, for light exposed C_{60} solutions. This confirms C_{60} aggregation is due to oxidation, as oxidation only proceeds in the presence of light as indicated by Figure 6.1b. Typical correlation functions, $g^{(1)}(t)$, with fits for light exposed solutions are shown in Figure 6.1d. During light exposure, there is an emergence of a second and third decay both of which continue to show an increase in a_2, a_3, $R_{h,2}$ and $R_{h,3}$ with light exposure time ($t_{h\nu}$). The emergence of well defined clusters is thus evidently an effect of the light exposure.

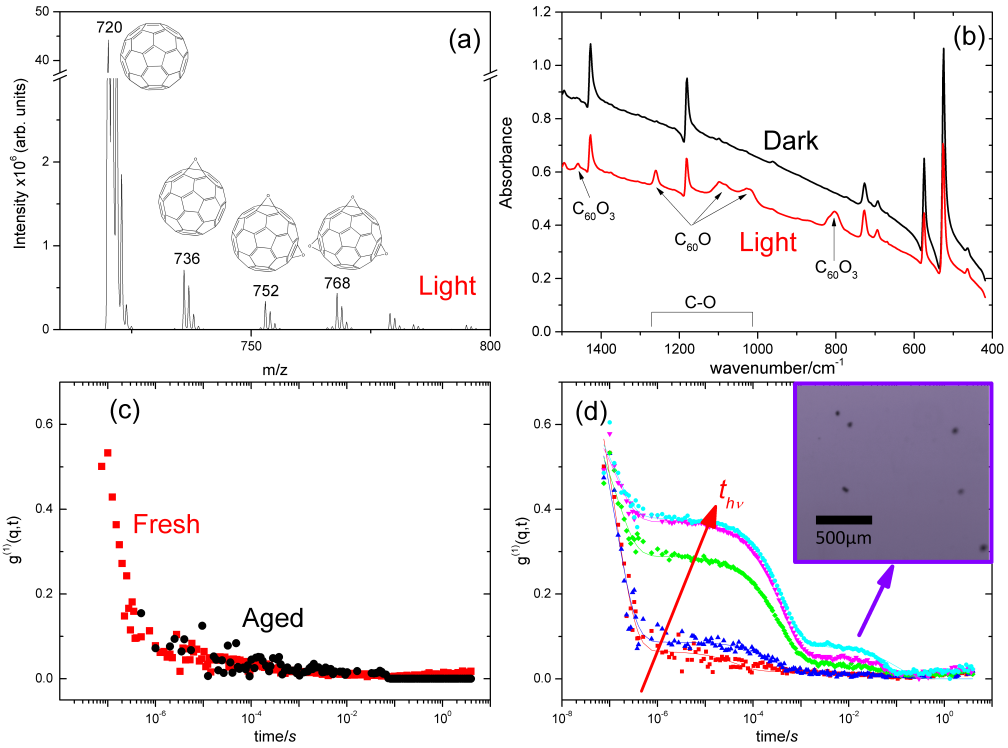


Figure 6.1: (a) Mass spectroscopy of C_{60} in toluene exposed for 21 h (and diluted with IPA for injection), where peaks corresponding to $C_{60}O_x$ with x=0 to 3 are illustrated with possible epoxides formed. (b) FTIR spectra of C_{60} and $C_{60}O_x$ embedded in KBr discs. $C_{60}O_x$ solution was exposed to laser light for 2 weeks prior to sample preparation. Additional features can be observed in light exposed sample in the region expected for C-O bonds. (c) DLS correlation function, $g^1(q,t)$, for a control study of freshly prepared (▪) and aged in the dark for 14 days (•) 0.3 wt% C_{60} in toluene. (d) DLS correlation function, $g^1(q,t)$, for a 0.3 wt% C_{60} in toluene at various times of light exposure following t=0 (▪), 1 (▲), 5 (◆), 15 (▼), 20 (●) h. Solid lines are fits using Equation 3.4. There is the appearance of a second decay after 1 h and the appearance and growth of a third decay after 5 h. Inset shows transmission microscope image of C_{60} clusters ,on the micron scale, after 16 h light exposure.

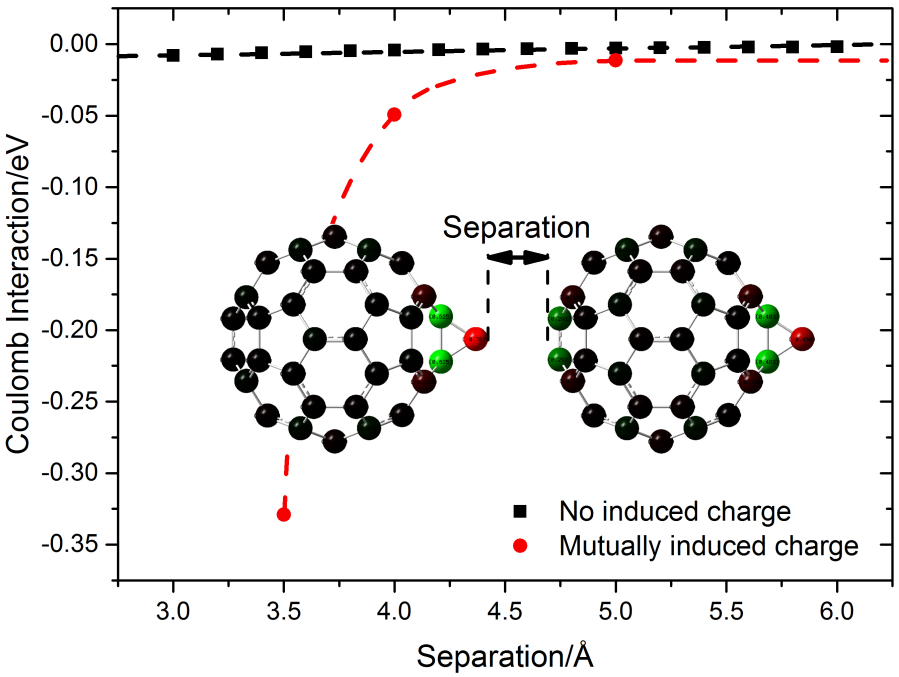
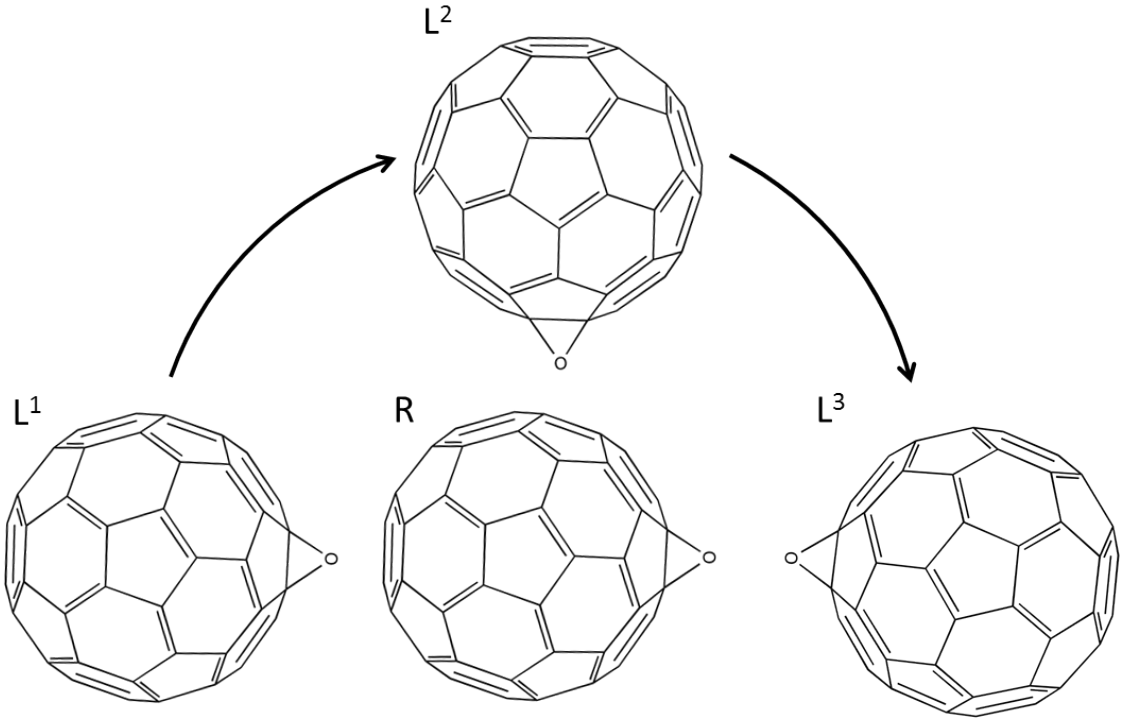


Figure 6.2: Calculated energetic landscape for separation of $C_{60}O$ molecules using point charges from (▪) quantum chemical calculation on a single $C_{60}O$ molecule, (•) a quantum chemical calculation of a pair of $C_{60}O$ molecules at 3.5, 4.0, and 5.0 Å. The separation distances are given by the closest atomic approach, i.e. the distance from the oxygen atom to the closest carbon on the neighbouring molecule, and is indicated on the figure.

In order to quantify and understand the attraction between fullerene epoxide molecules, quantum chemical calculations were carried out [ii]. Initially, a large dipole moment on a single $C_{60}O$ molecule is predicted. The dipole moment is strongly localised close to the oxygen atom, with a partial charge of -0.45 e on the oxygen, and 0.49 e on the nearest carbons. The four next nearest carbons have partial charges of -0.15 eV, and all other carbons are close to neutral (-0.03 e < qatom < 0.03 e). This results in a very small Coulomb binding between $C_{60}O$ molecule pairs of 0.006 eV at 3.5 Å (Figure 6.2), much lower than the average thermal energy at room temperature (≈0.025 eV). Quantum chemical calculations on a pair of $C_{60}O$ molecules reveal a significant induced dipole on regions of neighbouring $C_{60}O$ close to the oxygen atom, leading to a much larger Coulomb interaction between molecules (0.33 eV at 3.5 Å, Fig. 6.2). As these induced dipole interactions diminish rapidly with separation, a much steeper energy gradient with distance is formed. Induced charges on the righthand side $C_{60}O$ are located on the four

[ii] Calculations were carried out in collaboration with Sheridan Few

nearest carbons to the oxygen atom.



Scheme 6.2: Schematic of a $C_{60}O_x$ molecule rotating around another. The interactions will be identical from L^1 to L^2 and oxygen atoms will begin to repel each other going from L^2 to L^3.

There are two notable implications from this result. Firstly the relative orientation of the two molecules is considered and depicted in Scheme 6.2. As the lefthand molecule (L^1), with the oxygen atom pointed inwards, is rotated around the righthand molecule towards L^2, the Coulomb binding will remain unchanged. Then, when the two oxygen atoms approach each other, going from L^2 to L^3, there will be a point at which the molecules will repel, however these repulsions occur seldom and are in a significant minority. Secondly, it is expected that the Coulomb binding between a C_{60} and $C_{60}O$ would be similar to that shown in Figure 6.2 between a pair of $C_{60}O$ molecules. Although solvent interactions are not included in these calculations, which could result in a significantly smaller barrier to molecule separation, these results nonetheless provide an indication of a strong Coulomb binding between $C_{60}O$ molecule pairs.

In conclusion, from quantum chemical calculations, a $C_{60}O$ molecule can bind electrostatically to another $C_{60}O$ or to a C_{60} molecule. There is near-isotropic binding between a pair of $C_{60}O$ molecules, with binding only not able to take place when the two oxygen atoms are facing each other. As mentioned previously, there is 0.7 wt% $C_{60}O_x$ formation, which is a very low fraction. For the clusters to form it is very likely that they consist of both C_{60} and $C_{60}O_x$, with $C_{60}O_2$

and $C_{60}O_3$ able to form multiple bonds to other molecules.

Two methods were chosen to probe the predicted low binding energy, agitation (Figure 6.3) and temperature (Figure 6.3). Two 0.3 wt% C_{60} solutions were exposed to light for 21 and 13 hours respectively one was then placed on a vortexer (Grant Bio PV-1) for 7 minutes at 3000 rpm and the other heated to 65 °C for 19.5 hours. After agitation or thermal stress there is a decrease in amplitude (a_2) back towards the original values. After the break up of clusters, the oxidised C_{60} was left to cluster in solution with minimal additional light exposure, in the growth phase. This confirmed the need for fullerene oxidation to occur in order for the fullerenes to cluster. The recovery rate of fullerene association appears to correlate with $t_{h\nu}$. This is expected since a larger fullerene population would be oxidised over longer light exposure times.

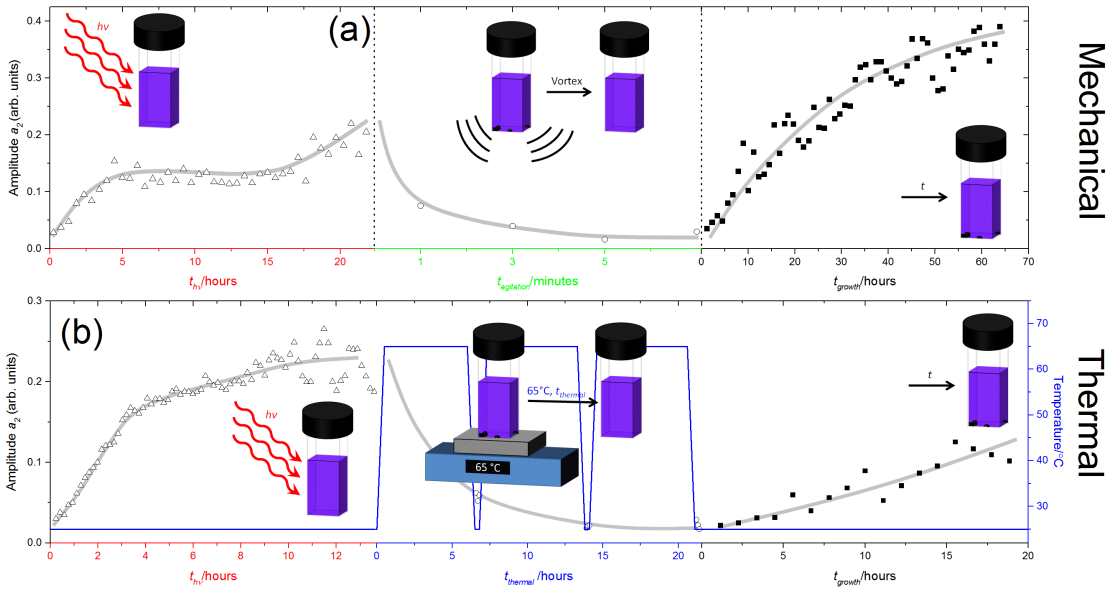


Figure 6.3: Amplitude, a_2, obtained from DLS using Equation 3.4, corresponding to 100s nm fullerene clusters in 0.3 wt% C_{60}/toluene solutions for various processing conditions. (a) Mechanical agitation. The solution was initially exposed to light for 21 h and then placed on a vortexer with measurements taken every two minutes. Once the scattering amplitude dropped to the initial level the $C_{60}O_x$ clusters were allowed to grow while DLS measurements were taken every hour to minimise further oxidation. (b) Solution temperature (blue line, scale on right axis). The sample was initially exposed to light for 13 h and the scattering measurement carried out as previously. The solution is then heated in the dark to 65 °C for 6.5 hours, cooled to 25 °C and allowed to equilibrate for 30 minutes before measurement was carried out again. This was repeated 3 times until the scattering amplitude was approximately equal to its starting value (~0.03). The $C_{60}O_x$ solution is then kept in the dark and measured every hour. This would result in minimal extra oxidation and demonstrates the reversibility of $C_{60}O_x$ clustering. Gray lines are guides to the eye.

In order to quantify the effects of fullerene concentration, temperature during light exposure, solvent quality and laser power on the oxidation and clustering phenomena, further measurements were were carried out and are summarised in Figure 6.4. As expected lower concentrations (a) and lower laser power (d) lead to smaller and fewer clusters formed. However, the temperature dependence (b) of cluster formation was found to be non-monotonic. A faster growth in the number of ~100 nm clusters is observed at 45 °C which then grow into larger micron sized clusters compared to 25 °C. At sufficiently high temperatures, though, namely for 55 and 65 °C, no clustering was observed, corroborating earlier results on cluster dissociation (Figure 6.3b). In this case the clusters are unable to form due to the higher thermal energy. This supports the finding of a low Coulomb interaction strength between a pair of $C_{60}O$ molecules. In other words, the miscibility of $C_{60}O_x$ increases with temperature, becoming miscible at concentrations above ≈50 °C.

Four different solvents were considered (Figure 6.4c): toluene (Tol), chlorobenzene (CB) and oxygenated (Tol-O) and anhydrous toluene (Tol-A), to evaluate the effect of solvent polarity and oxygen content within the solvent on oxidation and clustering. The reported miscibility of C_{60} in chlorobenzene is 0.63 wt% [198]. Comparing solvents with different polarity, one could expect that the more polar solvent (CB) would prevent cluster formation due to inhibited interactions between $C_{60}O_x$; this is not the case, as the cluster size, $R_{h,2}$, and a_2 follow the same trend as Tol. Focussing on the solutions with different oxygen concentrations, as seen in Figure 6.5 the initial rate of a_2 is dependent on the oxygen concentration within the solution. At early times, 0 to 4 h, from Tol-O to Tol-A there is a difference in the induction time, with clusters growing at earlier times in Tol-O. Over longer time periods, >5 h the value of a_2 is higher for Tol-A than for Tol-O, at these times, a_3 for Tol-O has increased to become higher than for Tol-A as more fullerene oxide clusters have formed on the micron scale (Figure 6.5). High levels of oxidation lead to micron sized clusters which deplete smaller clusters by absorbing them; low levels of oxidation lead to a much larger population of small clusters. It appears as though the species with multiple oxygen atoms may have an important role in the formation of micron sized clusters. The differentiation between reaction and diffusion-limited aggregation mechanisms could not be reliably achieved via a kinetic approach due to the simultaneous oxidation and the eventual formation of clusters outside of a Brownian size regime. A deconvolution of the two processes would be necessary in order to separate oxidation and aggregation kinetics.

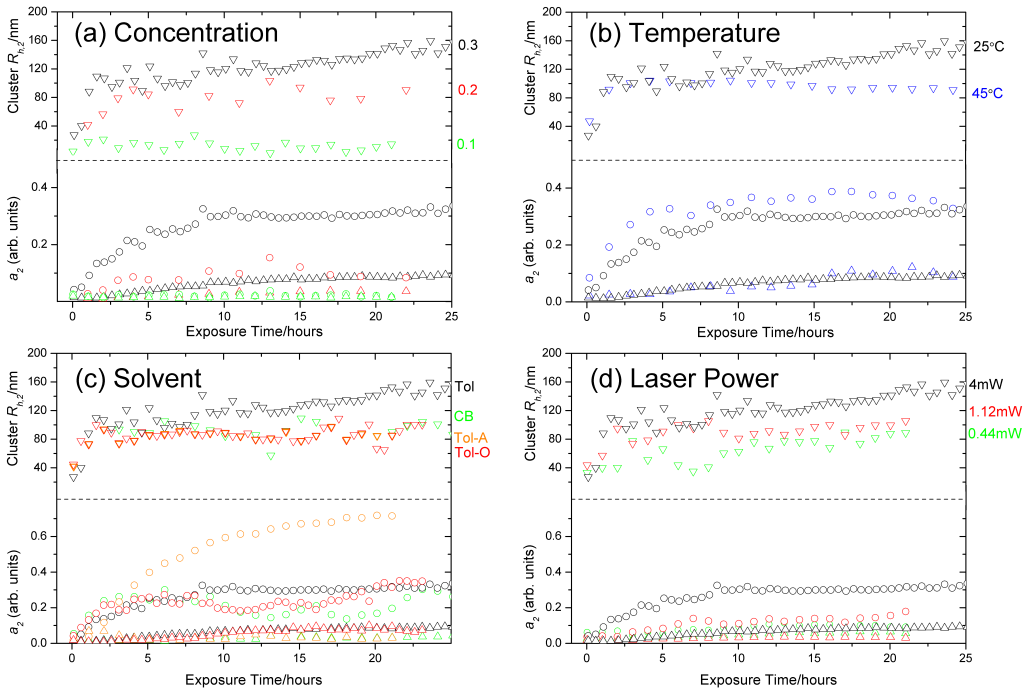


Figure 6.4: DLS results comparing different solution conditions for light induced aggregation and oxidation of C_{60}. For all experiments 0.3wt% C_{60} in toluene is shown in Black for comparison. Symbols $\triangledown$ denote cluster R_h, $\bigcirc$ a_2 and $\triangle$ a_3. The relevant parameter is listed to the right of the graph. The conditions explored were: a: Concentration (0.1-0.3 wt%), b: Temperature (25-45 °C), 55 and 65 °C did not result in cluster formation, c: Solvent (toluene (Tol), chlorobenzene (CB), anhydrous toluene (Tol-A) and oxygenated toluene (Tol-O)) and d: Laser power (0.44-4 mW).

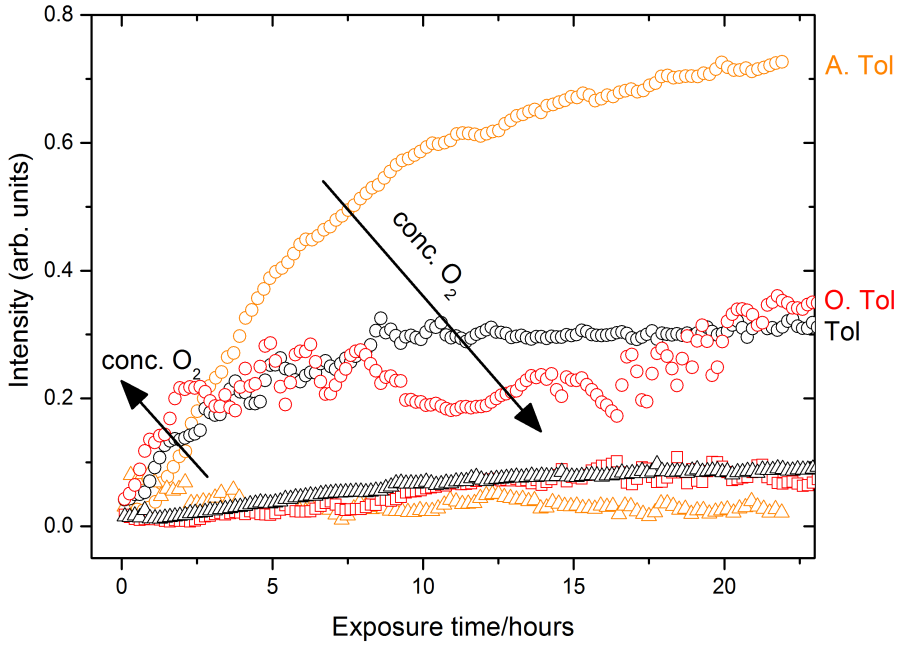


Figure 6.5: DLS results from varying O_2 levels within the solution, form Figure 6.4c, focussing on the scattering intensity, a_2 (○) and a_3 (△).

6.1.4 Cluster Formation

To elucidate the mechanism behind cluster formation a series of intermittent laser experiments were carried out. The three cases studied were with: the laser always on the sample, on for 6 minutes out of every hour, and on for 6 minutes out of every 26 minutes, this is shown graphically in Figure 6.6. For this, there are two methods by which 'time' could be considered, one from which the experiment starts (time), the other only considered the time at which the sample is exposed to light (exposure time, $t_{h\nu}$). As is seen in Figure 6.7a using the time from when the experiment starts, values for a_2 and a_3, show a trend with light exposure. There is a higher a_2 for the less frequently exposed solution and the opposite for a_3. Similar to the trend observed for O-Tol, Tol and A-Tol with increased oxidation, a_3 has higher values than for a_2. The hydrodynamic cluster size, via $R_{h,2}$, is not largely affected by the intermittent light exposure. Figure 6.7c shows two aspects of fullerene clustering, the first is that it takes an hour of light exposure for a defined correlation function to appear, the second is that after 31 hours of light exposure, if the light is turned off, clustering still takes place, indicating that fullerene epoxide production is not the rate limiting step for cluster formation.

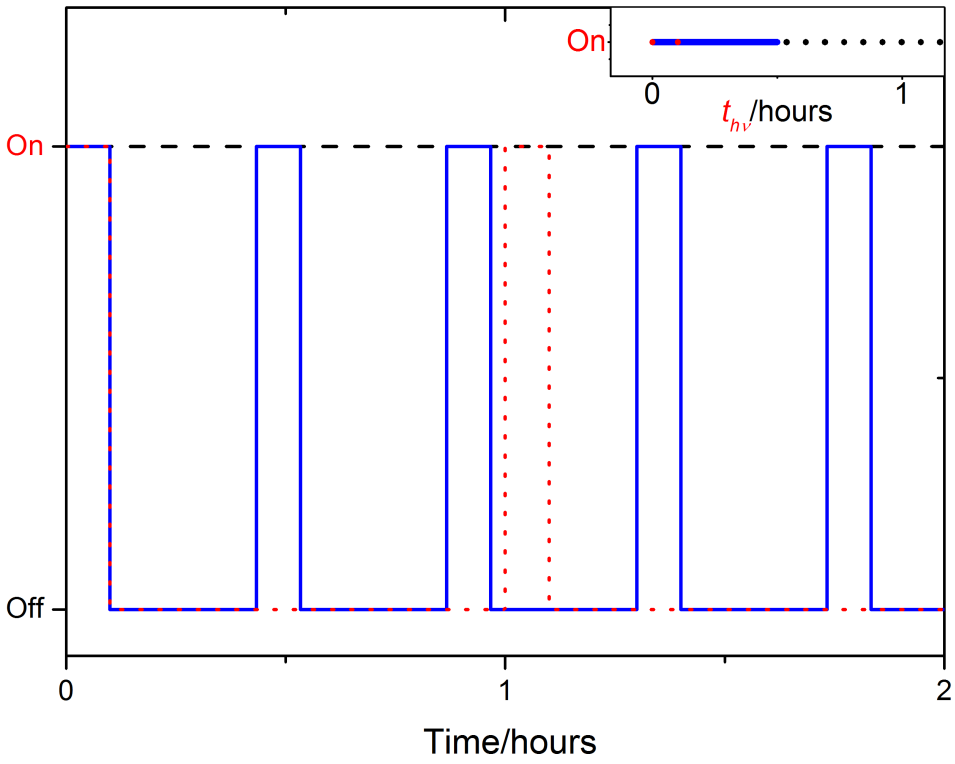


Figure 6.6: Graphical representation of the intermittent laser experiments carried out. The three pulsed regimes were: (– – –) always on, (—) 6 minutes on, 20 minutes off and (· · ·) 6 minutes on, 54 minutes off. Inset shows equivalent for light exposure times ($t_{h\nu}$).

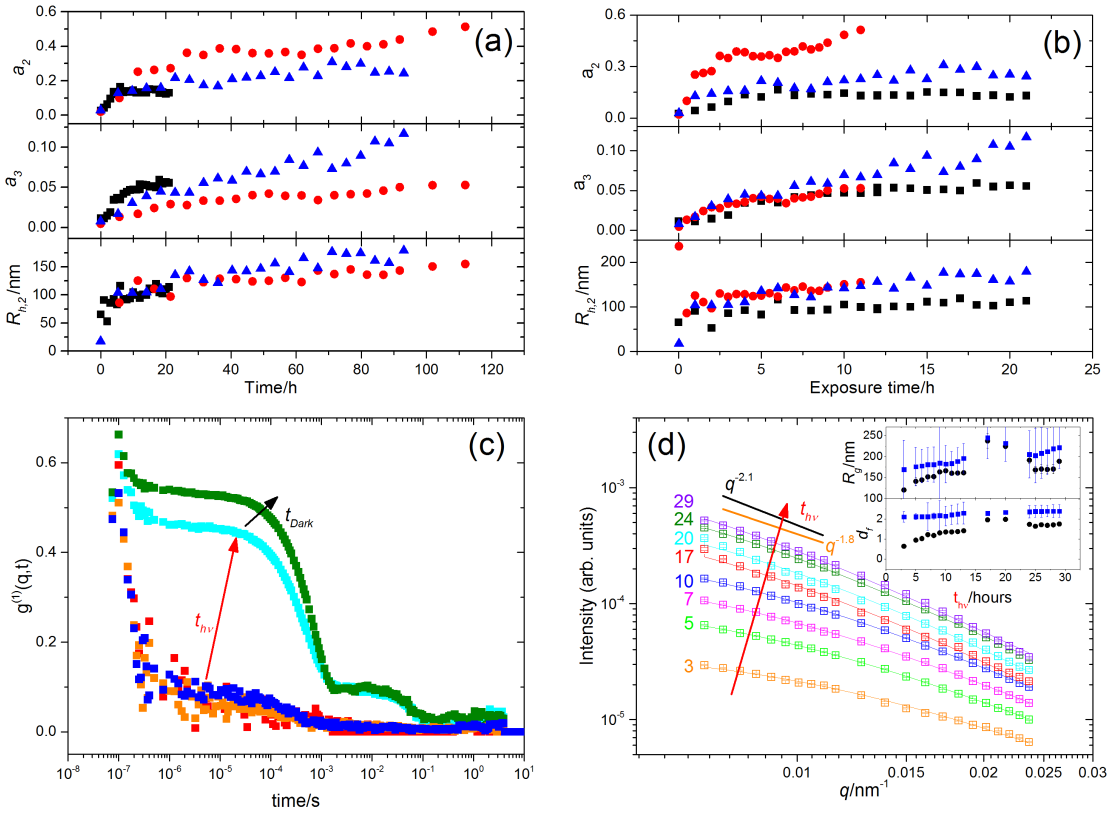


Figure 6.7: (a-b) Results from intermittent laser experiments with DLS, a_2 and $R_{h,2}$ collapse with (a) time and (b) exposure time ($t_{h\nu}$) whereas a trend is observed with a_3 using the three regimes described in Figure 6.6. (■) always on, (▲) 6 minutes on, 20 minutes off and (●) 6 minutes on, 54 minutes off. (c) Correlation functions of freshly prepared (■) C_{60} exposed to light for 45 mins (■), 1 h (■) and 31 h (●) after which the solution is left in the dark for a further 12 h (●). This indicates a delay or lag time between the initial epoxidation and cluster formation and that cluster formation is not limited by $C_{60}O_x$ population as there is additional growth in cluster $R_{h,2}$ with no additional epoxide production. (d) Static Light Scattering of a 0.3 wt% C_{60}/toluene solution exposed to a 4 mW, 633 nm laser for a period up to 24 hours. The inset shows an increasing R_g via Guinier analysis (•) and fits to the fractal model (■) by Teixeira [90]. There is also an increase in d_f by fits to the fractal model [90] (■) or the power-law (•) between $7.1 \leq q \leq 10.5 \times 10^{-3}$ nm^{-1}. During light exposure time ($t_{h\nu}$) the system develops from a relative loose structure to a more compact structure, indicated by the increasing fractal dimension. R_g follows the same trend as seen in $R_{h,2}$.

The mechanism for light induced fullerene cluster formation is more complex than the majority of models provided within the wider literature, which do not take into account dipoles on individual particles or asymmetric bond formation. Here, an attempt to reconcile experimental

data with known aggregation mechanisms is made.

Stage I: **$C_{60}O_x$ production.** Prior to any bonds forming between $C_{60}O_x$ and C_{60}, there must be the formation of $C_{60}O_x$ molecules which, as shown in Figure 6.1 is due to light exposure. Once enough $C_{60}O_x$ molecules are produced, induced dipole interactions between two fullerenes, one of which must be fullerene oxide begin the clustering process. Of course there would need to be a significant number of these fullerene interactions in order for the smaller 50-200 nm clusters to form. This is shown by the delay time of ≈1 h for a defined correlation function to appear in DLS. (Figure 6.7c, ▪)

Stage II: **Continued growth and production of 100s nm clusters** (a_2 and $R_{h,2}$). There are two possible limiting factors for cluster formation rate at this stage: the probability of an epoxide binding to another molecule, or a lack of epoxides within solution. Cluster formation is not limited by $C_{60}O_x$ population, as is shown in Fig 6.7a and c cluster formation is limited only by time and not by fullerene epoxide population. Therefore the rate limiting step at this stage is bond formation between molecules.

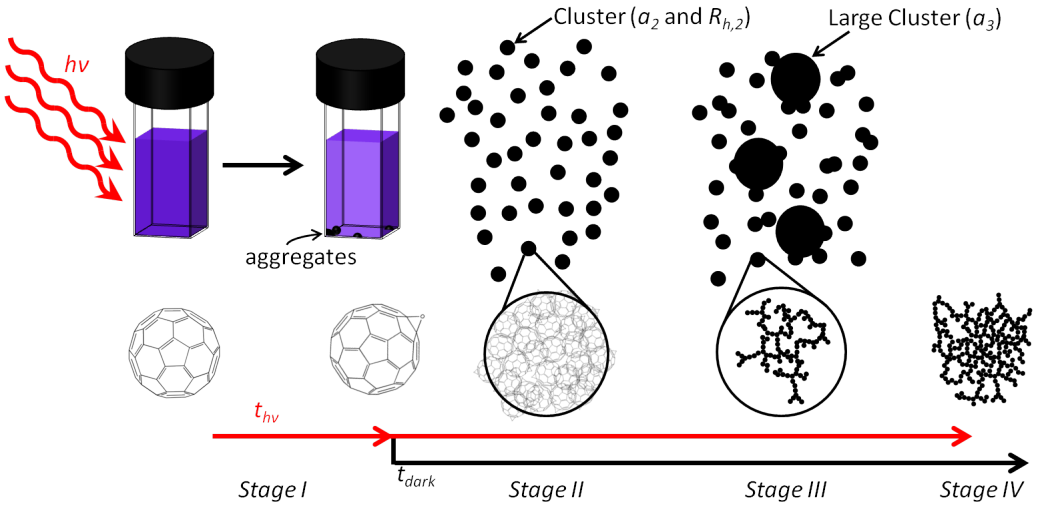
Stage III: **Micron-sized large cluster growth.** Once a significant number of 100s nm clusters are produced, there is a decrease observed in a_2 seen most clearly at $t_{h\nu}$ ≈15 h in Tol-O (Figure 6.7c). At the point of this decrease in a_2 there is a corresponding increase in a_3. Although one would, and should expect to see a size regime between the clusters of 100s nm to those on the micron scale, these are not observed. This may be due to several reasons for example, the lack of decay time resolution with the small changes in size or a low number of clusters in between both sizes which would not provide a sufficient scattering signal.

Stage IV: **Densification of clusters.** To elucidate the clustering mechanism via a structural approach SLS was carried out, this is seen in Figure 6.7d. Two methods were used to extract d_f and R_g from the scattering data, the first was via Guinier's approximation and fitting power laws between $7.1 \leq q \leq 10.5 \times 10^{-3}$ nm^{-1}. The second uses a fractal model derived by Teixeira [90] (Equations 3.11 to 3.14), this model allows one to fit scattering from fractal-like aggregates which are composed of several, smaller spherical particles and was initially developed for small angle neutron scattering. It was necessary for both methods to be used as Guinier's approximation only applies when $qR_g < 1$ which is not the case for the radii obtained from SLS and so the fractal model corroborates these results.

Due to the number of free parameters and limited q range within which SLS data was collected, the model was subject to the following constraints: $\rho_{particle}$ and $\rho_{solvent}$ were set to arbitrary values (2 and 6.35×10^{-4} nm^{-1} respectively) and R_0 was set to 0.5 nm. No background contribution was used as a background subtraction of molecularly dispersed C_{60}/toluene solution had already been carried out. The volume fraction was set to a fixed value, 3.49×10^{-10}, obtained by allowing unconstrained fits of the data and selecting the mean. The values obtained for d_f and R_g are highly dependent on the assumptions and constraints described, especially for the background and volume fraction, therefore the results from these fits are only used qualitatively. Allowing the two parameters to vary gave the same trend in d_f and R_g however at different

values (d_f could range from 1.4 to 2.5 and R_g from 99 to 320 nm) Further information and details of this model can be found in Ref. 90.

Although both methods lead to different values, the trend observed is the same. It can be seen from the inset of Figure 6.7d that there is an increase in both R_g and d_f. The R_g follows the same trend as seen for $R_{h,2}$ with R_g increasing from 100 to 200 nm. The increase in d_f could indicate that the aggregation process is via monomer-cluster aggregation which produces denser clusters than cluster-cluster aggregation. The most likely mechanism is the poisoned Eden model [43, 46], as the aggregation is limited by the formation of a dipole between the oxygen and carbon atoms of two molecules as well as aggregation being limited by site of where the oxygen atom is. Due to the limited q range it is not possible to find d_f accurately. It is necessary that $\frac{q_{max}}{q_{min}} \geq 10$ and for fractal aggregates it would be necessary to have $R_g^{-1} \leq q \leq R_0^{-1}$ (where R_0 is the radius of an individual particle from which the clusters are formed). The values for d_f previously reported for C_{60}/solvent systems are: 2.1 [83] for C_{60}/benzene and 1.8-2.4 for C_{60}/water [88]. Here, d_f increases from 2.09 to 2.46. This indicates clusters which are starting as relatively diffuse structures becoming increasingly compact with time. A rationale for the increasing d_f is due to the potential for $C_{60}O$ or C_{60} molecules to diffuse into the 100s nm clusters and fill any gaps within the fractal geometry therefore making the fractal cluster more dense and have a higher fractal dimension. Another possibility is random bond breaking and readjustment causing a more dense object to form. A similar mechanism for protein crystallisation from individual protein molecules to large aggregates has been alluded to in the literature [202]. The work by Meng et al. [88] studied C_{60} cluster growth via light scattering and stated there was a negative surface charge on C_{60} clusters, via electrophoretic mobility studies, which could be due to the oxygen atoms on the $C_{60}O_x$ molecules. A schematic describing the light induced cluster formation is given in Scheme 6.3.



Scheme 6.3: Schematic of light exposure of C_{60}/toluene solutions in ambient conditions, and subsequent formation of fullerene epoxide and microscopic fullerene particles.

6.2 Oxidised C_{60} Clusters in Thin Films

Given the impact of C_{60} clusters in thin film morphology in Section 5.2 it would be expected that the clusters formed by light exposure would have a similar effect. For the C_{60} clusters induced by polymer addition in solution, the clusters above ~100 nm were nucleation sites which the molecularly dispersed C_{60} within the PS matrix were attracted to. Thin composite films were fabricated using the clustered fullerene epoxide solutions and the impact on thin film morphology of light exposure in solution was examined. P3HT and light exposed PCBM were also studied within thin films.

6.2.1 Experimental

C_{60}/toluene solutions were filtered with a 220 nm PTFE filter and exposed to a laser light source (λ=633 nm) for the specified length of time. A 100 μL aliquot of light-exposed solution was removed after the necessary time and after 21 h of light exposure an equal volume of 5 wt% PS/toluene was added to each light exposed C_{60}/toluene solution. The solution was gently mixed until homogenous and left for 1 hour. This procedure is shown in Figure 6.8. The thin film fabrication procedure described previously in Section 3.2 was followed, which gave ≈5 wt% C_{60} in the solid state. Samples were then annealed at the specified temperature and time. A similar procedure was carried out using a 0.5 wt% PCBM/toluene solution with 65 kg/mol PS, 100 kg/mol regiorandom P3HT (RRa-P3HT) (Sigma Aldrich) and 50 kg/mol regioregular P3HT (RR-P3HT) (synthesised by J. H. Bannock) with PDIs of 1.1, 3 and 1.1 respectively. The RR-P3HT/toluene solutions were heated to 50 °C prior to deposition.

6.2.2 Results and Discussion

Thin PS/C_{60} films were made using the light exposed fullerene solutions. For the first series of experiments C_{60}/toluene solutions were exposed for 0 to 21 hours and the thin films were annealed at 150 °C for 1 hour. There are surface asperities observed in all films, which decrease in number with longer solution exposure times (Figure 6.9). Similar asperities have been assigned for both C_{60} nucleation [9] and PS thin film dewetting [143]. C_{60} diffusion through a film is expected to occur within seconds [212] whereas dewetting takes place on significantly longer timescales. *In situ* annealing showed slower kinetics for the development of the number of these features with increasing C_{60}/toluene light exposure (Figure 6.10). Prior work has shown similar morphologies, seen in Ref. 9, specifically Figure 1k, upon longer annealing times can form morphologies similar to those seen in Figure 5.16e. Thus the features observed on these films are due to C_{60} nucleation.

Image analysis shows clear trends with C_{60}/toluene light exposure. Figure 6.11a shows a decrease in the number of clusters on the images shown in Figure 6.9 as the light exposure C_{60}/toluene solution increases; whilst Figure 6.11b shows the evolution of the clusters with annealing time at various C_{60}/toluene solution light exposure times. An interesting observation

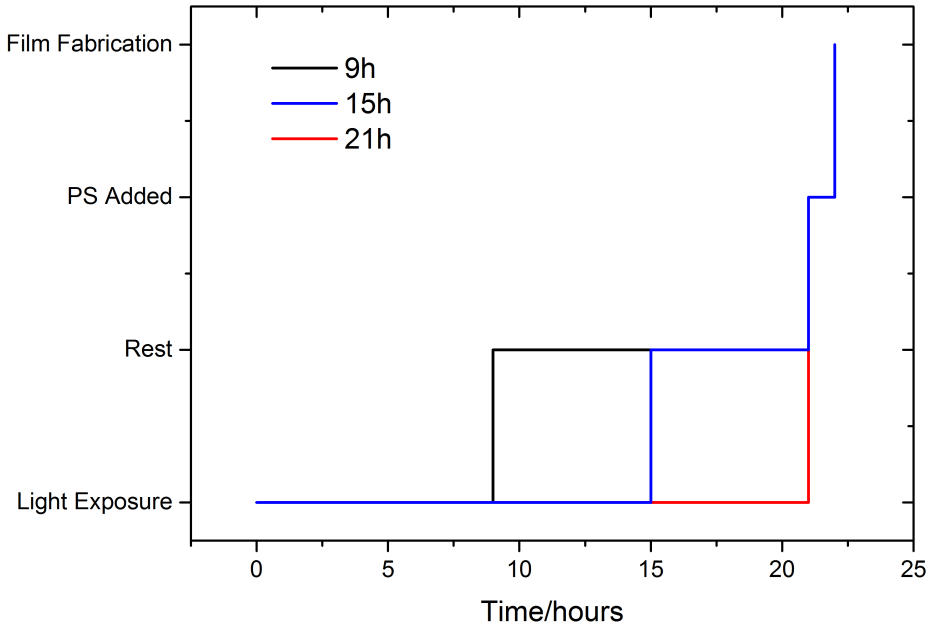


Figure 6.8: Thin film fabrication sequence of light exposed C_{60}/toluene solutions. Once the necessary light exposure had been carried out, the sample was left to rest in the dark before PS/toluene solution was added and the film was fabricated with all solutions being the same age. Exposure times of 9, 15 and 21 hours are shown.

with solution light exposure time is that the trend follows $k-\exp^{t_{h\nu}}$. This gives some indication to a significant increase in micron sized clusters forming at ≈15 hours of light exposure in solution, corresponding to *Stage III* in the clustering mechanism proposed previously.

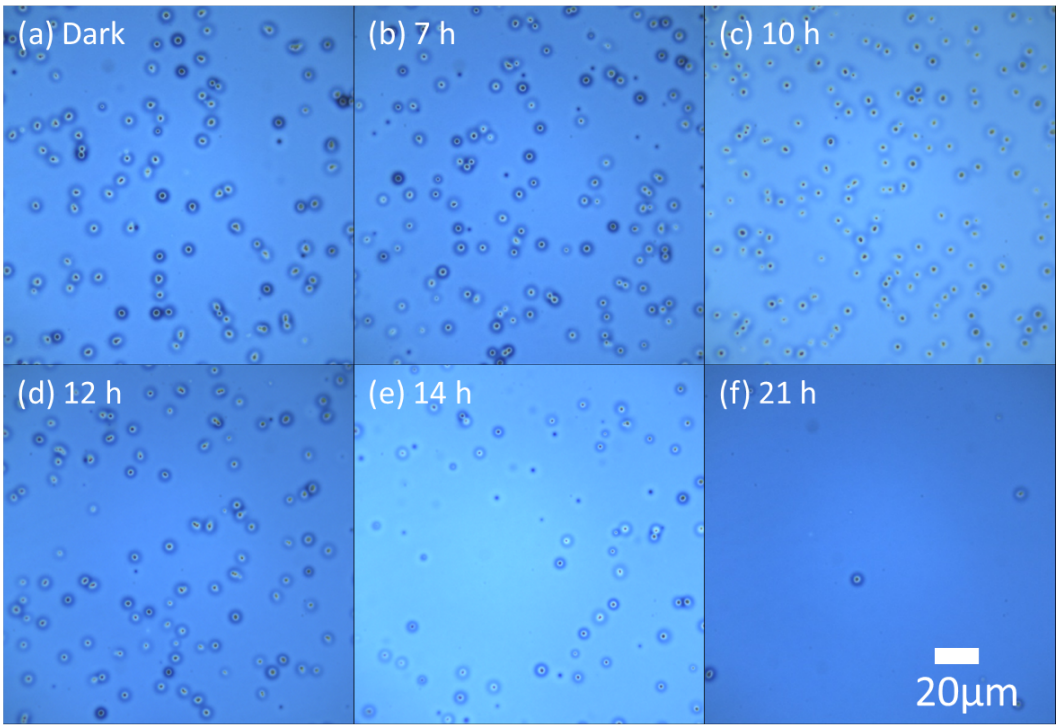


Figure 6.9: Optical microscopy images of PS/C_{60} thin films (h=120 nm) annealed at 150 °C for 1 h after various light exposure times noted on each image.

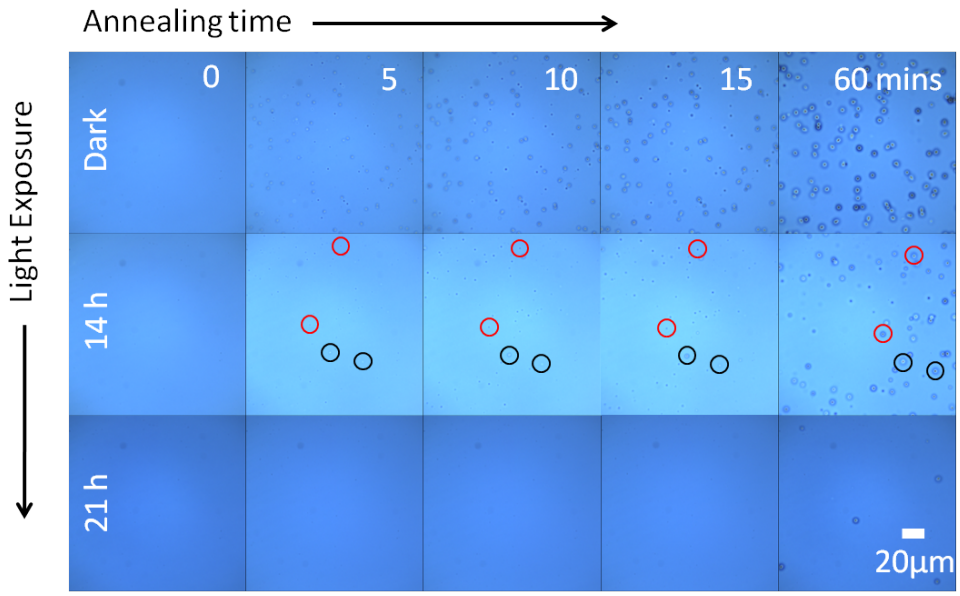


Figure 6.10: OM images from *in situ* annealing of 120 nm thin PS/C_{60} films fabricated using C_{60}/toluene solutions exposed to laser light for 0, 14 and 21 hours. Annealing time is indicated along the top row in minutes. Black and red circled regions are discussed in the text.

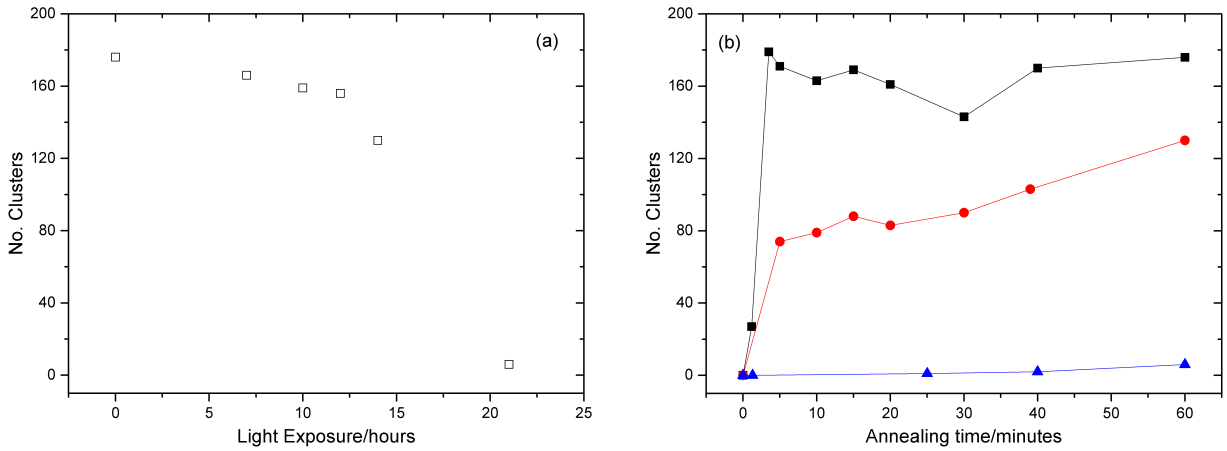


Figure 6.11: Image analysis of OM images shown in (a) Figures 6.9 and (b) 6.10 for 0 (■), 14 (●) and 21 h (▲) solution light exposure giving the number of C_{60} clusters on thin films.

Further image analysis such as the area fraction (A_f) and the average size of clusters proved difficult due to their evolution over time. This is demonstrated in Figure 6.10 with the black and red highlighted regions in the films prepared from the C_{60}/toluene solution exposed to light for 14 h. The black highlighted regions in Figure 6.10 show an initially white region where a 'black

spot' develops after 15-20 minutes. Another cluster is shown with the red highlighted region. Here there is an initially black spot which then develops a ring around it after 30 minutes of annealing. This is most likely due to the depth of the film within which a C_{60} cluster nucleates. If it was near the surface of the film then it may follow the red highlighted series, whereas if it was in the middle of near the bottom surface then these could be the black highlighted regions.

A temperature study for the films exposed for 0, 7 and 14 hours was conducted with results shown in Figure 6.12. The film prepared from the C_{60}/toluene solution not exposed to light and annealed at 180 °C for an 30 minutes (Figure 6.12d) showed the expected morphology (seen previously in Figure 5.16e and Ref. 9), whereas the morphologies seen in Figure 6.12e and f are different to those seen previously.

There are a several plausible explanations for the observed film structures: (i) the $C_{60}O_x$ clusters formed in solution are wetting the substrate surface, (ii) the $C_{60}O_x$ clusters are large and so during the spin coating process are pushed to the edge of the silicon substrate, (iii) due to the micron scale $C_{60}O_x$ clusters formed in solution, there is a significant decrease in the dissolved C_{60} concentration within the solution and (iv) the $C_{60}O_x$ are large, do not take part in the growth process and remain on the sub-micron length scale. Some of these will now be ruled out. The films annealed at 180 °C (Figure 6.12d-f) have a very similar morphology to those seen in Section 5.2, specifically Figure 5.24e. Dissolution experiments there demonstrated that there was no wetting layer of C_{60} at the substrate interface. This only takes into account the morphologies observed after annealing at 180 °C, not at 150 °C, however previous work has suggested that the morphologies are formed via the same mechanism [9]. There may be attraction between $C_{60}O_x$ and the silicon dioxide on the silicon substrate. Close examination at the edge of the films showed no increase in the concentration of C_{60} clusters via optical microscopy, ruling out (ii). For (iii) to be the case there must be a definite correlation between the total number of C_{60} clusters in solution and the thin film surface. There is a similarity between the films prepared from solutions exposed for 0 and 7 h, which should have different concentrations of dispersed and clustered C_{60}. Given the mechanism proposed in the previous chapter for C_{60} clusters induced by polymer addition, the clusters which were too large to diffuse were nucleation sites to which individual C_{60} molecules are attracted, therefore (iv) seems an unlikely explanation. There are two explanations which have not been fully ruled out (i) and (iii). To confirm the presence of a wetting layer, techniques such as neutron reflectivity, depth profiling with secondary ion mass spectroscopy or a combination of focussed ion beam milling and TEM would be necessary. Testing the depletion of C_{60} in solution is significantly easier and so a concentration series of 1, 3 and 5 wt% C_{60}/PS thin films was therefore carried out.

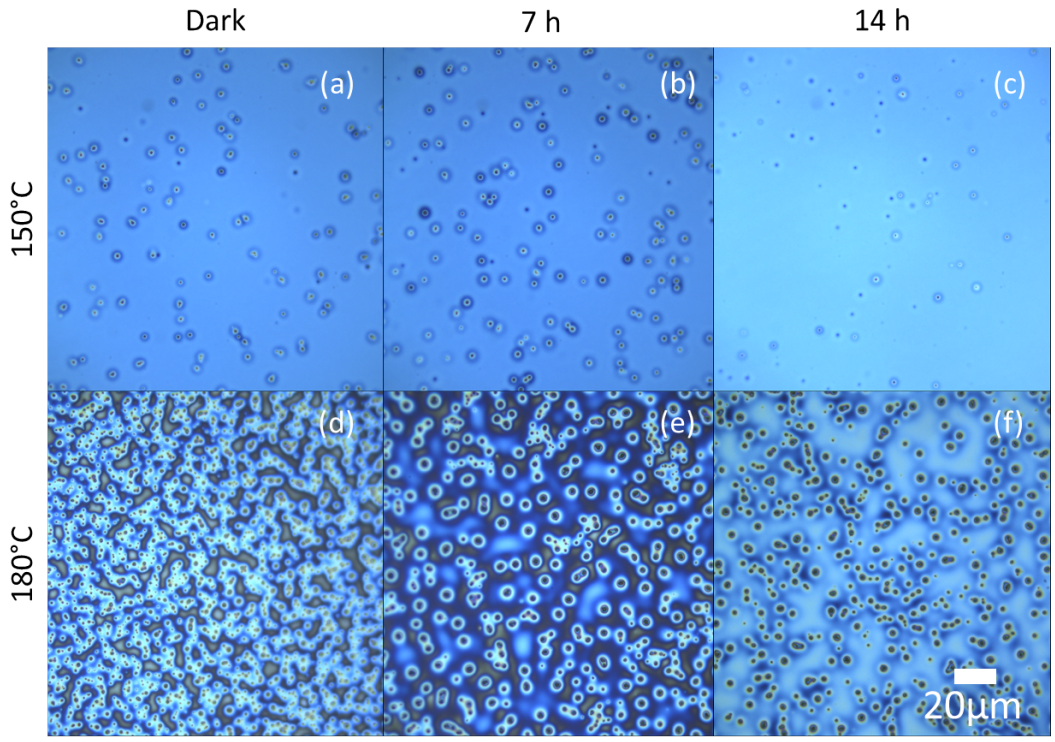


Figure 6.12: (a-f) Optical microscopy images of films fabricated from solutions exposed to light for 0, 7 and 14 hours annealed at (a-c) 150 °C for 1 hour and (d-f) 180 °C for 30 minutes.

As is seen in Figure 6.13a-c there is a trend with C_{60} loading and annealed film morphology. Image analysis demonstrates that films at 1 and 3 wt% C_{60} have a similar number of clusters upon annealing as those made from 21 h light exposed C_{60}/toluene solutions. This adds weight to argument (iii) that micron scale C_{60} aggregates remove mass from the C_{60}/toluene solution upon light exposure. Based on this assumption, an approximate calculation can be carried out for the concentration of C_{60} within the micron sized aggregates in solution. To fabricate a 120 nm 5 wt% C_{60}/PS film, a ~5 wt% PS/toluene stock solution and a concentration of ~0.3 wt% C_{60}/toluene was used (i.e. the final solution concentration would be 0.15 wt% C_{60}/2.5 wt% PS/toluene). For 1 and 3 wt% C_{60} films having the same thickness and film casting conditions this drops to 0.1 and 0.15 wt% C_{60}/toluene respectively. This estimates a 50% decrease in bulk solution concentration with the remaining C_{60} aggregating with $C_{60}O_x$ in solution. However, given that there is no change in the colour of the solution, corresponding to a decrease in concentration, this seems to be an over estimate.

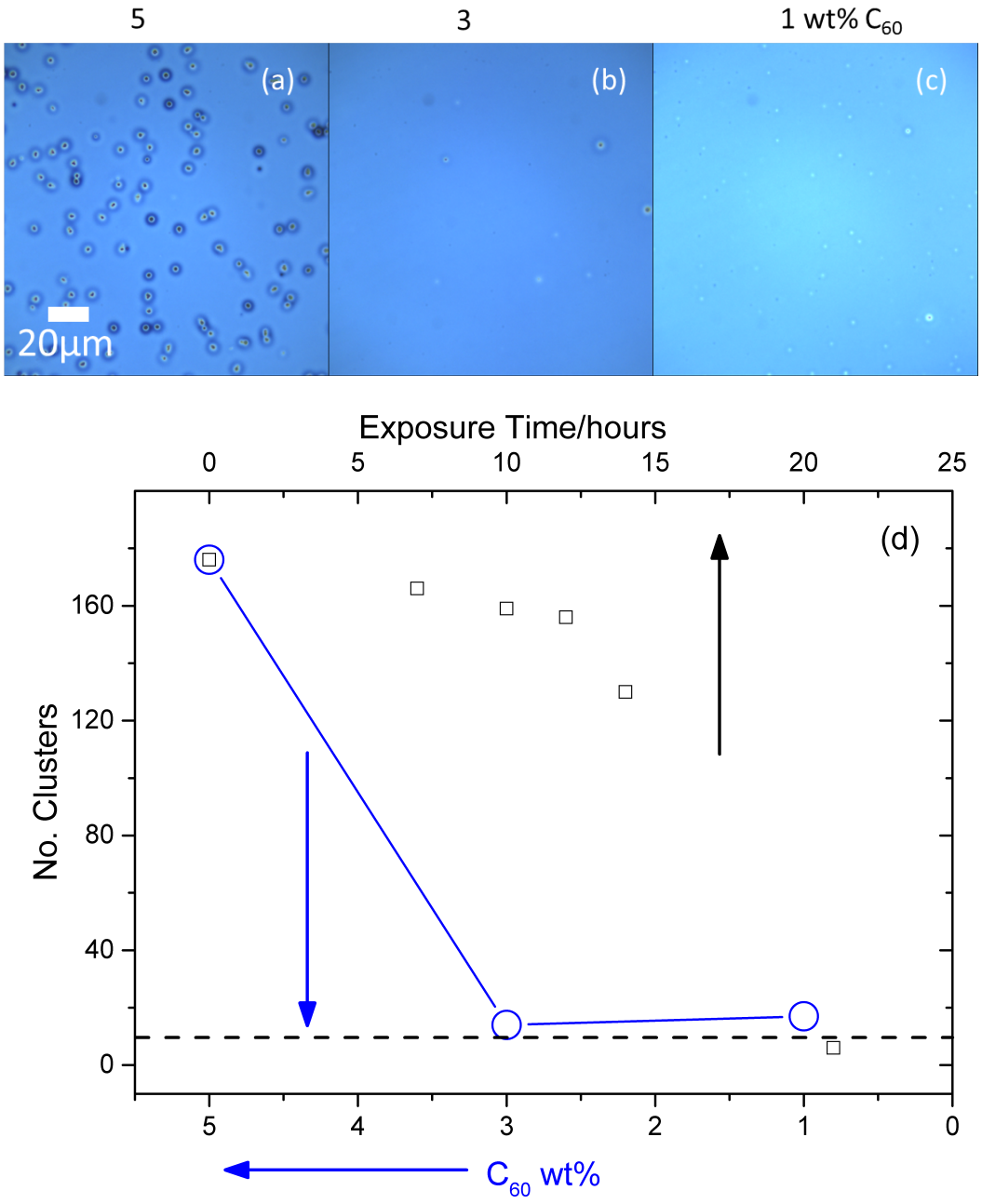


Figure 6.13: (a-c) Optical microscopy images of C_{60} concentration series in thin films with 5, 3 and 1 wt% C_{60} annealed at 150 °C for 1 hour. (d) Results from image analysis of (a-c) (in blue) overlaid with data shown in Figure 6.11a on the top axis. The dashed line indicates an approximate level (at y=10) which indicates that the films at 1 and 3 wt% are similar to that at 21 h of solution light exposure.

As was shown previously in Figure 6.3 providing mechanical or thermal energy to light exposed C_{60}/toluene solutions rejuvenates the solution to its original, unclustered, state. Thin films were

prepared from solutions prior to light exposure, after 21 h exposure and after 21 h exposure followed by 7 minutes of agitation. The results can be seen via AFM of the as cast state in Figure 6.14a-c. The solution not exposed to light (a) has no C_{60} clusters, the light exposed solution (b) has a large cluster of 500-1000 nm and the agitated solution (c) has a significantly smaller cluster of 110±11 nm. This seemingly corroborates the results from light scattering where a mechanically agitated solution can be reverted back to an unclustered solution, however significantly more AFM images are necessary to ensure these are robust results. The 110±11 nm cluster seen in Figure 6.14c may arise from either the time between agitation and thin film fabrication (although this was carried out as quickly as possible) or, the more likely scenario, not all of the clusters are broken up upon agitation. Annealing the films and imaging with OM shows markedly different morphologies between the three films. As seen above 21 h light exposure in solution gives a significant decrease in C_{60} rich regions (Figure 6.14e). The difference between (d) and (f) is less clear. There are more clusters present in the film prepared form a light exposed, agitated solution. In the agitated, light exposed solution there would be a significant number of free $C_{60}O_x$ molecules in the PS matrix. Due to the existing interaction potential between two $C_{60}O_x$ molecules, it is possible that two molecules would find one another sooner and therefore produce more clusters. The result of an agitated solution giving a similar morphology to an unexposed solution provides a potential route to solution 'rejuvenation'.

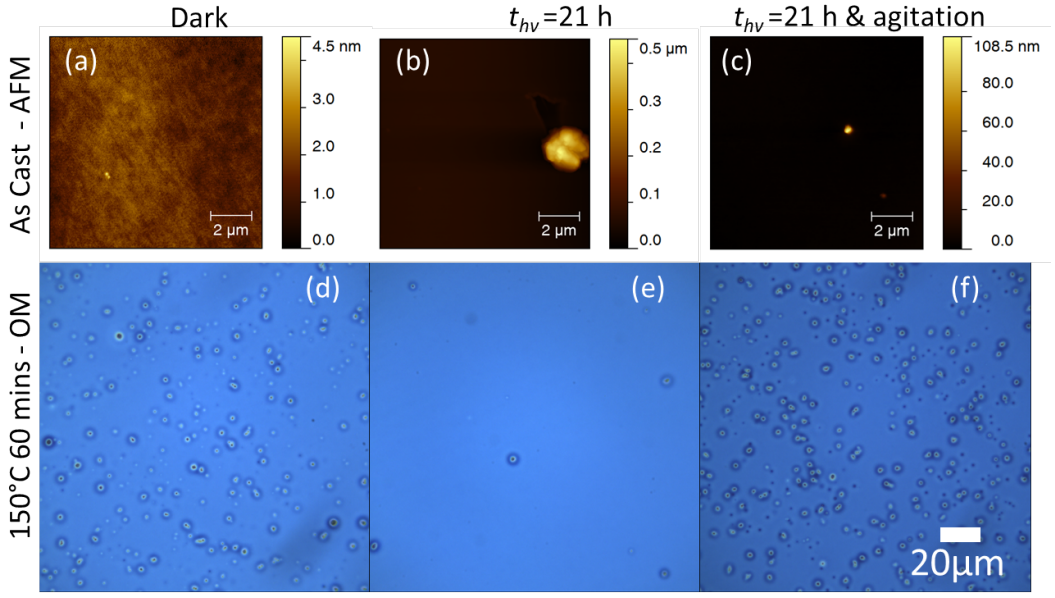


Figure 6.14: (a-c) AFM images of as cast films prepared from (a) unexposed, (b) 21 h light exposed and (c) 21 h light exposed and agitated C_{60}/toluene solutions. (d-f) Optical microscopy images of films shown in (a-c) annealed at 150°C for 1 hour.

6.3 Other systems studied

Light exposure of PCBM/toluene solutions was carried out with thin films fabricated using PS, regioregular (RR) and regiorandom (RRa) P3HT matricies. No aggregates were observed with light exposure of PCBM/toluene solutions (Figure 6.15), however, the films produced from light exposed solutions exhibit a different morphology from unexposed solutions. Light exposure was carried out using the same 4 mW, 633 nm HeNe laser as with the C_{60}/toluene solutions.

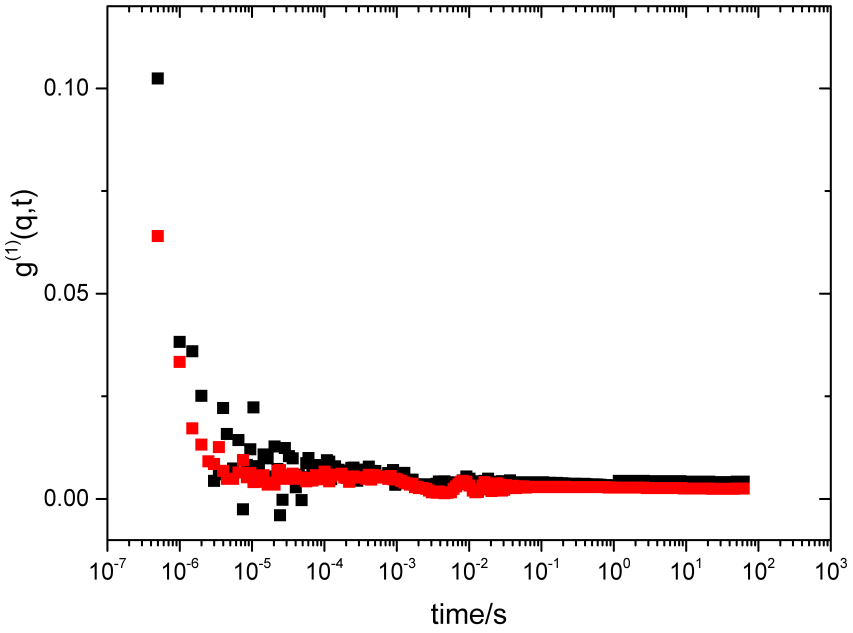


Figure 6.15: DLS correlation function, $g^1(t)$, for a control study of freshly prepared (■) and exposed to 633 nm HeNe laser for 12 hours (■) 0.5 wt% PCBM in toluene.

There is a decrease in the number of asperities after 19 h light exposure as seen in Figure 6.16 with an effect similar to that observed with PS/C_{60} thin film light exposure [213]. Experiments carried out with RRa-P3HT and RR-P3HT were less conclusive. PCBM/toluene solution exposed to light for 24 h appears to give fewer features on the film surface compared to the film prepared from the solution not exposed to light, this is seen best in Figure 6.17e and f. RR-P3HT/PCBM thin films on the other hand showed no discernible difference on the micro (Figure 6.18e-f) or nano scales (Figure 6.18h-i). The change in the thin film morphology could arise from a number of chemical changes such as oxidation of the fullerene cage as was observed in Section 6.1 or formation of fullerene dimers [213]. These could result in a change of fullerene miscibility within the polymer matrix and may also affect PCBM crystallisation.

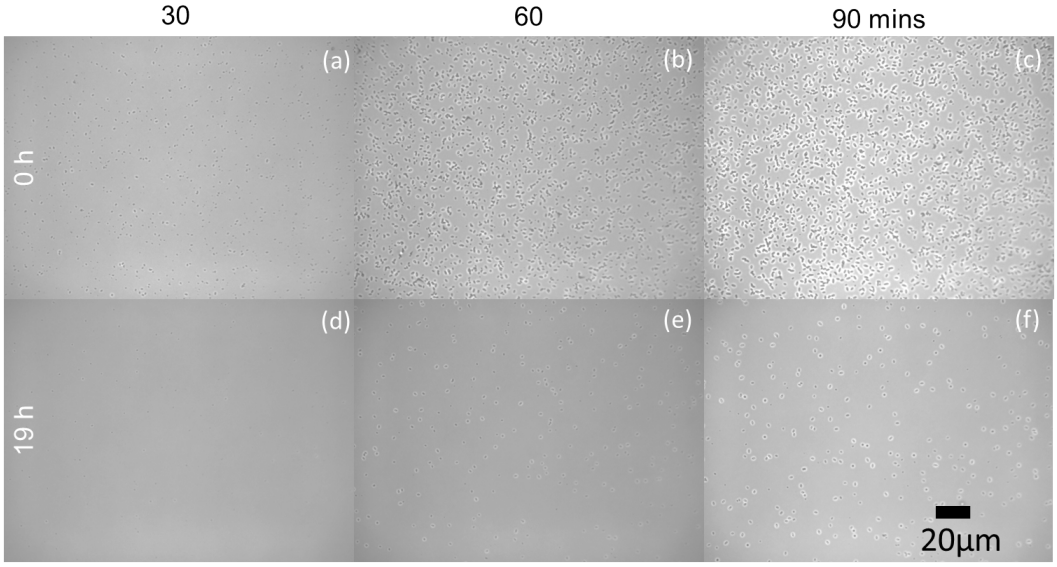


Figure 6.16: Optical microscopy images of 20 wt% PCBM/PS thin films (h=75 nm). (a-c) PCBM/toluene solution not exposed to light (d-f) PCBM/toluene solution exposure to laser light for 19 h. Films were annealed at 150 °C for times of (a, d) 30, (b, e) 60 and (c, f) 90 minutes are shown. (Images were taken with a black and white AVT Marlin camera)

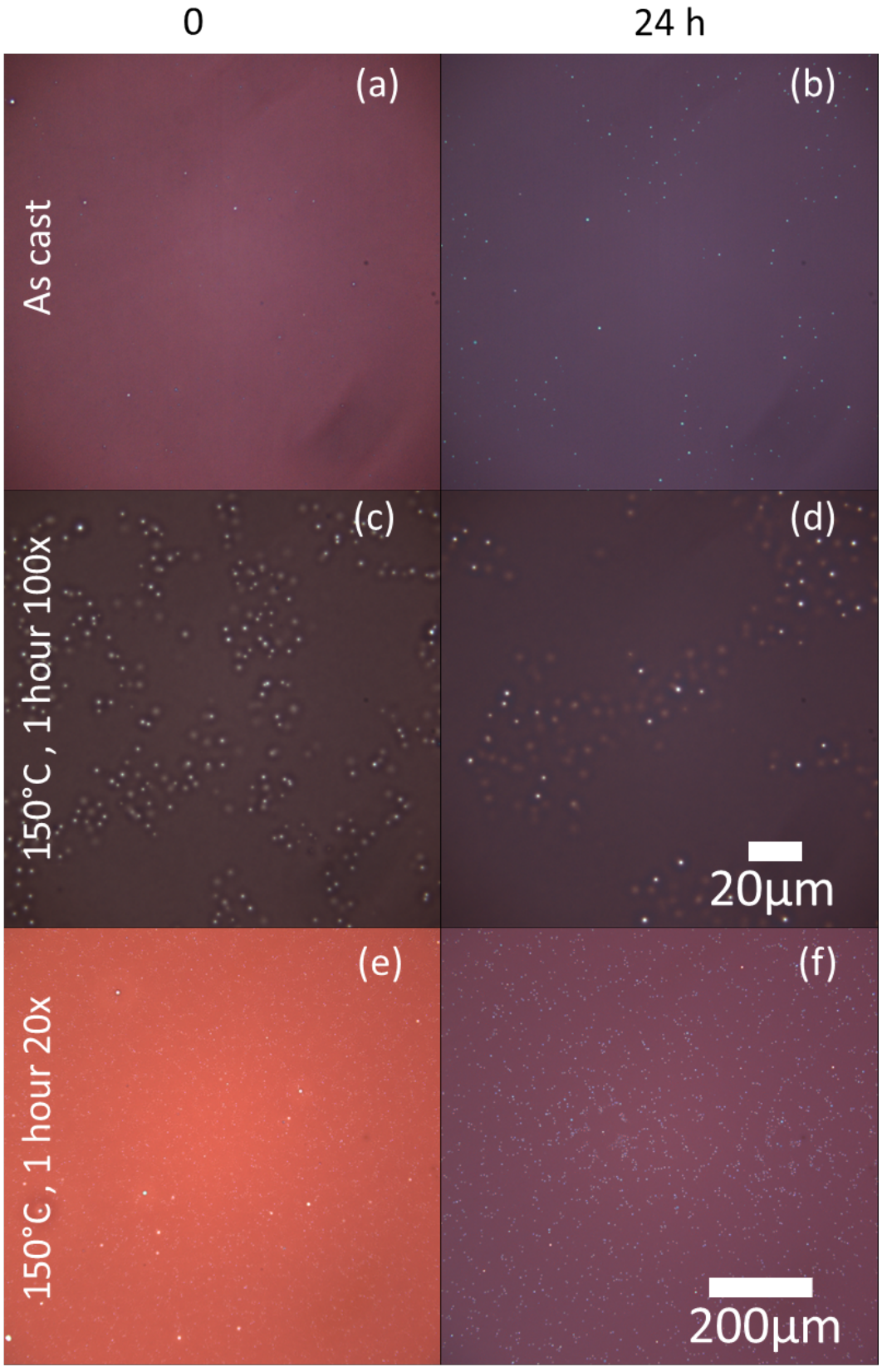


Figure 6.17: Optical microscopy images of 30 wt% PCBM/100k RRa P3HT thin films (h=70 nm) fabricated from a PCBM/toluene solution exposed to (a, c, e) 0 and (b, d, f) 24 h. (a-b) As cast and (c-f) annealed at 150 °C for 1 hour. Scale bar in (d) applies to (a-d) and scale bar in (f) applies to (e-f).

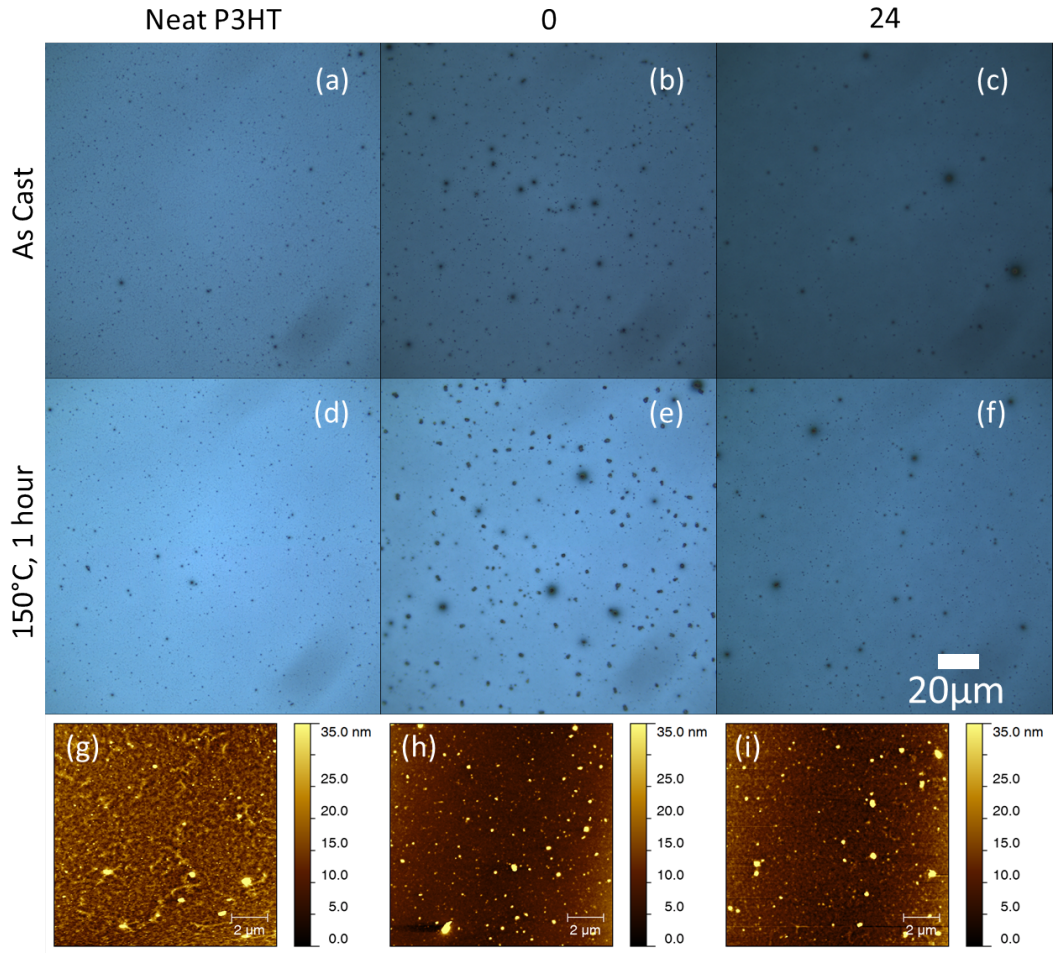


Figure 6.18: (a-f) Optical microscopy and (g-i) atomic force microscopy images of (a, d, g) 50k RR-P3HT and (b-c, e-f, h-i) 20wt% PCBM/50k RR-P3HT thin films (h=50 nm) fabricated from a PCBM/toluene solution exposed to light for (b, e, f) 0 and (c, f, i) 24 h. (a-c) show as cast films, and (d-i) films annealed at 150 °C for 1 hour.

6.4 Conclusions

Initially the light-induced fullerene oxidation and clustering in solution was investigated. Exposure to a 633 nm HeNe laser in ambient conditions causes the formation of fullerene epoxides ($C_{60}O_x$), confirmed by MS, NMR and FTIR spectroscopy. $C_{60}O_x$ and C_{60} clusters then form over time indicating a decrease in solubility. Clusters are formed due to Coulomb interactions between $C_{60}O_x$ pairs or $C_{60}O_x$ and C_{60}. $R_{h,2}$ is on the order of 100 nm and can be controlled via concentration, time, solvent, laser power and temperature (Figure 6.4). Clusters can also be formed to a lesser extent via exposure under ambient laboratory conditions, shown in Appendix 3. The clusters appear to be formed via a complex mechanism with four distinct stages (i) $C_{60}O_x$ production via light exposure (0-1 h), (ii) growth of cluster $R_{h,2}$ and number, (iii)

micron-scale cluster growth (15 h) and (iv) an increasing d_f and thus densification over time.

The HeNe laser used here is commonly used in light scattering systems, which, is a common technique to probe C_{60} aggregation [83, 84, 87, 88]. C_{60} oxidation upon light exposure reported here implies the studies which have employed light scattering techniques for C_{60} aggregation studies may be flawed, and other scattering techniques should be employed to confirm their results.

Oxidised and clustered C_{60}/toluene solutions are then shown to have an impact on thin film morphology with a significant decrease in the number of C_{60} clusters observed in thin films which were fabricated from solutions with $t_{h\nu}$>15 h, which correlates with *Stage III* of the cluster mechanism proposed. Comparisons to a concentration series of PS/C_{60} thin films indicated that approximately 50% of C_{60} in solution form aggregates on the micron scale. Thin films fabricated from light exposed, agitated solutions have a similar morphology to solutions not exposed to light, indicating that solutions can be rejuvenated. The applicability to systems relevant to OSCs was demonstrated with light exposed PCBM giving similar effects within PS and RRa-P3HT matrices as there was a decrease in the number of surface asperities, there is a less of an effect with RR-P3HT.

The potential impact of the fullerene epoxides lies in organic electronics [2] and other industries where fullerenes and their derivatives are commonly processed in solution prior to film formation [214]. Clustered C_{60}/toluene solutions can be mechanically or thermally treated to revert back to an unclustered state and are this could have potential benefits for long-term storage. Additionally, fullerene epoxides are used to synthesise further functionalised fullerenes [80]. Current methods to produce $C_{60}O_x$ either require a complex chemical synthesis [215] or high powered UV irradiation [82]. It appears that with this method fullerene epoxide production could be scaleable for example in a flow reactor and also there is the possibility for a specific cluster size to be obtained (by varying temperature, time, concentration, solvent etc) which could give a desired film morphology and optimal properties for a particular application.

7 Summary and Outlook

7.1 Summary

This thesis has carefully, experimentally, examined PS/fullerene/solvent systems and ensuing film formation. Initially, the effects of C_{60} on PS/toluene solutions, and subsequently the effect of PS on C_{60}/toluene are studied. The knowledge gained from PS/C_{60}/toluene mixtures was then transferred to PS/PCBM/toluene and PS/PCBM/chlorobenzene mixtures. This was followed by a study of C_{60} oxidation and cluster formation in solutions. Changes to thin film morphology on the micro- and nano-scale were observed with C_{60} aggregation both via PS addition and light exposure. From a careful review of the literature a number of areas where insufficient studies had been carried out were noted: (i) the effect of C_{60} addition to polymers chain dimensions in the dilute to semi-dilute regime, (ii) C_{60} and PCBM miscibility in PS/solvent solutions, (iii) impact of C_{60} aggregates on as cast and annealed thin film morphology, (iv) C_{60}/toluene and PCBM/toluene solution light exposure and (v) subsequent effect on thin film morphology.

(i) In Chapter 4 mixtures of PS/C_{60}/tol in dilute ($c << c^*$) to semidilute ($c > c^*$) regime were studied with a focus on PS R_g, R_h and mixture ξ. DLS and SLS were employed in the dilute regime and low C_{60} loadings (up to 0.09 wt%), there was no observed change in the the diffusion coefficient of PS, and hence no change in R_h with DLS. From SLS, there was no observed change in the M_w via a Zimm plot. Due to the light absorption of C_{60} higher concentrations could not be effectively studied (using the avalanche photodiode detector in the ALV light scattering system) and so SANS was necessary. For SANS, careful contrast matching experiments demonstrated that there was no change in PS R_g, in the dilute regime or semidilute regime or the mixture correlation length ξ. The correlation lengths obtained were comparable to those found in literature [20, 21] for a range of M_w from 20,000 to 1,000,000 g/mol. Others [36–39] have observed a decrease (≈50%) in polymer R_g at high colloidal loadings (≳8 wt%) which was not observed here; the highest C_{60} loading used in solution was 1 wt%.

(ii) Polymer induced C_{60} and PCBM aggregation below their respective miscibility limits in toluene and chlorobenzene was shown in Chapter 5 with a PS M_w range of 18000 to 775000 g/mol. C_{60} aggregation was shown to be PS M_w, PS concentration and time dependent. This is in agreement with some theoretical predictions [33–35] and experimental results [36–39]. A simple model based on the space filled by PS chains was given assuming 74% of the volume was occupied at the calculated c^*. From the experimental results, a finite miscibility of C_{60} in PS was estimated at 0.12 - 0.15 wt% from samples prepared from the solution state. This is

significantly lower than the values given in literature at 1-3 wt% [6, 7]. Thin polymer/fullerene films have applications in OSCs with complex morphologies necessary for optimal performance [1, 2]. An understanding of solution behaviour is necessary as is the subsequent film formation.

(iii) In Chapter 5 the effect of solution state, either homogenous or precipitated, was shown to alter thin film and bulk morphology via optical and atomic force microscopy. An alternate mechanism for the new morphologies in thin films was given based on the C_{60} aggregates (~100 nm) in solution acting as nucleation sites for free C_{60} molecules to be attracted to and grow further. Nucleating agents have been shown to improve organic electronic device properties [179, 180]. With careful solution processing using a mixture of polymer/C_{60}/PCBM/solvent, it may be possible to use C_{60} aggregates as ready-made nucleation sites allowing PCBM crystallisation to occur on a smaller length scale. Additionally, there are limits to the maximum film thickness and maximum C_{60} loading in thin films. This should also apply to other amorphous polymer/fullerene systems.

(iv) There are some contrasting reports in the literature on the light exposure of C_{60} in solution with degradation, photo-polymerisation and -oxidation reported [77–79]. Using a 4 mW, 633 nm HeNe laser, oxidation of C_{60} in toluene and chlorobenzene was demonstrated. Via mass, NMR and FTIR spectroscopies the formation of C_{60} epoxides, $C_{60}O_x$, with $1 < x < 3$, was shown. The $R_{h,2}$ of clusters containing C_{60} and $C_{60}O_x$ was shown to be time, laser power, solvent, concentration and temperature dependent. A mechanism for cluster formation was suggested with four distinct stages: (i) $C_{60}O_x$ production, (ii) growth of cluster size and number, (iii) micron-scale cluster growth and (iv) densification of clusters.

(v) Thin films prepared using light exposed C_{60}/toluene solutions showed a morphological evolution with light exposure time and the effect was found to be similar in thin films fabricated from light exposed PCBM/toluene solutions in a P3HT matrix. Aggregation was found to be reversible via mechanical and thermal energy with rejuvenated solutions giving a similar morphology to films prepared from C_{60}/toluene solutions which were not exposed to light.

In summary, two methods for fullerene cluster formation have been demonstrated, via the addition of a polymeric component or solution light exposure. The addition of polymer chains causes fullerene clustering below $c_{C_{60}/tol}$. This has polymer mass fraction, molecular weight and time dependences. The results from this work demonstrate that the understanding of polymer/fullerene solutions has significant consequences for thin film morphology and thus important implications for large scale processing of solution based polymer/fullerene blends, e.g. organic solar cells as the morphology of the active layer will greatly effect the efficiency of the device.

7.2 Outlook

The results presented in this thesis can be applied to a variety of solution processed nanocomposites. For a fundamental study, the effect of C_{60} addition on PS chain dimensions in theta conditions (cyclohexane at 34.5 °C) would be an interesting, complementary study to the results

presented in Chapter 4. Given previous work where high loadings of colloids were necessary to observe changes in polymer R_g, fullerenes with a higher solubility than C_{60}, such as PCBM, could be used. There appears to be an intrinsic miscibility limit for C_{60} in PS which is determined by the solution stage, which could also be explored further via comparisons to mixtures made from the solid state (as was attempted in Ref. 130).

With the interesting and important results from C_{60} aggregation in toluene with addition of polymer, as well as the solvent effects observed with PCBM in toluene aggregating but not in chlorobenzene, there is promise there for tuning the desired aggregation state of fullerenes via polymer M_w and concentration. Furthermore, there is scope for theoretical advancements for polymer/colloid theory as the current theories seem to apply to systems where the polymer is far more miscible in the solvent than the colloid. The theories seemingly only consider flexible polymers, a number of polymers of interest to OSCs are semi-crystalline and so add complexity. For systems such as P3HT/PCBM, the fullerene is far more miscible in a number of solvents [203]. Thus, there is aggregation of P3HT in solution prior to PCBM aggregation [100]. The only solvent given in Ref. 203 where P3HT has a higher miscibility than PCBM is in tetrahydrothiophene and so for an analogous system to PS/C_{60}/toluene, P3HT/PCBM/tetrahydrothiophene could be studied.

The differences in morphologies of the drop cast samples from precipitated and homogenous solutions may account somewhat for the disparity in the nanocomposite melt literature. Further studies could correlate the solution state with the structures of the drop cast state. The potential fractal nature of the C_{60} structures would also be of interest as well as using a range of different polymer matricies which may effect the morphology.

C_{60} epoxides are a precursor to functional fullerene synthesis [80]. If this synthetic route can be controlled it could be more efficient than complex synthesis [215] or high powered UV irradiation [82]. The mechanism of cluster formation consisting of C_{60} and $C_{60}O_x$ could be further understood by a series of experiments where C_{60}/toluene light exposure is carried out for a set time, the solution can then be mechanically or thermally reverted to dispersed C_{60} and $C_{60}O_x$molecules. Aggregation can then be monitored over a longer time period with measurements taken every few hours, thereby allowing the growth rate of clusters to be elucidated without excessive additional oxidation. A temperature study focusing on lower temperatures may also give more information with regards to the aggregation mechanism.

This thesis has demonstrated the modification of bulk and thin film morphology of polymer/fullerene blends which are dependent on the casting state, either homogenous or precipitated, and light exposure, of the initial solution. A control of thin film morphology is a necessity for many applications. Given the importance of fullerenes for OSCs this work will have a great impact in this field as large-scale solution-based processing is a necessity for commercialisation of OSC devices. Consistency in device performance is necessary and so the solution stage of the processing route must be well-understood.

Appendices

Appendix 1

Refractive Index Size-Exclusion Chromatography (RI-SEC) was performed using an Agilent 1200 Series GPC-SEC Analysis System fitted with two PLgel mixed-B columns in series running a chlorobenzene eluent and calibrated to polystyrene standards. Samples were dissolved in chlorobenzene and filtered with a 0.2 μm PTFE filter to remove particulate matter. Polymer eluted between 14 and 18 minutes. GPC traces for the polymers used in Chapter 5 are shown in Figure A1. NP's

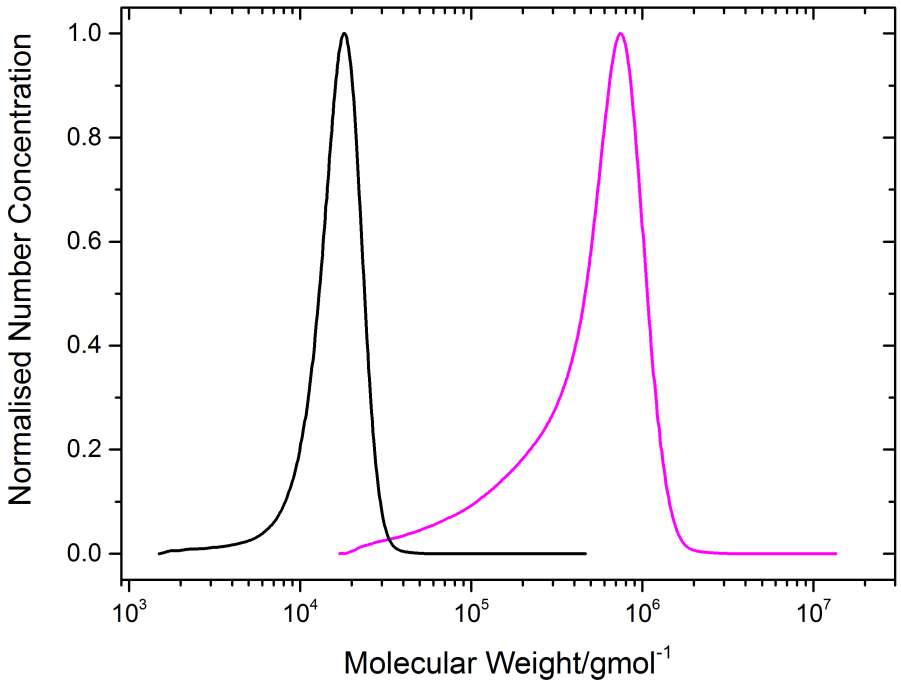


Figure A1: GPC traces for two of the polystyrene M_w used in Chapter 5 with 18000 and 775000 gmol^{-1} .

Appendix 2

NMR spectra of C_{60} after 0 and 21 hours of light exposure. A peak at 49 ppm can be observed in the light exposed sample, confirming the presence of an epoxide species.

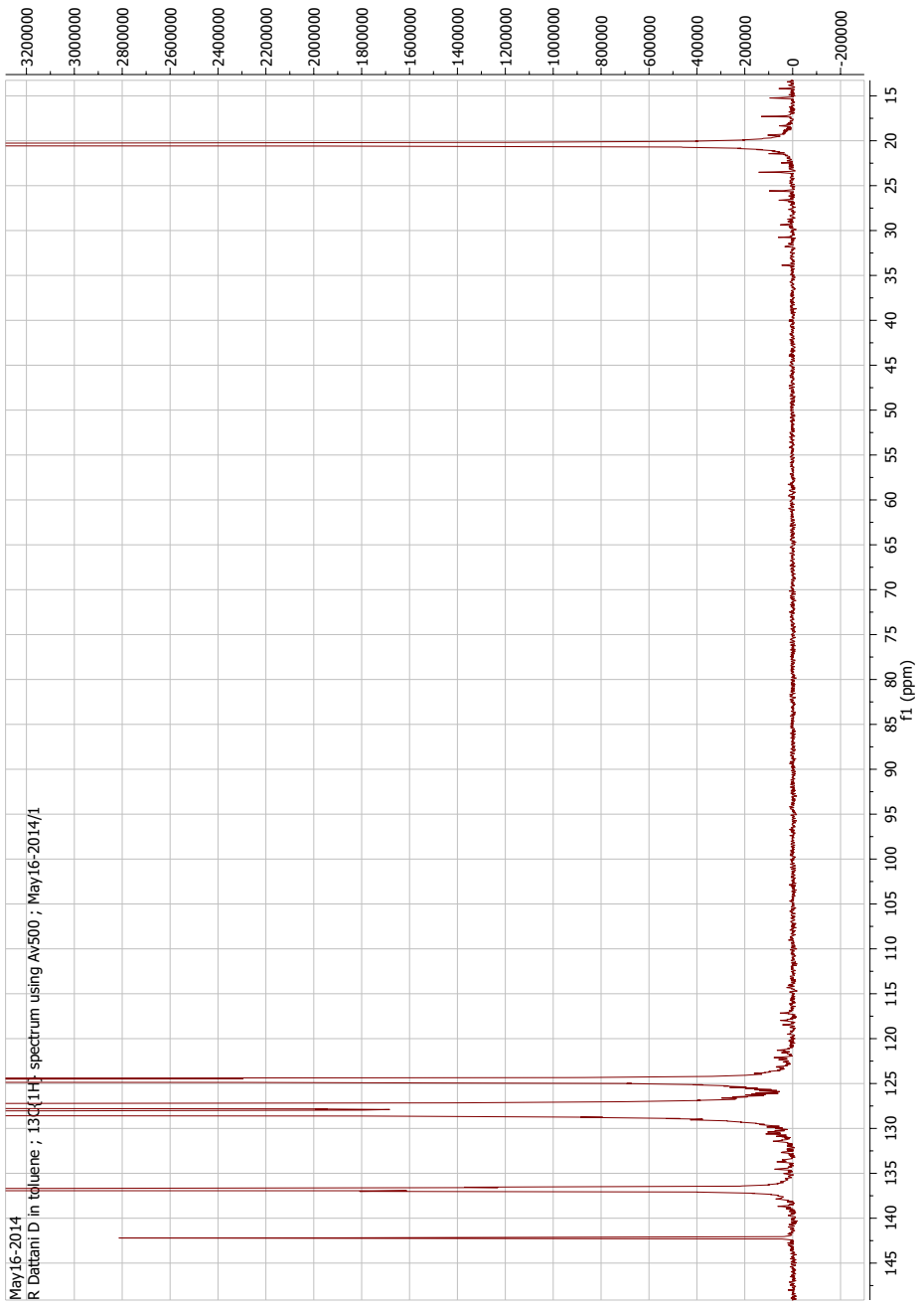


Figure A2: ^{13}C NMR of C_{60} in toluene.

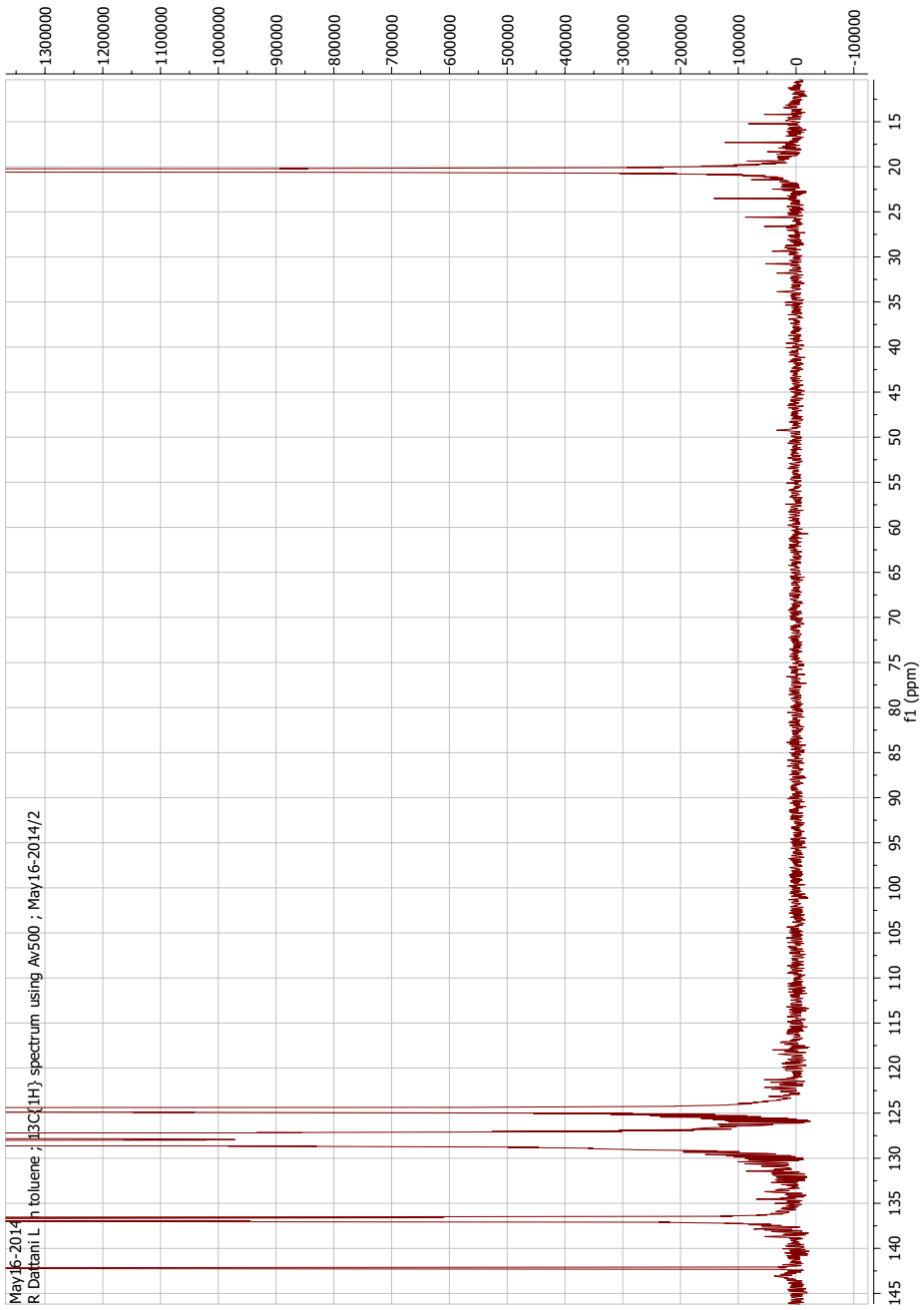


Figure A3: ^{13}C NMR of C_{60} in toluene exposed to red laser for 21 hours.

Appendix 3

A number of different light sources were trialled to obtain the most effective route to forming fullerene clusters in solution, seen in Figure A4. UV light exposure was carried out using a 100 W UV-A flood light at with $\lambda = 365$ nm (Spectroline SB-100 PA/FB). The high intensity white light was from Advanced Illumination (DL2230) with maximum irradiance of 1.34 mW/cm^2. The most effective light source found was a 4 mW, 633 nm HeNe laser, however there is still some cluster formation under ambient conditions. There are fewer clusters formed and this is most likely to be due to the photon flux, as a clear trend can be seen with light intensity from ambient to the 4 mW HeNe laser. UV irradiation does not produce clusters after a significantly longer exposure time which, given the results of C_{60} degradation, could be expected [77, 78].

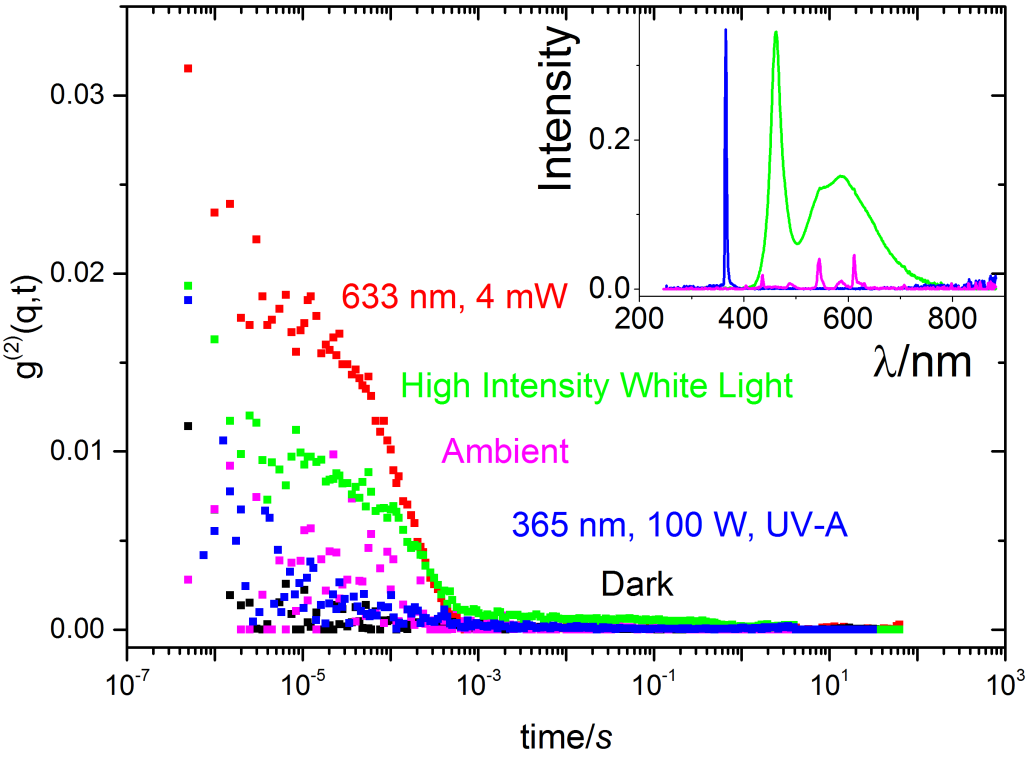


Figure A4: Correlation function $g^{(2)}(q,t)$ after 1 hour light exposure of 0.2 wt% C_{60}/toluene from 633 nm, 4 mW laser, high intensity white and ambient light. A 0.3 wt% C_{60}/toluene solution was exposed to 365 nm, 100 W UV light for 26 hours. Inset shows spectra of high intensity white, UV and ambient light, measured using a spectrophotometer (EPP2000c, StellarNet Inc.).

List of Figures

1.1 Schematic of a polymer chain under (a) low and (b) high magnification, illustrating a random walk compromising short rigid segments. 1

1.2 Polymer in solution from (a) dilute through to (b) overlap and (c) semidilute. . . 4

1.3 Schematics of a polymer/colloid system within the (a) colloid limit (CL) and (b) protein limit (PL). PS/C_{60} is clearly a system within the PL as $R_C \ll R_g^{poly}$. . . . 7

1.4 Simulated structures from the various kinetic growth models. Fractal dimensions (D) listed are for 3D objects and 2D objects are shown. Simulations were carried out by Meakin [42] and contain 1000 primary particles. Reproduced with permission from Ref. 41. Copyright Cambridge University Press. 9

2.1 Trend of increasing apparent diffusion coefficient as laser power increases, levelling off at high power. Adapted with permission from Ref. 60. Copyright 1999 American Chemical Society. 12

2.2 Phase diagrams for P3HT/PCBM (a) (Reproduced from Ref. 131) Onset of crystallisation (×) and (•) represent the liquidus lines. (b) (Reproduced from Ref. 132) melt crystallisation temperature of P3HT (▲), T_m of P3HT (•); melt crystallisation temperature (△), cold crystallisation temperature (□), T_m of PCBM (○); blend T_g (×). (c) (Reproduced from Ref. 133) blend T_g (△), blend T_m (◇), transition A (○), transition B (+), transition C (■), transition D (▼), P3HT liquid crystal transition (◆). (d) Combined phase diagrams from (a-c). From Ref. 131 : Blend T_m (△), Onset of recrystallisation (▲); Ref. 132: P3HT T_m (□), PCBM T_m (□) and Blend T_g (■); and Ref. 133: Blend T_g (•) and Blend T_m (○). (a) Adapted with permission from Ref. 131. Copyright 2008 John Wiley and Sons (b) Reprinted with permission from Ref. 132. Copyright 2009 American Chemical Society. (c) Reprinted with permission from Ref. 133. Copyright 2011 American Chemical Society. 21

3.1 (a) Typical correlation functions, obtained using a Malvern Nano-S, for a single species in solution, 60 nm diameter PS latex (□) and 220 nm diameter silica NPs (○). Inset shows cumulant fit for 60 nm PS latex particles, the gradient of the straight line fit can give D_0 and thus an R_h of 38 nm. (b) Correlation function for a mixture of two nanoparticles, 60 nm diameter PS latex and 220 nm diameter silica NPs. The correlation function can be fit using Equation 3.4 (—). The individual additive contributions are for the latex particles (—) and silica NPs (—). 34
3.2 Model SANS data for (a) sphere and hollow sphere with a shell of negligible thickness with radius of 0.5 nm, dashed line corresponds to 1/radius, and (b) ideal Gaussian polymer coil, R_g of 8 nm with power laws of -4 and -2. 39
3.3 Coherent SANS data for a 9.5 wt% 1 Mg/mol deuterated PS and 0.5 wt% C_{60} solution in deuterated toluene (◂). A form factor with q^{-4} (—), an OZ form factor (—) and a sum of the two (—) are shown. 41
3.4 Optical Microscopy image processing with Route 1 (a-d) giving cluster dimensions, area fraction (A_f) and number of surface features and Route 2 (e-h) giving characteristic length scale (λ^*) respectively. 43
3.5 AFM step height standard linecuts, averaged from the two lines shown in inset image. 44

4.1 Ternary diagram showing the points where this system was studied. For the some of the molecular weights used c^* is given. Note that experiments on 65k were only in the dilute regime thus c^* is not shown. Isopleths 1-4 are marked out for clarity. The black dashed line represents the reported miscibility limit ($c_{C_{60}/tol}$) of C_{60} in toluene (0.32 wt%) [198]. 47
4.2 Ternary diagram of PS/C_{60}/toluene showing the initial concentrated state of the solution used for isopleth 1b. The black dashed line represents the miscibility limit in toluene (0.32 wt%) [198]. 49
4.3 UV-Vis spectra as a function of C_{60} loading. Inset shows increasing absorbance at $\lambda = 633$ nm as a function of C_{60} loading. 53
4.4 Static Light scattering results from a 0.2 wt% C_{60}/toluene solution. Dashed line is drawn as a guide to the eye. 54
4.5 Viscosity of C_{60}/toluene solutions as a function of fullerene concentration. There is no change in viscosity with fullerene addition within measurement error. 55

4.6 Correlation function for 0.3 wt% C_{60} in toluene (•) and neat toluene (•) with a model for a particle with R_h of 0.35 nm measured at 173° corresponding to q=2.96×10^{-2} nm^{-1}. There is no clear decay occurring for this size regime and given the similarity between the C_{60}/toluene solution and toluene and it is not possible to observe individual fullerene molecules on the Malvern Nano-S DLS system. 56
4.7 Total Scattering Intensity from SANS for C_{60}/toluene solutions as a function of C_{60} concentration ranging from 0.1 to 2 wt%. 57
4.8 Total Scattering Intensity from SANS for various PS/C_{60}/toluene solutions with a concentration of 2.5 wt% 79k PS-h or 80k PS-d (as necessary) with 0.14 wt% C_{60}, using different SLD contrasts. (A) PS-d/C_{60}/tol-h (•), (B) PS-h/C_{60}/tol-d (•), (D) PS-h/C_{60}/tol-h (•) and (E) PS-h/C_{60}/tol-d/tol-h (•). 58
4.9 Graphic of the three SLD contrasts used. Contrast A uses deuterated PS (PS-d) and C_{60} with hydrogenous toluene (tol-h) (20k, 100k & 1M PS), so that the fullerene and polymer contributions can be observed. Contrast B uses hydrogenous PS (PS-h) and C_{60} in deuterated toluene (tol-d) (79k & 100k), here only the polymer contribution to the scattering is observed. Contrast C uses a mixture of PS-h and PS-d (100k) , thus the R_g of single chain PS in a semidilute regime can be found. 59
4.10 Zimm analysis of Static Light Scattering from isopleth 1 of (a) 65k PS/toluene and (c) PS/C_{60}/toluene with C_{60}:PS of 0.05. PS concentrations = 1.93 (▪), 0.97 (•), 0.49 (▲), 0.25 (▼) and 0.12 wt% (◆). (b) shows the extrapolation of the intercepts from (a) and (c) for PS/C_{60}/toluene (▪) PS/toluene (•) to zero concentration. For the higher concentrations of C_{60} only the high q portion of the data was extrapolated to zero. The intercept at zero concentration gives $1/M_w$, which for PS with and without C_{60} is 61.3 $kgmol^{-1}$. This is close to the expected 65 $kgmol^{-1}$. (d) Guinier plot of low q scattering. R_C of 195±25 nm and 90±10 nm could be fitted for PS concentrations of 1.93 and 0.97 wt% respectively. This is likely to arise from C_{60} aggregation taking place below $c_{C_{60}/tol}$ of 0.32 wt%. . . . 61
4.11 Dynamic Light Scattering of PS/C_{60}/toluene (C_{60}:PS of 0.05) from isopleth 1, θ = 80° (q = 0.019 nm^{-1}), at three concentrations, 1.9 (▪), 0.49 (▪) and 0.12 wt% PS (▪). Solid lines are fits to the data using Eq 3.4. Inset shows the result of a CONTIN analysis for the three concentrations. A second decay emerges for 1.9wt% PS, with an $R_h^{Cluster}$ in the region of 200 nm, following 12 hours of sample preparation. 62

4.12 (a) and (b) show fitted diffusion coefficient of the fast mode of the multiexponential fit (Equation 3.4) from DLS across the accessible q range for (a) PS/toluene and (b) PS/C_{60}/toluene (b); PS = 1.93 (▪), 0.97 (●), 0.49 (▲), 0.25 (▼) and 0.12 wt% (◆). (c) shows the extrapolation to zero concentration for isopleth 1 showing PS/toluene (▪) and PS/C_{60}/toluene with C_{60}:PS of 0.05 (●). As shown by the black line, there is no difference in the diffusion coefficient either with or without C_{60}. This corresponds to an R_h of 6.45 nm. (d) demonstrates the procedure described by Kanai and Muthukumar [193] where the values fitted for a_i in Equation 3.4 can inform the origin of the intensity of scattering in SLS. Here, this is shown for 1.93 wt% PS and 0.09 wt% C_{60}. Total intensity (▪) was split into single PS chains (●) and C_{60} aggregates (●). The diffusion coefficient via DLS is shown in the inset, demonstrating the bimodal distribution and hence the scattering intensity arising from two contributions. This confirms that the increase in scattering intensity at low q is from C_{60} aggregates. 63

4.13 Coherent scattering intensity from small angle neutron scattering for (a) 100k PS/C_{60}/toluene, where C_{60}:PS=1 and (b) 100k PS/toluene. PS = 0.15 (▪), 0.2 (●), 0.25 (▲), 0.3 (▼), 0.4 (◆) and 0.5 wt% (◀) . The inset in (a) shows fitted R_g and in (b) χ for C_{60}/PS/toluene (filled symbols) and PS/toluene (hollow symbols), the dashed line in (a) is a guide to the eye and is calculated using R_g=0.0125$M_w^{0.595}$ [4]. 65

4.14 Coherent scattering intensity from small angle neutron scattering for 79k PS on isopleth 3 (constant concentration of 2.40±0.15 wt% PS with C_{60} loadings from 0 to 0.96 wt%) using contrast B. No contribution from the C_{60} is observed due to contrast matching and was in order to parse out small differences in ξ, however the data clearly shows there is no change in correlation length, ξ, from PS/toluene to PS/C_{60}/toluene at 0.96 wt% C_{60}. ξ ranges from 3.44 to 3.54 nm in the fits (solid lines) shown. 66

4.15 Coherent scattering intensity from small angle neutron scattering for isopleth 4 (C_{60}:PS = 0.05). (a-c) Use contrast A (PS-d, C_{60} and tol-h); C_{60} = 0.15 (▪), 0.2 (●), 0.25 (▲), 0.3 (▼), 0.4 (◆) and 0.5 wt% (◀). (d) Is a comparison for contrast A (Circles) and B (Squares) (PS-h, C_{60} and Tol-d) to demonstrate the low q upturn was due to scattering contributions from C_{60}. 67

4.16 (a-b) Weighting factor, A, and (c-d) S_V for the three molecular weights (20k, 100k and 1M) studied on isopleth 1 and 5. For (a) and (c) the dashed black line indicates $c_{C_{60}/tol}$ (0.32 wt%) as determined by Ruoff et al. [198]. The values for A from the dilute 100k-d PS (100k-d dil) seen in isopleth 1 is also included. The data for 100k-h is included as a baseline for which the C_{60} aggregation is not observed due to contrast matching. (b) and (d) A and S_V as function of M_w for isopleth 4, at C_{60} = 0.3 (▽), 0.4 (◇) and 0.5 (◁) wt%. 69

4.17 (a) Fitted correlation length ξ against PS concentration in the overall PS/C_{60}/toluene solution for isopleth 4 (C_{60}:PS = 0.05) for the three M_w studied (filled symbols). The hollow symbols are literature data from King et al. [20] (100 kg/mol, black) and Hamada et al. [21] (17.5, 110 and 900 kg/mol, blue). Dashed lines indicate c^* for the 20k and 100k. c^* for 1M is not on this scale, as indicated by the arrow. (b) Reduced correlation length ξ/R_g of data from both isopleth 3 and 4 in the semidilute regime, covering a regime of C_{60}:PS from 0 to 0.41 and C_{60} loading from 0 to 0.96 wt% plotted against reduced concentration c/c^*. A line of best fit of the form $(1+\beta c/c^*)^{\alpha}$, where β=4 and α=-0.77 [200]. R_g was calculated using R_g[nm]=1.25×10$^{-5}M_w^{0.595}$. 70
4.18 Contrast C used to evaluate effect of C_{60} on single chains taken at either end of isopleth 4 (0.15 and 0.5wt% C_{60}). All samples contained 0.11±0.003wt% PS-h. Solid lines are fits to the data using the PolymerExclVolume model in SasView [194]. Inset shows fitted R_g with total concentration of PS (hydrogenous and deuterated) for PS-h/PS-d/tol-d (•) and C_{60}/PS-h/PS-d/tol-d (○) in the semidilute regime, confirming there is no change in R_g upon the addition of C_{60}. 71

5.1 Ternary diagram with samples studied for 65k PS/C_{60}/toluene mixtures, showing $c_{C_{60}/tol}$ miscibility line (– – –). 74
5.2 Images of C_{60}/toluene solutions (vials turned upside down to demonstrate C_{60} aggregates) close to the reported miscibility limit (0.32 wt%) [198]. Aggregates can clearly be observed between 0.3 and 0.28 wt%. No aggregates are seen at 0.27 wt% and so this is used as the new miscibility limit. Inset shows vials the right way around in the same order. 77
5.3 Images of macroscopic fullerene aggregates induced by polymer addition, from the (a) bottom of a vial and (b) wall of a vial. Image width is ≈1 cm. 78
5.4 SLS data showing PS/C_{60}/toluene mixtures. (a) Constant PS concentration at 0.30±0.01 wt% with C_{60} from 0.11 to 0.26 wt%. Inset shows fitted R_C via Guinier analysis. There is a clear trend with C_{60} loading leading to a detectable R_C. (b) Fixed C_{60} concentration of 0.25±0.01 wt% and varying PS concentrations from 0 to 1.02 wt%. Inset shows R_C via Guinier analysis, there appears to be a trend for increasing PS concentrations having larger aggregate sizes. For both graphs the color in the inset refers to the same colour within the I vs q plots. 79
5.5 C_{60} R_C via Guinier analysis as a function of C_{60} loading and PS concentration. There is a trend of a decreasing miscibility limit with increasing PS concentration. Light scattering was carried out after 48 hours of solution stirring. 80
5.6 (a-c) DLS correlation functions at constant PS concentration at (a) 0.30±0.01 (▪) (b) 0.6±0.1 (●) (c) 1.00±0.07 wt% (▲) with C_{60} from 0 to 0.28 wt%. (d) shows fitted R_h/R_h^{PS} via fits to Equation 3.4. There is no change in R_h^{PS} with C_{60} loading. 81

5.7 Ternary diagram of 65k PS/C_{60}/toluene showing homogenous (○) and precipitated (○) samples. $c_{C_{60}/tol}$ (– – –) is shown. 82
5.8 Time study of 0.29 wt% PS and 0.28 wt% C_{60} via SLS, the number of clusters observed within the solution decreases as they are forming micron scale precipitates at bottom of SLS cuvette and hence going out of the q range of the instrument. . 83
5.9 Scaling calculations for (a) occupied volume (V_{occ}) and (b) free volume (V_{free}) with four PS M_w shown. 18, 65, 100 and 775 kgmol^{-1}. Dashed line indicates the volume at which maximum packing efficiency is achieved i.e. c^*. 85
5.10 PS and C_{60} concentrations using data shown in Fig. 5.7 to magnify the effect of increasing PS concentration on C_{60} miscibility limit within PS/C_{60}/toluene mixtures. Homogenous (•) and precipitated (•) solutions are shown as before. $c_{C_{60}/tol}$ is shown at 0.27 wt% (– – –) as well as the published miscibility limit at 0.32 wt% [198]. The calculated miscibility limit (—) (described in the text) agrees well with the observed homogenous and precipitated phases, shown in green and red respectively. The plateau at ~0.15 wt% C_{60} indicates the finite miscibility of C_{60} in PS. 86
5.11 (a) Using the calculations described above, the modelled miscibility limit for C_{60}in PS/toluene is shown for 18, 65, 100 and 775 kgmol^{-1}. Homogenous (•) and aggregated samples (○) are indicated in the relevant colour. Note that experiments were only carried out using 18 and 775 kgmol^{-1} PS. (b) Static Light Scattering results at fixed concentration of PS/C_{60}/toluene at 0.3 wt% PS and 0.26 wt% C_{60} with varying PS M_w at 18k, 65k and 775k. Inset shows that there is no change in fullerene cluster size with M_w in dilute solutions. 88
5.12 Calibration for varying PS concentration with spin coater rpm. Three PS concentrations are used: 1, 2 and 5 wt%. The equations are from lines of best fit and were used to achieve the similar film thicknesses from solutions starting at different concentrations. 90
5.13 Demonstration of (a) minimum and (b) maximum film thickness' achievable from homogenous solutions with indications of C_{60} solid loading in the final film. This enables one to chose a PS concentration at which their desired C_{60} loading and film thickness can be met. Homogenous (•) and precipitated (•) solutions are shown as before. $c_{C_{60}/tol}$ is shown at 0.27 wt% (– – –) as well as the published miscibility limit at 0.32 wt% [198]. The calculated miscibility limit (—) (described in the text) agrees well with the observed homogenous and precipitated phases, shown in green and red respectively. Constant C_{60} solids mass fraction in the film are shown (⋯) with the mass % of C_{60}/PS noted. 91

5.14 Reproduction of Figure 5.10 to highlight solutions used in the thin film study. Thin films were fabricated from the circled solutions and are summarised in Table 5.2. Homogenous (•) and precipitated (•) solutions are shown as before. Constant C_{60} solids mass fraction in the film are shown ($\cdots$) with the mass % of C_{60}/PS noted. 92
5.15 (a-c, j-l) Optical microscopy and (d-f, m-o) AFM images with line cuts (g-i) of the lines indicated in the as cast 60 nm films in d-f and (j-o) films annealed at 180 °C for 30 minutes. Left images are made from P1C01, centre from P1.5C015 and on the right from P2C02. From the as cast films, homogenous solutions, P1C01 and P1.5C015 appear similar the micron lengthscale. In the nanoscale, clusters on the order of 10 nm visible in all films, with 200 nm clusters seen in P2C02, corresponding to those seen via SLS. After annealing it is clear that there are significantly more clusters in the solution which was originally homogenous, whereas P1.5C015 appears very similar to P2C02 on the micron scale. 94
5.16 (a-b, e-f) Optical microscopy and (c-d, g-h) AFM images of (a-d) as cast 130 nm 5 wt% C_{60}/PS films and (e-g) films annealed at 180 °C for 30 minutes. As expected from the previously shown 9 wt% C_{60} films, the sample spun from the precipitated state (P4C021) has some micron scale aggregates.There is a clear difference between the two samples, with the homogenous solution giving a morphology with fewer, but larger clusters and the precipitated giving smaller, but numerous clusters. 96
5.17 Radial profiles of films prepared from P2.3C012 (▪) and P4C021 (▪) after annealing at 180 °C for 30 minutes. Insets shows the FFT's of films from which the radial profiles are extracted. There is a clearly a structural peak present for the films fabricated from P2.3C012. 97
5.18 Optical Microscopy images of 9 wt% C_{60} loaded 60 nm thin films cast at different solution ages, from 0 to 5 days. 98
5.19 Area fraction of 9 wt% C_{60} loaded 60 nm thin films cast at different solution ages, from 0 to 5 days. 99
5.20 (a-c, g-i) OM and (d-f, j-l) AFM showing 9 wt% C_{60} at day 5 solution age 60 nm thin films in the (a-f) as cast state and (g-l) annealed at 180 °C for 30 minutes. White lines in j-l are line cuts used in Figure 5.21. 101
5.21 (a) Line cuts from AFM (Figures 5.20j-l) of 9 wt% C_{60} at day 5 solution age 60 nm thin films annealed at 180 °C for 30 minutes. (b-d) Cropped AFM images from Figures 5.20j-l zooming in on regions where line cuts were taken from. (b) P1C01, (c) P1.5C013 (d) P2C02. Small C_{60} clusters can be seen in the film prepared from P2C02 compared to P1C01 and P1.5C015. 102

5.22 (a-c, g-i) Optical and (d-f, j-l) atomic force microscopy of 60 nm 9 wt% C_{60} films annealed at 180 °C for 30 minutes, comparing films cast from solutions at (a-f) day 0 and (g-l) day 5. 103
5.23 (a-b, e-f) Optical and (c-d, g,h) atomic force microscopy of as cast 5 wt% C_{60} 130 nm thin films at (a-d) day 0 and (e-h) day 5 of solution age. 105
5.24 (a-b, e-f) Optical and (c-d, g,h) atomic force microscopy of 5 wt% C_{60} 130 nm thin films annealed at 180 °C for 30 minutes at (a-d) day 0 and (e-h) day 5 of solution age. 106
5.25 (a-f) AFM images of (a-b) 5 wt% C_{60} films annealed at 180 °C for 30 minutes and (c-d) a scratch in the film surface for thickness measurement. (e-h) THF dissolution experiment to show the micron-sized clusters observed via OM consist of 200 nm clusters. (i-j) OM images prior to dissolution for comparison. White lines in c-f are line cuts for height profiles in Figure 5.26. 108
5.26 Line cuts from AFM (a) of Figures 5.25e-f of 5 wt% C_{60} after the PS was washed off with THF. (b-c) 5 μm line cuts from Figures 5.25c-f to demonstrate there is no change PS thickness after annealing. 109
5.27 Optical microscopy of 130 nm films (a-b) as cast and (c-d) annealed at 140 °C for 2.5 hours. There is a clear difference between the two samples, with the precipitated solution giving a morphology with more clusters. 112
5.28 Optical microscopy of drop cast films on silicon substrates (a-d) as cast and (e-f) annealed at 180 °C for 30 mins. There is a clear difference between the two samples, with the sample prepared from the homogenous solution giving a vastly different morphology than that from the precipitated solution. The image width of the inset in (e) is 10 μm. 113
5.29 (a) Number density of 4-7 representative images of the as cast drop cast samples shown in Figure 5.28a-d and f. Due to the morphology shown in Figure 5.28e consistent, representative image analysis proved difficult. Typical images are shown in (b-d) of (b) as cast from P2.3C012, (c) as cast from P4C021 and (d) annealed from P4C021. 114
5.30 Optical microscopy of drop cast films on silicon substrates (a-b) cast at 60 °C, dried within 30 minutes, (c-d) cast at 25 °C, dried over 24-48 hours and (e-f) samples shown in (c-d) annealed at 180 °C for 30 mins. There is a clear difference between the two samples, with the sample prepared from the homogenous solution (a, c, e) giving a vastly different morphology than that from the precipitated solution (b, d, f). The scale bar in (c) applies to (a-d) and the scale bar in (e) applies to (e-f). 115
5.31 Scattering data for 0.63 wt% PCBM/CB and 2 wt% 775k PS/0.56 wt% PCBM/CB using (○) SLS and (□) SAXS, which in the configuration used did not have an overlap with SLS. 116

5.32 Ternary diagram of 775k PS/PCBM/Tol. Homogenous (•) and precipitated (•) are shown alongside the miscibility limit of PCBM in toluene ($c_{PCBM/Tol}$) at 0.9 wt% (– – –). (– – –) indicates miscibility of PCBM in 775k PS/toluene. Exact concentrations of solutions used are shown in Table 5.4. 117
5.33 Ternary diagram of 775k PS/PCBM/CB. Homogenous (•) and precipitated (•) are shown alongside the miscibility limit of PCBM in CB ($c_{PCBM/CB}$) of 2.6 wt% (– – –). Exact concentrations of solutions used are shown in Table refsec:App3 . 119

6.1 (a) Mass spectroscopy of C_{60} in toluene exposed for 21 h (and diluted with IPA for injection), where peaks corresponding to $C_{60}O_x$ with x=0 to 3 are illustrated with possible epoxides formed. (b) FTIR spectra of C_{60} and $C_{60}O_x$ embedded in KBr discs. $C_{60}O_x$ solution was exposed to laser light for 2 weeks prior to sample preparation. Additional features can be observed in light exposed sample in the region expected for C-O bonds. (c) DLS correlation function, $g^1(q,t)$, for a control study of freshly prepared (▪) and aged in the dark for 14 days (•) 0.3 wt% C_{60} in toluene. (d) DLS correlation function, $g^1(q,t)$, for a 0.3 wt% C_{60} in toluene at various times of light exposure following t=0 (▪), 1 (▲), 5 (◆), 15 (▼), 20 (•) h. Solid lines are fits using Equation 3.4. There is the appearance of a second decay after 1 h and the appearance and growth of a third decay after 5 h. Inset shows transmission microscope image of C_{60} clusters ,on the micron scale, after 16 h light exposure. 130
6.2 Calculated energetic landscape for separation of $C_{60}O$ molecules using point charges from (▪) quantum chemical calculation on a single $C_{60}O$ molecule, (•) a quantum chemical calculation of a pair of $C_{60}O$ molecules at 3.5, 4.0, and 5.0 Å. The separation distances are given by the closest atomic approach, i.e. the distance from the oxygen atom to the closest carbon on the neighbouring molecule, and is indicated on the figure. 131

6.3 Amplitude, a_2, obtained from DLS using Equation 3.4, corresponding to 100s nm fullerene clusters in 0.3 wt% C_{60}/toluene solutions for various processing conditions. (a) Mechanical agitation. The solution was initially exposed to light for 21 h and then placed on a vortexer with measurements taken every two minutes. Once the scattering amplitude dropped to the initial level the $C_{60}O_x$ clusters were allowed to grow while DLS measurements were taken every hour to minimise further oxidation. (b) Solution temperature (blue line, scale on right axis). The sample was initially exposed to light for 13 h and the scattering measurement carried out as previously. The solution is then heated in the dark to 65 °C for 6.5 hours, cooled to 25 °C and allowed to equilibrate for 30 minutes before measurement was carried out again. This was repeated 3 times until the scattering amplitude was approximately equal to its starting value (~0.03). The $C_{60}O_x$ solution is then kept in the dark and measured every hour. This would result in minimal extra oxidation and demonstrates the reversibility of $C_{60}O_x$ clustering. Gray lines are guides to the eye. 133

6.4 DLS results comparing different solution conditions for light induced aggregation and oxidation of C_{60}. For all experiments 0.3wt% C_{60} in toluene is shown in Black for comparison. Symbols $\triangledown$ denote cluster R_h, $\circ$ a_2 and $\triangle$ a_3. The relevant parameter is listed to the right of the graph. The conditions explored were: a: Concentration (0.1-0.3 wt%), b: Temperature (25-45 °C), 55 and 65 °C did not result in cluster formation, c: Solvent (toluene (Tol), chlorobenzene (CB), anhydrous toluene (Tol-A) and oxygenated toluene (Tol-O)) and d: Laser power (0.44-4 mW). 135

6.5 DLS results from varying O_2 levels within the solution, form Figure 6.4c, focussing on the scattering intensity, a_2 ($\circ$) and a_3 ($\triangle$). 136

6.6 Graphical representation of the intermittent laser experiments carried out. The three pulsed regimes were: (– – –) always on, (—) 6 minutes on, 20 minutes off and ($\cdots$) 6 minutes on, 54 minutes off. Inset shows equivalent for light exposure times ($t_{h\nu}$). 137

6.7 (a-b) Results from intermittent laser experiments with DLS, a_2 and $R_{h,2}$ collapse with (a) time and (b) exposure time ($t_{h\nu}$) whereas a trend is observed with a_3 using the three regimes described in Figure 6.6. (■) always on, (▲) 6 minutes on, 20 minutes off and (●) 6 minutes on, 54 minutes off. (c) Correlation functions of freshly prepared (■) C_{60} exposed to light for 45 mins (■), 1 h (■) and 31 h (●) after which the solution is left in the dark for a further 12 h (●). This indicates a delay or lag time between the initial epoxidation and cluster formation and that cluster formation is not limited by $C_{60}O_x$ population as there is additional growth in cluster $R_{h,2}$ with no additional epoxide production. (d) Static Light Scattering of a 0.3 wt% C_{60}/toluene solution exposed to a 4 mW, 633 nm laser for a period up to 24 hours. The inset shows an increasing R_g via Guinier analysis (●) and fits to the fractal model (■) by Teixeira [90]. There is also an increase in d_f by fits to the fractal model [90] (■) or the power-law (●) between $7.1 \leq q \leq 10.5$ $\times 10^{-3}$ nm^{-1}. During light exposure time ($t_{h\nu}$) the system develops from a relative loose structure to a more compact structure, indicated by the increasing fractal dimension. R_g follows the same trend as seen in $R_{h,2}$. 138

6.8 Thin film fabrication sequence of light exposed C_{60}/toluene solutions. Once the necessary light exposure had been carried out, the sample was left to rest in the dark before PS/toluene solution was added and the film was fabricated with all solutions being the same age. Exposure times of 9, 15 and 21 hours are shown. . 142

6.9 Optical microscopy images of PS/C_{60} thin films (h=120 nm) annealed at 150 °C for 1 h after various light exposure times noted on each image. 143

6.10 OM images from *in situ* annealing of 120 nm thin PS/C_{60} films fabricated using C_{60}/toluene solutions exposed to laser light for 0, 14 and 21 hours. Annealing time is indicated along the top row in minutes. Black and red circled regions are discussed in the text. 144

6.11 Image analysis of OM images shown in (a) Figures 6.9 and (b) 6.10 for 0 (■), 14 (●) and 21 h (▲) solution light exposure giving the number of C_{60} clusters on thin films. 144

6.12 (a-f) Optical microscopy images of films fabricated from solutions exposed to light for 0, 7 and 14 hours annealed at (a-c) 150 °C for 1 hour and (d-f) 180 °C for 30 minutes. 146

6.13 (a-c) Optical microscopy images of C_{60} concentration series in thin films with 5, 3 and 1 wt% C_{60} annealed at 150 °C for 1 hour. (d) Results from image analysis of (a-c) (in blue) overlaid with data shown in Figure 6.11a on the top axis. The dashed line indicates an approximate level (at y=10) which indicates that the films at 1 and 3 wt% are similar to that at 21 h of solution light exposure. . . . 147

6.14 (a-c) AFM images of as cast films prepared from (a) unexposed, (b) 21 h light exposed and (c) 21 h light exposed and agitated C_{60}/toluene solutions. (d-f) Optical microscopy images of films shown in (a-c) annealed at 150°C for 1 hour. . 148
6.15 DLS correlation function, $g^1(t)$, for a control study of freshly prepared (▪) and exposed to 633 nm HeNe laser for 12 hours (▪) 0.5 wt% PCBM in toluene. 149
6.16 Optical microscopy images of 20 wt% PCBM/PS thin films (h=75 nm). (a-c) PCBM/toluene solution not exposed to light (d-f) PCBM/toluene solution exposure to laser light for 19 h. Films were annealed at 150 °C for times of (a, d) 30, (b, e) 60 and (c, f) 90 minutes are shown. (Images were taken with a black and white AVT Marlin camera) 150
6.17 Optical microscopy images of 30 wt% PCBM/100k RRa P3HT thin films (h=70 nm) fabricated from a PCBM/toluene solution exposed to (a, c, e) 0 and (b, d, f) 24 h. (a-b) As cast and (c-f) annealed at 150 °C for 1 hour. Scale bar in (d) applies to (a-d) and scale bar in (f) applies to (e-f). 151
6.18 (a-f) Optical microscopy and (g-i) atomic force microscopy images of (a, d, g) 50k RR-P3HT and (b-c, e-f, h-i) 20wt% PCBM/50k RR-P3HT thin films (h=50 nm) fabricated from a PCBM/toluene solution exposed to light for (b, e, f) 0 and (c, f, i) 24 h. (a-c) show as cast films, and (d-i) films annealed at 150 °C for 1 hour. 152

A1 GPC traces for two of the polystyrene M_w used in Chapter 5 with 18000 and 775000 $gmol^{-1}$ 157
A2 ^{13}C NMR of C_{60} in toluene. 158
A3 ^{13}C NMR of C_{60} in toluene exposed to red laser for 21 hours. 159
A4 Correlation function $g^{(2)}(q,t)$ after 1 hour light exposure of 0.2 wt% C_{60}/toluene from 633 nm, 4 mW laser, high intensity white and ambient light. A 0.3 wt% C_{60}/toluene solution was exposed to 365 nm, 100 W UV light for 26 hours. Inset shows spectra of high intensity white, UV and ambient light, measured using a spectrophotometer (EPP2000c, StellarNet Inc.). 160

List of Tables

2.1 Surface energies of the substrates used in Refs. 156–160. 28

3.1 Summary of constants used in Equations 3.6 to 3.8 36
3.2 Summary of SLD's of components used in this investigation 38
3.3 Summary of form factors, $P(Q)$, and their corresponding shapes. The variables the polymer with excluded volume model are: excluded volume parameter, ν, $U = \frac{q^2a^2n^{2\nu}}{6}$, where a is the statistical segment length and n is the number of steps, γ is an incomplete gamma function so that $\gamma = \int_0^U dt \exp(-t)t^{x-1}$. For the polydisperse Gaussian chain: $x = \frac{R_g^2q^2}{1+2/h}$, here $h = \frac{M_w}{M_n}$ and for Porod scattering S_V is the specific surface area or surface to volume ratio [102, 195, 196]. 40
3.4 Summary of typical power laws, $I \propto q^{-\alpha}$ [102]. 41

4.1 Summary of isopleths in this chapter, with polystyrene M_w, solution regime, objective of isopleth and technique used. Concentrations of individual samples can be found in Table 4.2. 47
4.2 Summary of isopleths investigated, all concentrations (c_i) in the system are reported by the ratio of the mass of component i to the total mass of the solution (mass fraction of total ternary mass), ratio C_{60}:PS and polystyrene molecular weight. 51
4.3 Summary of constants used in Equations 3.4 to 3.8 52

5.1 Summary of PS/C_{60}/toluene mixtures investigated, all concentrations (c_i) in the system are reported by the ratio of the mass of component i to the total mass of the solution (mass fraction of total ternary mass), mass fraction of C_{60} and whether the system appeared stable (S) or precipitated (P) after two days of stirring. 76
5.2 Summary of solutions used in the following thin films study. Given are solution name, starting solution concentrations parameters, C_{60} mass fraction (to PS), state, either stable (S) or precipitated (P), and film thickness (h) studied. For simplicity, in the following discussion samples P1C01, P1.5C015 and P2C02 are referred to as 60 nm films, and P2.3C012 and P4C021 as 130 nm. 92
5.3 Expected and actual volume fractions (V_f) for the films studied. 104

5.4 Summary of 775k PS/PCBM/toluene mixtures investigated, all concentrations (c_i) in the system are reported by the ratio of the mass of component i to the total mass of the solution (mass fraction of total ternary mass), and and whether the system appeared stable (S) or aggregated (A) after two days of stirring. . . . 118
5.5 Summary of 775k PS/PCBM/chlorobenzene mixtures investigated, all concentrations (c_i) in the system are reported by the ratio of the mass of component i to the total mass of the solution (mass fraction of total ternary mass), and whether the system appeared stable (S) or aggregated (A) after two days of stirring. . . . 120
5.6 Summary of Hansen Solubility Parameters (HSPs) for components used, interaction radius (Ro) given for solutes and relative energy difference (RED) between solute/solvent pairs. A range of values is given for PCBM, with the centre of the range given for the HSPs and Ro, as there is no definite value in the literature [203, 204]. Shaded values are discussed within the text. 120

6.1 Summary of light induced degradation, polymerisation and oxidation of C_{60}/solvent systems as well as aggregation reported in literature [77–79, 83, 84]. 125
6.2 Summary of fitting parameters, size regimes and species. 128

List of Schematics

5.1 Schematic depicting presence of fullerene clusters within a PS thin film, showing differences within cluster formation depending on the casting solution. The clusters with a width of ~1 μm have previously been shown to have a 'raspberry' structure (i.e. a compact cluster composed of ~100 nm clusters) [8] but this is not depicted in the schematic for simplicity. 111

5.2 Schematic depicting presence of fullerene clusters (10-100's nm) alongside individual C_{60} molecules and undisturbed polystyrene chains. Fullerene agglomeration occurs for sufficiently large polymer concentration in solution, and increases for larger polymer M_w at constant mass fraction. 122

6.1 Schematic of laser light exposure set up, the laser was passed through the centre of the solution. 126

6.2 Schematic of a $C_{60}O_x$ molecule rotating around another. The interactions will be identical from L^1 to L^2 and oxygen atoms will begin to repel each other going from L^2 to L^3. 132

6.3 Schematic of light exposure of C_{60}/toluene solutions in ambient conditions, and subsequent formation of fullerene epoxide and microscopic fullerene particles. . . 140

Bibliography

[1] Vandewal, K.; Himmelberger, S.; Salleo, A. *Macromolecules* **2013**, *46*, 6379–6387.

[2] Thompson, B. C.; Fréchet, J. M. J. *Angewandte Chemie (International ed. in English)* **2008**, *47*, 58–77.

[3] Dattani, R.; Michels, R.; Nedoma, A. J.; Schweins, R.; Westacott, P.; Huber, K.; Cabral, J. T. *Macromolecules* **2014**, *47*, 6113–6120.

[4] Huber, K.; Bantle, S.; Lutz, P.; Burchard, W. *Macromolecules* **1985**, *18*, 1461–1467.

[5] Huber, K.; Burchard, W.; Akcasu, A. Z. *Macromolecules* **1985**, *18*, 2743–2747.

[6] Wong, H. C.; Sanz, A.; Douglas, J. F.; Cabral, J. T. *Journal of Molecular Liquids* **2010**, *153*, 79–87.

[7] Mackay, M. E.; Tuteja, A.; Duxbury, P. M.; Hawker, C. J.; Van Horn, B.; Guan, Z.; Chen, G.; Krishnan, R. S. *Science* **2006**, *311*, 1740–1743.

[8] Wong, H. C.; Cabral, J. T. *Physical Review Letters* **2010**, *105*, 38301.

[9] Wong, H. C.; Cabral, J. T. *Macromolecules* **2011**, *44*, 4530–4537.

[10] Yaklin, M. A.; Duxbury, P. M.; Mackay, M. E. *Soft Matter* **2008**, *4*, 2441–2447.

[11] Yasuda, T.; Shinohara, Y.; Matsuda, T.; Han, L.; Ishi-i, T. *Journal of Polymer Science Part A: Polymer Chemistry* **2013**, *51*, 2536–2544.

[12] Casey, A.; Ashraf, R. S.; Fei, Z.; Heeney, M. *Macromolecules* **2014**, *47*, 2279–2288.

[13] Ashraf, R. S.; Schroeder, B. C.; Bronstein, H. A.; Huang, Z.; Thomas, S.; Kline, R. J.; Brabec, C. J.; Rannou, P.; Anthopoulos, T. D.; Durrant, J. R.; McCulloch, I. *Advanced Materials* **2013**, *25*, 2029–34.

[14] de Gennes, P. G. *Scaling Concepts in Polymer Physics*; Cornell University Press, 1979.

[15] Doi, M. *Introduction to Polymer Physics*; Clarendon Press, 2001.

[16] Cabral, J. T. Polymer Blends: Equilibrium, Dynamics and Phase Separation. Ph.D. thesis, University of London, London, 2002.

[17] Strobl, G. R. *The Physics of Polymers: Concepts for Understanding Their Structures and Behavior*; Springer, 2007.

[18] Colby, R. H. *Rheologica Acta* **2009**, *49*, 425–442.

[19] Brown, W.; Nicolai, T. *Colloid & Polymer Science* **1990**, *268*, 977–990.

[20] King, J. S.; Boyer, W.; Wignall, G. D.; Ullman, R. *Macromolecules* **1985**, *18*, 709–718.

[21] Hamada, F.; Kinugasa, S.; Hayashi, H.; Nakajima, A. *Macromolecules* **1985**, *18*, 2290–2294.

[22] Flory, P. J. *The Journal of Chemical Physics* **1942**, *307*, 51–61.

[23] Huggins, M. L. *Annals of the New York Academy of Sciences* **1942**, *43*, 1–32.

[24] Ginzburg, V. V.; Balazs, A. C. *Macromolecules* **1999**, *32*, 5681–5688.

[25] Doi, M.; Edwards, S. F. *International Series of Monographs on Physics* **1988**, *73*.

[26] Hansen, C. M. *Hansen Solubility Parameters : A User's Handbook, Second Edition*; Taylor and Francis: Hoboken, 2007.

[27] Lekkerkerker, H. N.; Tuinier, R. *Colloids and the Depletion Interaction*; Lecture Notes in Physics; Springer, 2011; Vol. 833.

[28] Vrij, A. *Pure and Applied Chemistry* **1976**, *48*, 471–483.

[29] Asakura, S.; Oosawa, F. *The Journal of Chemical Physics* **1954**, *22*, 1255.

[30] Bechinger, C.; Rudhardt, D.; Leiderer, P.; Roth, R.; Dietrich, S. *Physical Review Letters* **1999**, *83*, 3960–3963.

[31] Odijk, T. *Macromolecules* **1996**, *29*, 1842–1843.

[32] de Gennes, P. G. *Comptes Rendus de l'Académie des Sciences* **1979**, *288*, 359–361.

[33] Sear, R. *Physical Review E* **1998**, *58*, 724–728.

[34] Sear, R. *Physical Review Letters* **2001**, *86*, 4696–4699.

[35] Schoot, P. V. D. *Macromolecules* **1998**, *31*, 4635–4638.

[36] Kramer, T.; Scholz, S.; Maskos, M.; Huber, K. *Journal of Colloid and Interface Science* **2004**, *279*, 447–57.

[37] Kramer, T.; Schweins, R.; Huber, K. *Macromolecules* **2005**, *38*, 151–159.

[38] Kramer, T.; Schweins, R.; Huber, K. *Macromolecules* **2005**, *38*, 9783–9793.

[39] Kramer, T.; Schweins, R.; Huber, K. *The Journal of Chemical Physics* **2005**, *123*, 014903.

[40] Polson, A.; Potgieter, G.; Largier, J.; Mears, G.; Joubert, F. *Biochimica et Biophysica Acta* **1964**, *82*, 463–475.

[41] Schaefer, D. *MRS Bulletin* **1988**, 22–27.

[42] Meakin, P. In *On Growth and Form*; Stanley, H. E., Ostrowsky, N., Eds.; Martinus Nijhoff Publishers: Dordrecht, 1986; Chapter 5, pp 11–135.

[43] Keefer, K. D. *MRS Proceedings* **1986**, *73*, 295–304.

[44] Di Biasio, A.; Bolle, G.; Cametti, C.; Codastefano, P.; Sciortino, F.; Tartaglia, P. *Physical Review E* **1994**, *50*, 1649–1652.

[45] Eden, M. A Two-Dimensional Growth Process. 4th Berkeley Symposium on Mathematical Statistics and Probability. 1961; pp 223–239.

[46] Keefer, K.; Schaefer, D. *Physical Review Letters* **1986**, *56*, 2376–2379.

[47] Verwey, E. J. W.; Overbeek, J. T. G. *Theory of the Stability of Lyophobic Colloids: The Interaction of Sol Particles Having an Electric Double Layer*; Elsevier Publishing Company, 1948; p 205.

[48] Lin, M. Y.; Lindsay, H. M.; Weitz, D. A.; Ball, R. C.; Klein, R.; Meakin, P. *Nature* **1989**, *339*, 360–362.

[49] Lint, M. Y.; Lindsay, H. M.; Weitzo, D. A.; Klein, R.; Ball, R. C.; Meakin, P. *Journal of Physics: Condensed Matter* **1990**, *2*, 3093–3113.

[50] Vold, M. J. *Journal of Colloid Science* **1959**, 168–174.

[51] Vold, M. J. *The Journal of Physical Chemistry* **1959**, *63*, 1608–1612.

[52] Vold, M. J. *The Journal of Physical Chemistry* **1960**, *64*, 1616–1619.

[53] Vold, M. *Journal of Colloid Science* **1963**, 684–695.

[54] Sutherland, D. *Journal of Colloid and Interface Science* **1966**, *22*, 300–302.

[55] Sutherland, D. N. *Journal of Colloid and Interface Science* **1967**, *25*, 373–380.

[56] Witten, T.; Sander, L. *Physical Review Letters* **1981**, *47*, 1400–1403.

[57] Meakin, P. *Physical Review Letters* **1983**, *51*, 1119–1122.

[58] Kolb, M.; Botet, R.; Jullien, R.; Herrmann, H. J. In *On Growth and Form*; Stanley, H. E., Ostrowsky, N., Eds.; Martinus Nijhoff Publishers, 1986; pp 222–226.

[59] Burroughes, J. H.; Bradley, D. D. C.; Brown, A. R.; Marks, R. N.; Mackay, K.; Friend, R. H.; Burns, P. L.; Holmes, A. B. *Nature* **1990**, *347*, 539–541.

[60] Sehgal, A.; Seery, T. A. P. *Macromolecules* **1999**, *32*, 7807–7814.

[61] Dadmun, M. Private Communication.

[62] Heffner, G. W.; Pearson, D. S. *Macromolecules* **1991**, *24*, 6295–6299.

[63] Hotta, S.; Soga, M.; Sonoda, N. *Synthetic Metals* **1988**, *26*, 267–279.

[64] McCullough, R. D. *Advanced Materials* **1998**, *10*, 93–116.

[65] Bannock, J. H. Private Communication.

[66] Huang, Y.; Cheng, H.; Han, C. C. *Macromolecules* **2010**, *43*, 10031–10037.

[67] McCulloch, B.; Ho, V.; Hoarfrost, M.; Stanley, C.; Do, C.; Heller, W. T.; Segalman, R. A. *Macromolecules* **2013**, *46*, 1899–1907.

[68] Wignall, G.; Ballard, D.; Schelten, J. *European Polymer Journal* **1974**, *10*, 861–865.

[69] Wirix, M. J. M.; Bomans, P. H. H.; Friedrich, H.; Sommerdijk, N. A. J. M.; de With, G. *Nano letters* **2014**, *14*, 2033–8.

[70] Wang, D.; Yuan, Y.; Mardiyati, Y.; Bubeck, C.; Koynov, K. *Macromolecules* **2013**, *46*, 6217–6224.

[71] Everett, D. *Pure and Applied Chemistry* **1972**, *31*, 557–638.

[72] Skrdla, P. J. *Langmuir* **2012**, *28*, 4842–57.

[73] Barros, K.; Luijten, E. *Physical Review Letters* **2014**, *113*, 017801.

[74] Migliardo, F.; Magazù, V.; Migliardo, M. *Journal of Molecular Liquids* **2004**, *110*, 3–6.

[75] Branca, C.; Magazù, V.; Mangione, A.; Migliardo, F.; Romeo, G. *Diamond and Related Materials* **2004**, *13*, 1333–1336.

[76] Tropin, T.; Avdeev, M.; Aksenov, V. *Crystallography Reports* **2007**, *52*, 483.

[77] Taylor, R.; Parsons, J. P.; Avent, A. G.; Rannard, S. P.; Dennis, T. J.; Hare, J. P.; Kroto, H. W.; Walton, D. R. M. *Nature* **1991**, *351*, 277–277.

[78] Juha, L.; Krása, J.; Láska, L.; Hamplová, V.; Soukup, L.; Engst, P.; Kubát, P. *Applied Physics B Photophysics and Laser Chemistry* **1993**, *57*, 83–84.

[79] Cataldo, F. *Polymer International* **1999**, *48*, 143–149.

[80] Tajima, Y.; Takeshi, K.; Shigemitsu, Y.; Numata, Y. *Molecules* **2012**, *17*, 6395–414.

[81] Wood, J. M.; Kahr, B.; Hoke, S. H.; Dejarme, L.; Cooks, R. G.; Ben-Amotz, D. *Journal of the American Chemical Society* **1991**, *113*, 5907–5908.

[82] Creegan, K. M.; Robbins, J. L.; Robbins, W. K.; Millar, J. M.; Sherwood, R. D.; Tindall, P. J.; Cox, D. M.; McCauley, J. P.; Jones, D. R. *Journal of the American Chemical Society* **1992**, *114*, 1103–1105.

[83] Ying, Q.; Marecek, J.; Chu, B. *Chemical Physics Letters* **1994**, *219*, 214–218.

[84] Ying, Q.; Marecek, J.; Chu, B. *The Journal of Chemical Physics* **1994**, *101*, 2665.

[85] Török, G.; Lebedev, V.; Cser, L. *Physics of the Solid State* **2002**, *44*, 572.

[86] Sun, Y.-P.; Bunker, C. E. *Nature* **1993**, *365*, 398.

[87] Nath, S.; Pal, H.; Sapre, A. V. *Chemical Physics Letters* **2000**, *327*, 143–148.

[88] Meng, Z.; Hashmi, S. M.; Elimelech, M. *Journal of Colloid and Interface Science* **2013**, *392*, 27–33.

[89] Guinier, A.; Fournet, G. *Small-angle Scattering of X-rays*; Structure of matter series; Wiley, 1955.

[90] Teixeira, J. *J. Appll. Cryst.* **1988**, *21*, 781–785.

[91] Asakura, S.; Oosawa, F. *Journal of Polymer Science* **1958**, *33*, 183–192.

[92] De Hek, H.; Vrij, A. *Journal of Colloid and Interface Science* **1979**, *70*, 592–594.

[93] De Hek, H.; Vrij, A. *Journal of Colloid and Interface Science* **1981**, *84*, 409–422.

[94] De Hek, H.; Vrij, A. *Journal of Colloid and Interface Science* **1982**, *88*, 258–273.

[95] Tuinier, R.; Rieger, J.; de Kruif, C. G. *Advances in Colloid and Interface Science* **2003**, *103*, 1–31.

[96] Mutch, K. J.; Duijneveldt, J. S. V.; Eastoe, J.; Grillo, I.; Heenan, R. K. *Langmuir* **2008**, *24*, 3053–60.

[97] Dominak, L. M.; Keating, C. D. *Langmuir* **2008**, *24*, 13565–71.

[98] Ye, X.; Narayanan, T.; Tong, P.; Huang, J.; Lin, M.; Carvalho, B.; Fetters, L. *Physical Review E* **1996**, *54*, 6500–6510.

[99] Ye, X.; Narayanan, T.; Tong, P.; Huang, J. *Physical Review Letters* **1996**, *76*, 4640–4643.

[100] Sobkowicz, M. J.; Jones, R. L.; Kline, R. J.; DeLongchamp, D. M. *Macromolecules* **2012**, *45*, 1046–1055.

[101] Nakatani, A. I.; Chen, W.; Schmidt, R. G.; Gordon, G. V.; Han, C. C. *Polymer* **2001**, *42*, 3713–3722.

[102] Higgins, J. S.; Benoit, H. C. *Polymers and Neutron Scattering*; Oxford Science Publications, 1994.

[103] Paul, D. R.; Newman, S. *Polymer Blends*; Academic Press Inc.: Orlando, 1978.

[104] Higgins, J. S.; Lipson, J. E. G.; White, R. P. *Philosophical Transactions. Series A, Mathematical, Physical, and Engineering Sciences* **2010**, *368*, 1009–25.

[105] Krause, S.; Roman, N. *Journal of Polymer Science Part A: General Papers* **1965**, *3*, 1631–1640.

[106] Tuteja, A.; Duxbury, P. M.; Mackay, M. E. *Physical Review Letters* **2008**, *100*, 77801.

[107] Sen, S.; Xie, Y.; Kumar, S.; Yang, H.; Bansal, A.; Ho, D.; Hall, L.; Hooper, J.; Schweizer, K. *Physical Review Letters* **2007**, *98*, 128302.

[108] Nusser, K.; Neueder, S.; Schneider, G. J.; Meyer, M.; Pyckhout-Hintzen, W.; Willner, L.; Radulescu, A.; Richter, D. *Macromolecules* **2010**, *43*, 9837–9847.

[109] Genix, A.-C.; Tatou, M.; Imaz, A.; Forcada, J.; Schweins, R.; Grillo, I.; Oberdisse, J. *Macromolecules* **2012**, *45*, 1663–1675.

[110] Crawford, M. K.; Smalley, R. J.; Cohen, G.; Hogan, B.; Wood, B.; Kumar, S. K.; Melnichenko, Y. B.; He, L.; Guise, W.; Hammouda, B. *Physical Review Letters* **2013**, *110*, 196001.

[111] Yin, W.; Dadmun, M. *ACS nano* **2011**, *5*, 4756–68.

[112] Rao, A.; Zhou, P.; Wang, K.-A.; Hager, G. T.; Holden, J. M.; Wang, Y.; Bi, X.-X.; Eklund, P. C.; Cornett, D. S.; Duncan, M. A.; Amster, I. J.; Lee, W. T.; Amster, J. *Science* **1993**, *259*, 955–957.

[113] Zhou, P.; Dong, Z.-H.; Rao, A. M.; Eklund, P. C. *Chemical Physics Letters* **1993**, *211*, 337–340.

[114] Eklund, P.; Rao, A.; Zhou, P.; Wang, Y.; Holden, J. *Thin Solid Films* **1995**, *257*, 185–203.

[115] Wang, Y.; Holden, J. M.; Dong, Z.-H.; Bi, X.-X.; Eldund, P. C. *Chemical Physics Letters* **1993**, *211*, 341–345.

[116] Wang, Y.; Holden, J. M.; Bi, X.-X.; Eklund, P. C. *Chemical Physics Letters* **1994**, *217*, 413–417.

[117] Yamamoto, Y.; Ichikawa, H.; Ueno, K.; Koma, A.; Saiki, K.; Shimada, T. *Physical Review B* **2004**, *70*, 155415.

[118] Alvarez-Zauco, E.; Sobral, H.; Basiuk, E.; Saniger-Blesa, J.; Villagrán-Muniz, M. *Applied Surface Science* **2005**, *248*, 243–247.

[119] Rao, A.; Wang, K.-A.; Holden, J.; Wang, Y.; Zhou, P.; Eklund, P.; Eloi, C.; Robertson, J. *Journal of Materials Research* **1993**, *8*, 2277–2281.

[120] Yao, M.; Andersson, B. M.; Stenmark, P.; Sundqvist, B.; Liu, B.; Wagberg, T. *Carbon* **2009**, *47*, 1181–1188.

[121] Iio, Y.; Kurihara, K.; Matsuyama, F.; Nokariya, R.; Iwata, N.; Yamamoto, H. *Journal of Physics: Conference Series* **2009**, *159*, 012019.

[122] Zheng, L.; Han, Y. *The Journal of Physical Chemistry B* **2012**, *116*, 1598–604.

[123] Masuhara, A.; Tan, Z.; Kasai, H.; Nakanishi, H.; Oikawa, H. *Japanese Journal of Applied Physics* **2009**, *48*, 050206.

[124] Jeong, J.; Kim, W.-S.; Park, S.-I.; Yoon, T.-S.; Chung, B. H. *The Journal of Physical Chemistry C* **2010**, *114*, 12976–12981.

[125] Dabirian, R.; Feng, X.; Ortolani, L.; Liscio, A.; Morandi, V.; Müllen, K.; Samorì, P.; Palermo, V. *Physical Chemistry Chemical Physics* **2010**, *12*, 4473–80.

[126] Jouault, N.; Dalmas, F.; Said, S.; Di Cola, E.; Schweins, R.; Jestin, J.; Boué, F. *Macromolecules* **2010**, *43*, 9881–9891.

[127] Kumar, S. K.; Jouault, N.; Benicewicz, B.; Neely, T. *Macromolecules* **2013**, 130423114749006.

[128] Jouault, N.; Zhao, D.; Kumar, S. K. *Macromolecules* **2014**, *47*, 5246–5255.

[129] Kropka, J. M.; Putz, K. W.; Pryamitsyn, V.; Ganesan, V.; Green, P. F. *Macromolecules* **2007**, *40*, 5424–5432.

[130] Weng, D.; Lee, H.; Levon, K.; Mao, J.; Scrivens, W.; Stephens, E.; Tour, J. *European Polymer Journal* **1999**, *35*, 867–878.

[131] Müller, C.; Ferenczi, T. A. M.; Campoy-Quiles, M.; Frost, J. M.; Bradley, D. D. C.; Smith, P.; Stingelin-Stutzmann, N.; Nelson, J. *Advanced Materials* **2008**, *20*, 3510–3515.

[132] Zhao, J.; Swinnen, A.; Van Assche, G.; Manca, J.; Vanderzande, D.; Mele, B. V. *The Journal of Physical Chemistry B* **2009**, *113*, 1587–1591.

[133] Hopkinson, P. E.; Staniec, P. a.; Pearson, A. J.; Dunbar, A. D. F.; Wang, T.; Ryan, A. J.; Jones, R. a. L.; Lidzey, D. G.; Donald, A. M. *Macromolecules* **2011**, *44*, 2908–2917.

[134] Nicolet, C.; Deribew, D.; Renaud, C.; Fleury, G.; Brochon, C.; Cloutet, E.; Vignau, L.; Wantz, G.; Cramail, H.; Geoghegan, M.; Hadziioannou, G. *The Journal of Physical Chemistry B* **2011**, *115*, 12717–27.

[135] Perkin Elmer, *Tg and Melting Point of a Series of Polyethylene Glycols Using the Material Pocket*.

[136] Chen, H.; Hegde, R.; Browning, J.; Dadmun, M. D. *Physical Chemistry Chemical Physics* **2012**, *14*, 5635–41.

[137] Kozub, D. R.; Vakhshouri, K.; Orme, L. M.; Wang, C.; Hexemer, A.; Gomez, E. D. *Macromolecules* **2011**, *44*, 5722–5726.

[138] Jamieson, F. C.; Domingo, E. B.; McCarthy-Ward, T.; Heeney, M.; Stingelin, N.; Durrant, J. R. *Chemical Science* **2012**, *3*, 485.

[139] Keddie, J.; Routh, A. F. *Fundamentals of Latex Film Formation - Processes and Properties*; Springer Laboratory, 2010.

[140] Halim, A.; Fu, Q.; Yong, Q.; Gurr, P. A.; Kentish, S. E.; Qiao, G. G. *Journal of Materials Chemistry A* **2014**, *2*, 4999.

[141] Böker, A.; He, J.; Emrick, T.; Russell, T. P. *Soft Matter* **2007**, *3*, 1231.

[142] Penkov, O. V.; Pukha, V. E.; Devizenko, A. Y.; Kim, H.-J.; Kim, D.-E. *Nano letters* **2014**, *14*, 2536–40.

[143] Reiter, G. *Physical Review Letters* **1992**, *68*, 75–78.

[144] Reiter, G. *Langmuir* **1993**, *9*, 1344–1351.

[145] Sharma, A.; Reiter, G. *Journal of Colloid and Interface Science* **1996**, *178*, 383–399.

[146] Xie, R.; Karim, A.; Douglas, J.; Han, C.; Weiss, R. *Physical Review Letters* **1998**, *81*, 1251–1254.

[147] Reiter, G.; Sharma, A.; Casoli, A.; David, M.-O.; Khanna, R.; Auroy, P. *Langmuir* **1999**, *15*, 2551–2558.

[148] Katzenstein, J. M.; Janes, D. W.; Cushen, J. D.; Hira, N. B.; McGuffin, D. L.; Prisco, N. A.; Ellison, C. J. *ACS Macro Letters* **2012**, *1*, 1150–1154.

[149] Botiz, I.; Freyberg, P.; Stingelin, N.; Yang, A. C.-M.; Reiter, G. *Macromolecules* **2013**, *46*, 2352–2356.

[150] Barnes, K. A.; Douglas, J. F.; Liu, D.-W.; Karim, A. *Advances in Colloid and Interface Science* **2001**, *94*, 83–104.

[151] Holmes, M.; Mackay, M.; Giunta, R. *Journal of Nanoparticle Research* **2007**, *9*, 753–763.

[152] Wong, H. C.; Higgins, A. M.; Wildes, A. R.; Douglas, J. F.; Cabral, J. T. *Advanced Materials* **2012**, *25*, 985–991.

[153] Wei, H. X.; Li, J.; Xu, Z. Q.; Cai, Y.; Tang, J. X.; Li, Y. Q. *Applied Physics Letters* **2010**, *97*, 083302.

[154] Wong, H. C. Polymer-fullerene mixtures: structure , dynamics and engineering applications in bulk and thin films. Ph.D. thesis, Imperial College London, 2011.

[155] Bandyopadhyay, D.; Grolman, D.; Singh, G.; Douglas, J. F.; Karim, A. *Polymer* **2013**, *54*, 6206–6209.

[156] Parnell, A. J.; Dunbar, A. D. F.; Pearson, A. J.; Staniec, P. A.; Dennison, A. J. C.; Hamamatsu, H.; Skoda, M. W. A.; Lidzey, D. G.; Jones, R. A. L. *Advanced Materials* **2010**, *22*, 2444.

[157] Campoy-Quiles, M.; Ferenczi, T.; Agostinelli, T.; Etchegoin, P. G.; Kim, Y.; Anthopoulos, T. D.; Stavrinou, P. N.; Bradley, D. D. C.; Nelson, J. *Nature Materials* **2008**, *7*, 158–164.

[158] Germack, D. S.; Chan, C. K.; Hamadani, B. H.; Richter, L. J.; Fischer, D. a.; Gundlach, D. J.; DeLongchamp, D. M. *Applied Physics Letters* **2009**, *94*, 233303.

[159] Germack, D. S.; Chan, C. K.; Kline, R. J.; Fischer, D. A.; Gundlach, D. J.; Toney, M. F.; Richter, L. J.; DeLongchamp, D. M. *Macromolecules* **2010**, *43*, 3828–3836.

[160] Van-Bavel, S. S.; Sourty, E.; de With, G.; Loos, J. *Nano Letters* **2009**, *9*, 507–13.

[161] Wang, H.; Gomez, E. D.; Kim, J.; Guan, Z.; Jaye, C.; Fischer, D. A.; Kahn, A.; Loo, Y.-L. *Chemistry of Materials* **2011**, *23*, 2020–2023.

[162] Jones, R. A. L.; Norton, L. J.; Kramer, E. J.; Bates, F. S.; Wiltzius, P. *Physical Review Letters* **1991**, *66*, 1326.

[163] Vaynzof, Y.; Kabra, D.; Zhao, L.; Chua, L. L.; Steiner, U.; Friend, R. H. *ACS Nano* **2010**, *5*, 329–336.

[164] Lee, J.-Y.; Zhang, Q.; Emrick, T.; Crosby, A. J. *Macromolecules* **2006**, *39*, 7392–7396.

[165] Liu, J.; Geng, J.; Liao, L.-D.; Thakor, N.; Gao, X.; Liu, B. *Polymer Chemistry* **2014**, *5*, 2854.

[166] Byeon, J. H.; Kim, J.-W. *ACS Macro Letters* **2014**, *3*, 369–373.

[167] Wei, Y.-Z.; Wang, G.-S.; Wu, Y.; Yue, Y.-H.; Wu, J.-T.; Lu, C.; Guo, L. *Journal of Materials Chemistry A* **2014**, *2*, 5516.

[168] Gao, Y.; Wu, J.; Wang, Q.; Wilkie, C. A.; O'Hare, D. *Journal of Materials Chemistry A* **2014**, *2*, 10996.

[169] Winey, K. I.; Vaia, R. A. *MRS Bulletin* **2011**, *32*, 314–322.

[170] Vollenberg, P.; Heikens, D. *Polymer* **1989**, *30*, 1656–1662.

[171] Singh, R. P.; Zhang, M.; Chan, D. *Journal of Materials Science* **2002**, *37*, 781–788.

[172] Cho, J.; Paul, D. *Polymer* **2001**, *42*, 1083–1094.

[173] Moll, J. F.; Akcora, P.; Rungta, A.; Gong, S.; Colby, R. H.; Benicewicz, B. C.; Kumar, S. K. *Macromolecules* **2011**, *44*, 7473–7477.

[174] Vaia, R. A.; Giannelis, E. P. *MRS Bulletin* **2011**, *26*, 394–401.

[175] http://autonomicmaterials.com/applications/, Accessed August 2014.

[176] Hager, M. D.; Greil, P.; Leyens, C.; van der Zwaag, S.; Schubert, U. S. *Advanced Materials* **2010**, *22*, 5424–30.

[177] Gupta, S.; Zhang, Q.; Emrick, T.; Balazs, A. C.; Russell, T. P. *Nature Materials* **2006**, *5*, 229–233.

[178] Sariciftci, N. S.; Smilowitz, L.; Heeger, A. J.; Wudl, F. *Science* **1992**, *258*, 1474–1476.

[179] Treat, N. D.; Nekuda Malik, J. A.; Reid, O.; Yu, L.; Shuttle, C. G.; Rumbles, G.; Hawker, C. J.; Chabinyc, M. L.; Smith, P.; Stingelin, N. *Nature Materials* **2013**, *12*, 628–33.

[180] Richards, J. J.; Rice, A. H.; Nelson, R. D.; Kim, F. S.; Jenekhe, S. A.; Luscombe, C. K.; Pozzo, D. C. *Advanced Functional Materials* **2013**, *23*, 514–522.

[181] Liang, Y.; Xu, Z.; Xia, J.; Tsai, S.-T.; Wu, Y.; Li, G.; Ray, C.; Yu, L. *Advanced Materials* **2010**, *22*, E135–8.

[182] Tang, H.; Lu, G.; Yang, X.; Haowei, T.; Guanghao, L.; Xiaoniu, Y. *IEEE Journal of Selected Topics in Quantum Electronics* **2010**, *16*, 1725–1731.

[183] Moon, J. S.; Takacs, C. J.; Cho, S.; Coffin, R. C.; Kim, H.; Bazan, G. C.; Heeger, A. J. *Nano Letters* **2010**, *10*, 4005–8.

[184] Diaz de Zerio Mendaza, A.; Bergqvist, J.; Bäcke, O.; Lindqvist, C.; Kroon, R.; Gao, F.; Andersson, M. R.; Olsson, E.; Inganäs, O.; Müller, C. *Journal of Materials Chemistry A* **2014**, *2*, 14354–14359.

[185] Hammond, M. R.; Kline, R. J.; Herzing, A. A.; Richter, L. J.; Germack, D. S.; Ro, H.-W.; Soles, C. L.; Fischer, D. a.; Xu, T.; Yu, L.; Toney, M. F.; Delongchamp, D. M. *ACS Nano* **2011**, *5*, 8248–57.

[186] Collins, B. A.; Li, Z.; Tumbleston, J. R.; Gann, E.; McNeill, C. R.; Ade, H. *Advanced Energy Materials* **2013**, *3*, 65–74.

[187] Liu, F.; Zhao, W.; Tumbleston, J. R.; Wang, C.; Gu, Y.; Wang, D.; Briseno, A. L.; Ade, H.; Russell, T. P. *Advanced Energy Materials* **2014**, *4*.

[188] Lou, S. J.; Szarko, J. M.; Xu, T.; Yu, L.; Marks, T. J.; Chen, L. X. *Journal of the American Chemical Society* **2011**, *133*, 20661–3.

[189] Siegert, A. J. F. *On the Fluctuations in Signals Returned by Many Independently Moving Scatterers*; Report (Massachusetts Institute of Technology. Radiation Laboratory); 1943; Vol. 465.

[190] Koppel, D. E. *Journal of Chemical Physics* **1972**, *57*.

[191] Provencher, S. W. *Computer Physics Communications* **1982**, *27*, 213–227.

[192] Zimm, B. H. *The Journal of Chemical Physics* **1948**, *16*, 1093.

[193] Kanai, S.; Muthukumar, M. *The Journal of Chemical Physics* **2007**, *127*, 244908.

[194] SasView, http://www.sasview.org/, Accessed November 2012.

[195] Hammouda, B. *Advances in Polymer Science* **1993**, *106*, 87–133.

[196] Hammouda, B.; Ho, D. L.; Kline, S. *Macromolecules* **2004**, *37*, 6932–6937.

[197] Hammouda, B.; Nakatani, A. I.; Waldow, D. A.; Han, C. C. *Macromolecules* **1992**, *25*, 2903–2906.

[198] Ruoff, R. S.; Tse, D. S.; Malhotra, R.; Lorents, D. C. *J Phys Chem* **1993**, *97*, 3379–3383.

[199] Brandrup, J.; Immergut, E. H.; Grulke, E. A.; Abe, A.; Bloch, D. R. *Polymer Handbook*, 4th ed.; John Wiley & Sons Inc, 2005.

[200] Freed, K. F. *Renormalization Group Theory of Macromolecules*; Wiley-Interscience, 1987.

[201] Daoud, M.; Cotton, J. P.; Farnoux, B.; Jannink, G.; Sarma, G.; Benoit, H.; Duplessix, C.; Picot, C.; de Gennes, P. G. *Macromolecules* **1975**, *8*, 804–818.

[202] Anderson, V. J.; Lekkerkerker, H. N. W. *Nature* **2002**, *416*, 811–5.

[203] Machui, F.; Langner, S.; Zhu, X.; Abbott, S.; Brabec, C. J. *Solar Energy Materials and Solar Cells* **2012**, *100*, 138–146.

[204] Hansen, C. M.; Smith, A. L. *Carbon* **2004**, *42*, 1591–1597.

[205] Brannock, G. R.; Paul, D. R. *Macromolecules* **1990**, *23*, 5240–5250.

[206] Koeppe, R.; Sariciftci, N. S. *Photochemical & Photobiological Sciences* **2006**, *5*, 1122–31.

[207] Schuster, D. I.; Baran, P. S.; Hatch, R. K.; Khan, A. U.; Wilson, S. R. *Chemical Communications* **1998**, 2493–2494.

[208] Besler, B. H.; Merz, K. M.; Kollman, P. A. *Journal of Computational Chemistry* **1990**, *11*, 431–439.

[209] Nayyar, I. H.; Batista, E. R.; Tretiak, S.; Saxena, A.; Smith, D. L.; Martin, R. L. *The Journal of Physical Chemistry Letters* **2011**, *2*, 566–571.

[210] Tajima, Y.; Takeuchi, K. C60O3 fullerene triepoxides with C1, C2, or Cs symmetry; separation by two-step column chromatography first with silica gel and then with a substance having p-p interactions such as pyrene-modified silica gel. 2005; `http://www.google.com/patents/US20050154219`.

[211] Nizam, R.; Rizvi, S. M. A.; Azam, A. *Journal of Nanotechnology in Engineering and Medicine* **2011**, *2*, 011015.

[212] Treat, N. D.; Brady, M. A.; Smith, G.; Toney, M. F.; Kramer, E. J.; Hawker, C. J.; Chabinyc, M. L. *Advanced Energy Materials* **2011**, *1*, 82–89.

[213] Wong, H. C.; Li, Z.; Tan, C. H.; Zhong, H.; Huang, Z.; Bronstein, H.; McCulloch, I.; Cabral, J. T.; Durrant, J. R. *ACS Nano* **2014**,

[214] http://www.solennebv.com/combray.htm. Accessed July 2013.

[215] Balch, A. L.; Costa, D. A.; Lee, J. W.; Noll, B. C.; Olmstead, M. M. *Inorganic Chemistry* **1994**, *33*, 2071–2072.